UC San Diego
UC San Diego Electronic Theses and Dissertations

Title
A Novel Approach to Beam Steering Using Arrays Composed of Multiple Unique Radiating Modes

Permalink
https://escholarship.org/uc/item/5v12274v

Author
Labadie, Nathan Richard

Publication Date
2015

Peer reviewed|Thesis/dissertation

eScholarship.org Powered by the California Digital Library
University of California

UNIVERSITY OF CALIFORNIA, SAN DIEGO

SAN DIEGO STATE UNIVERSITY

A Novel Approach to Beam Steering Using Arrays Composed of Multiple Unique Radiating Modes

A dissertation submitted in partial satisfaction of the
requirements for the degree
Doctor of Philosophy

in

Engineering Sciences (Electrical and Computer Engineering)

by

Nathan Richard Labadie

Committee in charge:

University of California, San Diego

Professor Gabriel M. Rebeiz, Co-Chair
Professor Brian Keating
Professor Daniel Sievenpiper

San Diego State University

Professor Satish K. Sharma, Co-Chair
Professor Gustaaf Jacobs

2015

Copyright
Nathan Richard Labadie, 2015
All rights reserved.

The dissertation of Nathan Richard Labadie is approved, and it is acceptable in quality and form for publication on microfilm and electronically:

Co-Chair

Co-Chair

University of California, San Diego

San Diego State University

2015

DEDICATION

To my loving wife and our beautiful children.

TABLE OF CONTENTS

LIST OF FIGURES

LIST OF TABLES

ACKNOWLEDGEMENTS

First and foremost I would like to thank both of my advisors for their guidance and patience during these past few years. Without my advisors, this thesis and the body of work that it represents would not have been possible. I will always be grateful to Professor Sharma for prodding me to apply to the doctoral program after completing my M.S. under his mentorship. As he knows well, there were many changes in my personal and professional life in the years that followed. He never ceased to be my advocate during difficult times and always maintained a positive attitude regardless of the challenges that lay ahead. Our many and lengthy technical discussions over the years were invaluable to keeping the research efforts on track on topic. I am proud to be the first of hopefully many doctoral students graduated under your tutelage. I wish to thank Professor Rebeiz for giving me the opportunity to pursue research under his mentorship and benefit from his wealth of knowledge and experience. Sharing his ability to quickly reduce seemingly very complex problems into a set of well defined tasks has helped me to grow both academically and in my career as a practicing antenna engineer. Thank you to the additional committee members for making themselves available to evaluate my work and my capability as a researcher: Prof. Daniel Sievenpiper, Prof. Brian Keating, Prof. Gustaaf Jacobs and Prof. Vitaly Lomakin. Two chapters of this dissertation are the result of my attempt to answer a single insightful question raised by Prof. Sievenpiper during the second exam. I hope I have sufficiently provided the ”apples to apples” analysis you asked for. I am very grateful for the thoughtful exchanges with the committee members throughout the program.

My friends and colleagues at Cubic Defense Applications have been a consistent source of support for the last few years. My supervisor, Jeff Keefer, continually challenged me with new and interesting work while being kind and flexible enough to accommodate an academic schedule. Wayne Richards always reminded me not to rely

solely on one equation in some textbook but to reach a consensus in one's own mind from at least three different points of view. I was fortunate enough to pursue parallel industry research while completing my degree. To all the comrades of the Halo development team, Jeff Keefer, Wayne Richards, Kevin Priest, Rob Morse, Tyson Wooten, Jerome Cruz, Jesse Bowman, Kevin Kurpiewski, thank you!

The support of my family has played an integral role in the successful completion of the doctoral program. I will miss the many nights that my brother Tim accompanied me to the lab while I made measurements. He was always willing to offer advice and listen to the frustration that comes naturally when ”progress” is being made. Like my brother, I owe the inborn curiosity that has driven me this far to my mom and dad. Mom, I will never forget those days when we were young dancing to songs on the record player and filling endless pages of blank white paper with whatever our imagination and crayons conjured. I have never felt as free as I did in those moments. Dad, thank you for the time you took to show us how to build things in that garage full of every well-worn tool and component imaginable. You always taught us to make do with the things available to us. We installed flooring in RVs, built wings for ultralight airplanes, repaired pneumatic tools and spent time dreaming up many devices all with very few resources.

I can never give enough credit to my wife and daughters for their perseverance as plans were canceled, late nights were spent in the lab and vacations were postponed. Our daughter Violet has been asking me ”when will your school be over Daddy?” ever since I remember her able to form coherent sentences. Our youngest daughter Alyanna is too young to speak and thankfully too young to remember the struggle and sacrifice this has cost. My wife has sacrificed the most out of love and out of hope for a happier and better life ahead. Thank you my love for all that you have given. I know you are so happy to hear these final words, ”it's done...”.

Chapter 2, in part, is a reprint of the material as it appears in IEEE Transactions on Antennas and Propagation, 2012. Labadie, Nathan R.; Sharma, Satish K.; Rebeiz, Gabriel, IEEE, 2012. The dissertation/thesis author was the primary investigator and author of this paper.

Chapter 3, in part, is a reprint of the material as it appears in IEEE Transactions on Antennas and Propagation, 2014. Labadie, Nathan R.; Sharma, Satish K.; Rebeiz, Gabriel, IEEE, 2014, and IEEE Antennas and Propagation Society International Symposium, 2014, Labadie, Nathan R.; Powell, Jack R.; Sharma, Satish K.; Rebeiz, Gabriel, IEEE, 2014. The dissertation/thesis author was the primary investigator and author of this paper.

Chapter 4, in part, has been submitted as it may appear in IEEE Transactions on Antennas and Propagation, 2015. Labadie, Nathan R.; Sharma, Satish K.; Rebeiz, Gabriel, IEEE, 2015. The dissertation/thesis author was the primary investigator and author of this paper.

Chapter 5, in part, is currently being prepared for submission for publication of the material. Labadie, Nathan R.; Sharma, Satish K.; Rebeiz, Gabriel. The dissertation/thesis author was the primary investigator and author of this paper.

VITA

2004	B. S. in Physics *with Honors*, University of California, Davis
2009	M. S. in Electrical Engineering, San Diego State University
2015	Ph. D. in Engineering Sciences (Electrical and Computer Engineering), University of California, San Diego/San Diego State University
2011-present	Senior Antenna Engineer, Cubic Defense Applications, San Diego

PUBLICATIONS

N. R. Labadie, S. K. Sharma, G. Rebeiz, “Investigations on a Novel Folded Ring Resonator Antenna With Multiband Characteristics,” *IEEE Trans. Antennas Propag.*, vol.60, no.7, pp.3083–3090, July 2012.

N. R. Labadie, S. K. Sharma, G. Rebeiz, “A Circularly Polarized Multiple Radiating Mode Microstrip Antenna for Satellite Receive Applications,” *IEEE Trans. Antennas Propag.*, vol.62, no.7, pp.3490–3500, July 2014.

N. R. Labadie, S. K. Sharma, G. Rebeiz, “A novel approach to beam steering using arrays composed of multiple unique radiating modes,” *IEEE Trans. Antennas Propag.*, 2015 (under review).

N. R. Labadie, S. K. Sharma, G. Rebeiz, “Investigations on the use of Multiple Unique Radiating Modes for 2D Beam Steering,” *IEEE Trans. Antennas Propag.*, 2015 (to be submitted).

N. R. Labadie, S. K. Sharma, G. Rebeiz, “A Compact Folded Ring Resonator Antenna with Multiband Characteristics, *IEEE Antennas and Propagation Society International Symposium*, July 2012.

N. R. Labadie, S. K. Sharma, G. Rebeiz, “Multimode antenna element with hemispherical beam peak and null steering,” *IEEE Antennas and Propagation Society International Symposium*, July 2012.

N. R. Labadie, S. K. Sharma, G. Rebeiz, “1D beam steering using multiple radiating modes,” *IEEE Antennas and Propagation Society International Symposium (APSURSI)*, pp.1365–1366, 6-11 July 2014.

N. R. Labadie, S. K. Sharma, G. Rebeiz, “Investigation of hybrid phased arrays composed of multiple mode subarrays,” *IEEE Antennas and Propagation Society International Symposium (APSURSI)*, pp.1367–1368, 6-11 July 2014.

N. R. Labadie, J. R. Powell, S. K. Sharma, G. Rebeiz, “The effect of material loss on the axial ratio symmetry of circular microstrip patch antennas,” *IEEE Antennas and Propagation Society International Symposium (APSURSI)*, pp.1061–1062, 6-11 July 2014.

ABSTRACT OF THE DISSERTATION

A Novel Approach to Beam Steering Using Arrays Composed of Multiple Unique Radiating Modes

by

Nathan Richard Labadie

Doctor of Philosophy in Engineering Sciences (Electrical and Computer Engineering)

University of California, San Diego, 2015
San Diego State University, 2015

Professor Gabriel M. Rebeiz, Co-Chair
Professor Satish K. Sharma, Co-Chair

Phased array antennas have found wide application in both radar and wireless communications systems particularly as implementation costs continue to decrease. The primary advantages of electronically scanned arrays are speed of beam scan and versatility of beamforming compared to mechanically scanned fixed beam antennas. These benefits come at the cost of a few well known design issues including element pattern rolloff and mutual coupling between elements. Our primary contribution to the field of research is the demonstration of significant improvement in phased array scan performance using multiple unique radiating modes. In short, orthogonal radiating modes have minimal coupling by definition and can also be generated with reduced rolloff at wide scan angles. In this dissertation, we present a combination of analysis, full-wave electromagnetic simulation and measured data to support our claims.

The novel folded ring resonator (FRR) antenna is introduced as a wideband and multi-band element embedded in a grounded dielectric substrate. Multiple radiating modes of a small ground plane excited by a four element FRR array were also investigated. A novel hemispherical null steering antenna composed of two collocated radiating elements, each supporting a unique radiating mode, is presented in the context of an anti-jam GPS receiver application. Both the antenna aperture and active feed network were fabricated and measured showing excellent agreement with analytical and simulated data. The concept of using an antenna supporting multiple radiating modes for beam steering is also explored. A 16 element hybrid linear phased array was fabricated and measured demonstrating significantly improved scan range and scanned gain compared to a conventional phased array. This idea is expanded to 2 dimensional scanning arrays by analysis and simulation of a hybrid phased array composed of novel multiple mode monopole on patch antenna sub-arrays. Finally, we fabricated and characterized the 2D scanning hybrid phased array demonstrating wide angle scanning with high antenna efficiency.

Chapter 1

Introduction

Wireless communications systems represent a large class of technologies that are virtually ubiquitous in our daily life. From personal mobile devices to national infrastructure, such systems enable the transmission and reception of large amounts of information over the air with propagation speeds at or near the speed of light. This has had a truly transformative effect on our societies both in the way we relate to each other and to our devices. As wireless technology continues to advance, we find we are living a world in which even the most mundane devices such as home ventilation systems, lighting and refrigerators are connected via wireless networks. All of these systems regardless of their application require engineered interfaces from the wired world of digital and analog circuits to free space propagation. These engineered interfaces are commonly referred to as antennas and represent the specialized discipline of antenna engineering.

It is often cited that the first wireless electromagnetic system was created by Professor Heinrich Rudolph Hertz in 1886 [1]. By generating a spark across the gap of a half-wavelength dipole element, he successfully propagated a broadband human made signal over a short distance. The signal was detected by a nearby loop antenna in his laboratory. By this time, James Clerk Maxwell had already unified the theories of electricity and magnetism in the set of $Maxwell's\ Equations$, which fully describe electromagnetic propagation [2]. However, the understanding of the practical aspects of propagation and antenna design were still in their infancy. Approximately 15 years after Professor Hertz's experiments, the first long range transatlantic transmissions were achieved by Guglielmo Marconi using low frequency grounded wireless waves [3]. He also produced the first truly microwave transmitter placing a half-wavelength dipole at the focal point of a cylindrical parabolic reflector both spatially filtering the antenna beam pattern and bandpass filtering the spark gap generated source.

The advent of radar technology during World War II brought about new applications for wireless technology and new demands in performance. With the discovery of the magnetron and klystron tubes capable of kW power amplification, many wireless systems were migrating to higher frequencies [3]. By this time, the benefits of operating in the various bands of the microwave frequency range were well known in terms of desirable propagation characteristics and reduced wireless system size. In the decades that followed, traditional electromagnetic analysis methods were supplemented with numerical methods implemented on increasingly fast computing platforms. Method of moments (MoM) [4], finite difference time domain (FDTD) [5] and finite element method (FEM) [6] among others enabled the design of sophisticated antennas optimized to specific application.

Antenna farms such as the one pictured in Fig. 1.1 are centralized locations that service a wide array of applications including high data rate point -to-point links, high power commercial broadcast, low data rate telemetry and mobile device telephony among others. As such, these antenna farms are excellent examples of the diverse antenna designs needed to optimize the performance of specialized wireless communications systems. Successful antenna design requires a deep understanding of the system requirements of

Figure 1.1: Wide variety of antenna types used in the antenna farm atop Mt. Soledad in La Jolla, CA.

the intended application, the operational conditions and the fundamental properties of the various classes of antennas available. In the following section, we discuss a specialized class of antennas in which the aperture is distributed among many elements each of which is independently excited. These phased array antennas find applications in radar and communications spanning several orders of magnitude in frequency from UHF up to W-band.

1.1 Phased Array Properties

The primary advantage of the phased array is the ability to control the illumination of the aperture through a passive or active transmission line feed network. In an active electronically scanned array (AESA), the beam forming and beam steering properties can be modified orders of magnitude faster than a mechanically gimbaled fixed beam antenna of equivalent size. The earliest known fixed phased array antenna was constructed by Karl

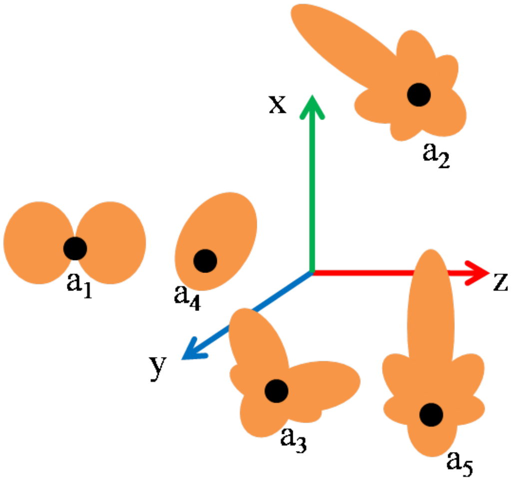

Figure 1.2: The most general array consisting of an arbitrary collection of radiating elements at arbitrary locations in space.

Braun in 1905 in which he positioned three antennas achieving a high directivity radiation pattern [7]. In the decades that followed, a number of prominent researchers continued to develop the theoretical underpinnings of array theory and verifying their work in experimentation. As noted in [8], the publishing of the three-volume series *Microwave Scanning Arrays* in the mid-1960s was a watershed event in the history of phased array antenna research. Phased array antennas remain an active research discipline on a large number of fronts including radiating element optimization, RF front end design, thermal management, low-cost lightweight materials and optimal beamforming among others. In this section, we will develop some fundamental concepts in phased array research which provide the foundation to our novel body of work.

The most general array consists of an arbitrary collection of elements at arbitrary locations in space as shown in Fig. 1.2. In this most general case, the resulting radiation pattern resulting from exciting the collection of elements in an arbitrary manner can be expressed as

$$\vec{E}_A(\theta,\phi) = \sum_{n=1}^{N} a_n \vec{E}_n(\theta,\phi) \tag{1.1}$$

where a_n are the complex weights and $\vec{E}_n$ are the collection of element patterns. The

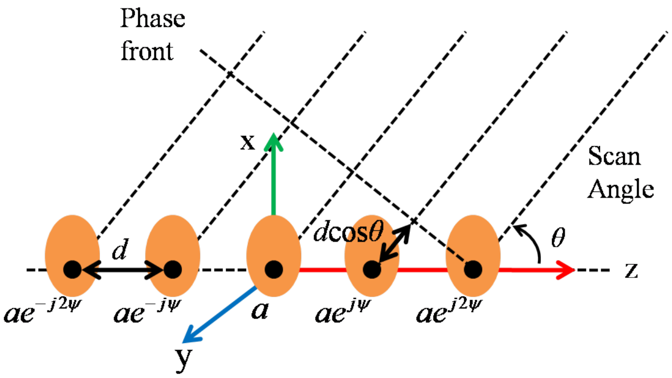

Figure 1.3: A linear array consisting of identical radiating elements located at fixed intervals along the Z-axis.

vectorized field pattern indicates the presence of multiple polarization components. Making some simplifying assumptions, equation 1.1 can be manipulated into more tractable forms making analysis of the phased array behavior much easier.

1.1.1 Element Pattern Rolloff

A uniform amplitude linear array makes several simplifying assumptions about the properties of the array. The first assumption is that all element radiation patterns have the same shape, which is typical of most phased arrays. Second, all elements are oriented in the same way and positioned along a line at fixed intervals as shown in Fig. 1.3. Finally, we make two assumptions about the amplitude and phase relationships between the elements in the array. All elements are excited with equal amplitude and with a progressive phase shift β determined by the location of the element in the array. The equation describing the resulting uniform linear array pattern is defined by

$$\vec{E}_A(\theta,\phi) = a\vec{E}(\theta,\phi)\sum_{n=1}^{N}\exp(jn\psi) \tag{1.2}$$

where ψ is

$$\psi = kd\cos(\theta) + \beta, \tag{1.3}$$

k is the wave number and d is the interelement spacing. The summation term is a factor independent of the element properties and is often call the array factor. With some simple algebraic manipulation, the array pattern can be rewritten with the array factor in closed form

$$\vec{E}_A(\theta,\phi) = a\vec{E}(\theta,\phi)\frac{\sin(\frac{N}{2}\psi)}{\sin(\frac{1}{2}\psi)} \tag{1.4}$$

Fig. 1.4 plots the uniform linear array radiation pattern for three different 16 element uniform linear arrays. The element factor (EF), array factor (AF) and array pattern (AP) of each are plotted for comparison. The first array in Fig. 1.4a is composed of ideal isotropic elements related by a progressive phase shift of $\beta = 163^\circ$. In this case, the AF and AP are identical. Many real directional antenna element patterns can be approximated by the cosine function, $\vec{E}(\theta,\phi) = \cos(\theta)\hat{\theta}$, as shown in Fig. 1.4b. The effect of element pattern rolloff is quite apparent as the scan angle of the array has decreased from 65° to 62° and the peak of the normalized AP has dropped by 7 dB relative to the AF. The performance can be recovered to some extent by using an element pattern with a natural skew toward the scan angle of the array factor as shown in Fig. 1.4c. Within the main beam and nearby sidelobes, the AF and AP show negligible deviation. In order to use this approach in a practical scenario, the element pattern would need to be realigned to the array factor as it is scanned. In chapters 4 and 5, we will demonstrate the use of multiple unique radiating modes to reconfigure element patterns and improve array scan performance.

1.1.2 Mutual Coupling

Mutual coupling describes the degree to which energy incident on a single port in the array is seen at the other ports in the array. The array can be represented pair wise as shown in Fig. 1.5 where the interactions between elements are described through a

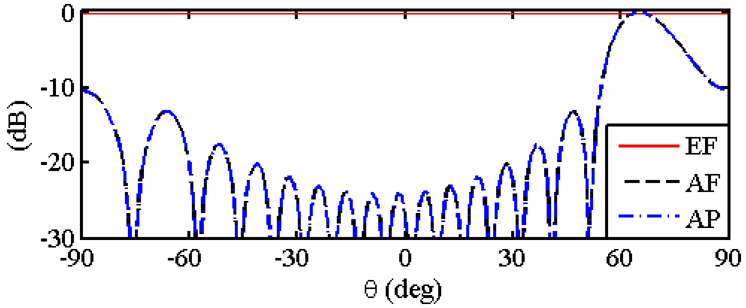

(a) Isotropic element

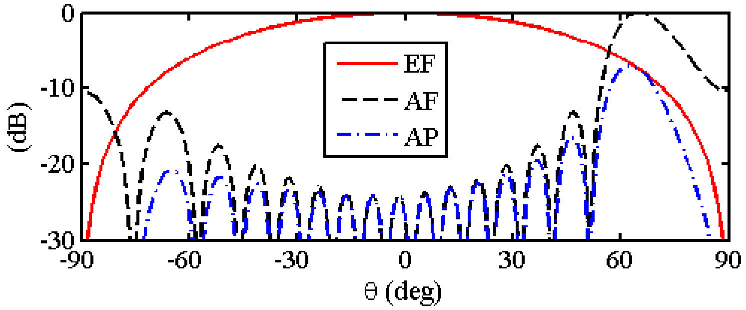

(b) Cosine element

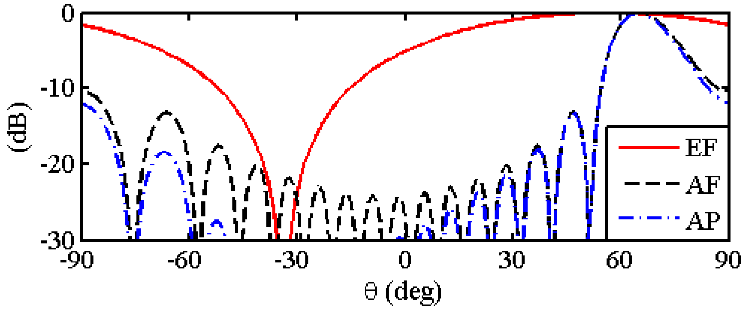

(c) Scanned element

Figure 1.4: Scanned uniform amplitude linear array patterns assuming different element patterns.

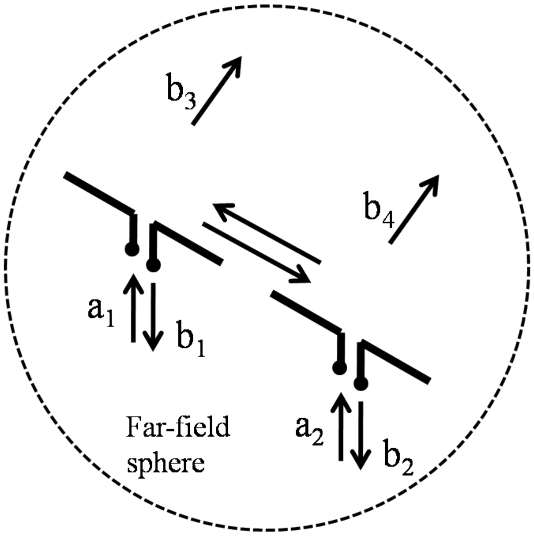

Figure 1.5: Representation of the transmit mode coupling between pairs of antennas in an array.

matrix of scattering parameters [9]. A larger array can be analyzed two elements at a time. Depending on whether the excitations are internal sources or waves impinging from free space, the mutual coupling model must be developed for the transmit or receive array modes separately [10]. In this section, we will briefly discuss the mutual coupling model for a two element transmit mode array.

Following the derivation in [9], the radiated power for each element is related to the incident and reflected voltage waves by

$$P_1 = |a_1|^2 - |b_1|^2 \quad (a_2 = 0), \qquad P_2 = |a_2|^2 - |b_2|^2 \quad (a_1 = 0) \tag{1.5}$$

where the subscript indicates the excited element while the other element is match terminated. The embedded element pattern refers to the radiation pattern due to a direct excitation of a single element modulated by scattering from adjacent elements [11]. When exciting a single element and match terminating all others, the total radiation pattern can be expressed in terms of the normalized embedded patterns $\vec{f}_3$ and $\vec{f}_4$ [12]

$$\vec{f}_T(\theta,\phi) = b_3\vec{f}_3(\theta,\phi) + b_4\vec{f}_4(\theta,\phi) \tag{1.6}$$

where b_3 and b_4 are the coefficients of the voltage waves propagating away from the antennas into free space. The symbol $\vec{F}$ used here (rather than $\vec{E}$)is the element pattern with the radial dependence removed. Specialized scattering parameters are introduced to relate all of the incident, reflected and transmitted voltage waves in the two element array.

$$b_1 = S_{11}a_1 + S_{12}a_2, \qquad b_2 = S_{21}a_1 + S_{22}a_2 \tag{1.7a}$$

$$b_3 = S_{31}a_1 + S_{32}a_2, \qquad b_4 = S_{41}a_1 + S_{42}a_2 \tag{1.7b}$$

The parameters S_{31} and S_{42} represent how efficiently each antenna radiates in the presence of the other. Input impedance matching level indicated by S_{11} and S_{22} while S_{12} and S_{21} are coupling between ports.

Using the definition of radiated power as an integral over the Poynting vector of the total pattern $\vec{f}_T$ [13], the radiated power is related to the voltage wave coefficients

$$P_{rad} = |b_3|^2 + |b_4|^2 + 2\Re\{b_3 b_4 \tau\} \tag{1.8}$$

where τ is the cross-coupling term between the embedded element patterns

$$\tau = \frac{1}{Z_0}\int_0^{2\pi}\int_0^{\pi} \vec{f}_3(\theta,\phi)\cdot\vec{f}_4^{\,*}(\theta,\phi)\sin\theta d\theta d\phi \tag{1.9}$$

In order to simplify the analysis, it is assumed that two element array is reciprocal ($S_{12} = S_{21}$ and $S_{31} = S_{42}$) and the input match to each antenna is identical ($S_{11} = S_{22}$). Without making any assumptions about the nature of the normalized embedded element patterns $\vec{f}_3$ and $\vec{f}_4$, the following two equations describe the optimal mutual coupling S_{12} for maximized gain, which is proportional to S_{31}.

$$G_{max} \propto |S_{31}|^2_{max} = \frac{1}{1+|\tau|} \tag{1.10}$$

$$S_{11} = \pm S_{21} = \sqrt{\frac{1}{2}\frac{|\tau|}{1+|\tau|}} \tag{1.11}$$

One important observation is that gain is not maximized by zero mutual coupling in the general case. The discussion in [9] focuses on the case of identical element patterns with displaced phase centers. As the interelement spacing decreases towards zero, the cross-coupling term reaches its maximum of 1. This is contrast to the prior work in [14] which discussed spatially displaced beams with a common phase center. The extreme case of non-overlapping orthogonal beams was considered which corresponds to $\tau = 0$. The context of that work was to quantify the coupling between beams of differing degrees of overlap in a multibeam array. Also noted in [9] is the difference in active reflection coefficient between the two types of arrays. The input reflection coefficient to each element in an array with displaced phase centers degrades at angles away from broadside even in the optimal case. If orthogonal element patterns are used, the minimum active reflection coefficient is zero for all angles. This is an important motivation for the fully multiple mode array proposed in chapters 4 and 5.

1.2 Literature Review

There are a vast number of publications related to phased array research. The purpose of this section is to review a relatively small subset of these publications that directly relate to our research. We have categorized 3 approaches to phased array design in such a way as to establish the context and novelty of our work. Fig. 1.6 divides the functionality of a phased array into the aperture and feed network. The aperture refers to the radiating portion of the antenna while all non-radiating transmission line structures belong to the feed network. In approach 1, the phased array aperture consists of a number of identical radiating elements (or modes), which is the conventional approach. In the receive mode, the outputs of these elements are then combined in the feed network. The feed network can combine in a straightforward summing of phase and amplitude weighted signals or implement more sophisticated combining by forming orthogonal modes. In contrast, orthogonal multiple modes can also be formed in the aperture itself as depicted for approach 2. In this case, the radiating modes are determined by unique element geometries and feed arrangements. There is a large body of existing work using this approach to produce highly uncorrelated element patterns for use in MIMO applications. We have highlighted in yellow our novel application of these modes to phased array beam steering. The third approach is mentioned as it is an alternative method to improve phased array performance by modifying the element radiation patterns at the aperture rather than in the feed network. Each of these approaches is described in greater detail in the following subsections.

1.2.1 Approach 1: Fixed Identical Modes

Due to ease of analysis and implementation, the bulk of phased array technology falls into the category of approach 1. That is, most such arrays consists of identical elements with fixed patterns which are combined in the feed network. This approach also provides a desirable degree of isolation between the aperture and all other transmission, power and control circuitry. The feed network typically consists of passive power combiners/dividers along with active circuitry to modify the phase and amplitude of the signal to or from each element. Depending on the array geometry, the feed network topology may be quite different.

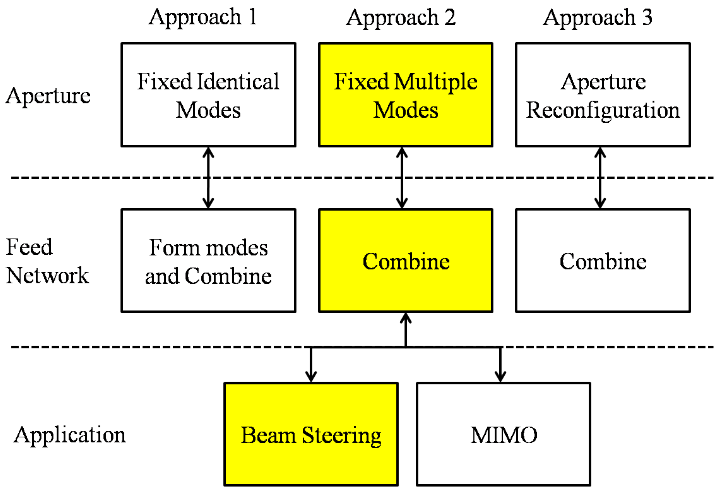

Figure 1.6: Three approaches to phased array design used to establish the novelty and context of the work presented in this dissertation. The highlighted approach is the central topic of this dissertation

Our approach is seen as distinct from the large body of work in which the modes themselves are formed in the feed network. In [15], this approach is thoroughly discussed and referenced particularly in the context of the amplitude and phase modes of a circular array. For example, an array of identical single mode radiators (i.e. $\lambda/2$ dipoles) can be connected to a mode forming network. This feed network will produce the proper amplitude and phase weights at each of the radiating elements to produce a desired radiating mode. Typically, a collection of N elements supports up to N radiating modes. The collection of available radiating modes comprise an orthogonal basis from which desired beam patterns can be synthesized. Although very useful, such feed networks can be quite complex and potentially lossy due to the large number of microwave coupling structures involved. In contrast, our approach uses the radiating element itself to generate the desired mode. That is, the geometry of the radiator is designed to support a desired current distribution associated with a particular radiating mode.

1.2.2 Approach 2: Fixed Multiple Modes

Much work has been devoted to understanding the modal nature of antenna radiation patterns [16], [17]. The theory of characteristic modes uses an eigenmode expansion to derive the supported real current modes on conducting and dielectric bodies of arbitrary shape [18, 19]. This method not only provides physical insight into the behavior of the antenna but also allows antenna geometries to be synthesized from a set of desired radiation pattern properties [20]. Such a modal approach to antenna design has also been useful in realizing multimode or multiple mode antenna apertures [21]. Ideally, the multiple mode antenna would support multiple characteristic current modes on the same aperture and operating in the same frequency band. Because of the ability to achieve high isolation between orthogonal characteristic modes, there is a potential savings in the footprint of the multiple mode antenna compared to two separate apertures each supporting identical modes with the same level of isolation. A large body of work has been dedicated to designing and characterizing multiple mode antenna elements for multiple input multiple output (MIMO) applications [22, 23, 24, 25, 26, 27, 28, 29, 21, 30, 31, 32, 33, 34]. Isolation between uncorrelated radiating modes provides diversity gain with the added benefit that modes are collocated on the same aperture. Several examples of multiple mode antennas used in MIMO applications are pictured in Fig. 1.7.

It is worth mentioning the fundamental research using characteristic mode theory applied to multi-antenna systems as discussed in [35]. A MoM based code is developed to solve for the characteristic modes present on one or more wire radiators. One example uses their method to identify the mode or modes responsible for unwanted coupling in a two element array. This allows the researcher to intelligently design an isolating structure to suppress the undesired coupling mode while minimizing impact on desired radiating modes. Several examples also demonstrate the ability to select optimal feed point number and location on a wire radiator to excite a desired mode that is stable over a wide bandwidth. Although we do not specifically use characteristic mode theory, we certainly recognize its relevance to our research. Our work uses existing antenna aperture geometries and assesses their fully implemented performance when configured to radiate a number of different modes. In a sense, we look at the problem in reverse with respect to [35]. That is, we emphasize practical implementations of multiple mode antennas that improve phased array behavior with respect to scan range and efficiency.

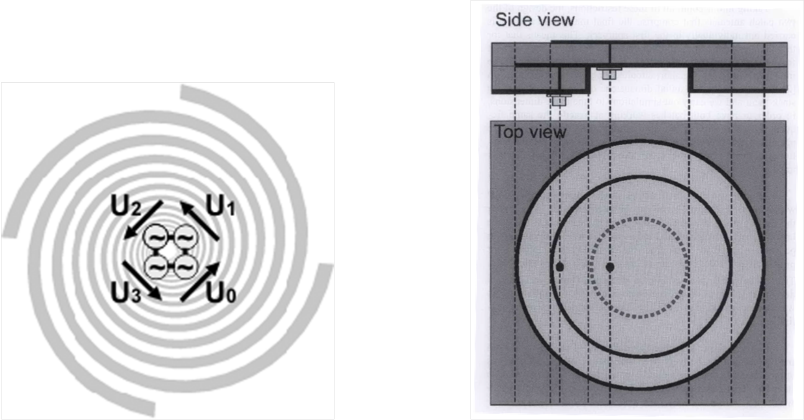

(a) Wideband spiral [24]

(b) Stacked patch [28]

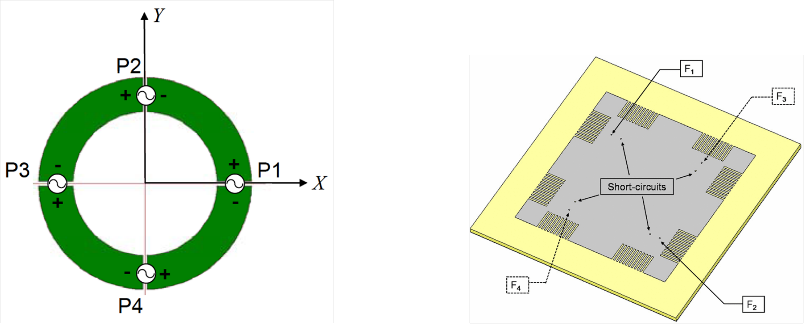

(c) Segmented annular patch [21]

(d) Mode frequency convergence patch [32]

Figure 1.7: Literature examples of multiple mode antennas designed for MIMO applications.

In this dissertation, we examine the use of multiple mode antennas to improve the beam steering performance of deterministic arrays, or phased arrays. To our knowledge, the first discussion of using element pattern reconfiguration to improve array pattern performance is contained in [36]. Concentrically stacked patch antennas are used to generate two independent radiating modes at each location in a 2 dimensional array. Reduction in the array pattern grating lobe is demonstrated for the appropriate complex weighting of the modes at each array location. This dissertation expands on this concept by rigorously characterizing the improvement in scan performance for such arrays employing multiple mode elements. We refer to these elements as sub-arrays of collocated elements each supporting a unique radiating mode with minimal coupling.

1.2.3 Approach 3: Aperture Reconfiguration

There are other approaches for improving the array scan performance based on element pattern reconfiguration. Most of these methods involve the use of parasitic scattering elements that are switched or loaded in such a way as to alter the element pattern in a desired manner [37, 38, 39, 40]. Therefore, the element pattern reconfiguration actually takes place at the aperture. This is in fact the primary architectural difference between those approaches and our proposed method. Element pattern reconfiguration using multiple radiating modes involves changing the amplitude and phase relationships between the modes in the feed network, much like the phased array itself. There are some benefits to this including minimizing additional circuitry at the aperture and allowing for simultaneous multiple beam formation such as can be done in a digital beam former.

1.3 Research Resources

Engineering research typically begins with mathematically based analysis that provides fundamental insight into the problem at hand. Predictions about the viability of potential solutions are made at this stage are then tested both in numerical simulation and measurement of fabricated prototypes. This process usually requires a wide array of expensive resources including software and hardware. A brief description of the

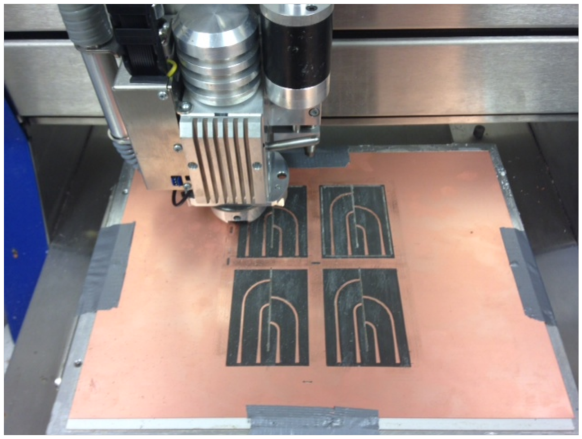

Figure 1.8: SDSU AML's LPKF S42 PCB fabrication machine shown building components for the prototypes used in chapter 4.

resources used in the course of our research and acknowledgment of the contributors are given in this section.

Numerical analysis and electromagnetic simulation were performed with the help of two software applications made available to us by San Diego State University (SDSU). Matrix Laboratory (MATLAB) was used to implement custom computational code for generating and manipulating radiation pattern data, generating plots featured in this thesis and many other post-processing algorithms [41]. Some examples of our MATLAB code are given in appendix A. Ansys High Frequency Simulation Software (HFSS) is a full-wave electromagnetic simulation tool which uses a proprietary version of the finite element method (FEM) [42]. The primary frequency domain solver is well suited for the types of narrow to moderate bandwidth structures considered in this dissertation.

Our prototypes were fabricated using material and equipment available in the SDSU Antenna and Microwave Laboratory (AML). Fig. 1.8 shows the LPKF ProtoMat S42 in the process of milling out a set of transmission line structures used in one of our novel phased array structures. The S42 has a trace accuracy of approximately 0.2 mil and wide array of milling, cutting and drilling bits for fast and accurate 2 layer PCB board fabrication [43] Scattering parameter measurements for all prototypes were obtained

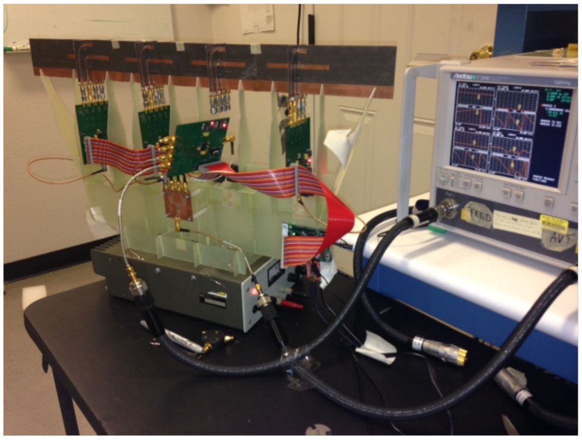

Figure 1.9: SDSU AML's Anritsu 37269D Lightning series vector network analyzer (VNA) shown characterizing the prototype in chapter 4.

using the Anritsu 37269D Lightning series vector network analyzer (VNA) available in SDSU's AML as shown in Fig. 1.9. This particular model maintains a dynamic range in excess of 90 dB over the frequency range from 40 MHz to 40 GHz [44]. The antenna measurement chamber in SDSU's AML also uses the Anritsu VNA when taking complex radiation pattern measurements as shown in Fig. 1.10a. The noise floor of the VNA is less than -80 dBm across the operating bandwidth making high SNR measurements possible even when high free space loss is present. Fig. 1.10b illustrates the azimuth over elevation (also known as phi over theta)combined spherical near field and far field scanner supplied to SDSU by Orbit FR. The upper positioner maps the azimuth (ϕ) of the radiation pattern relative to the line through the probe and AUT centers of rotation. Elevation patterns (θ) are mapped by the movement of the lower positioner as it rotates the turntable on which the AUT pedestal stands. The system is housed in a 12'L×10'W×8'H anechoic chamber supplied by Satimo, which together with the hardware enables radiation pattern measurements from 1 GHz to 18 GHz.

Cubic corporation also provided use of its antenna measurement laboratory for measuring some of the larger array prototypes. Beginning in 2011, the dissertation author has been employed as a full-time senior antenna engineer at Cubic. He wrote the require-

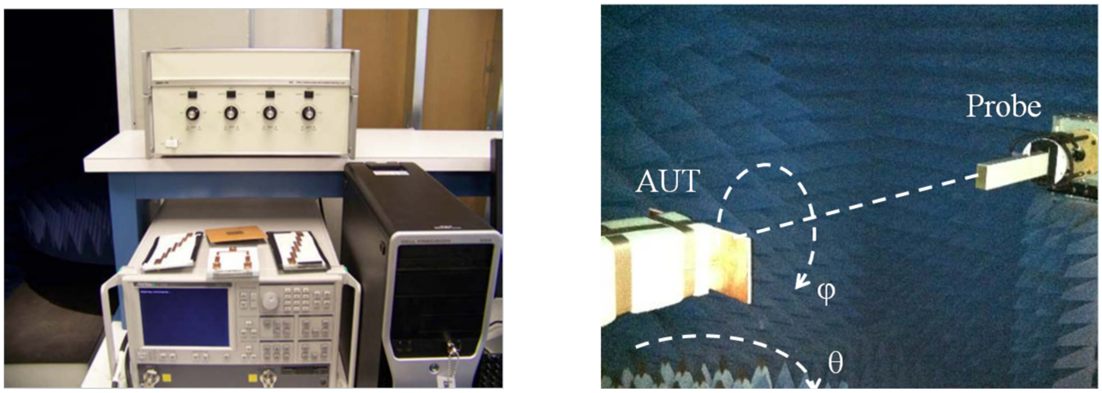

(a) Orbit FR motion control and data acquisition work station

(b) Satimo anechoic chamber and Orbit FR positioners

Figure 1.10: SDSU antenna measurement laboratory.

ments, procured and oversaw the construction of the spherical near field scanner depicted in Fig. 1.11b. The 25'L×16'W×12'H antenna chamber is the result of the combined efforts of NSI, Anechoic Systems and Cubic facilities. In its present configuration, the measurement equipment supports testing of antennas ranging in frequency from 1 GHz to 20 GHz and up to 5 ft in diameter. Near field Systems (NSI) supplied the chamber positioners, Agilent programmable network analyzer (PNA), Dell Workstation and other supporting hardware in the system. Data collection and processing relies primarily on the NSI2000 software application.

1.4 Thesis Overview

In chapter 2, a novel loop antenna based on the volumetric folded ring resonator (FRR) structure is proposed. It is shown that the FRR antenna can be represented by an equivalent circuit model for approximate analysis with sufficient accuracy as verified against a method of moments (MoM) simulation in a version of numerical electromagnetic code (NEC). Two practical implementations are presented: The first version is a single FRR antenna embedded in a dielectric substrate and excited by a 50 Ω

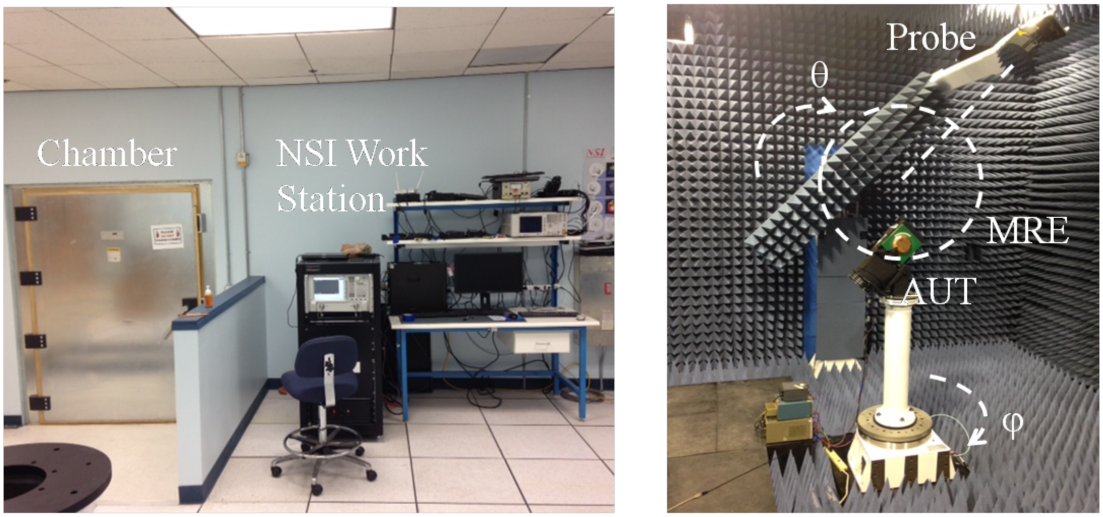

(a) NSI workstation for positioner control, data collection and data processing

(b) NSI, Anechoic Systems and Cubic facilities built antenna chamber.

Figure 1.11: Cubic corporation antenna measurement laboratory.

coaxial feed line. Parametric studies of the structural parameters are presented showing three resonances that can be impedance matched achieving positive gain. In the second implementation, the FRR is embedded in a slotted ground plane for improved matching and radiation performance. Two bands, one at 3.6 GHz and another between 4.75 GHz to 5.8 GHz, are matched to better than $|S_{11}|$ = -10 dB and maintain a constant 2.5 dBi gain with $> 90\%$ radiation efficiency. The simulated reflection coefficient and gain radiation patterns agree well with measurements. As a precursor to the multiple mode research to follow, this antenna is implemented in a 4 element sub-array configuration. Given the separate ground plane current modes excited by each port, the sub-array is a type of multiple mode antenna.

A beam peak and null steering multiple radiating mode based microstrip patch antenna is presented in chapter 3 for satellite receive applications operating at L1 Global Positioning System (GPS) band. Two collocated microstrip patch antennas were designed to produce TM_{11} and TM_{21} radiating modes. These orthogonal and circularly polarized radiation patterns were combined enabling full hemispherical steering of a single beam peak and null. Using theoretical analysis and full-wave simulation, the multiple mode aperture was designed to operate over a 25 MHz bandwidth centered at 1.575 GHz, which covers the L1 GPS band. Impedance and radiation pattern measurements of the passive antenna aperture were in close agreement with the simulated data. Next, this antenna was integrated with an active feed network allowing full hemispherical control over the beam null position and limited beam peak scan in $\approx 5^\circ$ increments. Using a simple calibration scheme, the measured beam peak and null elevation angles were programmed to within $< 10^\circ$ of the intended value based on simulation. Azimuthal positions were consistently offset by $\approx 20^\circ$ from the simulated value, which could be resolved in the board layout by phase matching the transmission lines and test point locations. The antenna maintained high total efficiency $> 68\%$ and low axial ratio < 3 dB over all steering angles.

Chapter 4 presents a novel approach to beam steering using an array composed of elements each supporting a unique radiating mode. The 1 dimensional beam synthesis properties of the novel ideal multiple mode dipole array are quantified using a Fourier decomposition and synthesis method. Significant improvement in scan range is demonstrated compared to a conventional linear dipole reference array. A hybrid phased array composed of multiple mode sub-arrays is also proposed and shown to be an efficient tradeoff between performance improvement and design complexity. Reasonable agreement is obtained between the simulated and measured impedance and radiation pattern properties of a four element multiple mode array. Finally, a 16 element hybrid phased array composed of four 4 element multiple mode sub-arrays is fabricated and measured. The array is shown to have a 3 dB scan range of $\pm 68^\circ$, which is in good agreement to the simulated value of $\pm 69^\circ$ at the design frequency of 4.6 GHz. Additionally, the 3 dB bandwidth of the array is more than 1 GHz at broadside. This bandwidth reduces to approximately 300 MHz at the widest scan angles, which is consistent with an equivalent conventional linear array.

In chapter 5, the multiple mode approach to beam steering is extended to the case of 2 dimensional scanning arrays. An arbitrary element radiation pattern and a desired array pattern are each expressed in terms of their respective spherical harmonic coefficients. Beam pattern synthesis for a collection of arbitrary elements is accomplished by deriving the relationship between the two sets of spherical harmonic coefficients. Three candidate arrays are defined on the basis of the type and number of radiating elements used in each array. A conventional patch antenna array consisting of a total of four elements each with two feed points is the baseline array against which the other two are compared. The novel hybrid phased array contains the same number of patch antennas but with four additional collocated active monopole elements. The third array consists of nine patch antennas in which the array aperture has been oversampled by using smaller patch antennas with smaller spacing. The hybrid phased array produces the highest peak gain of 12.5 dBi with a 3 dB scan range that is 26° wider than the oversampled array and 36° wider than the baseline patch array in the $\phi = 0^\circ$ scan plane. Sidelobe and cross-polarization levels are also significantly improved over the baseline array. In terms of complexity, the hybrid phased array contains 50% more feed points than the baseline array but 33% less than the oversampled array.

Chapter 2

Investigations on a Novel Folded Ring Resonator Antenna with Multiband Characteristics

2.1 Introduction

Loop antennas are a fundamental class of antennas with transmit and receive applications spanning the microwave frequency spectrum. Such antennas are characterized by closed current paths established on radiating elements, which conform to a variety of closed planar or volumetric geometries. Typically, the first resonance at which efficient radiation occurs requires the electrical length of the current loop to be approximately $\lambda/2$ or λ [45]. The current supporting element can be meandered and folded in order to decrease the overall electrical size of the antenna. However, compactness is achieved at the cost of reduced radiation resistance and high reactance making impedance matching more challenging. Bandwidth and gain also diminish with reduced electrical size. Consequently, compact loop antennas are mainly used in the receive mode [13].

There are a variety of methods available to both miniaturize the loop antenna and improve its matching characteristics. The single layer multi-turn solenoidal antenna increases the radiation resistance while maintaining the same loop diameter. However, it is desirable to choose a design approach that allows antenna fabrication on a low profile planar substrate. Planar meander line loop antennas have been shown to be compact and deliver good matching and radiation characteristics [46, 47, 48]. Another approach is to fold the loop and wrap it around the substrate material near the edge of the ground plane. Wideband and multiband versions of this folded loop antenna concept have also been reported [49, 50].

We have recently proposed a novel metamaterial structure known as the volumetric folded ring resonator (FRR) [51, 52]. As shown in Fig. 2.1, the structure is essentially a closed loop resonator folded volumetrically to fit in a cubic volume. The primary structural parameters are the cube dimension a, wire radius b, and gap width g. Given the compactness of the structure, we present the implementation of the FRR as a compact loop antenna structure in this chapter. Section 2.2 explores the resonant behavior of the FRR antenna through the use of an equivalent circuit model. A practical implementation of the FRR antenna as a folded wire embedded in a dielectric is presented in section 2.3. Matching and radiation performance improvements by embedding the FRR antenna in a slotted ground plane are investigated in section 2.4. Section 2.5 compares the simulated and measured performances of the prototype FRR antenna in a slotted ground plane.

2.2 Analytical Model

An approximate analytical model is first developed in order to understand the underlying principles responsible for the FRR antenna behavior. First, a wire model of the FRR antenna was built in a numerical electromagnetic code (NEC) [53]. The FRR

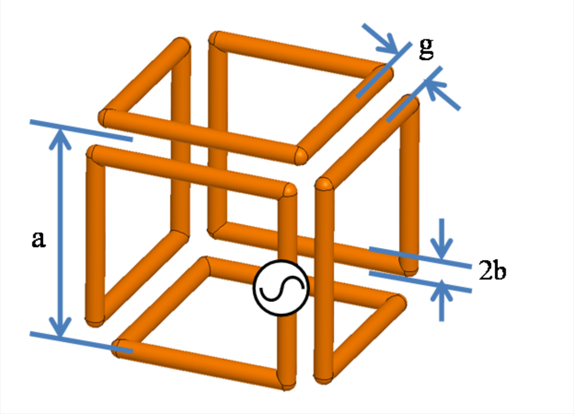

Figure 2.1: Numerical Electromagnetic Code (NEC) model of the folded ring resonator (FRR) antenna.

structure is composed of 6 small loops on the faces of a cubic volume enclosing it, and all six loops are connected together by virtue of the folding geometry. Our model will show that the FRR antenna is in fact a compact loop antenna composed of capacitively- and inductively- coupled electrically small-loop antennas. Assuming that the total antenna length at first resonance is one wavelength or less, we can further assume that current on each loop is approximately uniform. This can be justified by considering that the circumference of each loop is less than $\lambda/6$. Therefore, the equivalent circuit model of a small loop antenna has been used to represent each loop in the FRR antenna as shown in Fig. 2.2. The radiation resistance R_r, loss resistance R_L, external inductance L_A, and internal inductance L_i are given in equations 2.1 [13].

$$R_r = 20\left(\frac{4a}{\lambda}\right)^4 \tag{2.1a}$$

$$R_L = \frac{4a}{2\pi b}\sqrt{\frac{\omega\mu_0}{2\sigma}} \tag{2.1b}$$

$$L_A = 2\mu_0\frac{a}{\pi} \tag{2.1c}$$

$$L_i = \frac{2a}{\pi b}\sqrt{\frac{\mu_0}{2\omega\sigma}} \tag{2.1d}$$

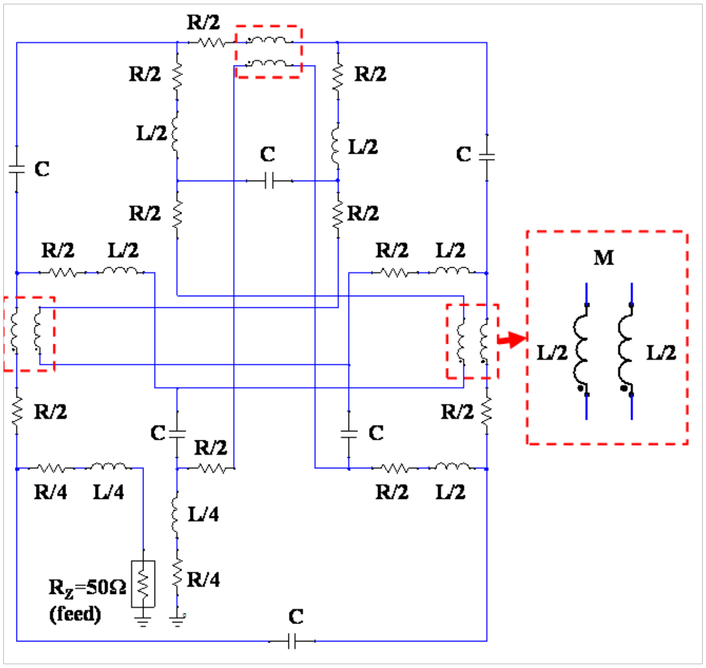

Figure 2.2: Equivalent circuit model of the FRR in Ansoft Designer.

Each of the six loops is capacitively coupled to two adjacent loops as shown in Fig. 2.1, and the conductors responsible for this coupling can be represented as a two-wire transmission line section. Using this model, a coupling capacitor C_t is inserted between the loops and an additional inductance L_t is added to the loop inductances. These two-wire distributed reactances are described by equations 2.2a and 2.2b as in [54]:

$$C_t = \frac{\pi\varepsilon}{\cosh^{-1}\left(\frac{g}{2b}\right)} \tag{2.2a}$$

$$L_t = {Z_0}^2 C_t \tag{2.2b}$$

where Z_0 is:

$$Z_0 = 276 \log\left(\frac{g}{b}\right) \tag{2.3}$$

Each loop is inductively coupled to one nearly coaxial loop on the opposite side

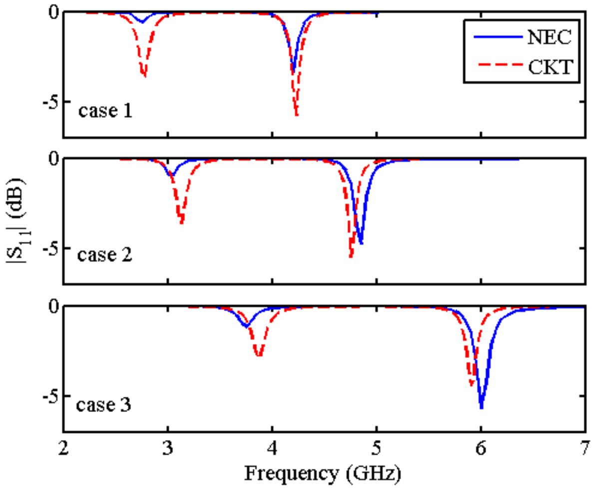

Figure 2.3: Simulated reflection coefficient magnitude comparison between the NEC model and the equivalent circuit model.

of the cube. Since we can assume approximately uniform current distribution on the small loops, a simple model of the mutual inductance, M, can be used. Although we have square loops, the formulas simplified from [55] for circular loops are used with an equivalent loop radius, r.

$$\beta = \sqrt{\frac{4r^2}{4r^2 + a^2}} \tag{2.4a}$$

$$M = \mu r \sqrt{4 + \beta^2} \left[\left(1 - \frac{\beta^2}{2} \right) K(\beta) - E(\beta) \right] \tag{2.4b}$$

The simplified mutual inductance model is given in terms of the complete elliptic functions $K(\beta)$ and $E(\beta)$ [56].

The first two resonances of the FRR antenna obtained using both the NEC simulations and the equivalent circuit model are shown in Fig. 2.3. Table 2.1 lists the physical dimensions and circuit parameters corresponding to the 3 cases shown in Fig. 2.3. Both the simulated and analytical models are in excellent agreement for either small gap widths or loop radii. The slight disagreement can be attributed to the breakdown of the assumption of uniform currents along each small loop at higher frequencies.

Table 2.1: FRR dimensions and computed circuit parameters corresponding to the equivalent circuit model plots of Fig. 2.3

Case	Dimensions	Value	Circuit Parameter	Value
1	a	6.0 mm	R	5.4 Ω
	g	0.25 mm	L	32.0 nH
	b	0.01 mm	C	49.5 fF
			M	3.3 nH
2	a	6.0 mm	R	5.2 Ω
	g	0.5 mm	L	32.0 nH
	b	0.01 mm	C	38.8 fF
			M	3.2 nH
3	a	5.0 mm	R	4.3 Ω
	g	0.5 mm	L	25.4 nH
	b	0.01 mm	C	31.7 fF
			M	2.6 nH

The current distributions along the length of wire are plotted for each resonance frequency in Fig. 2.4. At f_1= 2.75 GHz, the structure supports a 1λ current distribution equal to the length of the FRR wire length of 103.2 mm. The free space wavelength at f_1 is 109.1 mm, which is close to the wire length. Therefore, given the gap spacing g = 0.25 mm, the reactive coupling between the different loops at f_1 miniaturizes the antenna modestly. However, the free space wavelength at f_2= 4.2 GHz is 71.4 mm where the antenna supports a 2λ current distribution. The effective wavelength along the wire length is 51.6 mm, which is significantly less than the free space value. Mutual reactive coupling between resonant structures is known to cause the resonant frequencies to occur closer to one another as coupling increases. This explains why the highest resonance occurs at a frequency lower than the free space wavelength. This also explains why the lowest resonance does not appear to be significantly miniaturized. The lowest resonance is effectively pulled up in frequency while the highest resonance is pulled down due to the reactive coupling.

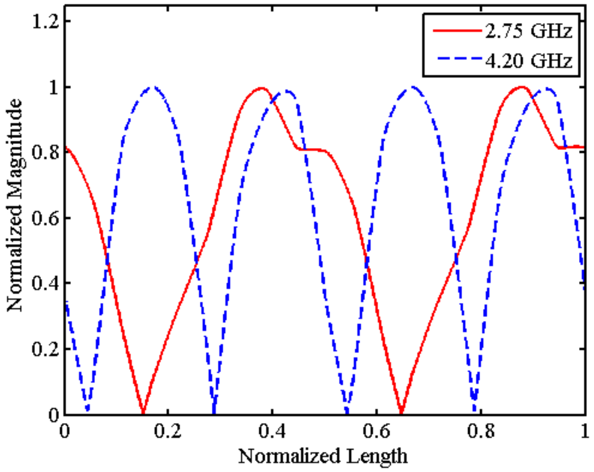

Figure 2.4: Current distribution along the length of FRR wire as simulated in NEC2.

2.3 Isolated FRR Antenna

A practical version of the FRR antenna has been implemented as a folded wire embedded in a dielectric substrate (Fig. 2.5), and the antenna simulations are performed using Ansoft's High Frequency Structure Simulator (HFSS). The antenna parameters include the wire line width w, gap width g, via radius r, and substrate height h. The SMA feed is offset from the FRR by a small gap of 0.2 mm on a 1x1 mm patch. The inner conductor of the coaxial feed is connected to the small upper patch while the outer coaxial shield is connected to a similar patch below. Fig. 2.5 indicates the upper and lower surfaces of the FRR. Several key parameters were varied to identify their effect on the FRR impedance and radiation characteristics. The nominal structural parameters are: w = 1.0 mm, g= 0.35 mm, h = 120 mil (3.048 mm), c= 6 mm, f = 1.0 mm, and r = 0.5 mm. Rogers 5880 ($\varepsilon_r = 2.2$) was chosen as the substrate material.

The analytical model assumed that all six connected loops were of equal dimension. In this implementation, the structure has no symmetry and contains several loop sizes. The wire structure also has a non-uniform cross-section. These factors contribute to the increased number of resonances seen in this model when compared to only two

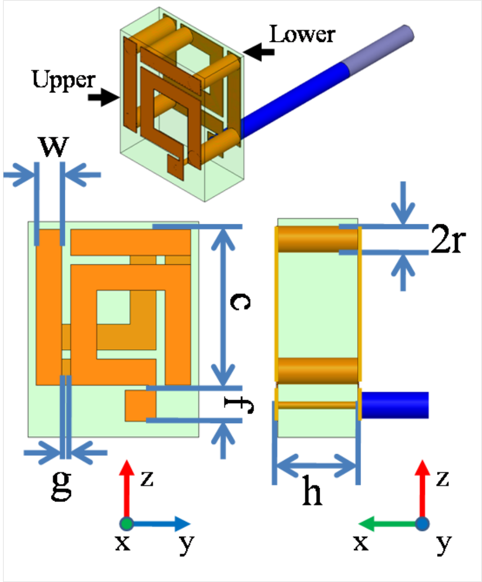

Figure 2.5: Ansoft HFSS model of the isolated FRR implemented as a folded wire inside a dielectric substrate.

resonances in the analytical model. The surface current distribution for nominal structural parameters is plotted for both the top and bottom conducting surfaces in Fig. 2.6. At the lowest resonance (f_1 = 3.68 GHz), there are two current peaks in the current distribution along the wire at the feed point and on the bottom ring in agreement with Fig. 2.4 for the approximate analytical model.

The simulated radiation pattern at 3.68 GHz is consistent with a compact loop antenna (Fig. 2.7). In fact, the electrical size of the antenna at the lowest resonance is $0.11\lambda_g \times 0.13\lambda_g \times 0.06\lambda_g$. The second resonance at 4.75 GHz shows a similar omni-directional pattern. At each resonance of the FRR antenna, the βc values are $\beta_1 c = 0.46$, $\beta_2 c = 0.59$, and $\beta_3 c = 0.75$. Since $\beta_3 c = 0.75$, we can expect a higher directivity pattern which is broadside to the circulating current distributions. Given the asymmetric FRR shape and complex current distribution among the 6 connected conducting loops, it is not straightforward to predict the location of the beam peak. HFSS simulations show that the 6 GHz radiation pattern peaks at $\theta = 45^\circ$ and $\phi = 260^\circ$ as shown in Fig. 2.7. The

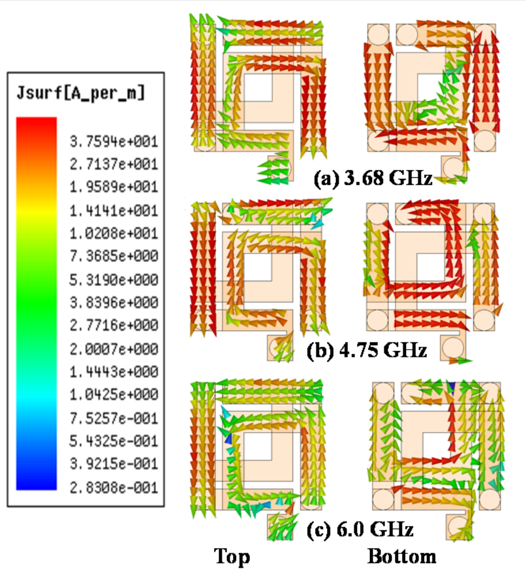

Figure 2.6: Top and bottom FRR surface current distributions at the three resonant frequencies.

effect of the wire width on the reflection coefficient magnitude performance is plotted for several values of w in Fig. 2.8. Peak realized gains for the corresponding radiation patterns are: 1.57 dBi (3.675 GHz), 0.72 dBi (4.75 GHz), and 2.54 dBi (6.0 GHz).

2.4 FRR in Slotted Ground Plane

By embedding the FRR antenna in a slotted ground plane, improved matching can be obtained at the FRR resonances. The ground plane is located on the bottom side of the substrate and is defined by the parameters as shown in Fig. 2.9. The nominal ground plane and slot dimensions are $a = 6.75$ mm, $b = 6.5$ mm, $w_a = 0.375$ mm, $w_b = 0.25$ mm, $W = 25$ mm, $L = 20$ mm, and $d = 0$ mm. The slot dimensions a and b are varied independently of all other geometrical parameters. Therefore, as the slot dimensions are varied, the distance from the FRR to the ground plane also changes accordingly. Both the FRR and ground plane compose the radiating structure. However, the FRR occupies only 7% of the nominal ground plane area leaving considerable room for other

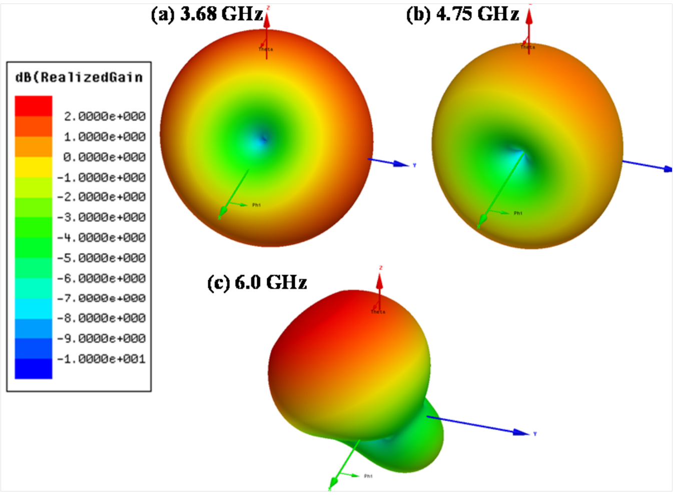

Figure 2.7: Simulated 3D radiation patterns of the planar FRR antenna at the three resonant frequencies.

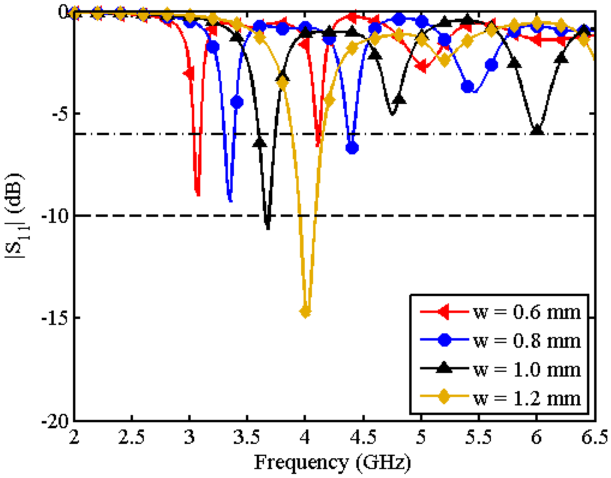

Figure 2.8: Parametric study of the reflection coefficient magnitude for line width variation.

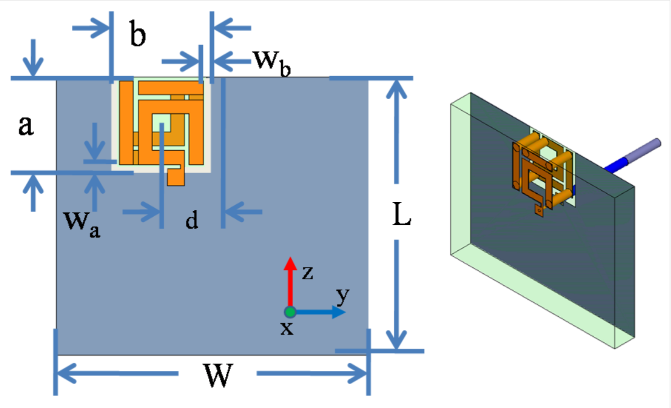

Figure 2.9: Ansoft HFSS model of the FRR embedded in a slotted ground plane (nominal ground plane and slot dimensions are $a = 6.75$ mm, $b = 6.5$ mm, $w_a = 0.375$ mm, $w_b = 0.25$ mm, $W = 25$ mm, $L = 20$ mm, and $d = 0$ mm).

circuit components when integrated into a device. Parametric sweeps over the ground plane dimensions were performed to investigate and optimize the impedance bandwidth. Clearly, the positions of the resonances have not changed. However, the impedance matching near the resonances has greatly improved primarily due to the changes in the antenna input impedance.

Fig. 2.10 shows that the radiation resistance has increased near the resonances due to current flowing on the ground plane. The reactance is also reduced over both bands since the ground plane is capacitively coupled to the FRR and introduces an inductance near resonance. Also, the additional resonance in the impedance profile at 2.78 GHz introduced by the coupling of the FRR to the ground plane is of interest. The input resistance is very large at almost 1000 Ω. Although it may be possible to choose ground plane and slot dimensions in order to match this mode to 50 Ω, it would not be possible to match the other modes simultaneously and efficiently. In view of the above, we have focused our attention on the resonances between 3 GHz and 6.5 GHz only in the following parametric studies.

The current distributions in Fig. 2.11 support the reasoning about how the slotted ground plane improves matching levels. Ground plane currents also play a significant

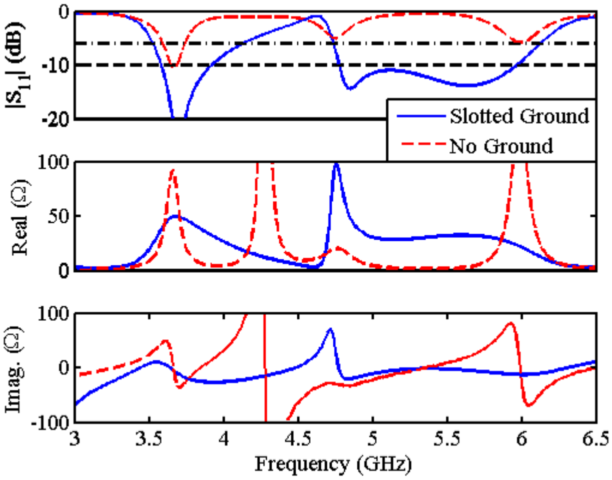

Figure 2.10: Isolated FRR and FRR in slotted ground plane comparisons for reflection coefficient magnitude (top), radiation resistance (middle), and reactance (bottom).

part in the resulting radiation patterns. In fact, the slotted ground plane radiation patterns are rotated by 90° around the Z-axis with respect to the isolated FRR. This is due to strong currents along the ground plane edges parallel to the Y-axis that radiate much like dipole antennas, and explains the nearly omni-directional patterns and nulls along the Y-axis. The radiation pattern at 5.8 GHz shows significant deformation along the Z-axis. At this frequency, there are induced currents along the ground plane edges parallel to the Z-axis. At the same time, currents parallel to the Y-axis are diminished. This increases the gain broadside to the ground plane and reduces the endfire gain as evident from the 3D radiation pattern.

2.4.1 Slot Dimensions

The location of the lowest band is sensitive to the slot dimension a as shown in Fig. 2.12. However, the upper band is affected primarily in the impedance matching level. For a large enough slot, $a > 8$ mm, the $S_{11} = -6$ dB bandwidth of the upper band increases to approximately 40%. The -6 dB impedance match criterion is used

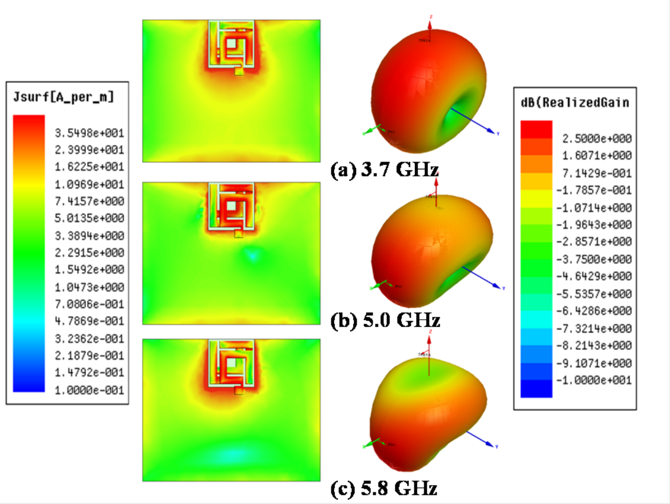

Figure 2.11: Magnitude surface current distributions and 3D radiation patterns at the lower band frequency and upper band edge frequencies.

because most of the wireless communication handheld devices accept this matching level. Fig. 2.13 shows that the band locations are not significantly affected by varying the slot dimension b. It is also seen that the slot dimension b provides significant control over the matching level in each band.

2.4.2 Ground Plane Size

Ground plane size is one of the most important factors in the performance of compact antennas since the ground plane may support strong induced currents. Therefore, the ground plane becomes part of the antenna showing impact on both the circuit and radiation properties. Fig. 2.14 shows that the matching level of the lowest band is heavily dependent on the ground plane width W. The nominal width $W = 25$ mm is approximately half of the guided wavelength at 3.6 GHz, which is $\lambda_g = 56$ mm. Increasing or decreasing the width degrades the matching in this band since it is no longer resonant at this frequency. The FRR reflection coefficient magnitude is not as sensitive to the ground plane length L. As seen in Fig. 2.11, most of the ground plane currents are distributed

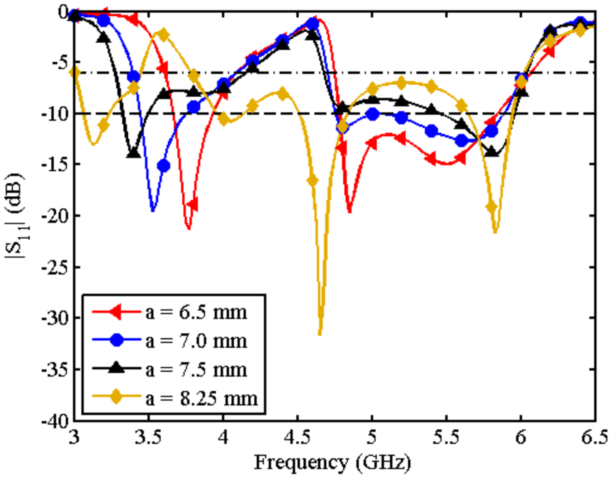

Figure 2.12: Parametric study of the reflection coefficient magnitude for ground slot dimension *a* variation.

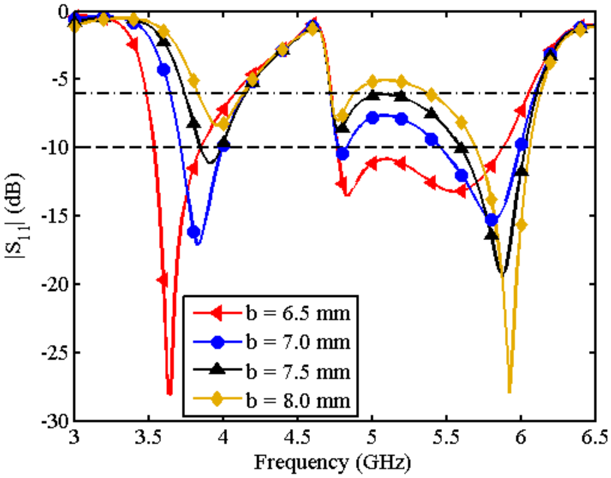

Figure 2.13: Parametric study of reflection coefficient magnitude for ground slot dimension *b* variation.

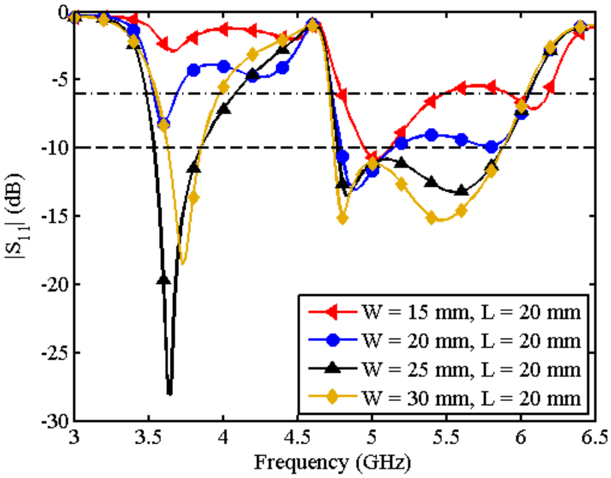

Figure 2.14: Parametric study of the reflection coefficient magnitude for ground plane width variation.

along the edges parallel to the Y-axis. Even at the smallest length $L = 15$ mm, sufficient matching is maintained.

2.4.3 Offset Placement

The exact placement of the FRR in the slotted ground plane may be of interest depending on the intended application. Therefore, the antenna offset d from the center of the ground plane has been investigated. The location of the two matched bands are relatively unaffected by the offset. However, the matching level of the first band and bandwidth of the second band change significantly. Although some variability in FRR location is allowable, offset values greater than $d = 4$ mm change the reflection coefficient magnitude profile considerably.

2.4.4 Radiation Properties

The gain profile of the nominal FRR in the slotted ground plane shows nearly constant gain of approximately 2.5 dBi across both bands (Fig. 2.15). The gain is defined

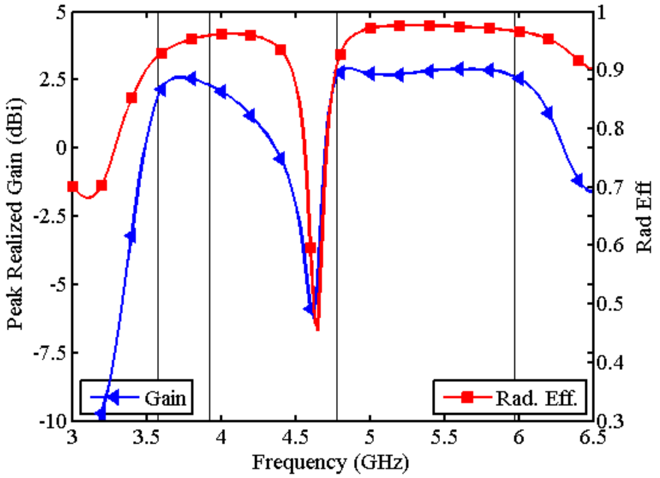

Figure 2.15: Simulated gain and radiation efficiency profile for the FRR in slotted ground plane using nominal structural parameters.

at the peak of the radiation pattern and not at a specific (constant) angle. The radiation efficiency is $> 90\%$ over both bands. Due to the increased aperture size of the radiating ground plane, there is considerable gain improvement over the isolated FRR at lower frequencies. The largest FRR dimension (electrical size) varies from $0.1\lambda_g$ to $0.2\lambda_g$ from the lowest frequency to highest frequency in either band, respectively. The range of electrical size for the largest ground plane dimension is $0.43\lambda_g$ to $0.74\lambda_g$.

2.5 Experimental Verification

The FRR antenna prototype, as shown in Fig. 2.16, was fabricated based on the nominal antenna parameters for both the FRR and slotted ground plane. Single-sided copper-clad Rogers 5880 substrate material with a 62 mil (1.5748 mm) thickness was used. The top and bottom conducting features were milled on the same 62 mil (1.5748 mm) substrate using an LPKF milling machine. Subsequently, the top and bottom layers were clamped together and the 5 vias and RG-178 coaxial feed line were soldered in place. Due to the LPKF machine tolerances, we could expect as much as 0.1 mm fabrication

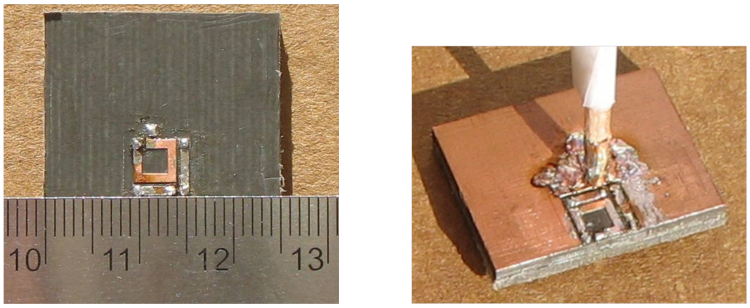

(a) Top view (b) Bottom view

Figure 2.16: FRR prototype antenna in slotted ground plane fabricated on an LPKF milling machine. Nominal structural parameters were used.

error in both the line and gap widths since each requires two separate edge cuts. The FRR in slotted ground plane was re-simulated using a line width $w = 0.9$ mm and gap width $g = 0.4$ mm.

Fig. 2.17 presents the measured and simulated reflection coefficients for the FRR in slotted ground plane. There is some disagreement in the location and bandwidth of the first resonance. The upper band differs slightly in matching level and cutoff frequency near 6 GHz. We attribute these differences to the achievable fabrication tolerances noted earlier. Gain radiation pattern measurements were conducted in the Antenna and Microwave Laboratory's anechoic chamber at San Diego State University. Fig. 2.18 and Fig. 2.19 present the simulated and measured E_θ and E_ϕ gain pattern cuts in XZ plane at $\phi = 0°$, and the YZ plane cuts at $\phi = 90°$. The co-polarized patterns are similar in both shape and gain level. Measured cross-polarization patterns also tend to agree in both shape and gain level. However, given the size of the antenna, mounting and misalignment errors, some disagreement is expected.

Nulls in the measured radiation patterns near $\theta = 180°$ are attributed to the scattering effects of the chamber's antenna under test (AUT) positioning post. Ripples occurring in the measured co-polarized patterns show increased amplitude with frequency. This effect is attributed to currents flowing along the coaxial feed line and contributing

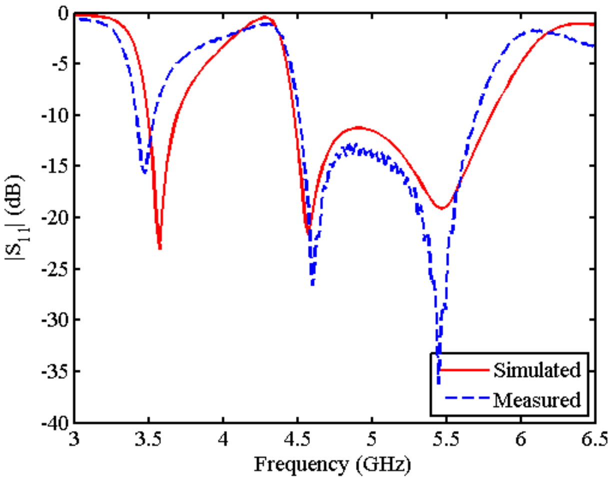

Figure 2.17: Measured and simulated reflection coefficient magnitude plots using the actual line and gap widths.

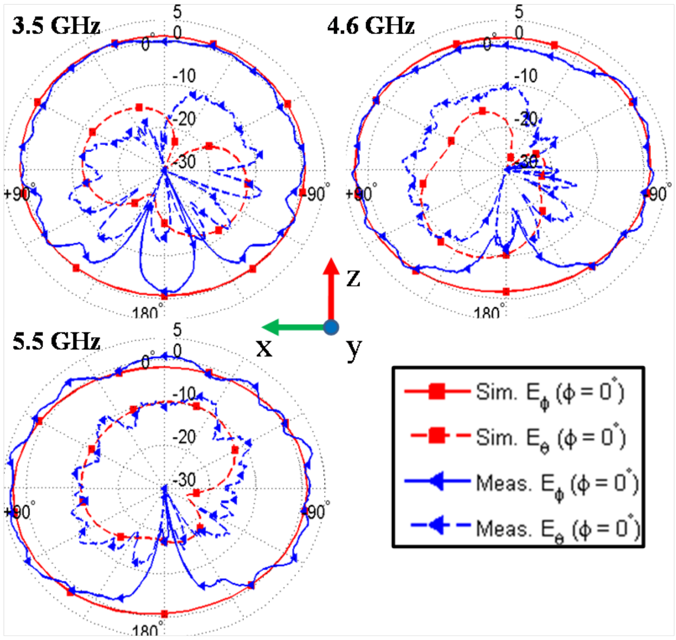

Figure 2.18: Measured and simulated E_ϕ and E_θ cuts in the XZ plane ($\phi = 0°$).

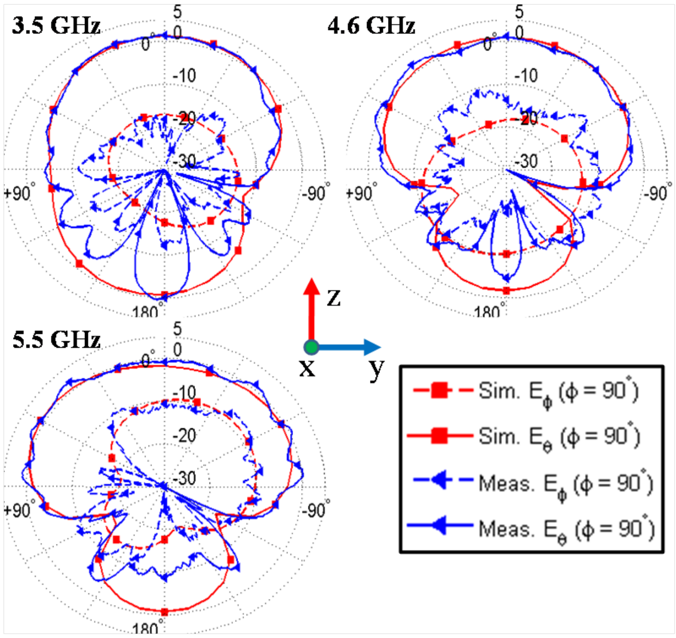

Figure 2.19: Measured and simulated E_ϕ and E_θ cuts in the YZ plane ($\phi = 90°$).

to the radiation pattern. A balun or other method to decouple the coaxial shield from the antenna and ground plane should have been used. It is worth mentioning if the measured gain is averaged over 1 period of ripple, the averaged measured gain agrees to within a fraction of a dB with the simulated gain. This is further shown in the peak gain measurements (Fig. 2.20).

2.6 4 Element FRR Sub-Array

The FRR is compact when installed on a half-wavelength (guided wavelength) ground plane and tends to excite currents confined to the embedded edge with relatively less coupling to the adjacent edges. With this in mind, we briefly present some simulated data for a 4 element sub-array in which each ground plane edge contains an embedded FRR as shown in Fig. 2.21. This sub-array is implemented on a 25 mm×25 mm square slab of grounded FR4 dielectric. The total antenna size including ground plane ranges from approximately 0.25λ to 0.5λ over the operational frequency band from 3.2 GHz

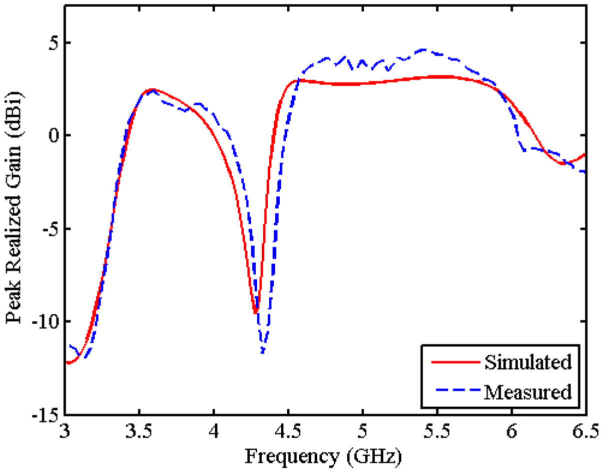

Figure 2.20: Measured and simulated peak gain profiles for the actual dimensions of the fabricated FRR antenna in slotted ground plane.

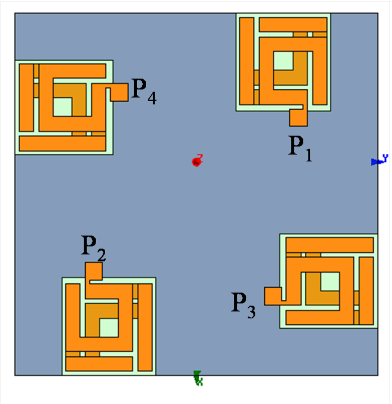

Figure 2.21: 4 element sub-array of FRR elements on a small ground plane.

to 6 GHz. The embedded element radiation patterns associated with each antenna port are presented in Fig. 2.22. This sub-array shows significant pattern diversity in that the elements appear to have very little overlap. Pattern diversity can be attributed to the currents being primarily confined along a single radiating edge of the ground plane. When viewed as a single aperture, this element can be classified as a multiple mode antenna since each radiation pattern is associated with a different current mode on the ground plane.

The scattering parameters plotted in Fig. 2.23 demonstrate wide impedance

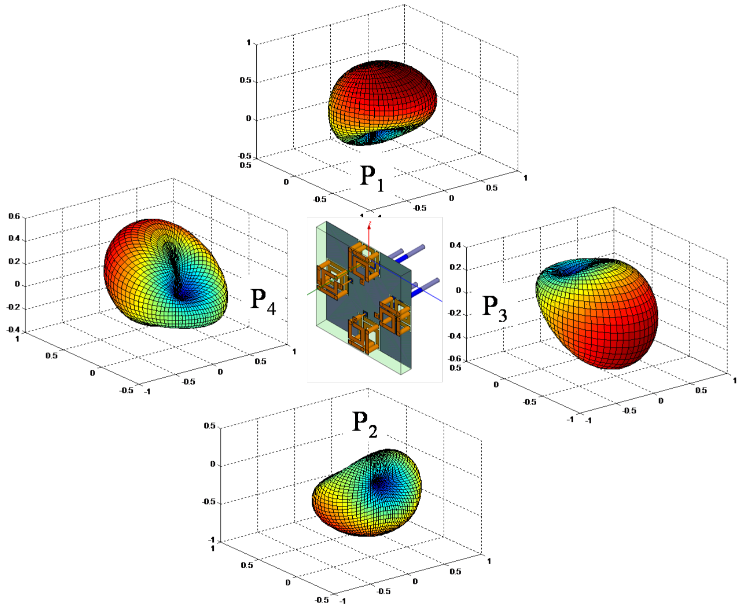

Figure 2.22: Embedded element patterns for each port of the 4 element FRR sub-array.

matching in two bands and the low level of mutual coupling across these bands. Not surprisingly, the diametrically opposed elements show the highest level of coupling as the embedded element patterns for these share the same polarization. Ideally, we would like the isolation level to be even higher for improved antenna efficiency. This is particularly important when forming beams involving multiple ports with significant phase shifts. Clearly, a more direct approach to exciting multiple modes on the same or collocated apertures is needed. We will pursue that goal by exciting orthogonal modes on collocated circular patch antennas as presented in the following chapter.

2.7 Conclusions

A compact antenna based on the folded ring resonator (FRR) metamaterial structure was presented. Implemented as a folded wire embedded in a dielectric substrate, the FRR antenna was shown to have closely spaced resonances. By coupling the FRR

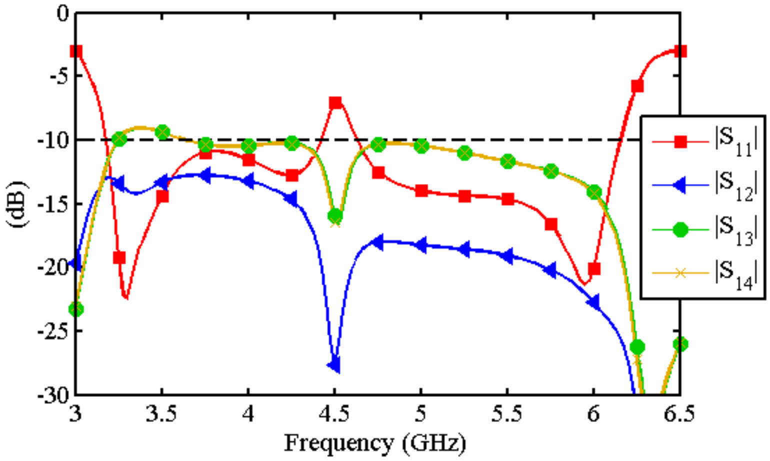

Figure 2.23: Unique scattering parameters of the 4 element FRR sub-array as implemented on a 25 mm×25 mm square slab of grounded FR4 dielectric.

antenna with a slotted ground plane, impedance matching was improved near the resonances. The result is a stable radiation resistance and near zero reactance over two bands matched better than -10 dB. Induced ground plane edge currents along the Y-axis, produce highly linearly polarized radiation patterns. Peak gains of approximately 2.5 dBi and radiation efficiency greater than 90% are maintained over the two bands. Additionally, simulated data was presented for a 4 element FRR sub-array showing good pattern diversity and reasonable port isolation. Given the role played by the small ground plane in producing the embedded radiation pattern, we contend that this antenna can also be called a multiport, multiple mode antenna. In the following chapter we will explore this idea further using element aperture geometries producing well defined and highly isolated radiating modes.

Acknowledgments

Chapter 2, in part, is a reprint of the material as it appears in IEEE Transactions on Antennas and Propagation, 2012. Labadie, Nathan R.; Sharma, Satish K.; Rebeiz, Gabriel, IEEE, 2012. The dissertation/thesis author was the primary investigator and author of this paper.

The authors would like to acknowledge Elias Mireles, and Shiv Varanasi for their help in the operation of the LPKF milling machine.

Chapter 3

A Circularly Polarized Multiple Radiating Mode Microstrip Antenna for Satellite Receive Applications

3.1 Introduction

Pattern reconfigurable antennas offer an additional degree of freedom in the design of communications systems with which to mitigate potential threats in the electromagnetic environment. GPS receivers for example are notoriously susceptible to low power jammers and scattered signals from multipath. Receivers deployed in these environments benefit from the use of reconfigurable null forming antennas. A common implementation consists of a patch array of N elements fed by a beamforming network to generate N-1 scannable nulls [57, 58, 59]. Active and switched parasitic beamforming array approaches can require sophisticated algorithms to compute the required complex weighting at each antenna element [60, 61, 62, 63]. Another approach is to excite N orthogonal radiating modes on the same element or collocated elements and use phase and amplitude weighting to scan N-1 beam peaks and nulls. The approach taken in [64] realizes a circularly polarized (CP) directional pattern and a linearly polarized (LP) omnidirectional pattern excited on the same rectangular patch. However, only low elevation azimuthal jammers can be effectively nulled while maintaining CP in the main beam direction. Collocated patch antennas in [65] produce CP directional modes capable of azimuthal ring nulls. An LP multiple mode antenna using amplitude weighting and switched phase to achieve full hemispherical beam peak and null steering was reported in [66]. In [67], the authors investigated another LP antenna composed of multiple concentric circular patch antennas excited by feedpoints with the same symmetry as each mode's current distribution.

In this chapter, we propose a novel circularly polarized multiple mode patch antenna capable of full hemispherical null steering and limited beam peak steering as a continuation of our research presented in [68]. A low axial ratio ($<$ 3 dB) is maintained within the main beam for all scan angles. Both the radiating aperture and active feed network needed to support radiation pattern reconfiguration were designed, fabricated and measured. The aperture consists of a circular patch supporting a TM_{11} mode nested within a concentric shorted annular patch on the same dielectric substrate. In section 3.2, we use the cavity model for shorted annular patch antennas to gain insight into the nature of the beam forming capability of our proposed multiple mode antenna. This analysis is supplemented by full-wave analysis and measured impedance results for a passive multiple mode aperture and feed network as presented in section 3.3. A reconfigurable active feedwork design is presented in 3.4 which is later used to steer the antenna radiation pattern. Finally, we present the results for the fabricated and integrated antenna in section 3.5. Custom MATLAB code was used to perform the cavity model analysis and most post-processing associated with simulation and measured data. All simulation results are based on full wave analysis performed using Ansys High Frequency Structure Simulator

(HFSS). San Diego State University's Antenna and Microwave Laboratory was used to fabricate and measure all antenna and feed network protoypes.

3.2 Analysis and Theory of Operation

The primary research goal was to achieve full hemispherical null steering and limited beam peak steering using a fully integrated radiating element and feed network. Although, prior research has shown that using a combination of elements producing orthogonal radiating modes results in a set of steerable nulls controlled by the complex weighting of the modes [64, 65, 66, 67], none has sufficiently discussed the theoretical basis for this phenomena. In this section, we develop a simple analytical model used to investigate a novel configuration of two microstrip patch antennas each supporting a unique radiating mode. Collocated patch antennas were chosen for their simplicity, design versatility and adequate performance. Specifically, we used an inner TM_{11} patch concentrically nested within a TM_{21} shorted annular ring patch antenna as shown in Fig. 3.1. The shorted annular ring patch has been shown to deliver highly versatile radiation pattern and impedance performance over a wide range of design parameters [69].

The expected radiation pattern performance for the multiple mode antenna can be quickly analyzed using a mode-matching cavity model for each patch antenna as formulated in [69]. Evaluating the performance of each mode independently assumes that there is little mutual coupling between them. Data presented in following sections validates this assumption. We also assumed that the phase centers are collocated since the patches are concentrically located on the same substrate. The analysis process consists of (1) finding the general field solutions for the cavity mode-matching at the feed point, (2) solving for the coefficients of the particular cavity field solution using boundary conditions, (3) evaluating the tangential fields at the circumferential radiating aperture

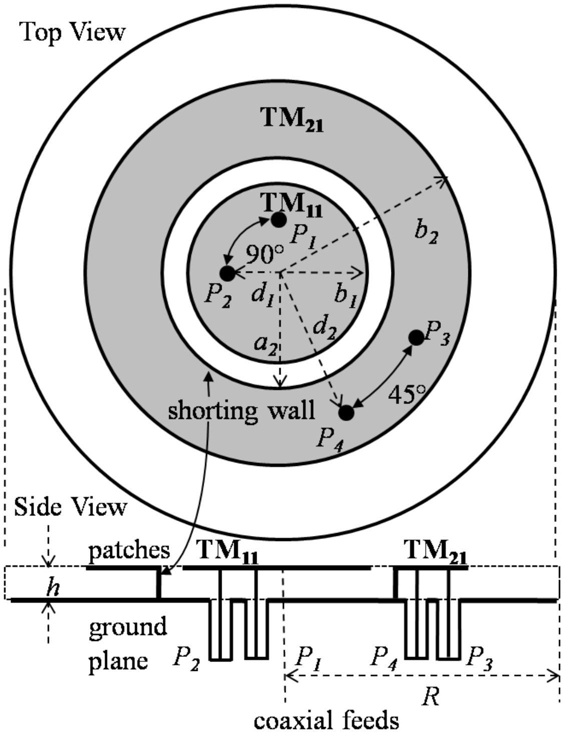

Figure 3.1: Geometry of circularly polarized multiple mode antenna aperture with direct coaxial feeding.

of the patch, (4) computing equivalent current sources that produce the same radiated far-fields as the aperture fields, (5) computing the vector potentials of the equivalent current sources and (6) transforming the vector potentials into the far-field. Using the results of [69], each linear polarization of the mode radiation pattern was calculated independently from the following far-field equations, where *n* indicates the mode number (TM_{n1}).

$$
\begin{aligned}
E^n_\phi(\phi,\theta) &= \frac{j^{n+1}}{2} h \cos\left(n\phi - \phi^n_0\right) && (3.1)\\
&\quad \times \left[k_0 b_n f\left(k_1 b_n\right) J'_n\left(k_0 b_n \sin\theta\right)\right.\\
&\quad \left.+ j k_1 b_n \sin\theta f'_{n1}\left(k_1 b_n\right) J_n\left(k_0 b_n \sin\theta\right)\right]\\
&\quad \times \left(1 - R^{TM}\right)\\
E^n_\theta(\phi,\theta) &= n k_0 b_n h \frac{j^{n+1}}{2} \frac{\sin(n\phi - \phi^n_0)}{k_0 b_n \sin\theta} && (3.2)\\
&\quad \times f_{n2}\left(k_1 b_n\right) J_n\left(k_0 b_n \sin\theta\right)\left(1 + R^{TE}\right)
\end{aligned}
$$

The parameters k_0 and k_1 are the phase constants in a vacuum and the substrate medium, respectively. Given the cylindrical symmetry of the shorted annular patch antenna, it is not surprising that the far-field equations contain Bessel's functions of the first and second kinds, J_n and Y_n (contained within f_n), respectively. The functions f_n and f'_n defined in [69] are expressed in terms of the Bessel's functions and weighting coefficients, which are themselves determined by the geometry of the cavity (i.e. the boundary conditions). Fresnel coefficients, R^{TE} and R^{TM} are included to account for the effect of the dielectric on the radiation pattern near $\theta = 90^\circ$.

Since we are interested in satellite receive applications, two feed points per mode are used to produce circularly polarized radiation. For a single mode, the two feed points are fed in quadrature with equal amplitude and a relative 90° phase shift. The physical angular separation of each pair of feed points is determined by the symmetry of the mode and given by $\phi^n_s = \pi/2n$. Assuming two feed points are used to excite each mode at an angular spacing of ϕ^n_s, the total LP field components for each mode can be expressed as follows.

$$\begin{aligned}\widetilde{E}_{\phi}^{n}(\phi,\theta) &= E_{\phi}^{n}(\phi,\theta)+j^{p}E_{\phi}^{n}(\phi+\phi_{s}^{n},\theta) && (3.3)\\ \widetilde{E}_{\theta}^{n}(\phi,\theta) &= E_{\theta}^{n}(\phi,\theta)+j^{p}E_{\theta}^{n}(\phi+\phi_{s}^{n},\theta) && (3.4)\\ p &= +1(lhcp),-1(rhcp) && (3.5)\end{aligned}$$

The CP fields for each mode can be readily obtained from the LP components, $\widetilde{E}_{\phi}^{n}$ and $\widetilde{E}_{\theta}^{n}$.

$$\begin{aligned}E_{rhcp}^{n}(\phi,\theta) &= \frac{1}{\sqrt{2}}[\left(Re\{\widetilde{E}_{\theta}^{n}\}-Im\{\widetilde{E}_{\phi}^{n}\}\right) && (3.6)\\ &\quad +j\left(Im\{\widetilde{E}_{\theta}^{n}\}+Re\{\widetilde{E}_{\phi}^{n}\}\right)]\\ E_{lhcp}^{n}(\phi,\theta) &= \frac{1}{\sqrt{2}}[\left(Re\{\widetilde{E}_{\theta}^{n}\}+Im\{\widetilde{E}_{\phi}^{n}\}\right) && (3.7)\\ &\quad +j\left(Im\{\widetilde{E}_{\theta}^{n}\}-Re\{\widetilde{E}_{\phi}^{n}\}\right)]\end{aligned}$$

The total CP far-field patterns are determined by the weighted sum of the individual mode radiation patterns.

$$E_{rhcp}^{T}(\phi,\theta)=\sum_{n=0}^{N}C_{n}E_{rhcp}^{n}(\phi,\theta) \tag{3.8}$$

$$E_{lhcp}^{T}(\phi,\theta)=\sum_{n=0}^{N}C_{n}E_{lhcp}^{n}(\phi,\theta) \tag{3.9}$$

In this chapter, only two modes are excited which reduces equations 3.8 and 3.9 to

$$E_{rhcp}^{T}(\phi,\theta)=\gamma[E_{rhcp}^{1}(\phi,\theta)+\alpha E_{rhcp}^{2}(\phi,\theta)\exp(j\beta)] \tag{3.10}$$

$$E_{lhcp}^{T}(\phi,\theta)=\gamma[E_{lhcp}^{1}(\phi,\theta)+\alpha E_{lhcp}^{2}(\phi,\theta)\exp(j\beta)] \tag{3.11}$$

The complex radiation patterns for the two circular patch modes are plotted in Fig. 3.2. As stated in [64], the phase shift β between modes changes the azimuthal location of the null while the null elevation is controlled by the mode amplitude ratio α. The phase difference between modes is specified by $\beta = \angle P_3 - \angle P_1 = \angle P_4 - \angle P_2$. Similarly, the amplitude ratio between modes is denoted by $\alpha = |P_3|/|P_1| = |P_4|/|P_2|$. Fig. 3.3 illustrates the mechanism for this behavior in the complex radiation patterns which are combined using a port amplitude ratio of 0 dB and a phase difference of 0° at 1575 MHz. Null formation is due to destructive interference of the far field radiation patterns associated with each mode. Such destructive interference occurs at angles where the two radiation patterns are both nearly equal in amplitude and out of phase by approximately 180°. Referring to Fig. 3.3a, there is a wide range of elevation angles where the mode radiation pattern amplitudes are nearly equal and 180° out of phase. For reference, a pattern amplitude difference of 3 dB with 180° phase difference corresponds to $\approx$ -11dB null depth relative to the largest of the two mode pattern amplitudes at that angle. Based on the upper plot in Fig. 3.3a, we can expect an elevation null from $\theta = 20^\circ$ to $\theta = 90^\circ$ for a null depth of better than -11 dB. Similarly, equal pattern amplitudes with a phase difference from 162° to 198° yield a null depth of -10 dB relative to the largest of the two-mode pattern amplitudes at that angle. Using this information, the -10 dB azimuth null width can be estimated from the lower plot in Fig. 3.3a as spanning $\phi = 145^\circ$ to $\phi = 181^\circ$. Fig. 3.3b confirms our estimates of the location, width and depth of the null. If the null depth is being measured relative to directivity of the beam peak in Fig. 3.3b, then both the null depth and width have increased by some amount due to the increased directivity of the beam peak relative to the two individual mode directivities. The design parameters used in this analysis are listed in Table 3.1.

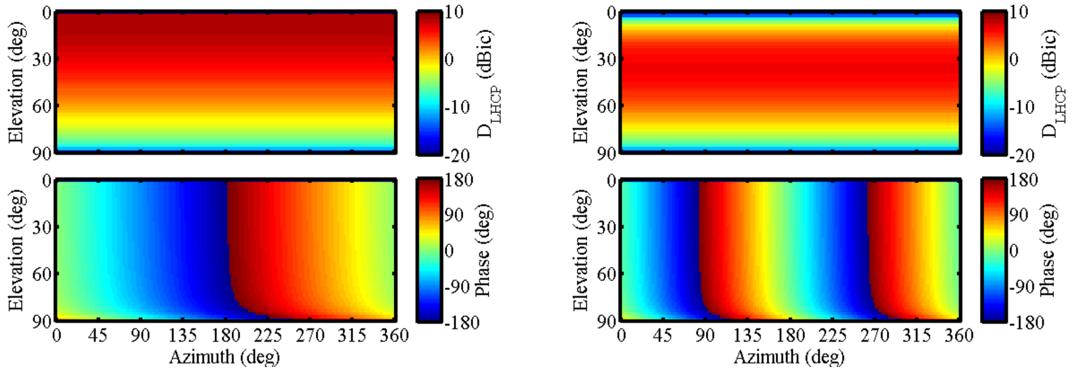

(a) TM_{11} (b) TM_{21}

Figure 3.2: Hemispherical plots of directivity and phase patterns for the individual circular patch antenna modes.

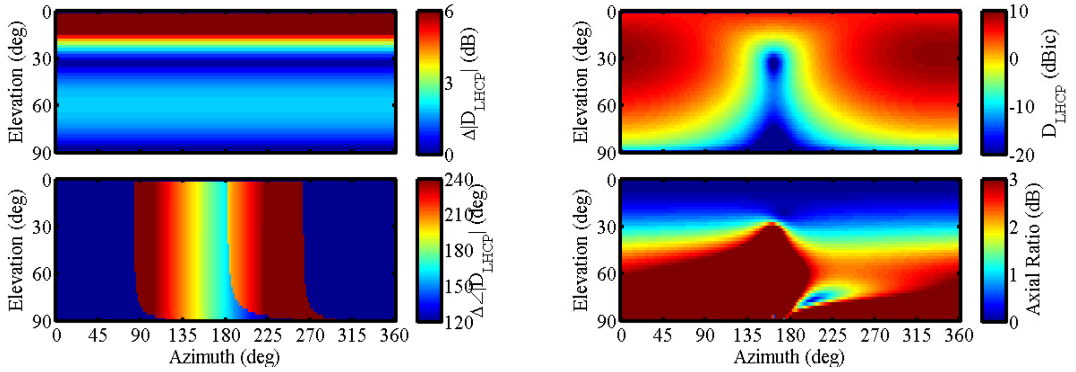

(a) $TM_{11}-TM_{21}$ ($\alpha=0$ dB, $\beta=0°$) (b) $TM_{11}+TM_{21}$ ($\alpha=0$ dB, $\beta=0°$)

Figure 3.3: Difference and sum of the two radiating modes with equal amplitude and phase excitation. The field quantities were determined by analysis (equations 3.3 to 3.11).

3.3 Passive Antenna Design

In this section, we investigate the impedance properties of the passive antenna aperture and passive portion of the feed network needed to generate CP radiation patterns. Fig. 3.4 shows a simulation model and photograph of the fabricated version of the multiple mode aperture and passive hybrid coupler feed network. The connection between the feed network and passive aperture is illustrated in Fig. 3.4a. Four connecting vias used to connect the passive aperture output ports (P_1, P_2, P_3 and P_4) to the corresponding hybrid input ports (also P_1, P_2, P_3 and P_4). In practice, the passive aperture substrate is

Table 3.1: Physical and electrical parameters used the analysis, simulation and fabrication of the CP multiple mode antenna.

Parameter	Description	TM_{11}	TM_{21}
f	center frequency (GHz)	1.575	
h	substrate height (mm)	3.2	
ε_r	substrate relative permittivity	2.15	
$\tan\delta$	substrate loss tangent	0.002	
σ_c	patch/ground conductivity (S/m)	5.8e7	
a	patch inner radius (mm)	0.0	41.0
d	radius of feed location (mm)	10.5	54.0
b	patch outer radius (mm)	36.3	75.75
R	ground plane radius (mm)	∞ (analysis), 200 (sim.)	
ϕ_s^n	angular feed location	0°	202.5°

stacked on top of the feed network substrate such that the patches are on the top and the hybrid couplers are on the bottom of the stackup. Finally, the 4 connecting vias are inserted through the 4 aligned holes in each substrate and soldered in place. First, the passive aperture was designed in HFSS based on the parameters listed in Table 3.1 derived through the analysis presented in the previous section. The analysis assumed an infinite ground plane, whereas the simulated ground plane size was chosen to be approximately one wavelength (200 mm) in diameter, which is sufficiently large to support the fringing fields of the patches. Fig. 3.5 shows that the aperture impedance parameters were in good agreement between simulation and measurement. For simplicity, symmetric S-parameters have been omitted from the plots (i.e. $S_{11} \approx S_{22}$, $S_{33} \approx S_{44}$, $S_{13} \approx S_{24}$, $S_{14} \approx S_{23}$). The overlapping -10 dB input impedance matching fractional bandwidth across both modes is approximately 1.4% (1.565 GHz to 1.587 GHz).

Second, the hybrid couplers needed to supply quadrature excitations to each pair of ports were designed in HFSS on 60 mil (1.524 mm) FR4 material ($\varepsilon_r = 4.4$, $\tan(\delta) = 0.02$). Again, acceptable agreement was obtained between simulated and measured impedance parameters for these passive feed structures as shown in Fig. 3.6. Phase differences were computed from the S-parameter measurements $\angle S_{P_2,H_2} -$

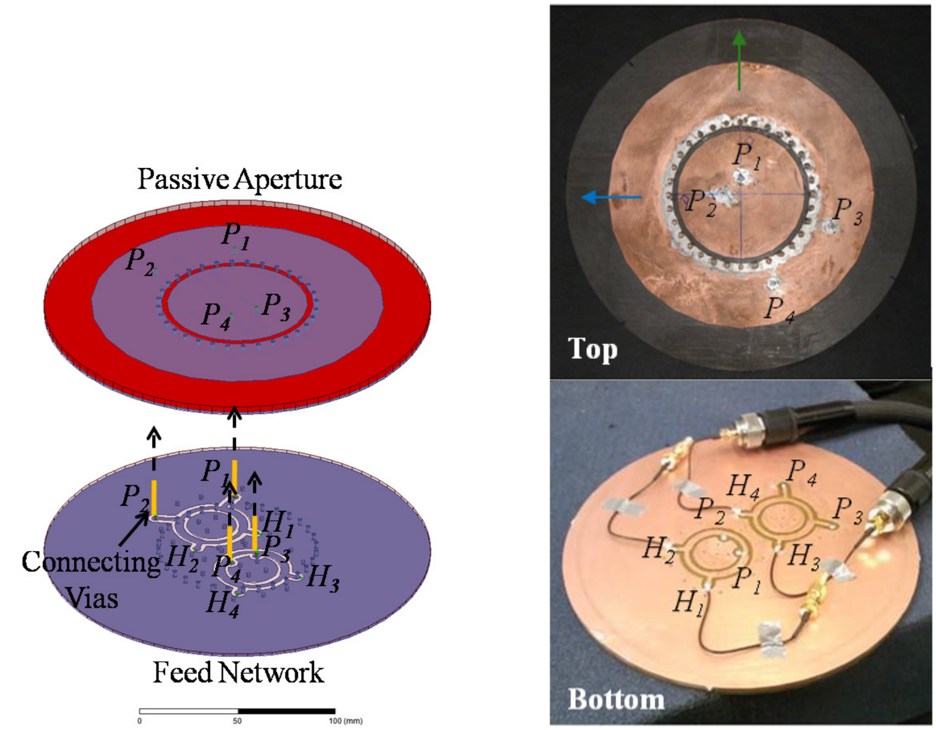

(a) HFSS simulated model. (b) Fabricated prototype.

Figure 3.4: Integrated aperture with passive feed network for impedance testing.

$\angle S_{P_1,H_2}$ (TM_{11}) and $\angle S_{P_4,H_4} - \angle S_{P_3,H_4}$ (TM_{21}), where the subscripts refer to the hybrid ports as indicated in Fig. 3.4. Similarly, the amplitude ratios were computed from $|20\log_{10}|S_{P_2,H_2}| - 20\log_{10}|S_{P_1,H_2}||$ (TM_{11}) and $|20\log_{10}|S_{P_4,H_4}| - 20\log_{10}|S_{P_3,H_4}||$ (TM_{21}). The measured response of the hybrid coupler for the TM_{21} mode shows some deviation from simulation possibly due to the uncalibrated U.FL cables used or some other fabrication issue. Using a 1 dB amplitude imbalance and ±5° phase imbalance as the maximum allowable deviations in the hybrid performance, we achieved an operational bandwidth from 1.45 GHz to 1.8 GHz.

Third, the multiple radiating mode apertures and hybrid couplers were integrated by connecting the labeled hybrid input ports to the corresponding aperture output ports using 22 gauge (0.65 mm diameter) copper wire (i.e. P_1 to P_1, P_2 to P_2, etc.). As expected, good agreement was also obtained between the simulated and measured impedance

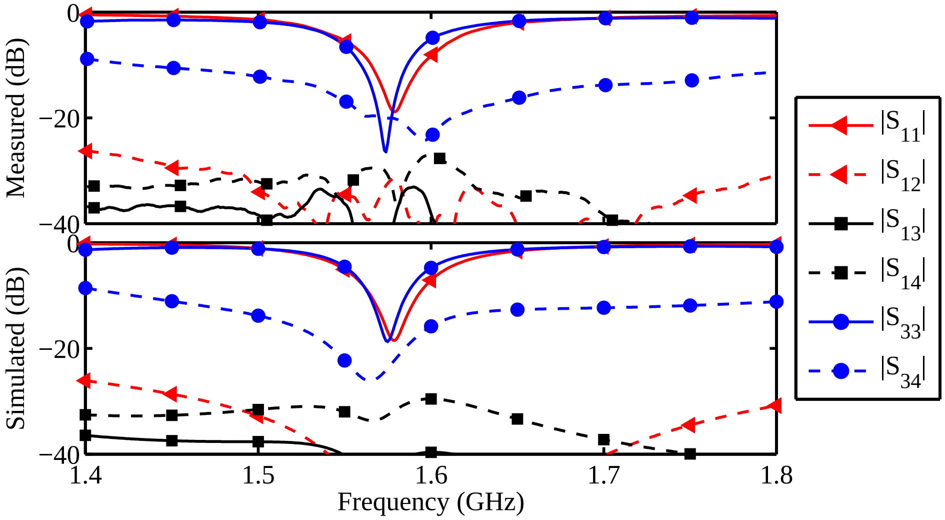

Figure 3.5: Simulated and measured scattering parameters of the patch antennas excited directly at the aperture (i.e. coax feeds from ground plane to patch).

parameters for the fully integrated passive antenna as shown in Fig. 3.7. The limiting factors for the bandwidth over which the antenna behaves as an efficient radiator are clearly the mutual coupling parameters S_{12} and S_{34}. In fact, these mutual coupling parameters between pairs of hybrid output ports (H_1, H_2 and H_3, H_4) represent the bandwidth over which the load to hybrid input ports (P_1, P_2 and P_3, P_4) presents a nearly 50 Ω impedance. In this case, the load is the output impedance of each of the antenna ports. Since the antennas are TM_{11} and TM_{21} patches on an electrically thin substrate, it is expected that the matched impedance bandwidth is on the order of a few percent with respect to a 50 Ω load. For the integrated passive antenna, the overlapping -10 dB fractional impedance bandwidth for both modes is 1.6%, or 25 MHz in absolute terms (1.562 GHz to 1.587 GHz). If used in a receive application such as GPS, this is enough bandwidth to accomodate a single 20 MHz channel. There are numerous techniques available to achieve a wider impedance bandwidth, and we are exploring such implementations as part of our ongoing research for related applications. This is particularly important if the antenna is intended to be used in a potentially harsh

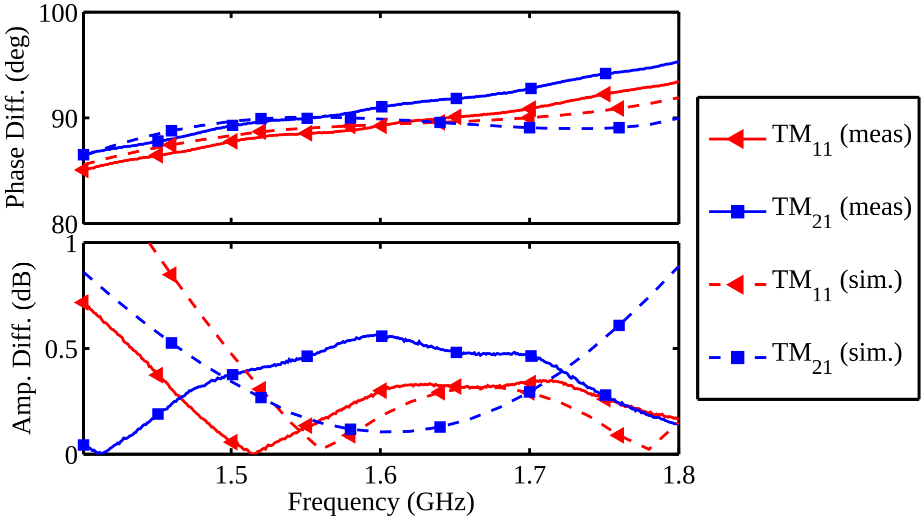

Figure 3.6: Simulated and measured amplitude and phase characteristics of the hybrid coupler output ports when disconnected from the antenna aperture.

environment where the antenna may become detuned. Some amount of impedance bandwidth margin is desirable in order for the receiver to remain operational.

3.4 Active Feed Network Design

In order to characterize the radiation pattern performance of the multiple mode antenna over a wide range of pattern reconfiguration, it was necessary to develop a feed network with many possible configuration states. The feed network should include independent amplitude and phase control of the received signals at the hybrid output ports. The functional block diagram shown in Fig. 3.8 depicts the required devices between the aperture output ports and the RF output port routed to an external receiver. Moving in the direction of the receiver, the RF signal transduced by the aperture first encounters the hybrid couplers, which were designed, fabricated and tested in the previous section. After combining in the couplers, the signal to noise ratio (SNR) for each mode is boosted by the low noise amplifier (LNA), which also provides a stable impedance match to

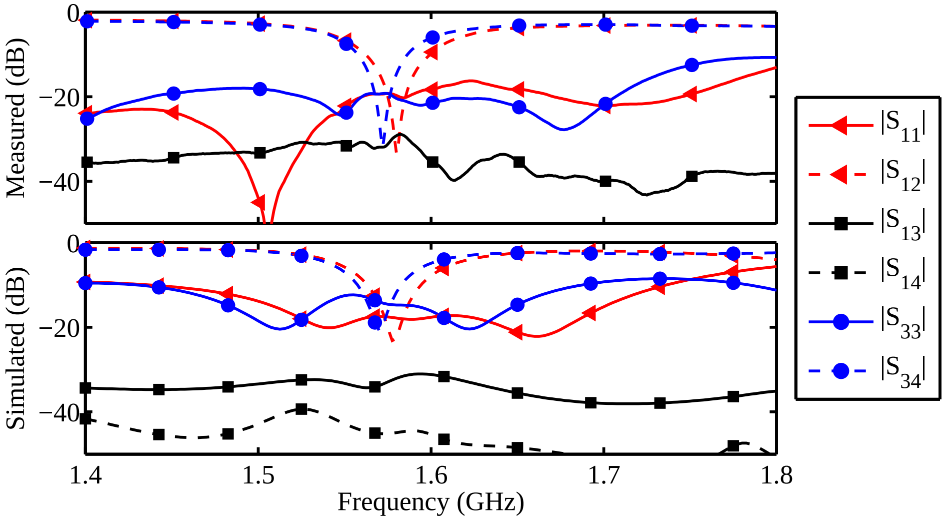

Figure 3.7: Simulated and measured scattering parameters of the multiple mode antenna aperture integrated with the passive hybrid coupler feed network.

the outputs of the hybrids. The RF signal then enters the mode control block where it undergoes a phase shift (PS) and amplitude adjustment in the variable gain amplifier (VGA) before final combining of both mode signal paths in the power combiner.

3.4.1 Component Selection

For this particular feed network, there are three types of active circuit blocks to be considered: (1) RF devices, (2) power supply circuitry and (3) control circuitry. The purpose of the control and power circuitry is simply to provide proper biasing and adjustment of the RF devices. In order to choose the appropriate RF devices, we developed a simple specification at the antenna subsystem level as summarized in Table 3.2. A low cost low noise amplifier (LNA) module was selected with approximately 15 dB of gain to provide adequate SNR and impedance buffering. For ease of calibration and measurement repeatability, a 6-bit digital step phase shifter (DP) and 6-bit digital step attenuator (DA) were selected to implement the mode control block. Table 3.2 also lists the expected RF performance of the active feed network based on datasheet

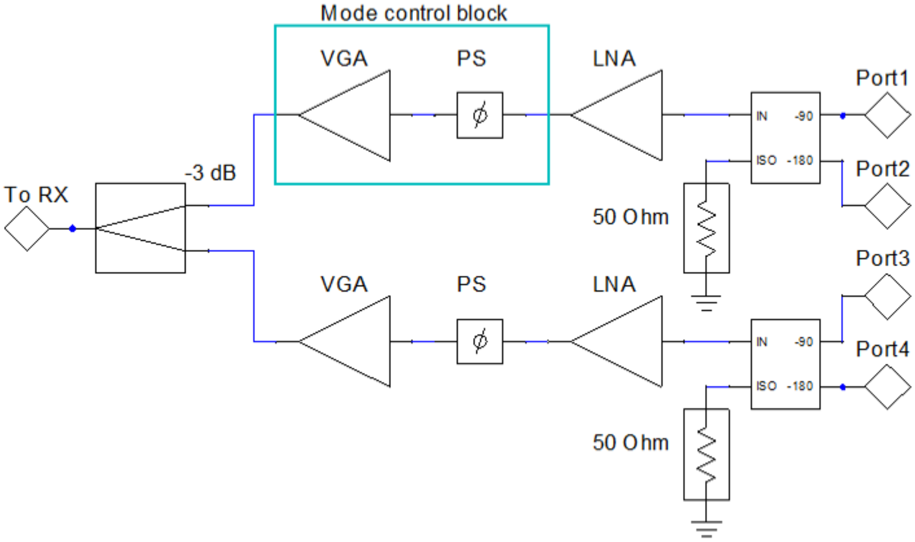

Figure 3.8: Functional block diagram of the active reconfigurable feed network (LNA = low noise amplifier, PS = phase shifter, VGA = variable gain amplifier/attenuator).

information and cascade analysis of the selected RF components. The selected RF devices collectively required three separate voltage supplies: +5 V, -5 V and +3.3 V. The appropriate voltage regulators were then chosen to provide each of the required voltages when sourced from a single 9 V supply.As with the passive implementation in section 3.3, the active feed network was designed on a 2 layer, 60 mil FR4 substrate. Given that the chosen frequency of operation is in L-band, the size of any one passive device (i.e. antenna aperture, hybrids, combiner) is much larger than any particular active device.

Table 3.2: Specified and expected RF performance of the active feed network based on the selected components.

Parameter	Specification	Selected Components
Frequency	1.575 GHz	1.575 GHz
Bandwidth	$>$20 MHz	$\approx$ 350 MHz
System NF	$<$20 dB (or $<$ NF_{VNA})	$<$5 dB
Att. Range	$\approx$30 dB	30 dB
Att. Increment	$<$1 dB	0.5 dB
Phase Range	360°	360°
Phase Increment	$<$10°	$\approx$ 6°

Therefore, the hybrid couplers and power combiner were designed and positioned on the feed network substrate first. Connecting traces, landing pads and vias for all other RF, power and control components were strategically placed during layout. Fig. 3.9 shows the component side (bottom view) of the fabricated and assembled feed network after integration with the multiple mode antenna aperture (top view).

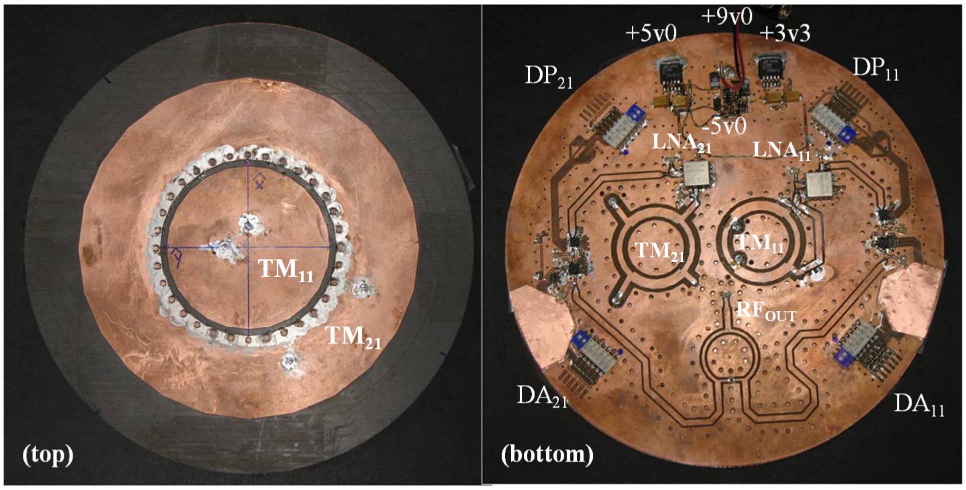

Figure 3.9: Top and bottom views of the fully integrated multiple mode antenna aperture with active reconfigurable feed network.

3.4.2 Feed Network Calibration

Calibration of the active feed network is critical in order to make direct comparisons between the analytical, simulated and measured radiation pattern performance data. The most accurate and direct method of calibration requires measurement of the radiation pattern for every configuration state. This is also the most time consuming method since there are a total of four 6-bit digital step devices each having 64 available states. A simpler method is to choose an initial configuration state as the reference and characterize each variable phase shifter and attenuator independently. The initial configuration state is denoted by the measured amplitude and phase parameters α_{ref} and β_{ref}. Assuming that the devices do not interact, we can synthesize any combination of these states by linear superposition of the calibration data taken for each device as defined in Eqns. 3.12 and 3.13. Furthermore, we simplified the task by inserting U.FL test points very near the hybrid output ports as shown in Fig. 3.10 so that the calibration data could be measured on a lab bench with a vector network analyzer (VNA).

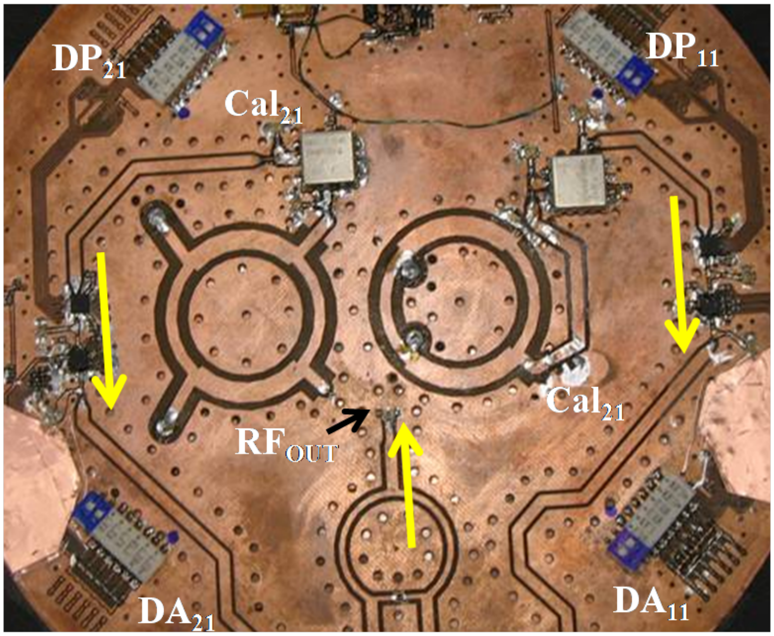

Figure 3.10: Closeup view of the calibration test points and signal paths for each mode.

A total of 192 complex S-parameter calibration measurements were recorded with $\approx 6^\circ$ phase and 0.5 dB amplitude precision as plotted in Fig. 3.11. It is important to note that the phase shifters (DP_{11} and DP_{21}) produce amplitude variations in addition to the intended phase shifts. Similarly, the attenuators (DA_{11} and DA_{21}) also introduce some amount of unintended phase shift. This means that to realize a particular set of mode weighting coefficients, we must find an optimal configuration of the four devices from among the calibration data. The mode weighting coefficients α and β are related to the calibration data as given in Eqns. 3.12 and 3.13. The parameters DA_{11}^{p}, DP_{11}^{q}, DA_{21}^{r} and DA_{21}^{s} are the measured complex S-parameters from each test point (Cal_{n1}) to the RF output for a particular configuration state. A configuration state is defined by a unique combination of the parameters ($p = 1 \cdots 32$, $q = 1 \cdots 64$, $r = 1 \cdots 32$, $s = 1 \cdots 64$), each of which is a setting number of the digital step phase shifters and attenuators as shown in Eqn. 3.13. Specifically, the setting number listed as a base 10 integer on the x-axis of Fig. 3.11 corresponds to a 6-bit setting of the 6 pin DIP switches connected to the parallel programming pins of each of the digital step attenuators and phase shifters. When one of the 6 switches is positioned in the "On" state, this corresponds to a binary 1, while a switch in the "Off" state corresponds to a binary 0.

$$\begin{aligned}
\alpha &= \left(|DA_{21}^{r}| - |DA_{11}^{p}| + |DP_{21}^{s}| - |DP_{11}^{q}|\right) - \alpha_{ref} \\
\alpha_{ref} &= \left(|DA_{21}^{0}| - |DA_{11}^{0}| + |DP_{21}^{0}| - |DP_{11}^{0}|\right) \qquad (3.12) \\
\beta &= \left(\angle DA_{21}^{r} - \angle DA_{11}^{p} + \angle DP_{21}^{s} - \angle DP_{11}^{q}\right) - \beta_{ref} \\
\beta_{ref} &= \left(\angle DA_{21}^{0} - \angle DA_{11}^{0} + \angle DP_{21}^{0} - \angle DP_{11}^{0}\right) \qquad (3.13)
\end{aligned}$$

The number of digital step attenuator configuration states was limited to 32, which translates to an attenuation range of ≈15 dB per attenuator. We found that the signal could not be reliably attenuated any further primarily due to signal leakage onto the control lines, which was able to propagate to the outputs of the attenuators. Ideally, our feed network would have been fabricated onto a four or more layer board in order to provide more isolation between the various signals (i.e. RF, power, and control). However, even with this limitation, we still achieved the desired 30 dB attenuation range between the two modes.

The active elements in the RF path between the hybrid coupler outputs and the final power combiner circuit have some impact on the output reflection coefficient of the antenna. Low noise amplifiers (LNA) were placed at the hybrid coupler output ports in order to prevent impedance changes from affecting the aperture performance. The

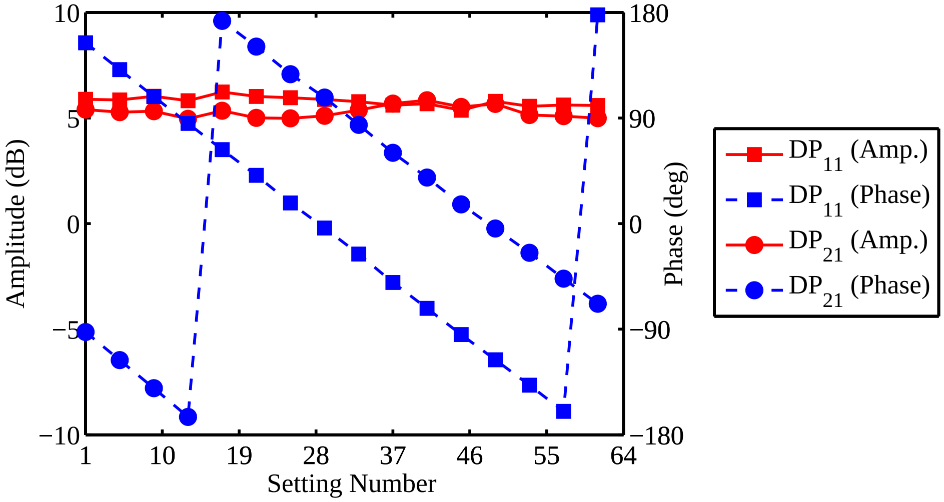

(a) Digital step phase shifter (DP)

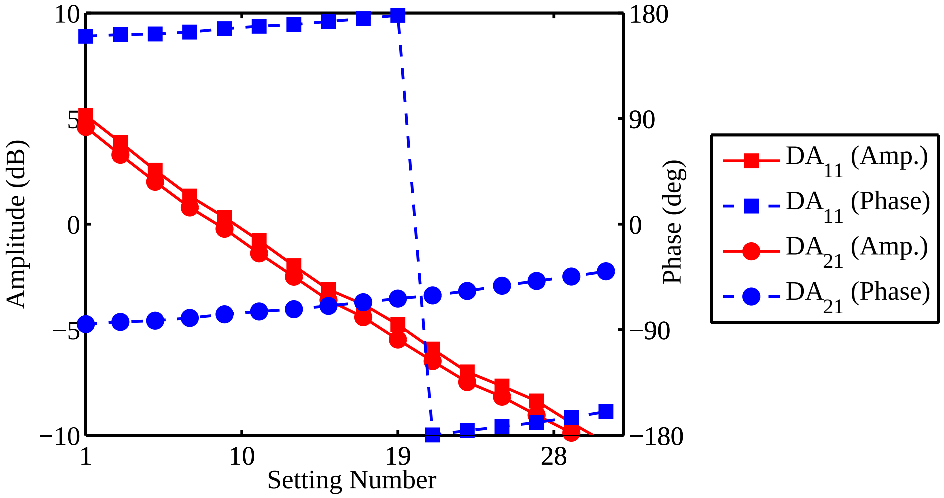

(b) Digital step attenuator (DA)

Figure 3.11: Calibration data showing the change in amplitude and phase as a function of the device setting.

digital step phase shifters were determined to have negligible impact on the output match over all settings of the 6-bit devices. However, the output impedance of the digital step attenuators does vary significantly with setting number. Measurements of the antenna output reflection coefficient at the power combiner were taken over 32 settings for each of the 6-bit digital step attenuators (32 settings each). As shown in Fig. 3.12, the output reflection coefficient remains below -10 dB for all settings. Device DA_{21} shows higher reflection coefficient variation and is due in part to undesired coupling between power, control and RF lines of the device. The traces for parallel interface control of device DA_{21} were necessarily routed under the component presenting both a leakage path and a smaller ground plane. One limitation of the 2-layer board used for the feed network is the inability to route all traces while maintaining sufficient isolation between them.

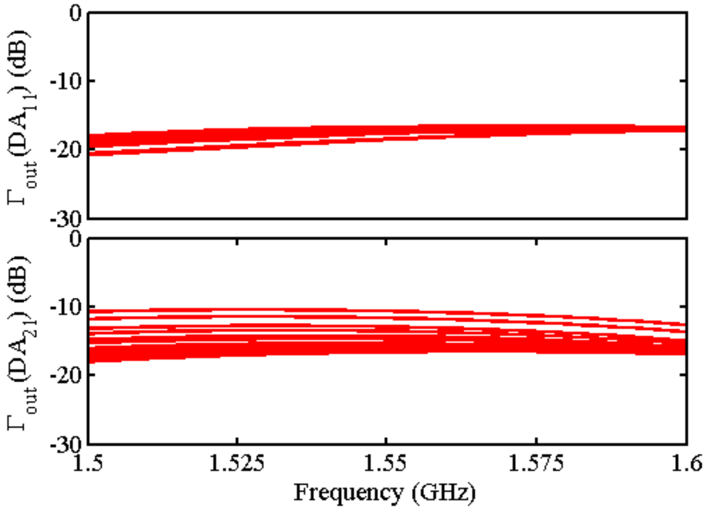

Figure 3.12: Plots of the output reflection coefficient (Γ_{out}) seen at the antenna output port (RF_{out}) for the 32 available settings for each of the 6-bit digital step attenuators (DA_{11} and DA_{21}).

3.5 Radiation Pattern Measurements

After integration and calibration, the integrated antenna was mounted in the combined spherical near-field and far-field anechoic chamber for radiation pattern characterization. The measurements were taken in two stages. First, we collected data on the passive individual mode patterns to verify that the passive antenna aperture and hybrid couplers were functioning as predicted in simulation. Second, the active RF circuitry was used to steer the beam peak and null using the calibration table data and compared to simulation and analytical data. Fig. 3.13 shows the integrated antenna mounted in the anechoic chamber and the HFSS simulation model used for comparison. All measured data was obtained using an Anritsu Lightning VNA, NSI WR-650 near field probe and Orbit FR's Spectrum Analysis data acquisition and processing software package all of which we have available in the Antenna and Microwave Laboratory (AML) at SDSU.

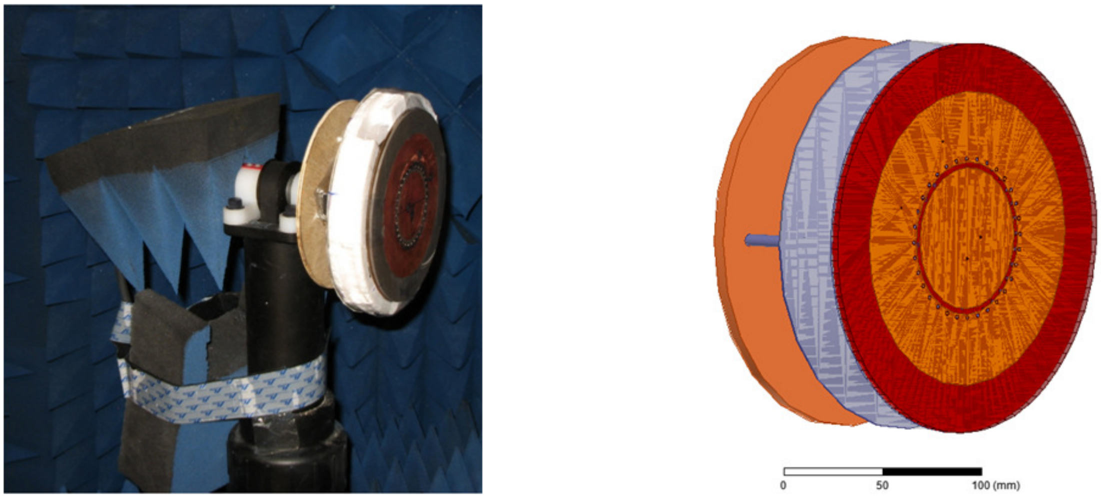

(a) Fabricated prototype

(b) HFSS simulated model

Figure 3.13: The integrated antenna composed of passive aperture and active feed network.

3.5.1 Individual Mode Patterns

The passive radiation pattern measurements of each mode were made by disconnecting the active circuitry at the test points located at the output of each hybrid coupler. We wanted to ensure the maximum isolation between the modes and eliminate other possible sources of complication. Each mode was measured one at a time while terminating the other in a 50 Ω load.

Fig. 3.14 compares the simulated and measured data at 1.575 GHz for both co-polarized amplitude pattern and axial ratio of the TM_{11} mode over the entire sphere. Since we are demonstrating full hemispherical null steering and partial hemispherical beam peak steering, it makes sense to plot these quantities over the entire sphere. There is considerable agreement seen in the simulated and measured patterns. To further quantify this agreement, we have plotted the co-polarized realized gain, cross-polarized realized gain and axial ratio of the beam peak versus frequency ($\phi = 0^\circ, \theta = 0^\circ$) in Fig. 3.15. Realized gain includes all the associated losses present in the antenna aperture and active feed network. The in-band data points (1.565 GHz to 1.585 GHz) show acceptable agreement. At center frequency (1.575 GHz), the measured co-polarized gain differs by 6.7% from simulated value while the axial ratio differs by only 4.5%. Above the center frequency, there is significant disagreement in the measured cross-polarized gain, which is much more sensitive to non-ideal chamber conditions (i.e. scattering from walls and mounting surfaces) due to its relatively low signal power.

The radiation pattern properties of the TM_{21} mode were measured in the same way as the TM_{11} mode. Again, close agreement is seen in the complete amplitude and axial ratio patterns plotted in Fig. 3.16 at the center frequency (1.575 GHz). There are several identifiable features in both the simulated and measured plots that agree in location and appearance including a deep null near angles ($\phi = 270^\circ, \theta = 0^\circ$), beam peak at angles ($\phi = 30^\circ, \theta = 36^\circ$) and bump in the axial ratio between azimuth angles $\phi = 100^\circ$

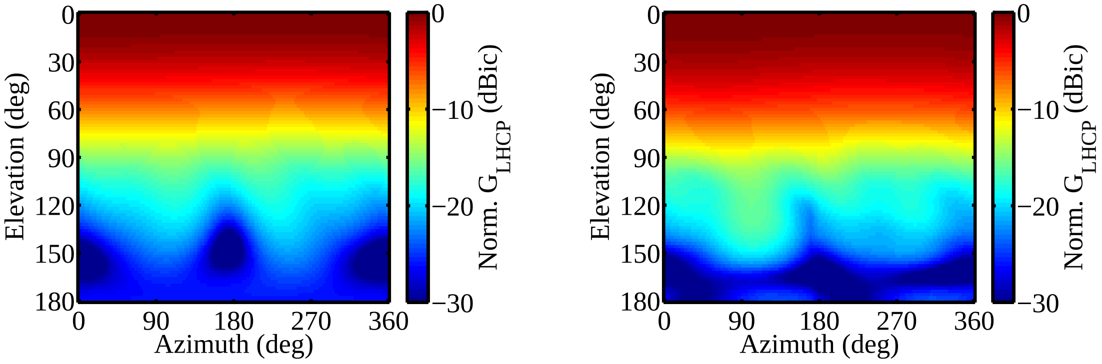

(a) Simulated

(b) Measured

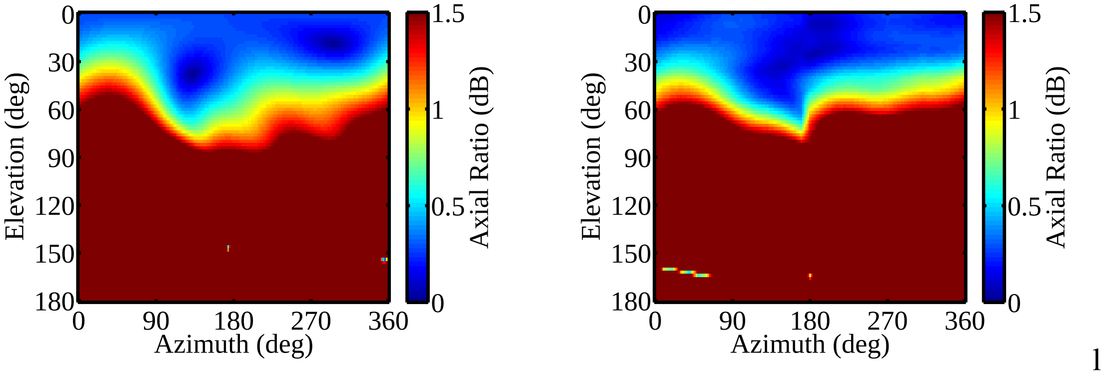

(c) Simulated

(d) Measured

Figure 3.14: Full spherical simulated and measured normalized gain and axial ratio patterns for TM_{11} at center frequency (1.575 GHz).

and $\phi = 160°$. The agreement between simulated and measured TM_{21} data is established by comparing the co-polarized realized gain, cross-polarized realized gain and axial ratio versus frequency as shown in Fig. 3.17. The elevation angle at which the beam peak of TM_{21} mode occurs is $\theta = 36°$. However, the TM_{21} radiation pattern is rotationally symmetric in azimuth, which means there is likely variation in both the realized gain and axial ratio as a function of azimuthal angle for a fixed elevation angle of the beam peak. Selecting realized gain or axial ratio at only a single angle may give a false measure of the overall mode performance. Therefore, Fig. 3.17a plots the maximum realized gain and axial ratio while Fig. 3.17b plots the minimum of the same parameters. Maximum realized gain was selected from the realized gain of the TM_{21} mode over all azimuth

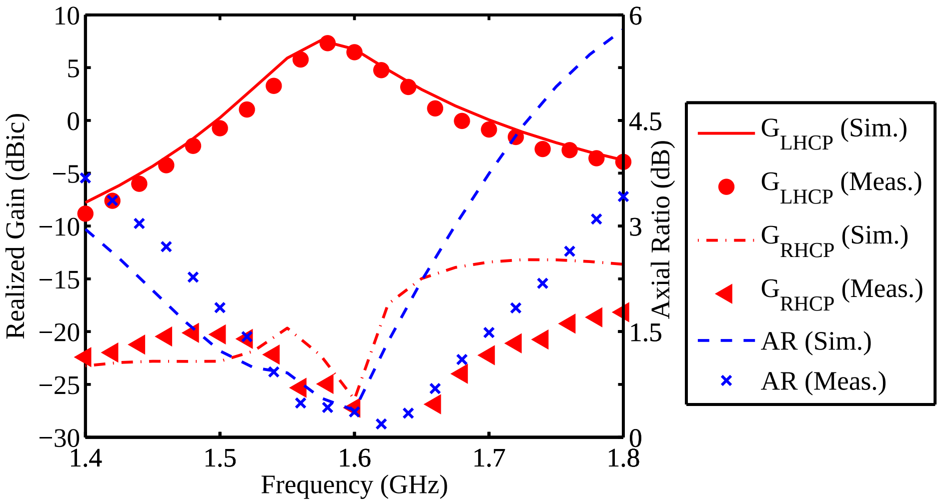

Figure 3.15: Simulated and measured TM_{11} mode radiation pattern properties at $(\theta = 0^\circ, \phi = 0^\circ)$ versus frequency.

angles and occurs at the elevation beam peak angle. Similarly, the worst case or minimum axial ratio was selected from all azimuth angles at the elevation angle of the beam peak.

The peak directivity and total antenna efficiency for each mode is plotted over frequency in Fig. 3.18. TM_{21} shows good agreement in both peak directivity and total efficiency. An approximately 3 dB decrease in directivity is observed for TM_{21} near 1.575 GHz. This is consistent with the radiation pattern transitioning from a directional to a conical radiation pattern. However, the peak directivity of TM_{11} consistently differs over frequency by approximately 0.7 dB from the simulated value. One possible source of this error is the relatively short distance between the probe and AUT (˜2 λ). Since TM_{11} is directional beam pointed at the probe on boresight, it is possible that the deviation in measured peak directivity is caused by multiple reflections (mutual coupling) between probe and AUT. At center frequency, 1.575 GHz, the TM_{11} and TM_{21} modes have total efficiencies of 68% (-1.7 dB) and 79% (-1.0 dB), respectively. Some inefficiency can be attributed to the lossy FR4 substrate used in the design of the hybrid couplers. It is expected that the higher order TM_{21} mode will suffer more loss since the radiating

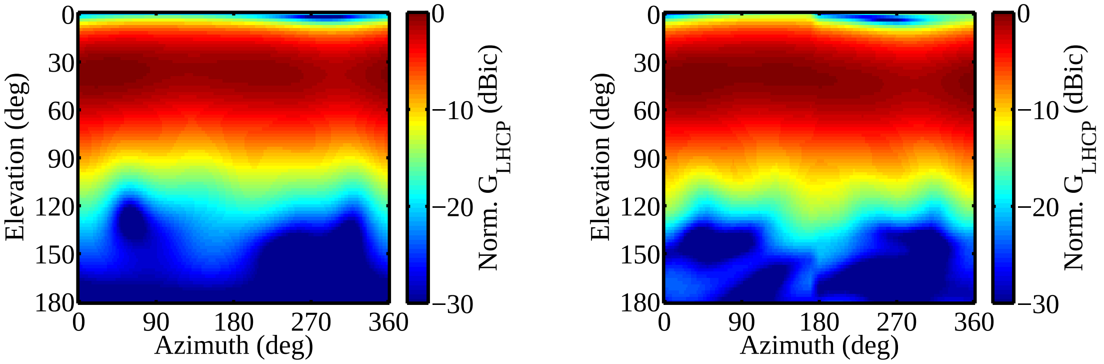

(a) Simulated (b) Measured

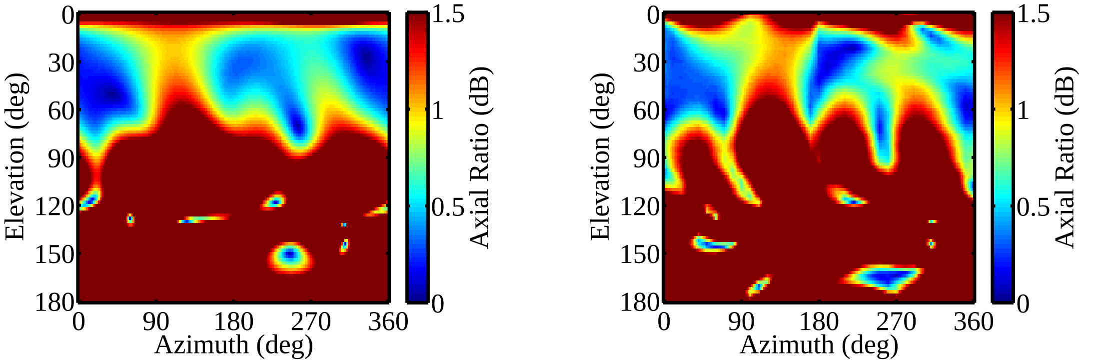

(c) Simulated (d) Measured

Figure 3.16: Full spherical simulated and measured normalized gain and axial ratio patterns for TM_{21} at center frequency (1.575 GHz).

currents must travel farther over its larger physical aperture.

3.5.2 Beam Peak and Null Steering

Finally, the active circuitry was reconnected to the hybrid coupler outputs in order to demonstrate the null and beam peak steering capabilities of the antenna. The entire antenna was powered from a single 9 V battery, which provided enough power for several full spherical measurements. A total of 11 configuration states were chosen to demonstrate the azimuth and elevation steering properties of the antenna. Each configuration state was optimally chosen from all combinations of the calibration data

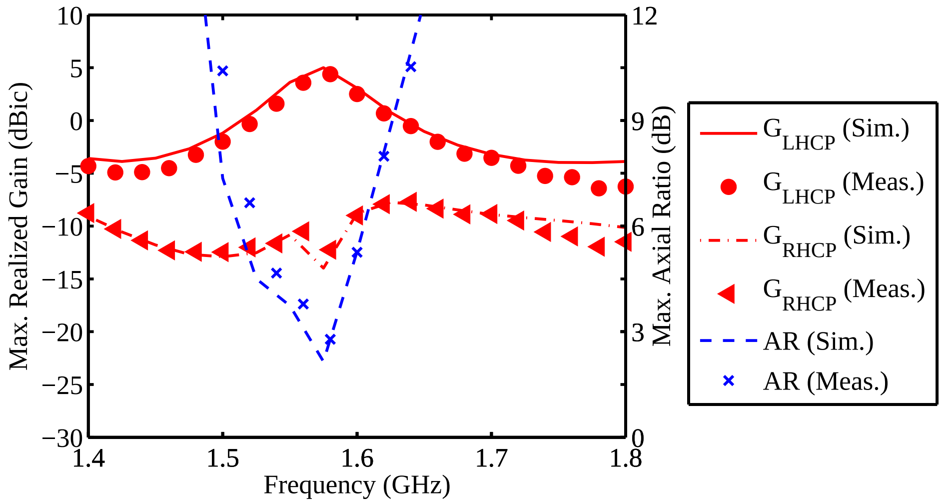

(a) Maximum over all azimuthal angles

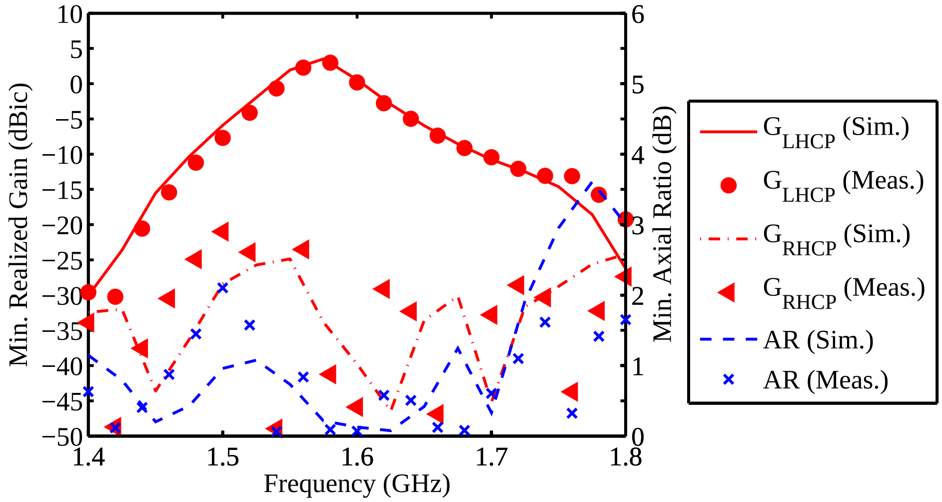

(b) Minimum over all azimuthal angles

Figure 3.17: Simulated and measured TM_{21} radiation pattern properties at $(\theta = 36^\circ, \phi = 0^\circ \cdots 360^\circ)$ versus frequency.

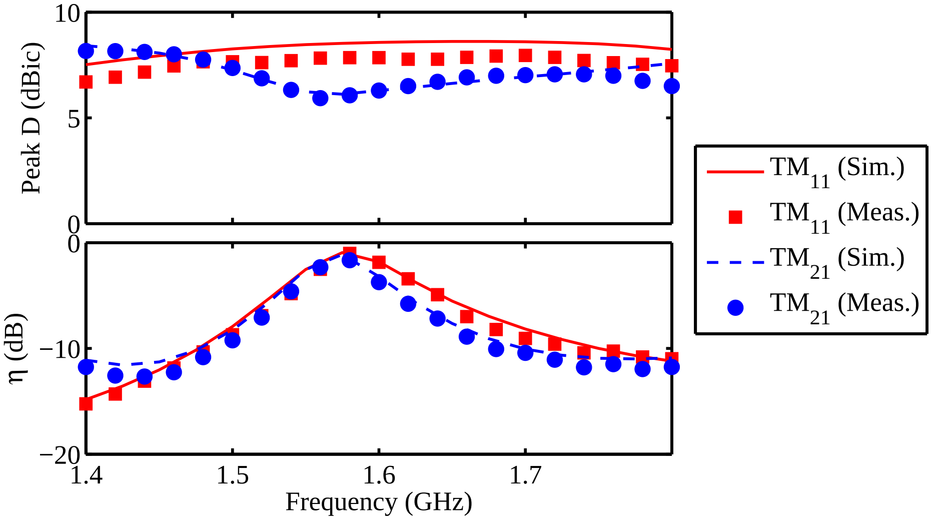

Figure 3.18: Simulated and measured peak directivity and total efficiency versus frequency showing that both modes share and overlapping band of efficient operation.

to deliver the desired mode weighting coefficients (α and β). Table 3.3 lists the 4 configuration states used to steer the beam in azimuth using only the relative phase offset between the two modes. Similarly, Table 3.4 lists the 7 configuration states used to steer the beam in elevation using only the amplitude ratio between the two modes. The state of each device (DP and DA) is given as a 6-bit binary number which represents the switch positions needed to program each device in direct parallel mode.

Table 3.3: Active feed network configuration states and device settings for azimuthal beam peak and null steering.

State	α (dB)	β (deg)	DP_{11}	DA_{11}	DP_{21}	DA_{21}
1	0	0	000111	001101	011011	001100
2	0	90	010011	001101	010111	001011
3	0	180	001101	001101	000010	001100
4	0	270	111001	001101	011101	001011

Full spherical near-field radiation pattern data was measured for each configuration state. Fig. 3.19 shows the measured normalized co-polarized radiation patterns for 4 cases of azimuth steering determined by the phase offset between the two modes. As

Table 3.4: Active feed network configuration states and device settings for elevation beam peak and null steering.

State	α (dB)	β (deg)	DP_{11}	DA_{11}	DP_{21}	DA_{21}
1	-15	0	011100	000011	111001	100000
2	-10	0	000110	000111	100000	011010
3	-5	0	110001	001001	000111	010001
4	0	0	000111	001101	011011	001100
5	5	0	000011	010011	010101	001000
6	10	0	001111	011101	011110	000111
7	15	0	000001	100000	001101	000001

the phase of TM_{21} increases with respect to TM_{11}, both the beam peak and null steer in the $-\phi$ direction. This can be understood by looking back at the analytical phase patterns for each mode in Fig. 3.2. The phase of each mode monotonically increases with azimuthal angle. Therefore, the angle at which the two modes differ by 180° will decrease as the phase of TM_{21} is increased relative to TM_{11}. The radiation patterns of only 4 of the 7 configuration states for elevation steering are shown in Fig. 3.20. These 4 cases demonstrate that using only the amplitude ratio between modes, the null and beam peak can be steered over a wide range of elevation angles.

Analysis, simulation and measurement of three important performance parameters are presented in Fig. 3.21 in order to quantify how predictably and practically the antenna beam can be steered. Peak directivity for both the beam peak and null is an important figure of merit that describes how well the antenna receives power from a particular direction and polarization. All three methods of determining the beam peak and null directivities are in close agreement for each configuration state both for the azimuthal and elevation scan cases. Differences between measured and simulated beam peak directivities are typically in the range from 0.5 dB to 1.0 dB. This is also the likely range of error inherent to the measurement process itself. The parameters ϕ_{scan} and θ_{scan} are the angular coordinates corresponding to either the beam peak or null as identified in the plot legend.

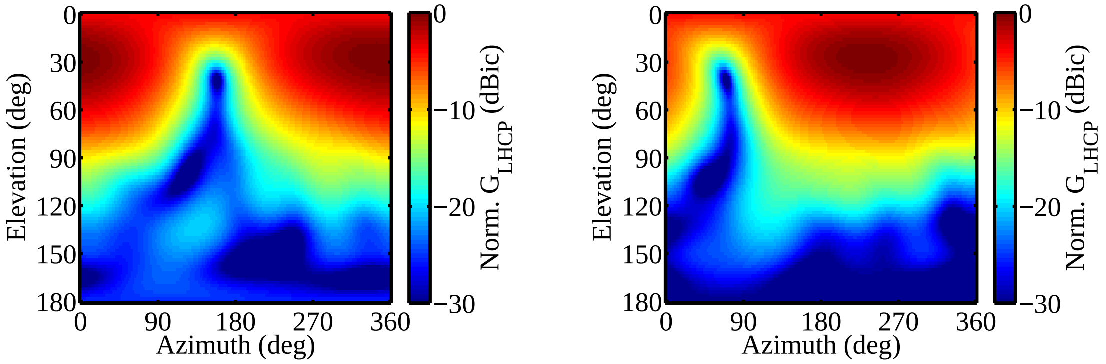

(a) $\alpha = 0$ dB, $\beta = 0°$ (b) $\alpha = 0$ dB, $\beta = 90°$

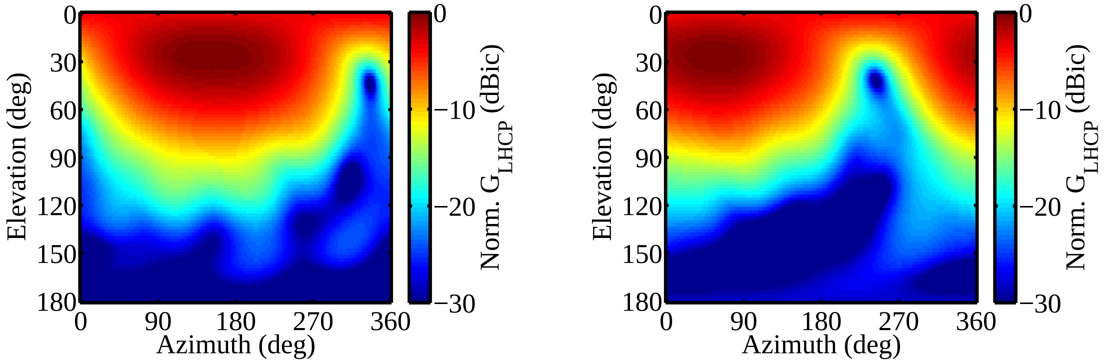

(c) $\alpha = 0$ dB, $\beta = 180°$ (d) $\alpha = 0$ dB, $\beta = 270°$

Figure 3.19: Normalized gain patterns for 4 configuration states demonstrating azimuthal beam peak and null steering.

Azimuthal Steering

In general, it is clear that applying a phase offset β produces a one-to-one change in the azimuthal angle of the beam peak and null. Also, the elevation angle of the beam peak and null remains constant to within $< 5°$. This demonstrates the degree of independence between the elevation and azimuth steering, which makes the beam control both simple to understand and simple to implement. Clearly, both the beam peak and null can be steered 360° in azimuth with a resolution of $\approx 5°$ and limited only by the 6-bit DP. The amplitude ratio α between the modes primarily produces a change in the beam peak and null elevation angle although the azimuthal angle tends to fluctuate. Over all

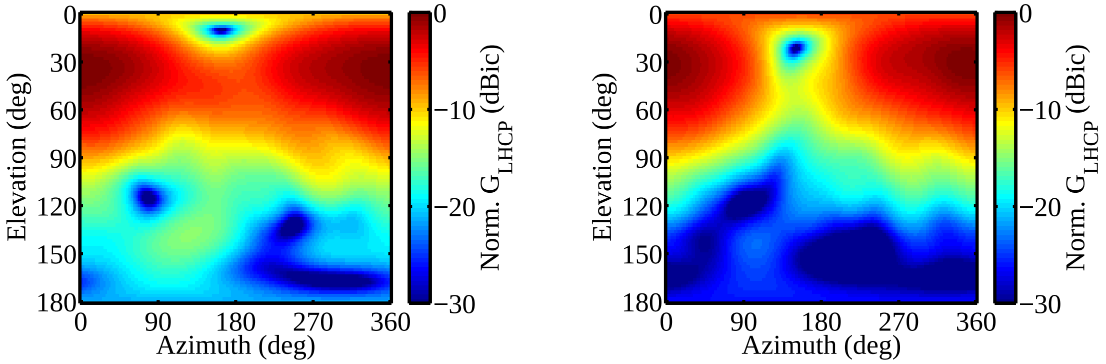

(a) $\alpha = 10$ dB, $\beta = 0°$ (b) $\alpha = 5$ dB, $\beta = 0°$

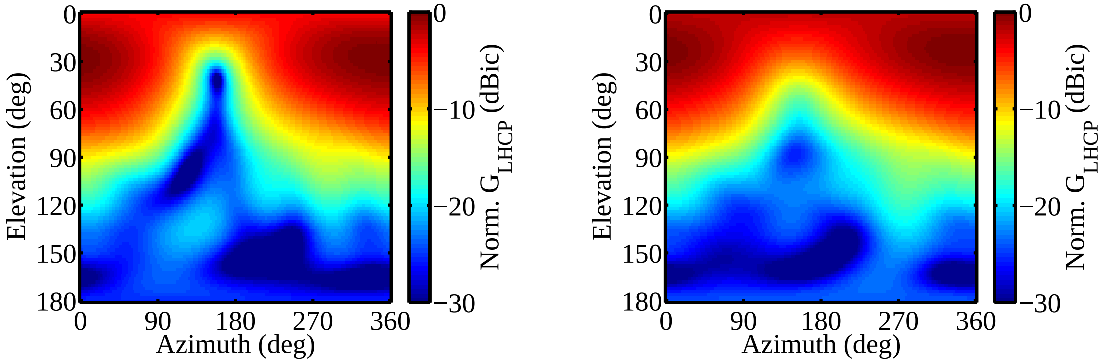

(c) $\alpha = 0$ dB, $\beta = 0°$ (d) $\alpha = -5$ dB, $\beta = 0°$

Figure 3.20: Normalized gain patterns for 4 configuration states demonstrating azimuthal beam peak and null steering.

elevation steering configuration states the change in azimuth location is $\delta\phi_{scan} = 24°$ for the null and the beam peak moves by as much as $\delta\phi_{scan} = 37°$.

Elevation Steering

A mode amplitude ratio range of 20 dB is required to steer the beam null from $\theta = 0°$ to $\theta = 90°$ while maintaining a null depth of ≈ 20 dB or less. We selected a DA with a minimum increment of 0.5 dB, which corresponds to a worst case elevation angle resolution of $\approx 5°$. This is due to the fact that the change in elevation angle is steepest in the range of α between -5 dB and 0 dB. The beam null is therefore steerable in approximately 5° increments over the entire hemisphere. The beam peak however has a scan range limited to a conical region defined by a measured elevation angle range from 16° to 36°. The minimum elevation scan angle is limited by the maximum achievable attenuation of the TM_{21} mode with respect to TM_{11}. A lower bound of -30 dB of mode isolation limits the maximum achievable attenuation based on the mutual coupling parameter S_{13} from Fig. 3.7. The maximum elevation scan angle is limited by the beam peak angle of the TM_{21} mode, which is 36° for our design.

Steering Error

The measured elevation angle of the beam null shows between 0° and 8° deviation from the simulated value over all configuration states (azimuth and elevation steering). This error can be linked to differences between the simulated and measured radiation pattern directivities, which is on the order of 0.5 dB to 1.0 dB. There is also a consistent offset between the simulated and measured azimuthal scan angles that varies from 15° and 20°. This is not unreasonable since the method of calibration did not account for the potential phase offset between the test points to the antenna apertures and this was not modeled in the simulation. The range of phase error corresponds to an unknown transmission line length on the order of a few millimeters in an FR4 substrate. However, such an issue could be greatly minimized by designing the feed network to have phase matching between test points and antenna aperture during layout. Modern PCB houses can maintain copper trace feature tolerances to within less than 1 mil, which makes the method useful even at higher frequencies.

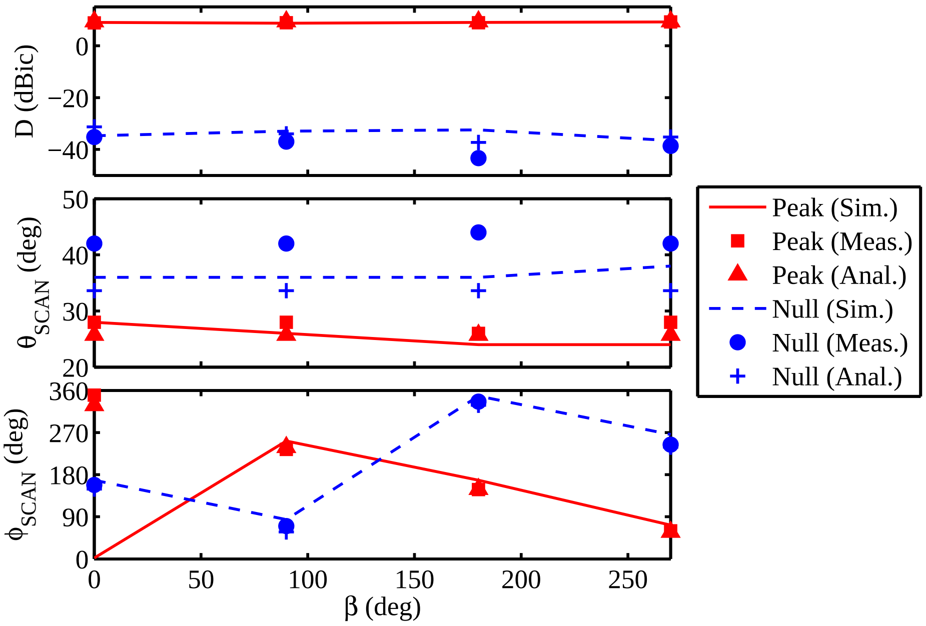

(a) Azimuthal scan.

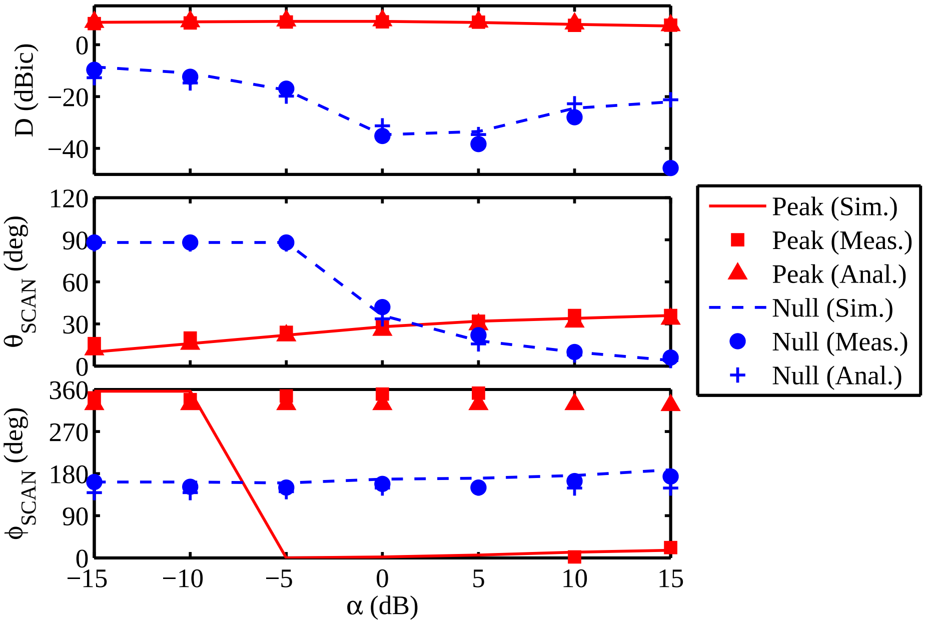

(b) Elevation scan.

Figure 3.21: Plots of the directivity (*D*) and angular location (ϕ_{scan},θ_{scan}) of the beam peak and null.

3.6 The Effect of Material Loss on the Axial Ratio Symmetry of Circular Microstrip Patch Antennas

A particularly critical point during the antenna design process is the selection of the proper material set needed to meet a variety engineering goals. There is typically a fundamental tradeoff in material selection between RF performance and cost. Lower cost materials often have relatively high RF loss characteristics in addition poorer tolerances on electrical, thermal and mechanical properties. A number of communications applications such as precision GPS reception rely on antennas with high degree of azimuthal symmetry in the circularly polarized (CP) radiation pattern. Proper angular spacing between pairs of feed points excited in quadrature and the use of sufficient numbers of such pairs contribute to high quality CP [70]. In this section, we use Ansys HFSS to demonstrate the effect of the dielectric loss tangent on the azimuthal axial ratio (AR) symmetry for the first 4 modes of the shorted annular ring microstrip patch (SARP) antenna (TM_{11}, TM_{21}, TM_{31} and TM_{41}).

3.6.1 Antenna Design

Fig. 3.22 shows the basic geometry of each of the 4 shorted annular ring microstrip patch antennas investigated in this section. The parameter $\phi_f = \frac{\pi}{2m}$ is the required angular separation between feed points for optimal CP pattern quality as function of the mode number m. Shorting vias provide an additional design parameter to achieve the desired radiation pattern over a wide range of patch dimensions [69]. This is particularly important when concentrically collocating these antennas in a nested configuration for null and beam steering as investigated in [71]. The analytical equations presented in [69] were used to derive initial design parameters for each of the 4 SARP antennas. Final design parameters for each antenna are listed in Table 3.5 and were obtained iteratively

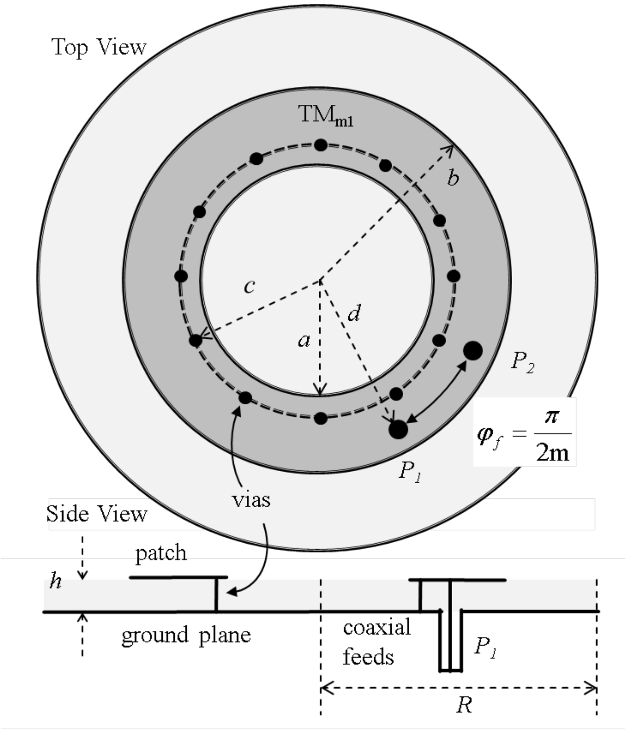

Figure 3.22: Geometry of the shorted annular ring microstrip patch antenna.

using Ansys' HFSS full wave electromagnetic simulation software.

Each antenna was designed in HFSS to present a matched load to the pair of simulated 50 Ω coaxial ports used for CP excitation ($|S_{11}| < -15$ dB) at the center frequency of 1.575 GHz (GPS L1 band). As expected, only the TM$_{11}$ radiation pattern is directional while the other 3 radiation patterns are omnidirectional as shown in Fig. 3.23. Of particular importance for this study is the azimuthal behavior AR near the beam peak for each mode. The elevation beam peaks have been determined to be 0°, 39°, 45° and 50° for the TM$_{11}$, TM$_{21}$, TM$_{31}$ and TM$_{41}$ modes, respectively.

3.6.2 Material Losses

Conceptually, a patch antenna is a leaky resonant cavity that supports standing electromagnetic waves while functioning as an efficient radiator. The standing waves

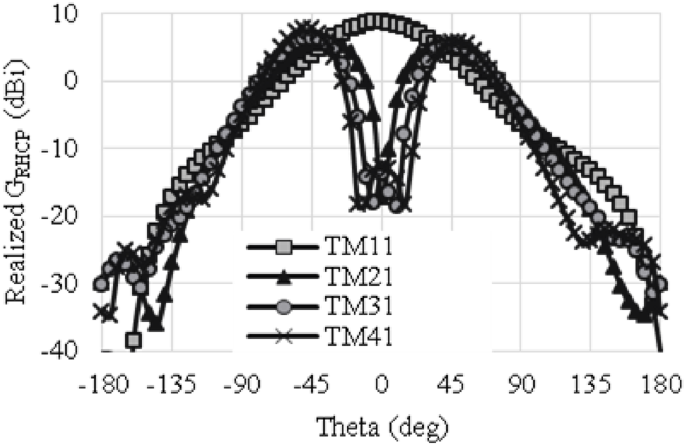

Figure 3.23: RHCP and LHCP realized gain elevation patterns for each mode at $\phi = 0°$ using a low loss dielectric.

are the sum of the incident and reflected waves within the cavity. A high loss tangent attenuates these waves as they travel away from the feed points toward the edges of the patch where some of the energy is radiated away and the remainder is reflected. This attenuation leads to a highly asymmetric current distribution as illustrated for the TM_{21} mode in Fig. 3.24a in contrast to the low loss tangent case in Fig. 3.24b. Effectively, the attenuation has introduced an additional equivalent linearly polarized (LP) current distribution as illustrated in Fig. 3.24b. Therefore, we can expect the AR to degrade at the

Table 3.5: Final design parameters used for each antenna in HFSS.

Parameter	TM_{11}	TM_{21}	TM_{31}	TM_{41}
ε_r	2.2	2.2	2.2	2.2
h	120mil	120 mil	120 mil	120 mil
a	N/A	38.3 mm	77.5 mm	117.0 mm
b	36.0 mm	75.3 mm	115.0 mm	155.2 mm
c	N/A	41.0 mm	81.8 mm	121.0 mm
d	10.5 mm	54.0 mm	94.0 mm	132.0 mm
ϕ_f	90°	45°	30°	22.5°
R	100.0 mm	100.0 mm	137.9 mm	200.0 mm

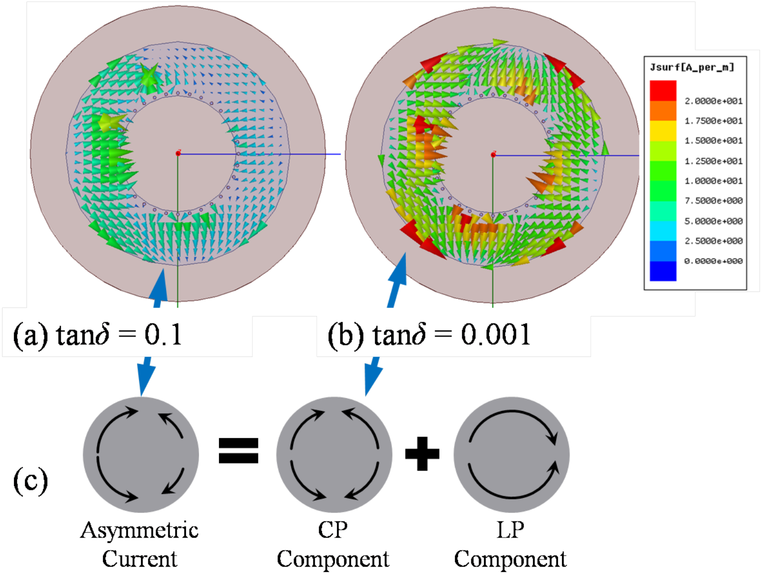

Figure 3.24: TM_{21} HFSS simulated current distributions for different loss tangent values corresponding to conceptual CP and LP components contributing to the asymmetric current.

azimuthal angle associated with the LP component. Several representative dielectric loss tangents ranging from 0.0009 to 0.1 were chosen to illustrate the how severely the AR is degraded. Fig. 3.25 plots the AR of TM_{21} mode over azimuth angle at the beam peak elevation angle of $\theta = 39°$. In the nearly lossless case, the AR remains less than 3 dB for all azimuth angles. As the loss tangent approaches values typical of low grade materials such as FR4, the AR increases to values ranging from 6 dB to 12 dB. As expected, the increase in axial ratio occurs primarily at one angle ($\phi \approx 135°$). Therefore, we can also expect additional AR degradation with increased mode number as shown in Fig. 3.26 due to increased physical size of the antenna.

We have demonstrated the effect of dielectric losses on the radiation patterns of 4 commonly used shorted annular patch antennas. Loss tangents typical of common low grade RF materials were shown to degrade the axial ratio significantly primarily at one azimuthal angle. This was explained by decomposing the asymmetric current distribution into effective LP and CP components. As expected, the effect becomes more pronounced

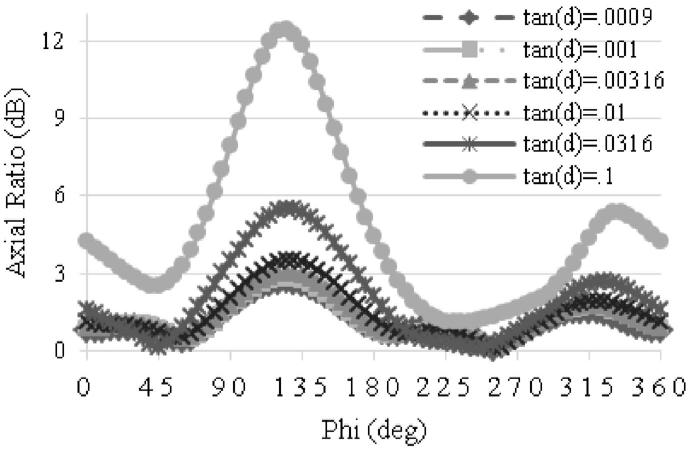

Figure 3.25: TM_{21} axial ratio versus azimuth at the beam peak elevation angle $\theta = 39^\circ$.

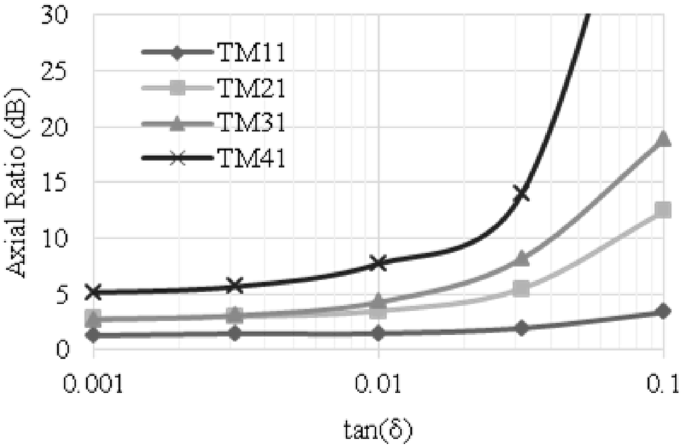

Figure 3.26: Maximum azimuthal axial ratio at the respective beam peak angle for each mode versus dielectric loss tangent.

with increasing mode number. Additional supporting data and material will be presented at the symposium.

3.7 Conclusions

We presented a novel pattern reconfigurable antenna designed for satellite receive applications in L-band. Using the beamforming capabilities of orthogonal radiating modes, we demonstrated full hemispherical steering of a single beam null and conical steering of a single beam peak. A circular patch antenna was chosen to excite the directional TM_{11} mode while TM_{21} was excited on a coplanar and concentric shorted annular ring patch. Fundamental field analysis was performed in order to show the amplitude and phase relationships between the 2 modes that are responsible for the beam steering properties. A passive multiple mode antenna aperture was fabricated and measured which showed acceptable agreement with simulated impedance and radiation performance. Finally, we demonstrated the practical beam steering properties of our antenna by integrating the antenna aperture with an active feed network composed of COTS (commercially off the shelf) components. Reasonable agreement was found between predicted and measurement beam peak and null positions. Most error was explained as a byproduct of the inherent measurement uncertainty and coarseness of the calibration process.

Some discussion was also devoted to the impact of material losses on axial ratio symmetry for circular patch antennas. The effect was shown to worsen with increasing mode number due to the increase of physical size and asymmetry of the current distribution. Several loss modes were characterized demonstrating that dielectric loss is the dominant contributor to axial ratio degradation. Therefore, the use of low loss materials is even more critical for multiple mode antennas.

This research is part of a larger effort to understand the potential benefits of antenna apertures supporting multiple simultaneous radiating modes. Research is underway to investigate the generation of multiple independently steerable nulls using more than 2 concentric patch antenna elements. The following chapter investigates the more general topic of beam steering using arrays composed of elements each supporting a unique radiating mode. Of interest is the comparison between this novel method and traditional phased array beam steering.

Acknowledgments

Chapter 3, in part, is a reprint of the material as it appears in IEEE Transactions on Antennas and Propagation, 2014. Labadie, Nathan R.; Sharma, Satish K.; Rebeiz, Gabriel, IEEE, 2014, and IEEE Antennas and Propagation Society International Symposium, 2014, Labadie, Nathan R.; Powell, Jack R.; Sharma, Satish K.; Rebeiz, Gabriel, IEEE, 2014. The dissertation/thesis author was the primary investigator and author of this paper.

The work was carried out in part under the National Science Foundation (NSF)s CAREER grant ECCS-0845822.

Chapter 4

A Novel Approach to 1D Beam Steering using Arrays Composed of Multiple Unique Radiating Modes

4.1 Introduction

Electronically scanned antenna arrays are commonly used both in radar and communications applications for their ability to form arbitrary beam patterns in real time with superior speed compared to their mechanically gimbaled counterparts. The direction of incoming or outgoing electromagnetic energy is determined by the complex weights applied to each antenna element, each of which is typically identical. The amount of energy transmitted or received in a particular direction is determined by the summation of the active element patterns in that direction. The active element pattern is the resulting radiation pattern for each element when excited in the presence of the other array elements which are terminated in matched loads [72]. These patterns and consequently the array pattern are influenced by two factors that can significantly reduce the realized gain of the array pattern as it scans away from the direction broadside to the array. First, element pattern gain decreases with angle away from the beam peak for typical unidirectional elements. Second, mutual interaction between array elements may cause additional loss in scanned array gain as power radiated from one element is absorbed by adjacent elements.

In a conventional phased array, maximum element spacing is typically limited to approximately half the free space wavelength in order to avoid grating lobes for the widest possible scan range. Therefore, one obvious approach to reduce mutual coupling and element pattern rolloff is miniaturize the element using dielectric loading, conductor meandering or other such technique that reduces the physical size of the radiating element. By reducing the physical size of the element, both the element directivity and interelement coupling can be reduced. The primary tradeoff here is a simultaneous reduction in element bandwidth.

Another useful method to realize wide scanning arrays uses wide angle impedance matching dielectric sheets [73, 74]. The dielectric sheet thickness and distance from the radiating elements are chosen to provide an efficient impedance transformation from free space to array aperture that is stable over a wide angle of incidence. This method is highly versatile and easy to implement. The technique does not specifically address the issue of element pattern gain rolloff with angle. Element pattern gain rolloff can be mitigated by making the array aperture conformal [75]. In the extreme, the aperture can be made cylindrical or hemispherical such that there is on average the same amount of array pattern gain in any particular direction. The primary tradeoff here is a reduction in the peak array pattern gain since there are only a subset of the total number of elements with peak gain in a particular direction.

Conventional phased array elements can also be augmented with parasitic elements, which are used to scan the element pattern [37, 38]. By tilting the element pattern beam in the direction of the array pattern beam, element pattern gain rolloff can be effectively eliminated over a wide range of angles. Additional control circuitry required to control the parasitic elements must be integrated into the aperture and represents a fundamental tradeoff when comparing to other design approaches.

In this chapter, we describe an alternative approach to beam steering using antenna elements each supporting a unique current mode and producing a unique radiation pattern. We refer to such an array as a multiple mode array. The null steering capabilities of a multiple mode array and potential enhancements to phased array performance have been previously investigated [76, 77, 71, 36]. The primary advantages in the multiple mode beam steering approach presented here are the reduction of unwanted mutual coupling and an increase in array scan range. This increase in array scan range is shown to be due both to the reduction in mutual coupling and to the increase in element pattern gain at wide scan angles for higher order dipole modes. Some preliminary results based on analytical and simulated data were presented in [78, 79]. With these benefits comes some design tradeoffs including increased physical size and potentially an increase in the number of unique elements needed to synthesize a desired beam pattern. These tradeoffs are explored by comparing analytical and full wave simulation data for the following array types: conventional phased arrays, multiple mode arrays and hybrid phased arrays composed of multiple mode sub-arrays. All simulation results were generated with Ansys HFSS and post-processed in MATLAB. Measured data for two dipole arrays based on the multiple mode array concept are presented in order to validate the simulation results. All measurements were performed at San Diego State's Antenna and Microwave Laboratory and Cubic Defense Applications Antenna Measurement Laboratory in San Diego.

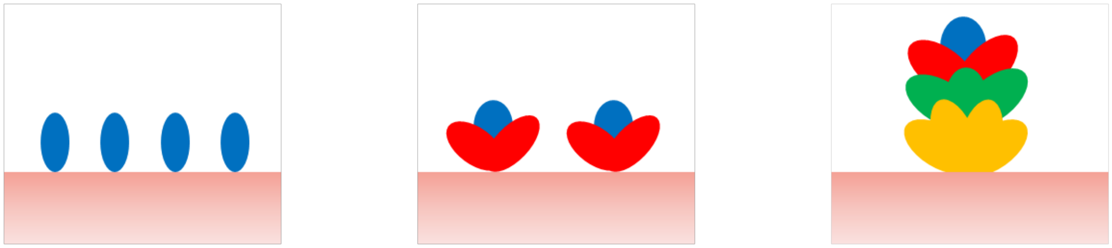

(a) Conventional (b) Hybrid (c) Multiple Mode

Figure 4.1: Illustration of array topologies as described in this chapter and in order of increasing number of unique radiating modes.

4.2 Multiple Mode Array

The three different array topologies explored in this chapter are illustrated in Fig. 4.1: conventional phased array, hybrid phased array and multiple mode array. In this section, we describe the theory, method of analysis and beam pattern synthesis properties of the multiple mode array. As shown in Fig. 4.1c, the multiple mode array is characterized by the use of multiple unique radiating modes in contrast to the conventional array, which uses elements supporting the same radiating mode. Additionally, the phase centers of the radiating elements in the multiple mode array may be collocated. This is in contrast to the conventional phased array that relies on the interelement spacing to produce an array factor that modulates the active element patterns.

4.2.1 Ideal Analysis

This chapter explores the simplest case of a linear array capable of beam steering in a single scan plane. The reference case of a linear array of half wavelength dipoles is shown in Fig. 4.2a. Fig. 4.2b and 4.2c illustrate the proposed array and its equivalent array in terms of half wavelength dipoles, respectively. Notice that the equivalent set of N dipoles corresponding to mode N have are themselves a linear array with a fixed progressive phase relationship of 180°. The convention for this chapter is to refer to

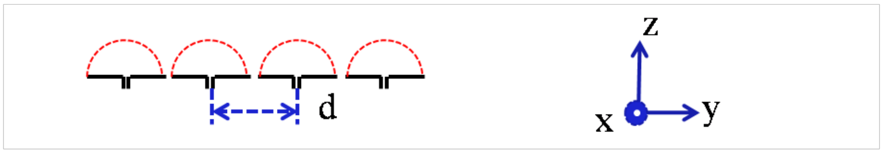

(a) Conventional $\lambda/2$ dipole array

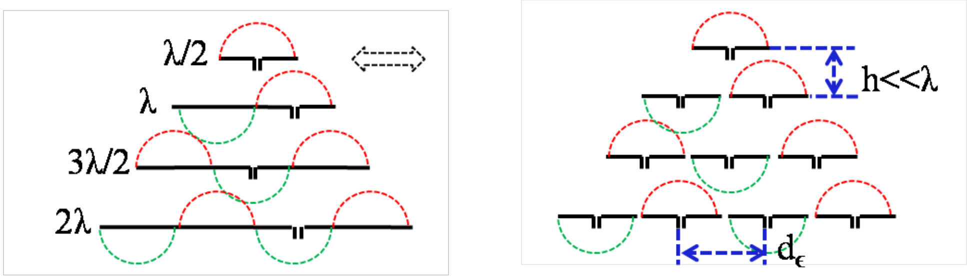

(b) Multiple mode dipole array

(c) Equivalent $\lambda/2$ dipole array

Figure 4.2: Ideal dipole array geometries.

those modes with even current distribution symmetry as ”even modes” and those with odd current distribution symmetry as ”odd modes”. The even or odd symmetry of each mode is also reflected in the phase radiation pattern. The far field radiation pattern of the multiple mode array can be described by

$$AP_M(\theta) = \sum_{m=1}^{M} A_m F_m(\theta) \exp(j(m-1)\psi_z). \tag{4.1}$$

where the radiation patterns of the individual modes are defined by

$$F_1(\theta) = F_D(\theta) \tag{4.2a}$$

$$F_2(\theta) = [\exp(j\frac{1}{2}\psi_{y0}) - \exp(-j\frac{1}{2}\psi_{y0})]F_D(\theta) \tag{4.2b}$$

$$F_3(\theta) = [\exp(j\psi_{y0}) - 1 + \exp(-j\psi_{y0})]F_D(\theta) \tag{4.2c}$$

$$\vdots \tag{4.2d}$$

$$F_m(\theta) = \sum_{k=1}^{m} (-1)^{k+1} \exp(j\frac{m-2k+1}{2}\psi_{y0})F_D(\theta). \tag{4.2e}$$

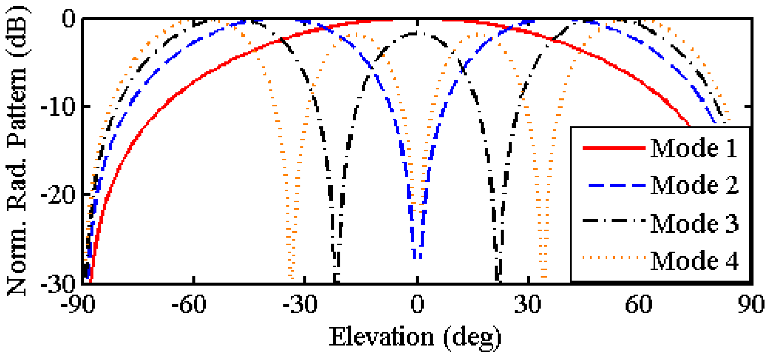

Figure 4.3: The first 4 unique radiating modes using the equivalent dipole array analysis.

where $\psi_{y0} = kd\sin(\theta)$, $\psi_z = kh\cos(\theta)$, M is the number of unique radiating modes, and A_m are the unknown complex weights. The dipole element patterns $F_D(\theta)$ are assumed to be of the same form as conventional center fed dipoles directed along the y-axis.

$$F_D(\theta) = \frac{\cos\left(\frac{kd_\varepsilon}{2}\sin\theta\right) - \cos\left(\frac{kd_\varepsilon}{2}\right)}{\cos\theta} \tag{4.3}$$

Plots of the first 4 radiation pattern modes are shown in Fig. 4.3. The parameter d_ε represents the length and spacing of the equivalent dipoles representing a particular mode. Clearly, the physical length and spacing will be reduced in the presence of dielectric loading. As shown for mode 4 in Fig. 4.4, the levels and locations of the radiation pattern lobes are dependent on this parameter. As the effective spacing, d_ε, is reduced, the outer lobes decrease in relative power and move further away from broadside. In the most extreme case of miniaturization, the odd mode radiation patterns will degenerate to those of simple dipoles. Similarly, the even mode radiation patterns will degenerate to unidirectional patterns.

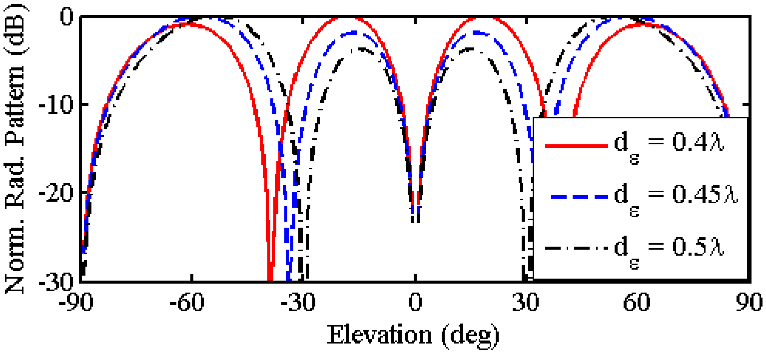

Figure 4.4: The effect of miniaturization (i.e. spacing between equivalent dipoles, d_ε) on the mode 4 radiation pattern.

4.2.2 Synthesis

The far field radiation pattern of the reference conventional linear dipole array can be approximately described by the following equations:

$$AP_D(\theta) = \frac{1}{N}\frac{\sin(\frac{N}{2}\psi_y)}{\sin(\frac{1}{2}\psi_y)}F_D(\theta). \tag{4.4}$$

where $\psi_y = kd\sin(\theta) + \beta_y$, N is the number of array elements, k is the propagation constant and d is the interelement spacing. We use a Fourier synthesis method similar to those described in [80, 59] in order make a direct comparison between the beam steering capability of the multiple mode dipole array and the reference case. This technique allows us to generate the optimal set of complex coefficients needed to most accurately generate the reference radiation pattern. First, the reference radiation pattern is expressed in terms of its Fourier coefficients.

$$AP_D(\theta) = \frac{1}{2}\widetilde{a}_0 + \sum_{n=1}^{N}[\widetilde{a}_n\cos(n\theta) + \widetilde{b}_n\sin(n\theta)]. \tag{4.5}$$

Second, each of the multiple mode array element patterns is also expressed in terms of its respective Fourier coefficients:

$$F_m(\theta)\exp(j(m-1)\psi_z) = \frac{1}{2}a_{m0} + \sum_{n=1}^{N}[a_{mn}\cos(n\theta) + b_{mn}\sin(n\theta)]. \tag{4.6}$$

Inserting equation 4.6 into 4.1 yields a Fourier series expansion of the multiple mode array pattern

$$AP_M(\theta) = \sum_{n=1}^{N}[(\sum_{m=1}^{M}A_m a_{mn})\cos(n\theta) + (\sum_{m=1}^{M}A_m b_{mn})\sin(n\theta)] + \frac{1}{2}\sum_{m=1}^{M}A_m a_{m0}. \tag{4.7}$$

Equating equations 4.7 with 4.5 and reordering the summations yields an over determined matrix equation in terms of the unknown complex weights $\begin{bmatrix} A \end{bmatrix}$.

$$\begin{bmatrix} A_1 \\ \vdots \\ A_M \end{bmatrix} = pinv \begin{bmatrix} a_{10} & \cdots & a_{M0} \\ \vdots & \ddots & \vdots \\ a_{1N} & \cdots & a_{MN} \\ b_{11} & \cdots & b_{M1} \\ \vdots & \ddots & \vdots \\ b_{1N} & \cdots & b_{MN} \end{bmatrix} \begin{bmatrix} \widetilde{a_0} \\ \vdots \\ \widetilde{a_N} \\ \widetilde{b_1} \\ \vdots \\ \widetilde{b_N} \end{bmatrix} \tag{4.8}$$

The optimal complex weights are recovered with singular value decomposition. Fig. 4.5 plots the scanned radiation patterns of a 7 element array reference radiation pattern and multiple mode arrays of varying numbers of modes. Although reasonable agreement is obtained within the main beam using 7 unique modes, there is considerable error in the far out sidelobes. Significantly better agreement over most elevation angles is obtained between the reference case and the multiple mode array when 8 unique modes are used. Fig. 4.6 presents the root mean square error (RMSE) of the multiple mode array synthesis

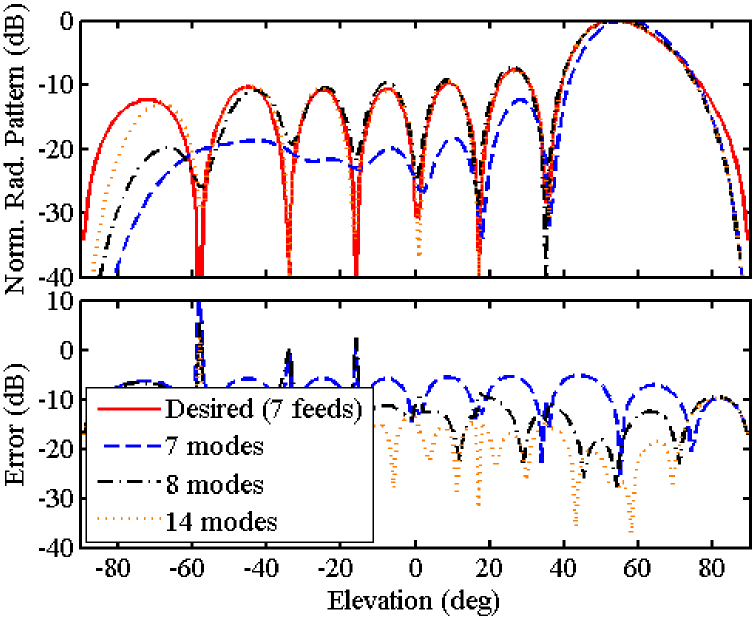

Figure 4.5: Investigation of the number of modes used in the multiple mode dipole array to sythesize a conventional array pattern with 7 elements.

of the 7-element conventional array radiation pattern as a function of the number of unique modes used and varying scan angles.

$$\varepsilon_{rms} = \sqrt{\frac{\sum_{i=1}^{N_\theta}(|AP_D(\theta_i)|^2 - |AP_M(\theta_i)|^2)^2}{N_\theta}} \qquad (4.9)$$

Based on this analysis, we conclude that N+1 unique modes are needed to sufficiently approximate the N element conventional reference array.

One assumption made in the analysis of the multiple mode array is that the distance in z between antenna elements $h << \lambda$. In principle, $h = 0$ if all modes are excited on the same aperture. In practice, it may be easier to excite these modes on individual radiators as shown previously in Fig. 4.2b. The spacing between dipoles in the z-axis introduces an undesired array factor that effects the synthesis capability of the multiple mode array. Three cases of dipole spacing shown in Fig. 4.4 illustrate the increasing synthesis error with increasing dipole spacing. Clearly, this spacing should be

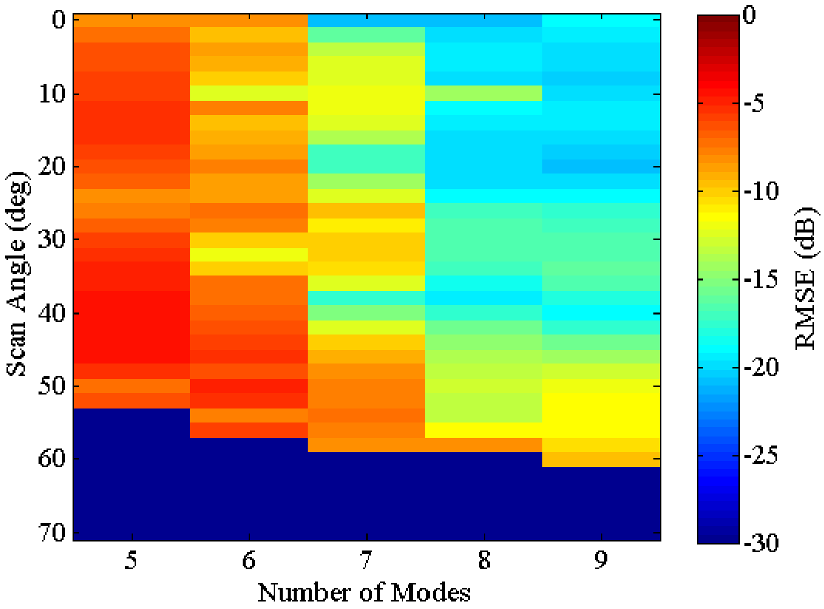

Figure 4.6: Plot of the root mean square error (RMSE) as a function of number of unique modes and array scan angle.

minimized in a practical design.

4.3 Hybrid Phased Array

In general, a hybrid phased array may be composed of N multiple mode subarrays each containing M number of unique modes such that $M \times N = C$, where C is an integer constant representing the total number of feed points. The 3 array topologies described in Fig. 4.1 are illustrated for linear dipole arrays each with a total of 8 feed points in Fig. 4.8. It is clear from Fig. 4.8 that the area occupied by the multiple mode array is the largest of the 3 topologies. As described in the previous section, each dipole in the multiple mode array is equivalent to a fixed phased M element array of half wavelength dipoles. If we define the array area as the area of the rectangle containing the entire array, then the area is proportional to number of modes. For large numbers of modes, the complexity of the feed network also increases as many feed points are

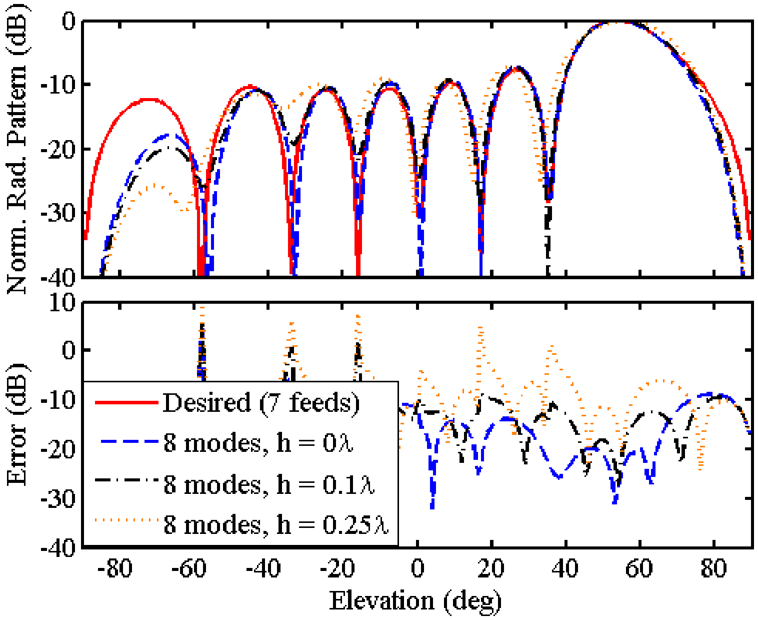

Figure 4.7: Effect on synthesis accuracy of the z-axis spacing, *h*, between the dipoles in the multiple mode dipole array.

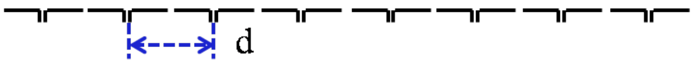

(a) Conventional 8 element λ/2 array.

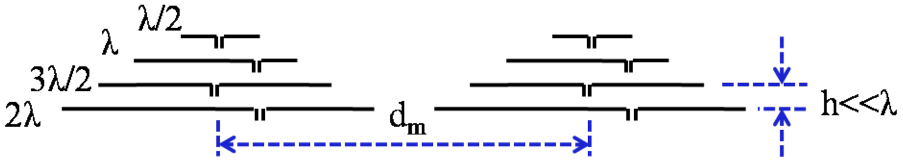

(b) Hybrid phased array composed of 2 multiple mode dipole sub-arrays.

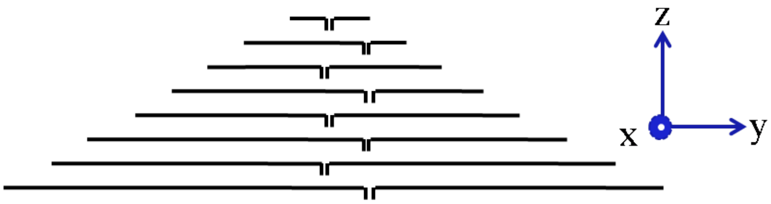

(c) An 8-element multiple mode dipole array.

Figure 4.8: 8 element linear dipole phased array topologies.

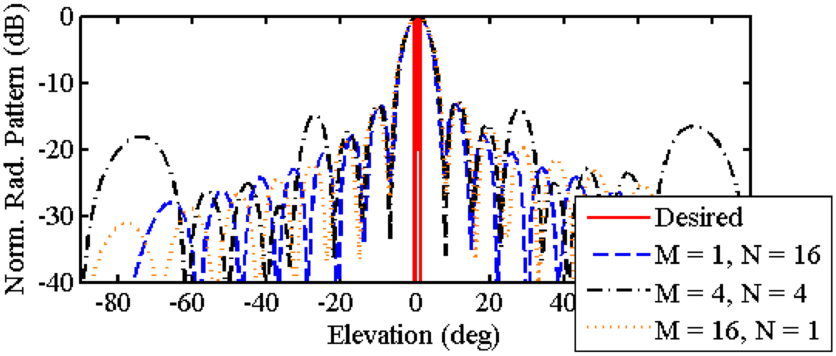

Figure 4.9: Synthesized radiation patterns for conventional ($M = 1$, $N = 16$), hybrid ($M = 4$, $N = 4$) and multiple mode ($M = 16$, $N = 1$) arrays where $C = 16$.

in the middle of the aperture and more susceptible to unwanted coupling. Therefore, there is sufficient reason to choose the minimum number of modes needed to realize the improved performance of the multiple mode sub-array.

4.3.1 Ideal Analysis and Synthesis

The analytical radiation pattern of the hybrid phased array is obtained by multiplying the multiple mode radiation pattern of equation 4.1 by the array factor of equation 4.4.

$$AP_H(\theta) = \frac{1}{N}\frac{\sin(\frac{N}{2}\psi_y)}{\sin(\frac{1}{2}\psi_y)}\sum_{m=1}^{M} A_m F_m(\theta)\exp(j(m-1)\psi_z). \tag{4.10}$$

We have assumed a constant number of feed points, $C = 16$, and number of unique modes, $M = 1, 2, 4, 8, 16$. In order to maximize directivity over scan angle, the desired radiation pattern is a simple pulse function with a beamwidth of 1° and sidelobe levels (SLL) of -100 dB. The boresight radiation patterns for the three arrays in Fig. 4.8 are plotted in Fig. 4.9. The hybrid array radiation pattern contains several anomalous lobes at $\theta = \pm 27°$ and $\theta = \pm 74°$. These are the result of the gaps between the sub-arrays, d_m. Fig. 4.10 illustrates the dependency of these lobe levels on the spacing between sub-arrays, d_m. This spacing should be minimized in a practical design to the extent that the highest order

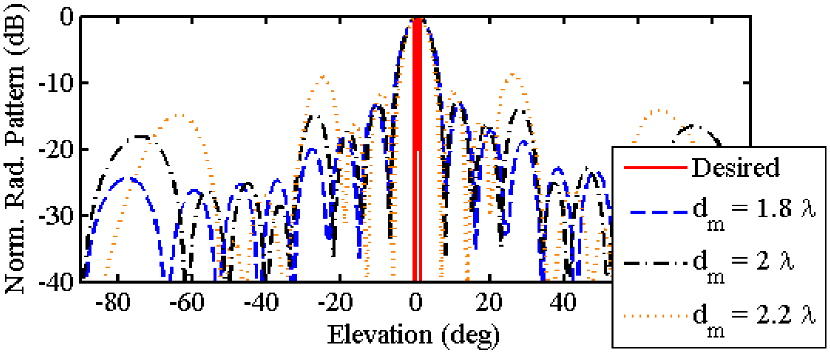

Figure 4.10: Dependency of the anomalous grating lobe levels on spacing between sub-arrays, d_m.

mode dipoles do not overlap or suffer degraded performance due to excessive mutual coupling.

Array pattern directivity is a relevant figure of merit with which to compare the different array topologies. Fig. 4.11 plots the directivity of each array as computed from the 3D analytical radiation patterns. The widest scanning array is the multiple mode array. The 4×4 hybrid phased array appears to have a slightly better directivity and scan range than the conventional array. However, the analysis up to this point has assumed no mutual coupling effects. In the following section, we will perform full wave analysis of the 1×16, 4×4 and 16×1 arrays in Ansys HFSS. We will show that the 4×4 hybrid phased array represents a reasonable tradeoff between the performance and implementation issues associated with the conventional and multiple mode arrays, respectively.

4.3.2 Full Wave Analysis

Full wave simulations of the three dipole arrays shown in Fig. 4.12 were performed in Ansys HFSS with design parameters listed in Table 4.1. Since the basic radiating elements are simple dipoles, cross-polarization within the scan plane containing the dipoles is expected to be very low. For the sake of brevity, we do not consider the

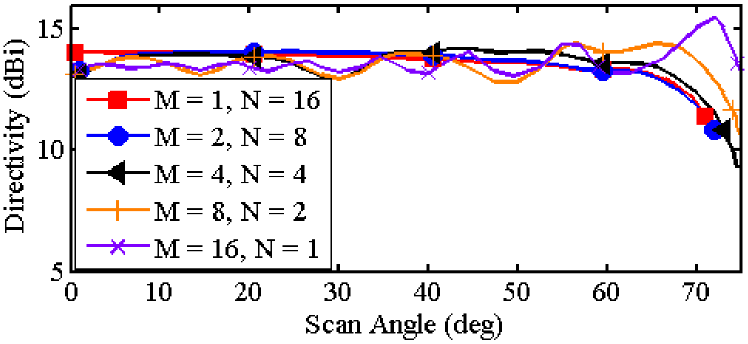

Figure 4.11: Comparison of array directivity versus scan angle for different numbers of unique radiating modes and a constant number of feed points.

Table 4.1: Final design parameters used for each array in HFSS.

Parameter	Conventional	Hybrid	Multiple Mode
M	1	4	16
C	16	16	16
L	0.435λ	N/A	N/A
h_f	0.25λ	0.25λ	0.1λ
A	$4.3\lambda^2$	$8.3\lambda^2$	$14.6\lambda^2$
d	$0.5\lambda^2$	N/A	N/A
d_m	N/A	0.5λ	N/A

polarization behavior out of the scan plane. The dipole lengths both for the hybrid and multiple mode arrays were optimized to yield both sufficient impedance match to 50 Ω ($|S_{11}| < -10$ dB) and proper radiation pattern mode, which is why L is listed as N/A for these arrays in Table 4.1. The dipole width used for all arrays is 0.06λ and the reflector widths used are 0.225λ, 0.225λ and 0.06λ for the conventional, hybrid and multiple mode arrays, respectively. The simulated complex radiation patterns for each array were used to synthesize a desired beam pattern with 3 parameters, scan angle (θ_{scan}), beamwidth (BW$= 1°$) and sidelobe level (SLL$= -100$ dB). Three scanned radiation patterns for each array type are presented in Fig. 4.13. All three arrays display similar behavior near the main lobe. The hybrid array shows the same anomalous lobes discussed in the previous analysis section and may suppressed by optimizing the sub-array spacing.

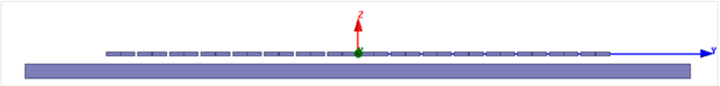

(a) Conventional $\lambda/2$ array.

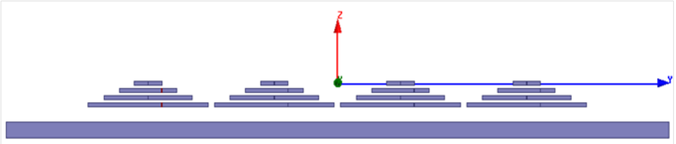

(b) Hybrid phased array composed of 4 multiple mode dipole sub-arrays.

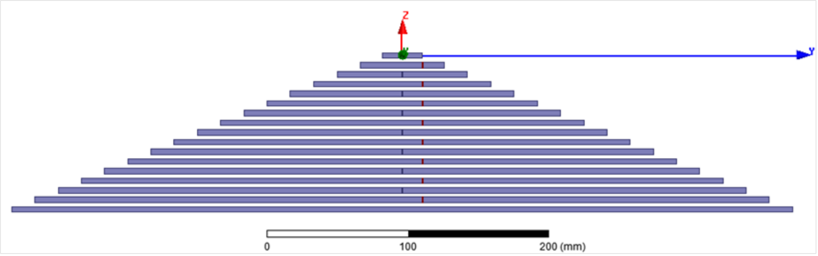

(c) Multiple mode array.

Figure 4.12: HFSS models of 16 element linear dipole phased arrays.

In our previous ideal array analysis which ignored mutual coupling, only the multiple mode array was shown to have significantly greater scanned directivity compared to the conventional array. Fig. 4.14 plots the peak scanned realized gain and total antenna efficiency over scan angle. This comparison makes the advantage of the hybrid phased array apparent. Similar to the multiple mode array, the hybrid phased array maintains nearly constant realized gain and total efficiency over a wide range of scan angles.

4.4 4 Element Multiple Mode Sub-Array

A 4-element multiple mode sub-array was designed to operate at 4.6 GHz in order to validate the previous analysis and simulation results presented in section 4.2. This same sub-array was later integrated into a 16-element hybrid phased array and will be discussed in section 4.5.

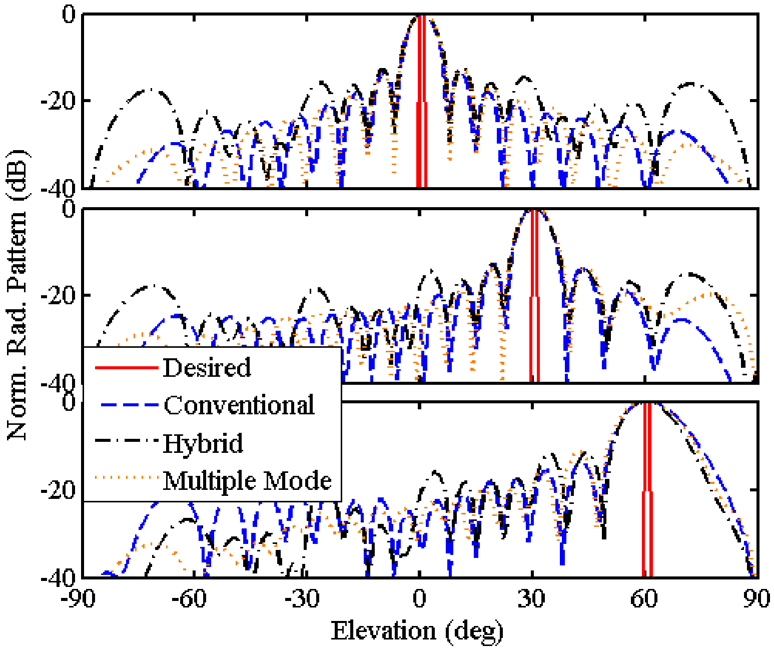

Figure 4.13: Three scanned array patterns for each of the array types as computed from HFSS simulated element pattern data.

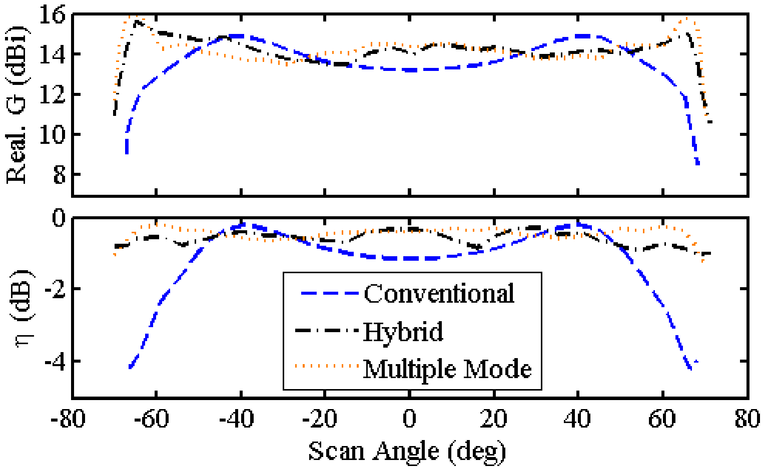

Figure 4.14: Comparison of scanned peak realized gain and total antenna efficiency for the three HFSS simulated arrays over their entire scan range.

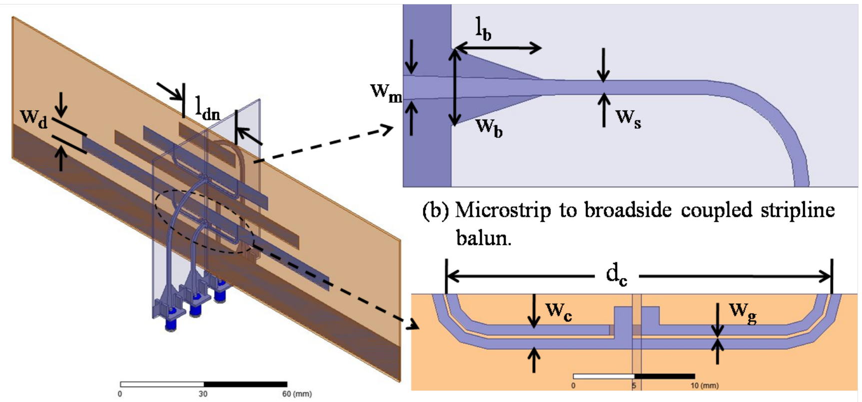

(b) Microstrip to broadside coupled stripline balun.

(a) 4-element multiple mode dipole array.

(c) Edge coupled stripline differential power combiner.

Figure 4.15: HFSS models for the 4 element multiple mode dipole array with feed network.

4.4.1 Element Feed Network

The most obvious issue with implementing the multiple mode array is finding a suitable feed network. Since elements are distributed along the z-axis, perpendicular to dipoles, the feed lines must cross over elements in order to feed the desired element. Therefore, we decided on an interlocking feed network solution as illustrated in Fig. 4.15a. In this arrangement, most of the feed network is contained in a substrate perpendicular to the dipole substrate. The feed lines transition from microstrip to differential broadside coupled stripline near the SMA connectors as shown in Fig. 4.15b. We expect little unwanted coupling between the feed lines and other dipoles due to the differential nature of the feed lines and their orientation with respect to the dipoles. Even mode dipoles are connected directly to their corresponding sets of broadside coupled striplines in the center of each dipole. Odd mode dipoles must be driven offset from the dipole center in order to present a reasonable output impedance to the feed network. Therefore, we designed a coplanar stripline power combiner at the outputs of the odd mode dipoles as shown in Fig. 4.15c. The lack of significant isolation between the both the antenna outputs and the combiner inputs is not an issue since the inputs are driven 180° out of phase. Additionally, using a symmetric feed arrangement for the odd mode dipoles provides

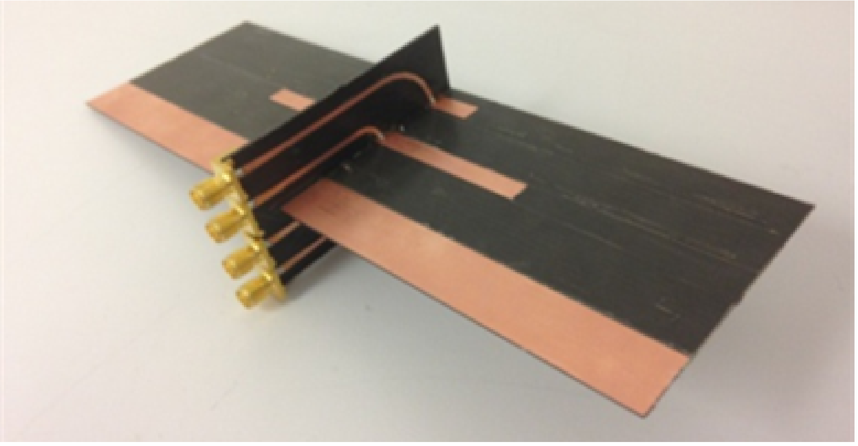

Figure 4.16: Fabricated 4 element multiple mode dipole array.

Table 4.2: 4 element multiple mode dipole array design parameters

(a) Balun

Parameter	Value (mm)
w_m	2.5
w_b	10.0
w_c	2.0
w_s	1.5
w_g	0.25
l_b	12.0
d_c	33.0

(b) Dipole array

Parameter	Value (mm)
w_d	6.0
l_{d1}	29.0
l_{d2}	64.0
l_{d3}	78.0
l_{d4}	127.0

greater rejection of even mode coupling from the adjacent elements.

4.4.2 Fabrication and Measurement

The 4 element multiple mode dipole array shown in Fig. 4.16 was fabricated with the design parameters shown in Table 4.2. Reasonable agreement was obtained between the simulated and measured scattering parameters presented in Fig. 4.17. The measured reflection coefficient for mode 2 shows the highest level of disagreement with the simulated data. We suspect that issues with the fabrication tolerances of the balun (i.e. the gap w_g) may have contributed to this disagreement. Because of this frequency

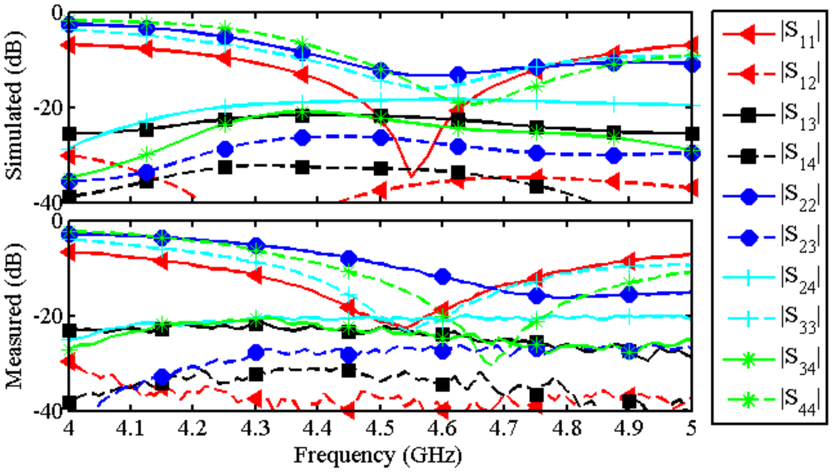

Figure 4.17: Full set of unique scattering parameters for the 4-element multiple mode array.

shift in the mode 2 reflection coefficient, we obtain a measured operational bandwidth of 6.4% as compared to the simulated 7.8%. The 3D realized gain patterns were measured for each of the four dipole elements. Fig. 4.18 shows reasonable agreement between the measured and simulated 2D cuts in the plane of the dipole array ($G_\theta(\phi = 90°)$).

In order to achieve the widest instantaneous bandwidth possible, it is important to implement phase and group delay matched RF paths from the antenna element apertures to the final combined output. When delay matching is not maintained, the phase relationships between elements may vary rapidly over frequency, distort the beam and therefore limit the useful bandwidth of the array. In a conventional receiving phased array, emphasis is typically placed on matching the phase and delay responses from the antenna output to the combined output. This is because the radiating elements are nearly identical in their phase and delay versus angle responses. This is certainly not true for a phased array employing multiple unique radiating modes. The differences in phase and delay versus angle responses between the unique radiating modes are critical to the novel approach to beam steering presented in this chapter. Group delay was computed for each element and averaged over the 3dB beamwidths of each lobe of the radiation

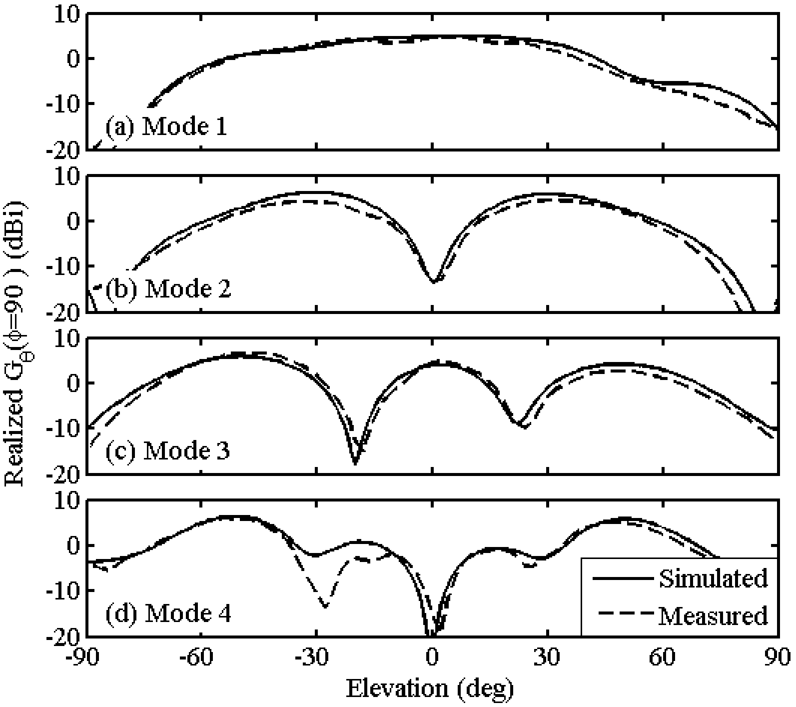

Figure 4.18: Active element radiation patterns for each element (mode) of the 4-element multiple mode array.

pattern and plotted in Fig. 4.19. The variation in group delay is approximately 0.3 ns over the frequency range from 4.2 to 4.6 GHz. In general, all four modes show roughly the same amount of delay. This is to be expected since the transmission line lengths in the interlocking feed network were designed to compensate for the different physical locations of each dipole in the sub array. Phase distortion was computed using a linear regression fit of the unwrapped phase for each mode as shown in Fig. 4.19. The total variation in phase is approximately 12° across all four modes over the frequency range from 4.2 to 4.8 GHz. Reasonable beam pattern quality for a 16 element array can be expected for phase deviations less than ±10°.

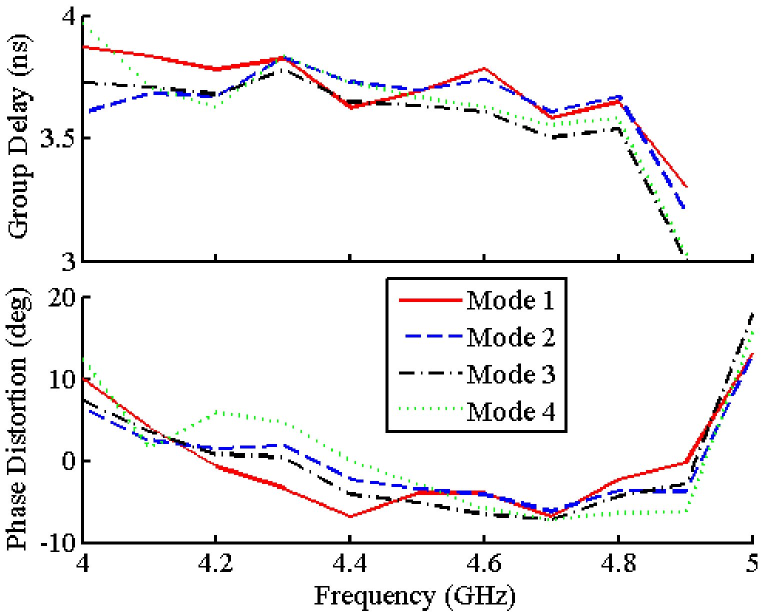

Figure 4.19: Plots of group delay and phase distortion versus frequency for all 4 modes of the sub-array.

4.5 16-Element Hybrid Phased Array

In the previous section, we presented measured data on the 4 element multiple mode array in order to validate the passive impedance and radiation properties of the novel array as simulated in HFSS. In this section, we use the same 4 element design as a sub-array in the 16 element hybrid phased array. The measured data presented here is intended to validate the prior analysis of the multiple mode and hybrid arrays, the Fourier synthesis method used and the array design as simulated in HFSS.

A functional block diagram of the novel 16 element array and the test setup used to characterize the array is shown in Fig. 4.20. The hybrid phased array includes programmable phase and amplitude shifting components that are controlled from a remote computer. A microcontroller (MCU) is used to translate messages from the laptop's USB (universal serial bus) interface to the UART interface (universal asynchronous receiver/transmitter). Messages from the UART interface are routed to the correct device

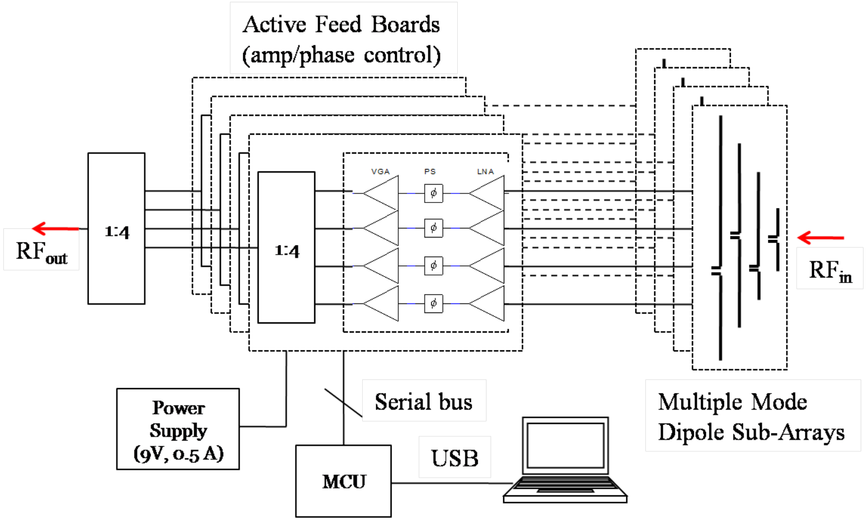

Figure 4.20: Functional block diagram of the 16-element hybrid phased array.

on the correct board using the serial bus. Each of the passive 4-element dipole arrays is connected to an active feed board. Each active feed board has a unique hardware defined address and contains four low noise amplifiers (LNA), four digital step phase shifters (DPS), four digital step attenuators (DAT) and other supporting circuitry. The combined RF output of each active feed board is connected to a final Wilkinson power combiner where it can be routed to the VNA receiver for measurement.

4.5.1 Passive Array Characterization

Each of the four multiple mode sub-arrays were fabricated and mounted in a custom test FR4 fixture. Reflection coefficient measurements were made in order to verify that the sub-array impedance parameters were nominal. Fig. 4.21 compares the measured reflection coefficients for each mode. The labeling convention used is $S_{m:n,p:q}$ where the subscripts m and p represent the sub-array number and n and q are the mode number. Effects of the adjacent sub-arrays are evident in the symmetric pairs of reflection coefficients for each mode. For example, the two inner sub-arrays show improved matching levels for mode 1 as compared to the two outer sub-arrays. The

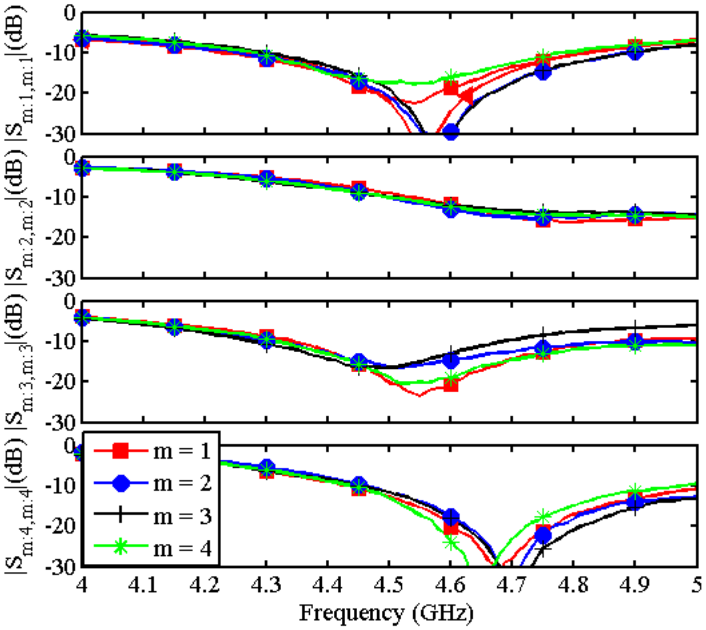

Figure 4.21: Measured passive output reflection coefficients for each hybrid phased array element grouped by mode.

mutual coupling parameters for the dipole elements on the same sub-array were presented in Fig. 4.17. A representative sample of coupling between elements on adjacent sub-arrays 2 and 3 is presented in Fig. 4.22. As expected, the highest level of coupling is between the mode 4 dipoles due to their closest proximity to one another. The measured coupling level for many modes is significantly lower than the simulated value. In contrast to the fabricated array, the simulated array model assumed a continuous substrate between sub-arrays. The air gaps between sub-arrays in the prototype may lower the contribution of surface waves to the coupling level. Additionally, the scattering parameters were measured outside of the chamber. It is possible that scattering from nearby objects presented an additional coupling path that influenced the measurements particular where the isolation is already more than 30 dB.

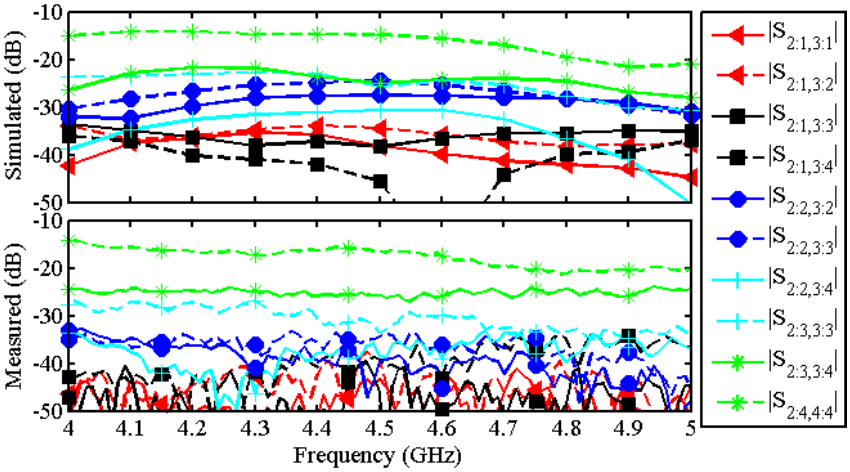

Figure 4.22: Scattering parameters for the coupling between elements of sub-arrays 2 and 3.

4.5.2 Active Feed Network

As described in the introduction to this section, each of the four multiple mode sub-arrays is connected to an active feed board used to make amplitude and phase adjustments of the RF signal before being combined. A fully assembled active feed board is shown in Fig. 4.23. These boards were designed by the author in Altium Designer, fabricated by Advanced Circuits and assembled by hand. Each board connects to each multiple mode sub-array via four end launch SMA inputs each of which is routed to a mode adjustment block on the board. The mode adjustment block is composed of an LNA with a gain of approximately 15 dB, a 360° digital step phase shifter (DPS) in 5.6° steps and a 31.5 dB digital step attenuator in 0.5 dB steps. A Wilkinson power combiner is used the combine the four outputs of the mode adjustment blocks. Power regulation, logic and control circuitry are included with each board. There is a single 20-pin connector used on each board to provide master 9V power and control of the RF devices on the serial bus. All 32 programmable RF devices are individually addressable using 5 control lines on the serial bus. A custom graphical user interface (GUI) as shown in Fig. 4.24 was developed using the C# programming language to provide a convenient way to communicate the desired complex weighting coefficients to the active feed boards.

4.5.3 Array Calibration

The active feed boards and supporting circuitry were integrated into the test setup as shown mounted in Cubic's anechoic chamber in Fig. 4.25. Additional absorber (not shown) was placed over the active feed boards on the lower sides of the array to reduce the effects of unwanted scattering of the array backlobe. The calibration process consists of the following four steps: (1) Measure each of 16 active element radiation patterns. (2) Compute the required complex weighting coefficients needed to synthesize a desired beam pattern. (3) Apply the computed complex weights and characterize the resulting array patterns. (4) Recover the array pattern gain by de-embedding the active feed network gain and associated mis-match losses. Steps (1) and (3) are basic antenna measurements and considered familiar to the reader. Steps (2) and (4) will be explained in detail.

Generate Complex Weights

Each active element pattern was measured by setting the element under test amplitude shift to 0 dB and phase shift to 0 deg. All other elements were set to the maximum attenuation of 31.5 dB and a 0° phase shift. We relied on the previously described Fourier synthesis method to generate the required complex weighting coefficients from the measured active element patterns. The computed calibration coefficients for two different scan angles are plotted in Fig. 4.26 along with the coefficients as measured on the active feed board. Most of the differences between the computed complex weights and those measured on the board occur where the attenuation is high. The isolation between the four channels on each board is not infinite, and we can expect some deviation

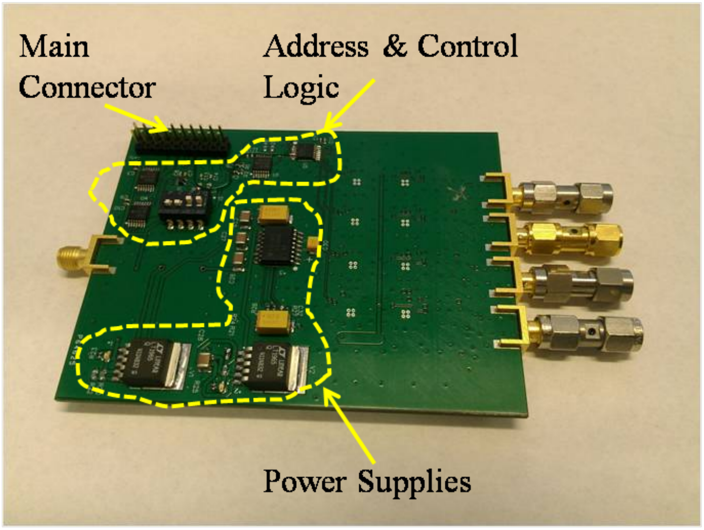

(a) Bottom view.

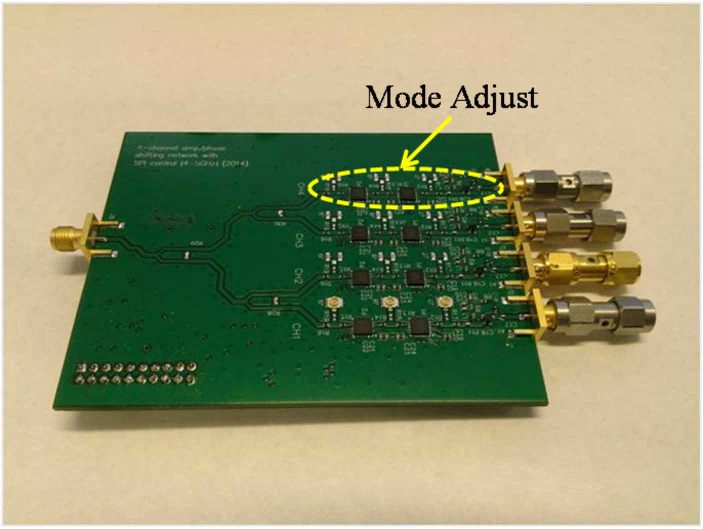

(b) Top view.

Figure 4.23: One of four fully assembled active feed network boards used to combine the outputs from each multiple mode sub-array.

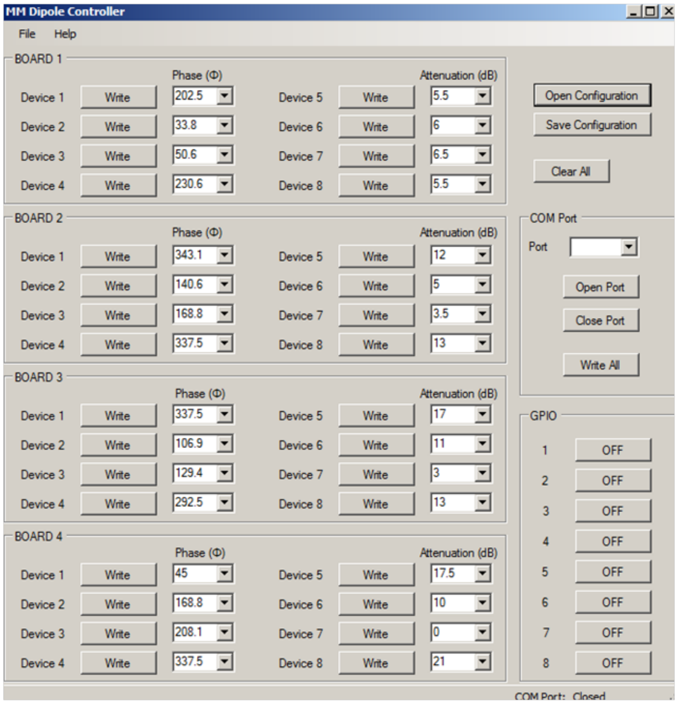

BOARD 1

	Phase (Φ)		Attenuation (dB)
Device 1	202.5	Device 5	5.5
Device 2	33.8	Device 6	6
Device 3	50.6	Device 7	6.5
Device 4	230.6	Device 8	5.5

BOARD 2

	Phase (Φ)		Attenuation (dB)
Device 1	343.1	Device 5	12
Device 2	140.6	Device 6	5
Device 3	168.8	Device 7	3.5
Device 4	337.5	Device 8	13

BOARD 3

	Phase (Φ)		Attenuation (dB)
Device 1	337.5	Device 5	17
Device 2	106.9	Device 6	11
Device 3	129.4	Device 7	3
Device 4	292.5	Device 8	13

BOARD 4

	Phase (Φ)		Attenuation (dB)
Device 1	45	Device 5	17.5
Device 2	168.8	Device 6	10
Device 3	208.1	Device 7	0
Device 4	337.5	Device 8	21

COM Port

Port:

GPIO

1	OFF
2	OFF
3	OFF
4	OFF
5	OFF
6	OFF
7	OFF
8	OFF

COM Port: Closed

Figure 4.24: Custom graphical user interface (GUI) used to control four active feed network boards each containing 8 programmable elements.

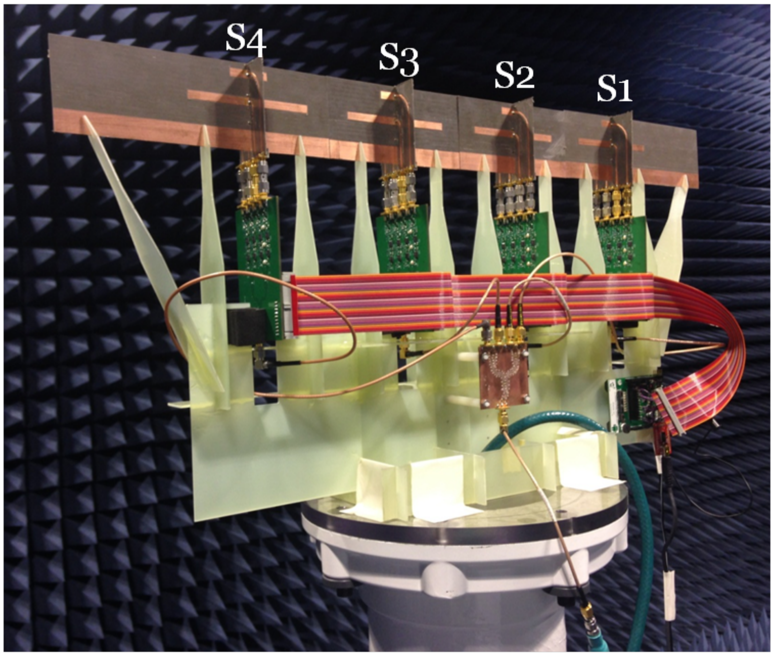

Figure 4.25: Fully assembled 16-element hybrid phased array as mounted in the anechoic chamber.

in phase as a result of leakage signals. In general, deviations in amplitude and phase may occur for the following reasons. The DPS is intended to apply a known shift in the phase of the incident signal. However, it is a non-ideal component and may also change the amplitude of the incident signal by as much as 1 dB depending on the impedance matching conditions. Similarly, the DAT may apply an unwanted phase shift to signal from one attenuation setting to another.

As in the analysis section 4.3, the desired beam pattern is essentially an impulse function over angle. When the desired pattern is located at $\theta_{scan} = 0^\circ$, the odd mode elements are heavily attenuated such that the array pattern is formed primarily from the received power from the even mode elements. This is not surprising since the array pattern at $\theta_{scan} = 0^\circ$ is also an even mode pattern. At the other extreme, where the array pattern is scanned to $\theta_{scan} = 70^\circ$, all but the highest order odd mode elements are heavily attenuated. This is also reasonable since the array pattern has a large odd component at such a large scan angle.

Array Pattern Gain

The purpose of this chapter is prove out the concept of using multiple unique radiating modes to form array pattern beams. Use of an active feed network was necessary to collect measured data demonstrating real-time beam steering in the RF domain. However, we would really like to disentangle the effects of the feed network from the measurements and recover the array pattern gain, $G_\theta(\phi = 90^\circ)$. The array pattern gain can be computed by normalizing the measured gain of the full array, $G_\theta^M(\phi = 90^\circ)$, to the active feed network channel gains, S_{21}^n. The active feed network channel scattering parameters were measured in a system with 50 Ω source and load impedances. In the fully assembled array, the inputs to the active feed network are loaded by the dipole impedances. Therefore, the actual array pattern gain will depend on the output reflection

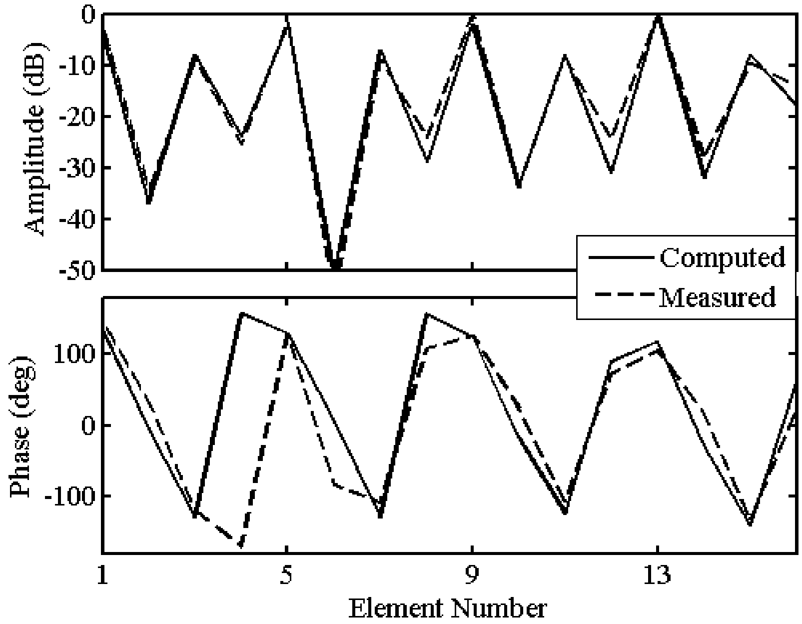

(a) $\theta_{scan} = 0°$

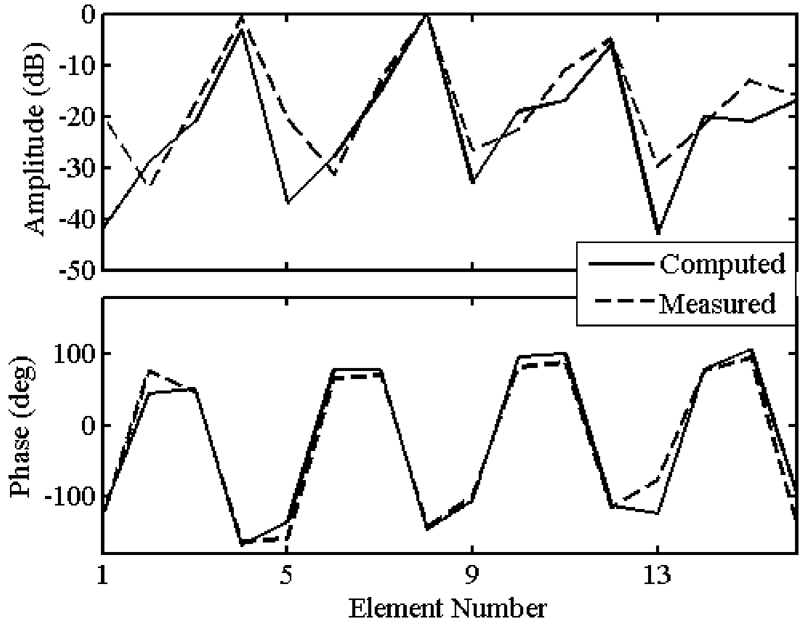

(b) $\theta_{scan} = 70°$

Figure 4.26: Computed and measured amplitude and phase coefficients used to scan the 16-element hybrid phased array beam.

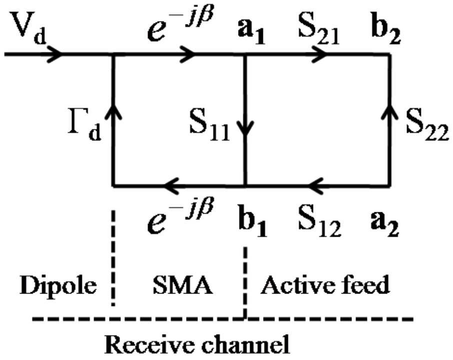

Figure 4.27: Signal flow graph model of a single receive channel

coefficient of the dipole, Γ_d, and the input reflection coefficient of the active feed network, S^n_{11}. The dipole and feed network are also connected by a male to male SMA adapter. We treat this adapter as a perfectly matched 50 Ω transmission line with a phase shift of $\exp(-j\beta)$. Fig. 4.27 illustrates the signal flow graph for a simplified model of a single receive channel on the array. Using this model, we derive the array pattern gain as shown in equation 4.11.

$$G_\theta = \frac{G^M_\theta}{\sum_{n=1}^{N} |S^n_{21}|^2(1-|S^n_{11}|^2)/|1-\Gamma^n_d S^n_{11}\exp(-j2\beta)|^2}. \tag{4.11}$$

4.5.4 Scanned Array Performance

In this section, we investigate and quantify the scanned performance of the fabricated 16 element hybrid phased array. Fig. 4.28 compares the desired, computed and measured normalized radiation patterns as viewed in the scan plane of the array ($\phi = 90°$). The computed radiation patterns have been derived in two ways: (1) computed based on simulated element radiation patterns and (2) computed based on measured element radiation patterns. Within the main beamwidth, good agreement is obtained between the computed and measured radiation patterns, and all three patterns point in nearly the same direction as the baseline impulse pattern. The highest level of agreement

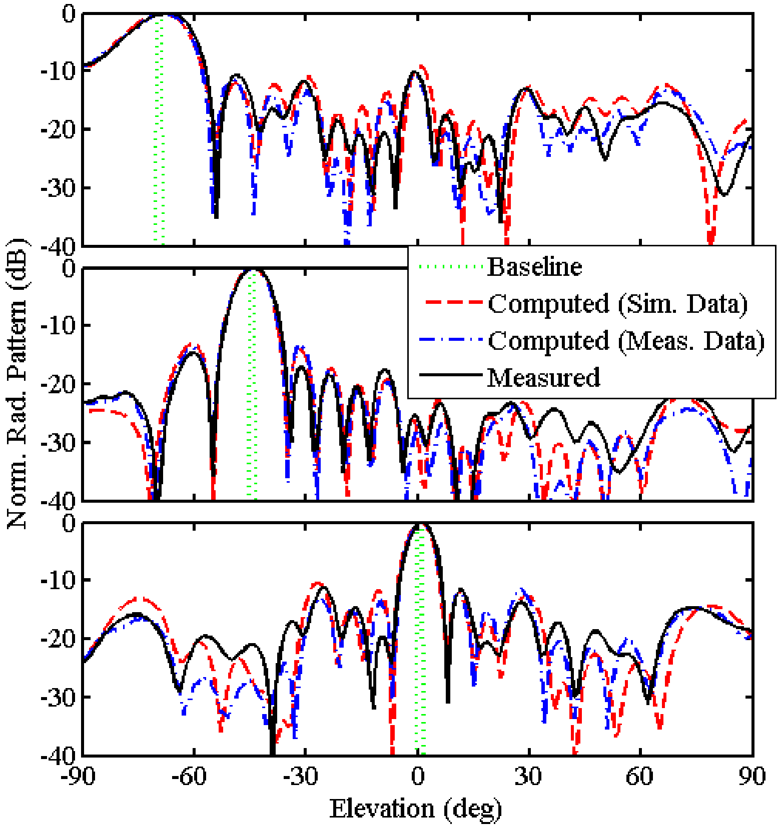

Figure 4.28: Comparative plot of the computed and measured normalized radiation patterns. The computed pattern based on measured active element patterns and the measured array pattern used the amplitude and phase coefficients shown in Fig. 4.26.

occurs between the two computed patterns. This is not surprising since for a 16-element array, the variations in element pattern are typically relatively slower than that of the array pattern. Therefore, even though the simulated and measured element patterns may differ, the differences are masked by the faster variations of the array factor. There is however considerable difference in sidelobe performance between the computed array pattern based on measured element data with respect to the other two array patterns. This disagreement can be attributed to the error in the actual amplitude and phase weights on the active feed boards as described in the previous section. Measured 3D radiation patterns are plotted in Fig. 4.29 for four scan angles ($\theta_{scan} = 0°, -30°, -60°$ and $-70°$). As explained in the analysis section 4.3, the radiation pattern for the hybrid phased array may exhibit anomalous lobes that are actually grating lobes due to the spacing between sub-arrays. In the 3D plots, these lobes can be clearly seen wrapping around the axes of the dipole elements. More closely packed sub-arrays would alleviate this problem.

In section 4.3, analytical and simulated data demonstrated that the hybrid phased array is capable of wide angle scanning with high efficiency. This is primary benefit to this novel approach to beam steering. Using the array pattern gain recovery method described in section 4.5.3, the array pattern gain, $G_\theta(\phi = 90^\circ)$, is plotted versus scan angle, θ_{scan}, in Fig. 4.30. There is considerable agreement between the measured and simulated array pattern gain. The measured total antenna efficiency, η, shows up to approximately 1.5 dB disagreement compared to the simulated data. Also, the measured η is greater than 0 dB for some scan angles. The error in the realized gain measurements is estimated to be approximately ± 0.5 dB as per the NSI performance specification for Cubic's spherical near field antenna measurement system. Also, the measured directivity, $D_\theta(\phi = 90^\circ)$, is higher than the simulated data by a consistent amount of approximately 1 dB. This is likely due to the fact that microwave absorber was used on the test fixture to reduce scattering of the backlobe. By absorbing the backlobe, the measured directivity is artificially high. Therefore, both the measurement error and artificially high directivity are the likely sources of error in the measured total antenna efficiency. Table 4.3 summarizes the scan range performance of the array over the frequency range from 4.0 GHz to 5.0 GHz. As expected, the widest scan range occurs near the calibration frequency, 4.6 GHz, for both the simulated and measured arrays. On either side of design frequency, the 3 dB scan range narrows significantly as the phase relationships between elements deviate further from their calibrated values. This phase deviation worsens with increasing scan angle and will be described later.

Realized gain, directivity and total antenna efficiency are plotted over frequency for the $\theta_{scan} = 0^\circ$ case in Fig. 4.31. The measured gain and efficiency appear to

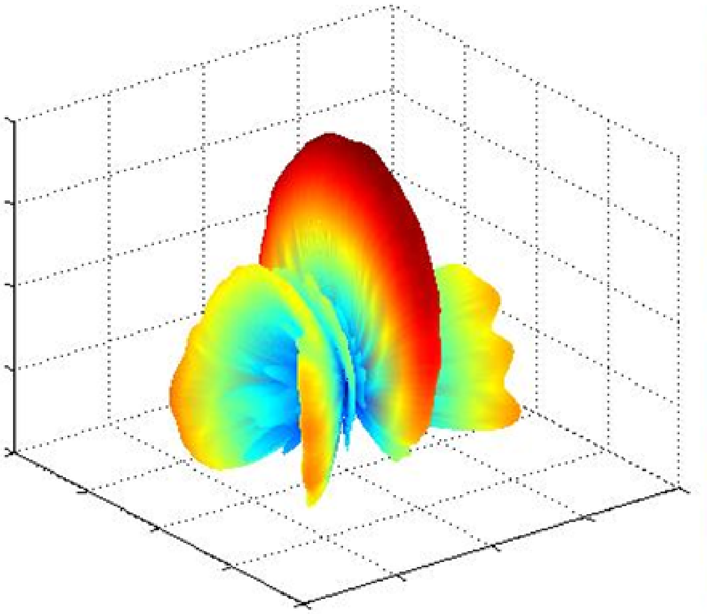

(a) $\theta_{scan} = 0°$

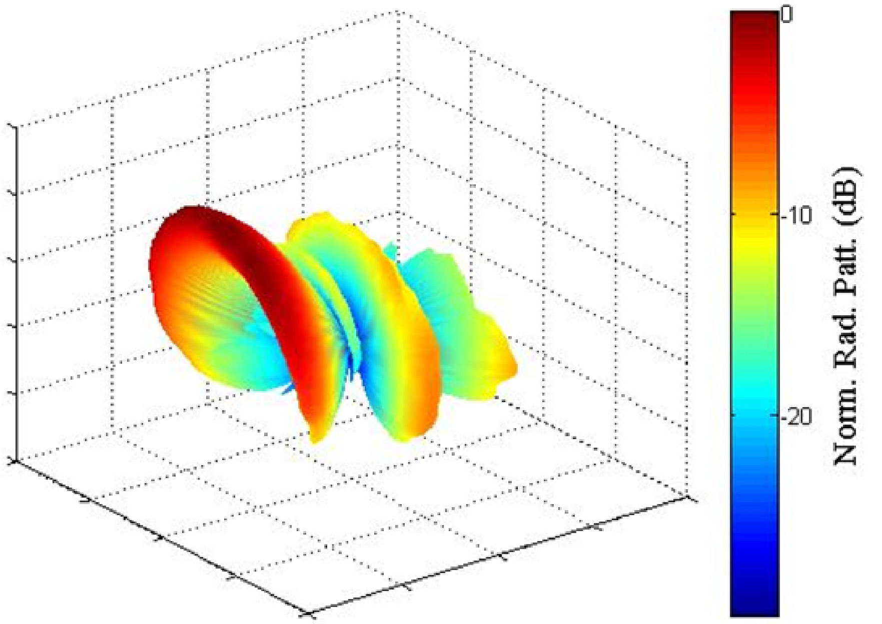

(b) $\theta_{scan} = -30°$

Figure 4.29: Measured 3D normalized radiation patterns for the 16-element hybrid phased array.

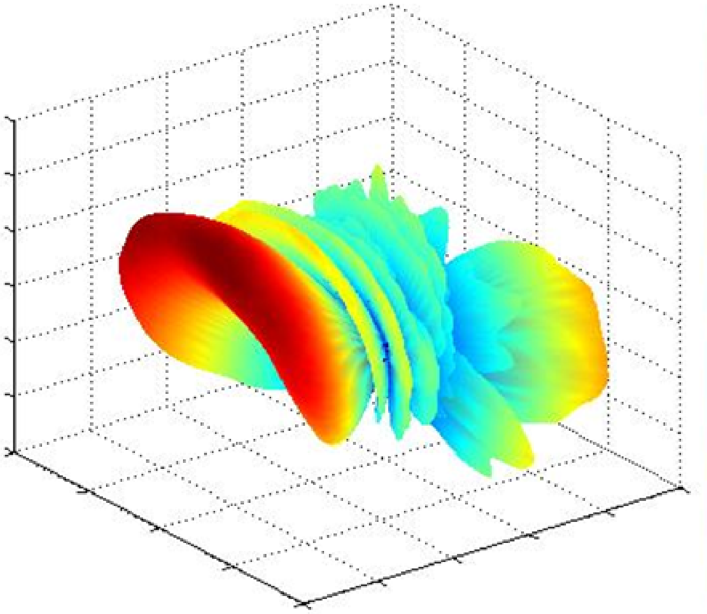

(c) $\theta_{scan} = -60°$

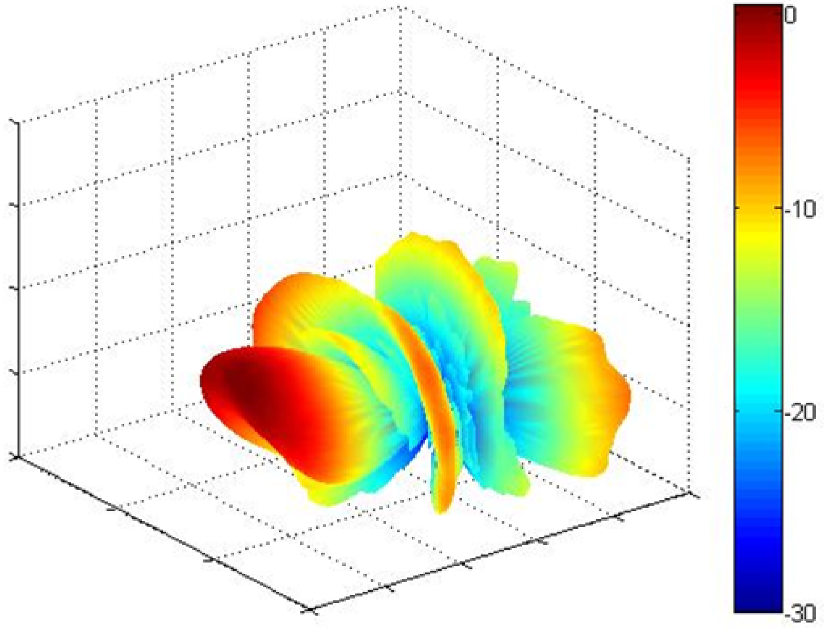

(d) $\theta_{scan} = -70°$

Figure 4.29: Measured 3D normalized radiation patterns for the 16-element hybrid phased array, continued.

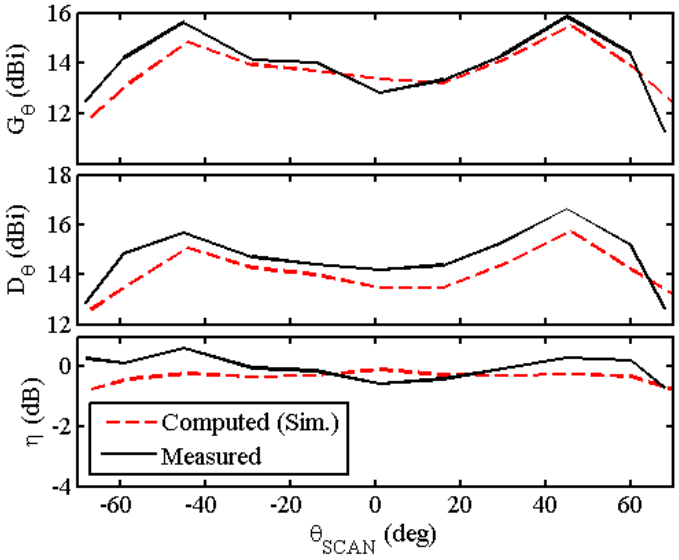

Figure 4.30: Comparative plot of scanned gain versus scan angle for measured data and computed from simulated data ($f = 4.6$ GHz)

.

Table 4.3: Summary of 16 element hybrid phased array 3 dB scan range.

	θ_{3dB}(deg)	
f (GHz)	Computed (Sim.)	Measured
4.0	±15	±0
4.1	±7.5	±7.5
4.2	±30	±15
4.3	±52	±45
4.4	±64	±59.5
4.5	±64	±68
4.6	±69	±68
4.7	±69	±68
4.8	±69	±64
4.9	±59	±64
5.0	±45	±45

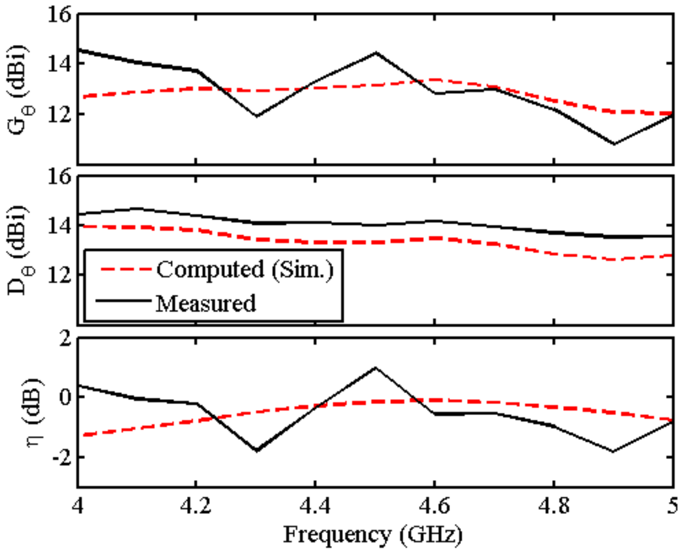

Figure 4.31: Comparative plot of scanned gain versus frequency for measured data and computed from simulated data ($\theta_{scan} = 0°$).

oscillate around the simulated value by approximately ±1 dB. In addition to the ±0.5 dB measurement error, these computed quantities are influenced by the assumptions made about the feed network and how it interacts with the dipole. For example, each channel was treated separately and did not include any coupling from all the other channels. Additionally, only the reflection coefficients at the antenna outputs and feed network inputs were considered. Given the number of devices in the RF chain, each with some level of impedance mismatch, there are multiple reflections that were not explicitly considered. The approximate nature of these assumptions are at least in part responsible for the fluctuations in the measured data. Table 4.4 summarizes the half power instantaneous bandwidth for the 16 element array at each scan angle. The fluctuations in the computed realized gain over frequency as seen in Fig. 4.31 are responsible for the disagreement between simulated and measured 3 dB bandwidth at some scan angles. These fluctuations are due to the error in the gain computation and approximate nature of assumptions about the feed network and its interaction with the dipole array. As discussed in section 4.2, the multiple mode array is essentially a linear phased array

Table 4.4: Summary of 16 element hybrid phased array 3 dB instantaneous bandwidth.

	Δf_{3dB}(GHz)	
θ_{scan} (deg)	Computed (Sim.)	Measured
-70	0.4	0.3
-60	0.4	0.4
-45	0.5	0.3
-30	0.5	0.4
-15	1.0	0.8
0	1.0	1.0
15	0.8	0.4
30	0.7	0.4
45	0.6	0.4
60	0.4	0.4
70	0.4	0.4

of fixed phased linear sub-arrays. Therefore, we can expect some of the same limits on instantaneous bandwidth that apply to conventional linear arrays. Equation 4.12 is an approximate measure of instantaneous 3 dB bandwidth that depends on the center frequency f_0, scan angle θ_{scan}, and number of array elements N [81]. This equation applies only to arrays employing phase shifting elements rather than true time delay (TTD) elements, which can produce inherently wideband scanned array behavior. For a conventional 16 element array operating near 4.6 GHz, that bandwidth varies from several GHz near broadside to approximately 300 MHz at $\theta_{scan} = 70°$. The hybrid phased array instantaneous bandwidth over scan angle is consistent with this analysis.

$$\Delta f_{3dB} = f_0 \sin\theta_{scan} \left[\frac{1}{\sin(\theta_{scan} - \frac{102}{N})} - \frac{1}{\sin(\theta_{scan} + \frac{102}{N})} \right] \tag{4.12}$$

4.6 Conclusions and Future Study

We have presented a novel approach to beam steering using an array composed of multiple unique radiating modes. This concept was described first by analysis of a purely multiple mode array. A hybrid phased array was shown to present an efficient tradeoff between the scan performance improvement and the design complexity associated with implementing a multiple radiating mode aperture. The results of the analysis sections were validated in the fabrication and measurement of a 4 element multiple mode linear dipole array. This multiple mode array was used as a sub-array in the 16 element hybrid phased array, which was also fabricated and tested. The significant improvement in scan range and scanned gain proposed in the analysis sections was verified in the radiation pattern measurements of the array. Near the design frequency of 4.6 GHz, the boresight array pattern was shown to have a peak gain of 12.8 dBi, an instantaneous bandwidth of greater than 1 GHz and a 3 dB scan range of ±68°. As with most phased array architectures, the use of multiple radiating modes does have limitations with respect to implementation complexity and mode bandwidth that limit its range of application. The ideas presented here are extended in the next chapter to 2 dimensional scanning arrays.

Acknowledgment

Chapter 4, in part, has been submitted as it may appear in IEEE Transactions on Antennas and Propagation, 2015. Labadie, Nathan R.; Sharma, Satish K.; Rebeiz, Gabriel, IEEE, 2015. The dissertation/thesis author was the primary investigator and author of this paper.

The work was carried out in part under the National Science Foundation (NSF)s CAREER grant ECCS-0845822. The authors would like to thank Nathan's Cubic colleague and hardware engineer Kevin Priest for his help in developing the GUI and

embedded code used to control the array as well as SDSU’s Mark Bruno for his help in assembling the active feed boards.

Chapter 5

Investigations on the use of Multiple Unique Radiating Modes for 2D Beam Steering

5.1 Introduction

In the previous chapter, we used Fourier series decomposition to synthesize desired 1D radiation patterns both from conventional and multiple mode element radiation patterns. However, many phased array applications require the ability to scan a beam in both θ and ϕ. In this chapter, the multiple mode approach to beam steering is extended to 2D scanning arrays in a manner analogous to the method presented in [82]. Fig. 5.1 illustrates the three 2D array topologies of interest. First, in section 5.2, we develop a method of 2D beam synthesis by deriving a relationship between the spherical harmonic coefficients of the composing elements of an array and a desired array pattern. Spherical harmonic representation is used since it is potentially more compact than the full radiation pattern data and is convenient for use with other signal processing algorithms [83]. A

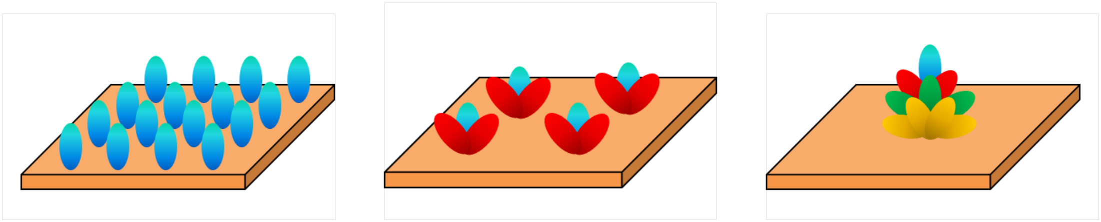

(a) Conventional phased array (b) Hybrid phased array. (c) Multiple mode array.

Figure 5.1: Illustration of 2D array topologies as described in this chapter and in order of increasing of number of unique radiating modes.

novel multiple mode antenna based on our work presented in [66] is developed in greater detail in section 5.3. Pair wise analysis of the cross-coupling between two such elements is presented in section 5.4 in order to predict an array geometry likely to produce maximum gain and optimal input impedance. Based on the analysis, three array geometries to be simulated and compared are defined in section 5.5. Full-wave electromagnetic simulation is usd in section 5.6 to show that a hybrid phased array composed of multiple mode sub-arrays can deliver improved scan performance compared to two representative conventional planar phased arrays. Finally, a 12 port hybrid phased array prototype is fabricated and characterized in section 5.7. Good agreement is obtained between simulated and measured data. All electromagnetic simulations were performed using Ansys HFSS [42] while MATLAB [41] was used to post-process the data.

5.2 Spherical Harmonics

In [84], the authors present a method of representing arbitrary radiation patterns in terms of spherical harmonic modes. Using scalar spherical harmonics and vector coefficients, a radiation pattern can be expressed with arbitrary precision assuming a sufficient number of modes are used. The authors cite several benefits of this method including reduction of the data set needed to represent a radiation pattern and ease of

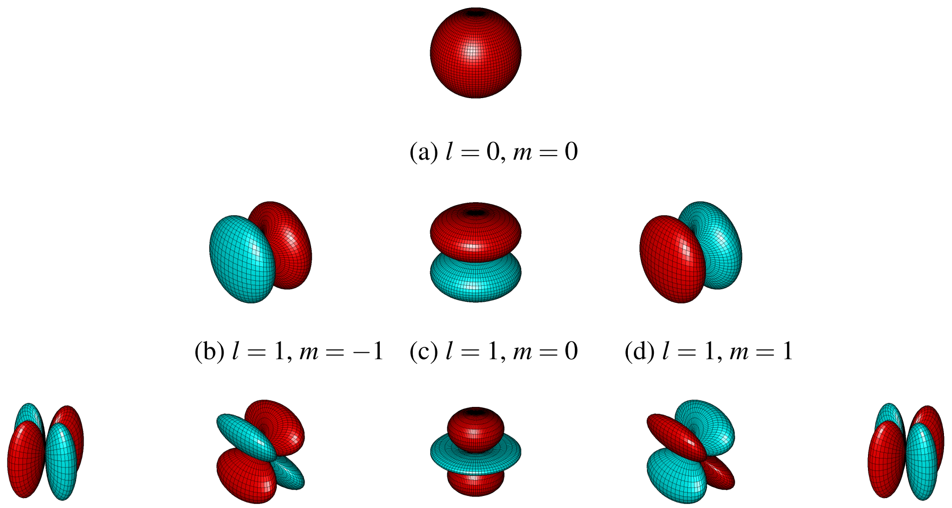

(a) $l=0, m=0$

(b) $l=1, m=-1$ (c) $l=1, m=0$ (d) $l=1, m=1$

(e) $l=2, m=-2$ (f) $l=2, m=-1$ (g) $l=2, m=0$ (h) $l=2, m=1$ (i) $l=2, m=2$

Figure 5.2: Plots of the first 9 real spherical harmonics modes where the color blue indicates a negative sign and the color red indicates a positive sign.

data manipulation in signal processing algorithms. The spherical harmonics are a 1 dimensional set of 2 dimensional modes analogous to the Fourier series modes. The basic equation used to compute the scalar spherical harmonic mode is given equation 5.1

$$Y_l^m(\theta,\phi) = sqrt\frac{(2l+1)}{4\pi}\frac{(l-m)!}{(l+m)!}P_l^m(\cos\theta)\exp(im\phi) \tag{5.1}$$

where $P_l^m(\cos\theta)$ are the associated Legendre functions of the first kind and the indices l and m are the order and degree of the mode, respectively.

$$l = 0,1,2,\ldots,(L-1) \tag{5.2a}$$

$$m = -l,(-l+1),\ldots,(l-1),l \tag{5.2b}$$

We will apply a similar method of modal decomposition and synthesis used in [82] to synthesize a desired radiation pattern from the spherical harmonic coefficients of a given set of radiating elements.

5.2.1 Spherical Harmonic Decomposition

Following the derivations in [84] for decomposing a radiation field pattern in terms of spherical harmonic modes, we can express a desired pattern $\vec{E}_D(\hat{r})$ as

$$\vec{E}_D(\hat{r}) = \sum_{p=1}^{P} \vec{a}_p Y_p(\hat{r}) \tag{5.3}$$

where $\vec{a}_p$ is the set of unknown coefficients, which can be solved for either by using direct integration or least squares approaches. Similarly, the radiation field pattern of a given array element is defined as

$$\vec{E}_q(\hat{r}) = \sum_{p=1}^{P} \vec{b}_{pq} Y_p(\hat{r}) \tag{5.4}$$

where the subscript q denotes the array element number, P is the highest mode number and $\vec{b}_p$ are the unknown mode coefficients. For simplicity, the subscripts l and m have been replaced by a single parameter

$$p = l^2 + l + m + 1 \tag{5.5}$$

There are total of $P = (L-1)^2 + 2(L-1) + 1 = L^2$ possible spherical harmonic modes determined by the highest mode order L.

5.2.2 Spherical Harmonic Synthesis

As was shown for the 1 dimensional Fourier modes in [82], the desired array pattern $\vec{E}_D(\hat{r})$ can be expressed in terms of the given set of element patterns $\vec{E}_q(\hat{r})$.

$$\vec{E}_D(\hat{r}) = \sum_{q=1}^{N} c_q \vec{E}_q(\hat{r}) \tag{5.6}$$

Furthermore, the spherical harmonic representation of $\vec{E}_q(\hat{r})$ can be substituted into equation 5.6 and the order of the summations rearranged.

$$\vec{E}_D(\hat{r}) = \sum_{p=1}^{P} \left[\sum_{q=1}^{N} c_q \vec{b}_{pq} \right] Y_p(\hat{r}) \tag{5.7}$$

A relationship between the spherical harmonic mode coefficients for the desired array pattern and given element patterns can be derived by equating equation 5.7 to equation 5.3.

$$\vec{a}_p = \sum_{q=1}^{N} c_q \vec{b}_{pq} \tag{5.8}$$

The summations in equation 5.8 can be expressed as the overdetermined matrix equation

$$\mathbf{A} = \mathbf{B} \cdot \mathbf{c} \tag{5.9}$$

where

$$\mathbf{a} = [\mathbf{a_p^x}, \mathbf{a_p^y}, \mathbf{a_p^z}]^\mathbf{T} \tag{5.10a}$$

$$\mathbf{B} = [\mathbf{b_{pq}^x}, \mathbf{b_{pq}^y}, \mathbf{b_{pq}^z}]^\mathbf{T} \tag{5.10b}$$

$$\mathbf{c} = [\mathbf{c_q}] \tag{5.10c}$$

The unknown mode coefficients **c** can be found by using the least squares approach to compute the pseudo-inverse of the known spherical harmonics coefficients matrix **B**.

$$\mathbf{c} = \mathbf{pinv}(\mathbf{B}) \cdot \mathbf{a} \tag{5.11}$$

The matrix equation is shown with more detail in the following equation.

$$\begin{bmatrix} c_1 \\ \vdots \\ c_N \end{bmatrix} = pinv \begin{bmatrix} b^x_{11} & \cdots & b^x_{N1} \\ \vdots & \ddots & \vdots \\ b^x_{1P} & \cdots & b^x_{NP} \\ b^y_{11} & \cdots & b^y_{N1} \\ \vdots & \ddots & \vdots \\ b^y_{1P} & \cdots & b^y_{NP} \\ b^z_{11} & \cdots & b^z_{N1} \\ \vdots & \ddots & \vdots \\ b^z_{1P} & \cdots & b^z_{NP} \end{bmatrix} \begin{bmatrix} a^x_1 \\ \vdots \\ a^x_P \\ a^y_1 \\ \vdots \\ a^y_P \\ a^z_1 \\ \vdots \\ a^z_P \end{bmatrix} \tag{5.12}$$

A more direct method to find the optimal weights **c** is to project the desired radiation pattern directly onto the element patterns. This can be accomplished using the a sample matrix inversion method [85] or by evaluating the inner product between the desired pattern and the element patterns.

$$c_q = \int_0^{2\pi} \int_0^{\pi} \vec{E}_D(\theta,\phi) \cdot \vec{E}^*_q(\theta,\phi) \sin(\theta) d\theta d\phi \tag{5.13}$$

We have elected to use the spherical harmonics as an intermediate basis for a couple reasons. Since it is truly an orthonormal basis, it lends itself well to signal processing manipulation including mode filtering and coordinate transformation. For example, the spherical harmonics coefficients for a desired beam shape and the collection of element patterns only need to be computed once. Using well established techniques, the desired beam can be rotated by an arbitrary set of Euler angles using only its coefficients. The element weights for the new array pattern orientation are then computed from the spherical harmonic coefficients alone.

One issue of concern using this method is the number of spherical harmonic coefficients needed to simultaneously represent the radiation patterns. In order for these to be a compact representation, we would like to minimize the number of coefficients needed. By substituting equations 5.3 and 5.4 into 5.13, we can relate the projection integral to the spherical harmonic coefficients.

$$c_q = \int_0^{2\pi}\int_0^{\pi}\sum_{p=1}^{P}\vec{a}_{pq}Y_p\cdot\sum_{r=1}^{P}\vec{b}^{*}_{rq}Y^{*}_{r}\sin(\theta)d\theta d\phi \tag{5.14}$$

$$= \sum_{p=1}^{P}\sum_{r=1}^{P}\vec{a}_{pq}\cdot\vec{b}^{*}_{rq}\int_0^{2\pi}\int_0^{\pi}Y_pY^{*}_{r}\sin(\theta)d\theta d\phi \tag{5.15}$$

Using the orthonormal properties of the spherical harmonics, the final expression for the element weights is

$$c_q = \sum_{p=1}^{P}\vec{a}_p\cdot\vec{b}^{*}_{pq} \tag{5.16}$$

The value of equation 5.16 is that it clearly shows that the element weight is unaffected if either the element or array pattern spherical harmonic coefficient is zero. Therefore, it makes sense to compute these coefficients in a coordinate system that minimizes them for either the element or array pattern. This detail is important in implementing an efficient algorithm. Typically, simulations and measurements of radiation patterns are referenced to the physical center of the array, which often coincides with the apparent phase center of the array. In this case, both the array pattern and the element phase pattern vary rapidly with angle requiring a large number of spherical harmonics. If the array pattern phase is instead translated in phase by $\vec{k}\cdot\vec{r}_q$ to the phase center of each element, then the number of modes required to represent an element pattern of moderate gain significantly decreases as illustrated in Fig. 5.3.

$$\tilde{\vec{E}}_{Dq} = \vec{E}_D\exp(-i\vec{k}\cdot\vec{r}_q) \tag{5.17}$$

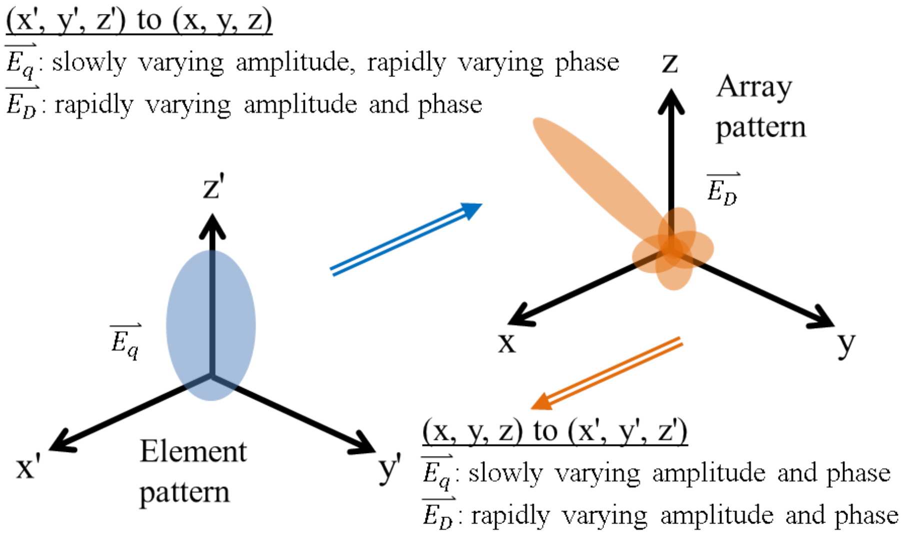

Figure 5.3: Illustration of the effect of coordinate system location with respect to element and array radiation patterns on the variation over angle.

As an example, the planar array pictured in 10×10 Fig. 5.4 is used to synthesize an ideal planar array pattern scanned to 45° based on the equation

$$E_D(\theta,\phi) = \frac{1}{N_x N_y} \frac{\sin(\frac{N}{2}\psi_x)}{\sin(\frac{1}{2}\psi_x)} \frac{\sin(\frac{N}{2}\psi_y)}{\sin(\frac{1}{2}\psi_y)} \tag{5.18}$$

where

$$\psi_x = kd_x \left[\sin(\theta)\cos(\phi) - \sin(\theta_{SCAN})\cos(\phi_{SCAN})\right] \tag{5.19a}$$

$$\psi_y = kd_y \left[\sin(\theta)\sin(\phi) - \sin(\theta_{SCAN})\sin(\phi_{SCAN})\right] \tag{5.19b}$$

A simple cosine element pattern was assumed.

$$E_q = \cos(\theta) \tag{5.20}$$

The distribution of spherical harmonic coefficient amplitudes for the two cases of coordinate system placement are plotted in Fig. 5.5. The element coefficient amplitudes were averaged over the collection of elements and normalized to a maximum of 0 dB.

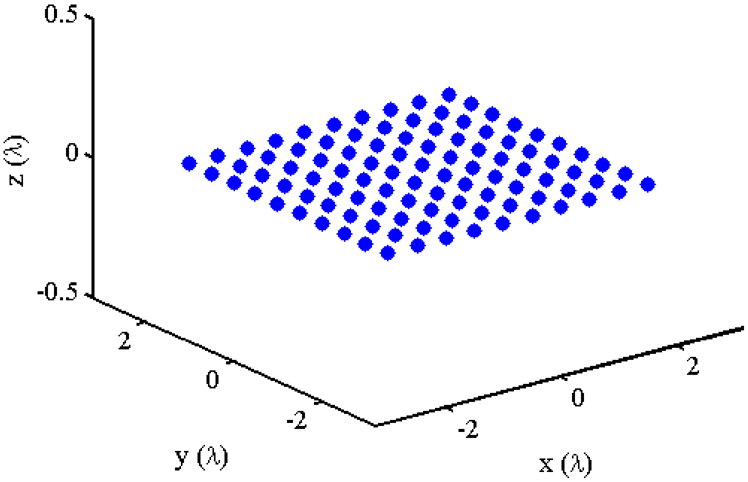

Figure 5.4: MATLAB depiction of a 10×10 planar array with $\lambda/2$ interelement spacing.

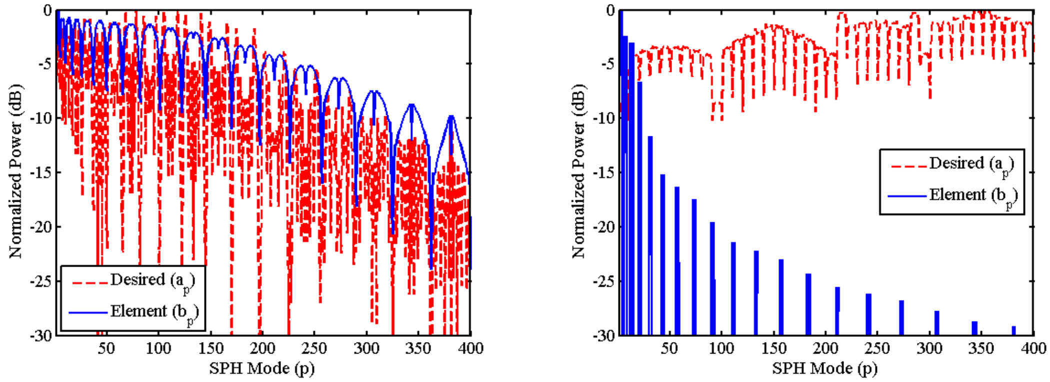

(a) Coordinate system at array phase center $(x', y', z' \rightarrow x, y, z)$.

(b) Coordinate system at element phase center $(x, y, z \rightarrow x', y', z')$.

Figure 5.5: Plots of spherical harmonic amplitude coefficient power for the two cases of coordinate system placement. Element coefficient power was averaged over the collection of elements.

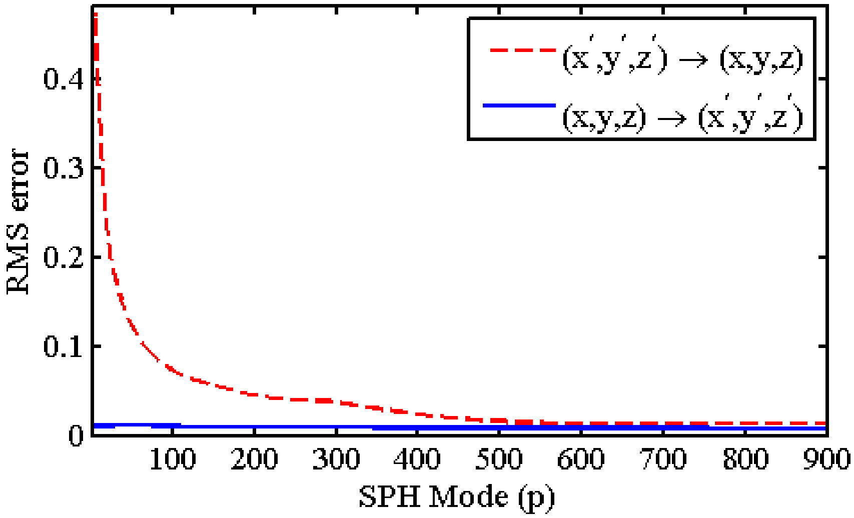

Figure 5.6: Comparison of the convergence of the synthesized pattern to the desired pattern in terms of the RMS error.

Clearly, relatively few spherical harmonic modes are required when the computations are centered at the phase center of each element. This improvement is also evident in rapid decrease of the root mean square (RMS) error of the synthesized pattern as shown in Fig. 5.6. Finally, we plot the synthesized array patterns for both cases of coordinate system placement assuming only 16 modes are used ($L = 4$). Clearly, some attention needs to be paid to the way in which the spherical harmonic coefficients are generated in the interest of efficiency.

5.3 Radiating Elements

A linearly polarized (LP) monopolar dielectric resonator antenna (DRA) on square patch antenna was shown to be capable of full hemispherical null steering using 3 independent modes in [66]. Other authors have subsequently proposed variations on this concept using only 2 independent feed points which requires a continuous range phase difference between modes [86, 87]. In this section, we describe and characterize a

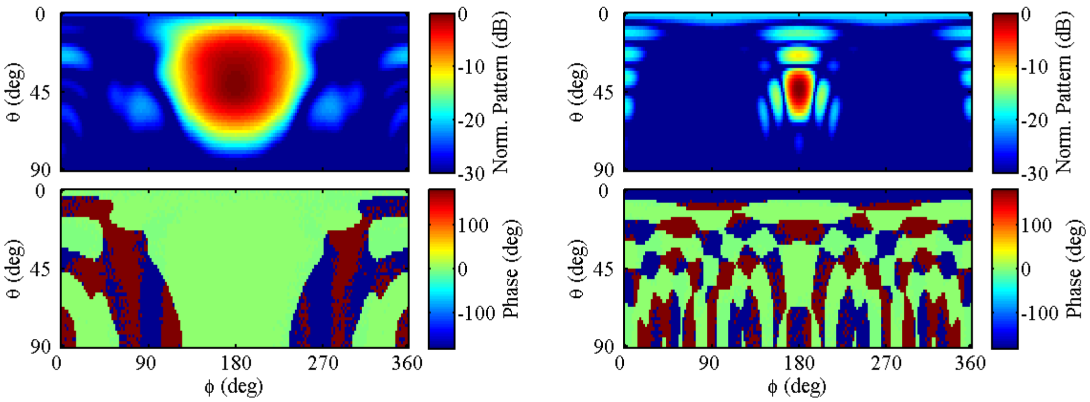

(a) Coordinate system at array phase center ($x', y', z' \rightarrow x, y, z$).

(b) Coordinate system at element phase center ($x, y, z \rightarrow x', y', z'$).

Figure 5.7: Plots of the synthesized array patterns assuming a total of 16 spherical harmonic modes ($L = 4$).

Table 5.1: Critical design parameters of the monopole on patch antenna sub-array.

Parameter	Value	Description
h_d	60 mil	dielectric thickness
w	21 mm	patch antenna width
x	3.5 mm	patch antenna feed distance from center
h_m	14 mm	wire monopole height
r_m	0.5 mm	wire monopole radius
ε_r	2.2	dielectric relative permittivity

multiple mode sub-array capable of conical beam peak steering and full hemispherical null steering. The sub-array is a simplified version of our work presented in [66] in that the monopolar DRA has been removed. The proposed multiple mode sub-array consists of a wire monopole mounted on top of a single square patch antenna as shown in Fig 5.8. The monopole is single-fed while the patch is excited at two points for steering along each polarization. Table 5.1 lists the design parameters of the monopole and patch antenna structures used in simulation. An infinite dielectric was used in the full-wave electromagnetic Ansys HFSS simulations since this configuration best illustrates the null and beam peak steering properties of the sub-array.

The scattering parameters for the given monopole on patch antenna dimensions are plotted in Fig. 5.9. As expected, the monopole exhibits a wideband -10 dB impedance match of approximately 22% while the patch antenna is inherently narrowband at 3%. The maximum in-band mutual coupling (S_{13}) is approximately -20 dB between the patch feeds (ports 1 and 2) and monopole feed (port 3). Efforts are currently underway to incorporate a wideband patch antenna in order to achieve an overall wideband multiple mode response.

Using the orthogonal omnidirectional and two directional modes, both beam and null steering are achieved through combining of the complex radiated fields. The null can be steered nearly anywhere in the upper quadrant of the hemisphere by changing the relative port amplitudes for a given fixed phase relationship between the monopole and patch modes. The ratios of port amplitudes are defined by

$$\alpha_1 = \frac{|A_2|}{|A_1|} \tag{5.21a}$$

$$\alpha_2 = \frac{\sqrt{|A_1|^2 + |A_2|^2}}{|A_3|} \tag{5.21b}$$

where the port amplitudes are subject to the normalization condition

$$|A_1|^2 + |A_2|^2 + |A_3|^2 = 1 \tag{5.22}$$

For given amplitude ratios α_1 and α_2, the required port amplitudes are

$$|A_1| = \sqrt{\frac{1}{1+\alpha_1^2} - \frac{1}{(1+\alpha_1^2)(1+\alpha_2^2)}} \tag{5.23a}$$

$$|A_2| = \alpha_1 |A_1| \tag{5.23b}$$

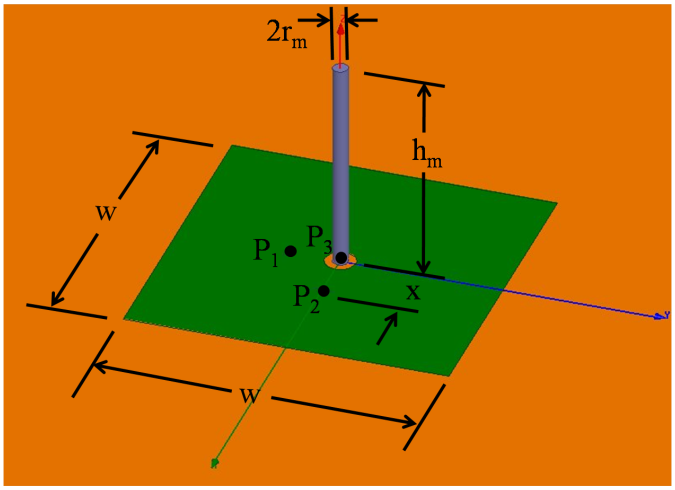

Figure 5.8: Monopole on square patch radiating element with three feed points. P_1 and P_2 excite the square patch along orthogonal polarizations while P_3 is used to excite the monopole.

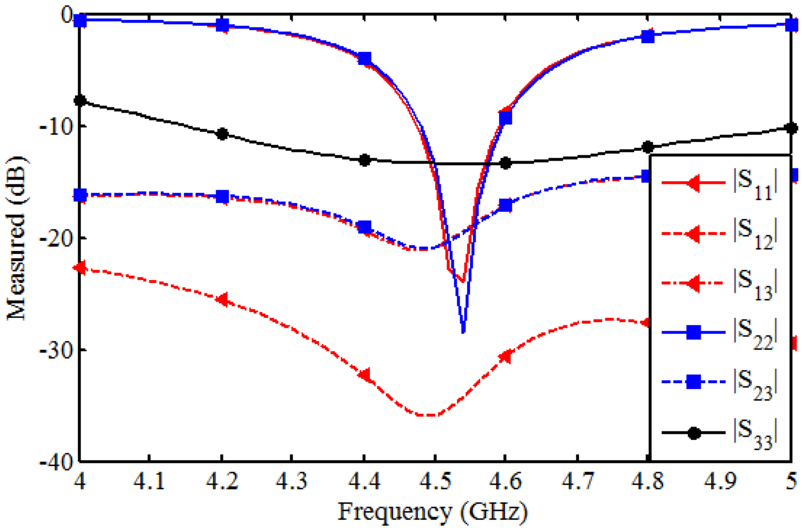

Figure 5.9: Monopole on square patch scattering parameters.

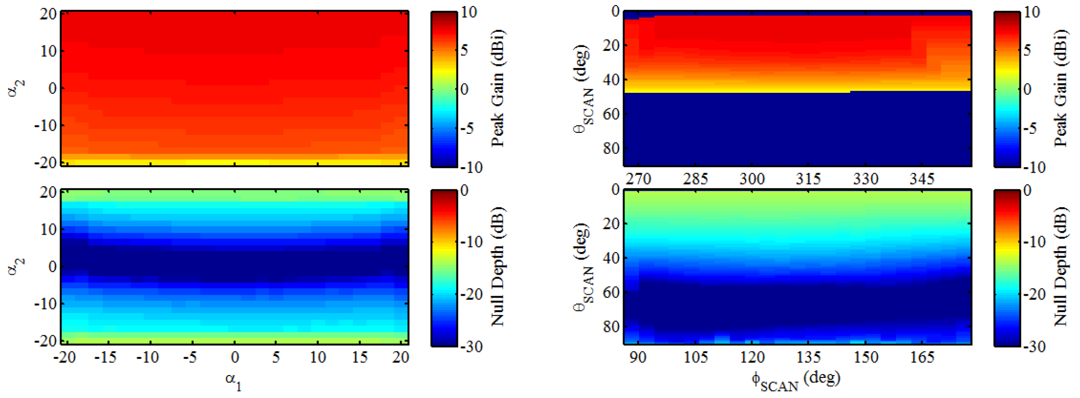

(a) Scan ratios α_1, α_2

(b) Scan angles θ_{SCAN}, ϕ_{SCAN}

Figure 5.10: Amplitude only scan performance in a single quadrant of the hemisphere for the monopole on patch sub-array

$$|A_3| = \frac{1}{1+\alpha_2^2} \tag{5.23c}$$

Nearly continuous null and beam steering in a single quadrant are shown in Fig. 5.10a as a function of the ratio of port amplitudes. The beam peak gain is fairly constant over azimuthal scan angle ϕ_{SCAN}, which is determined by the port amplitude ratio α_1. As the port amplitude ratio α_2 is decreased, the beam peak scans in the direction of increasing elevation angle θ_{SCAN}. The peak realized gain decreases from 7.7 dBi to 2.6 dBi as the weights on the higher gain directional modes, A_1 and A_2, decrease and shift to the lower gain omnidirectional mode, A_3. Over the entire azimuthal and elevation scan range, the null depth varies between -40 dB and -13.6 dB relative to the beam peak level. Fig. 5.10b plots the actual scan angle range for both the beam peak and null using the entire set of port amplitude ratio combinations. The beam peak scan range is contained within the quadrant defined by $268^\circ < \phi < 356^\circ$ and $0^\circ < \theta < 90^\circ$. At any particular azimuthal scan angle $268^\circ < \phi_{SCAN} < 356^\circ$, the beam peak elevation scan range is limited to $3^\circ < \theta_{SCAN} < 47^\circ$. However, the null is capable of scanning anywhere within the quadrant defined by $88^\circ < \phi < 176^\circ$ and $0^\circ < \theta < 90^\circ$. In order to achieve full conical beam peak steering and hemispherical null steering, appropriate phase shifts need to be applied between the 3 ports. The scanned beam peak and null can be shifted to the next quadrant by changing the phase relationship β_1 and β_2 between the patch modes and the monopole. Fig.5.11 demonstrates the ability of the steerable null and beam peak to occupy each of the four quadrants in the upper hemisphere.

$$\beta_1 = \angle A_1 - \angle A_3 \tag{5.24a}$$

$$\beta_2 = \angle A_2 - \angle A_3 \tag{5.24b}$$

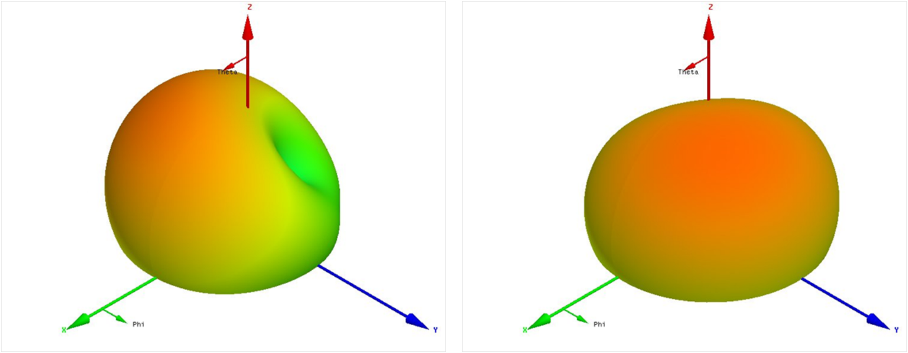

(a) $\beta_1 = 0°$, $\beta_2 = 0°$.

(b) $\beta_1 = 180°$, $\beta_2 = 0°$.

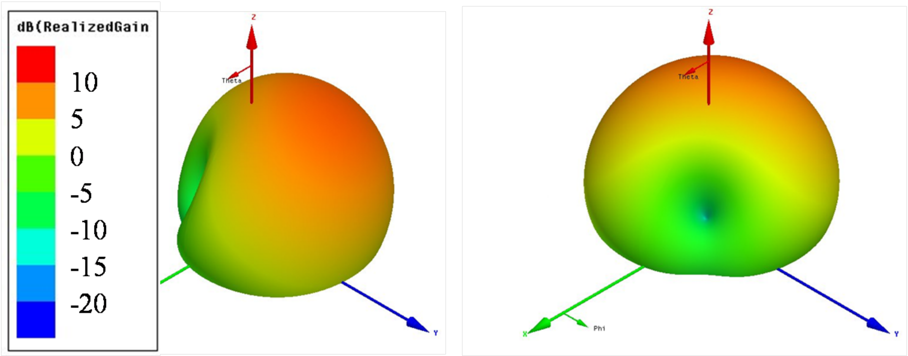

(c) $\beta_1 = 180°$, $\beta_2 = 180°$.

(d) $\beta_1 = 0°$, $\beta_2 = 180°$.

Figure 5.11: Movement of the scanned beam peak and null between quadrants by adjusting the monopole to patch modes phase β.

5.4 Element Pair Analysis

Some insight into the expected performance of an array composed of some combination of patch and/or monopole antennas by considering the interaction between element pairs. The three arrays considered later in this chapter consist of either patch antennas or patch and monopole antennas. Therefore, we will compare three cases of antenna pairs shown in Fig. 5.12 in order to make some predictions about the performance potential array geometries. The cross-coupling parameter, τ, introduced in [9] was shown to be critical in determining the maximum possible gain of the array and the optimal input reflection coefficient.

$$\tau = \int_0^{2\pi} \int_0^{\pi} \vec{f}^{(1)}(\theta,\phi) \cdot \vec{f}^{(}2)^{*}(\theta,\phi) \sin\theta d\theta d\phi \tag{5.25}$$

We use the notation in [9], where maximum possible gain for a two element array is proportional to the parameter $|S_{31}|$.

$$G_{max} \propto |S_{31}|^2_{max} = \frac{1}{1+|\tau|} \tag{5.26}$$

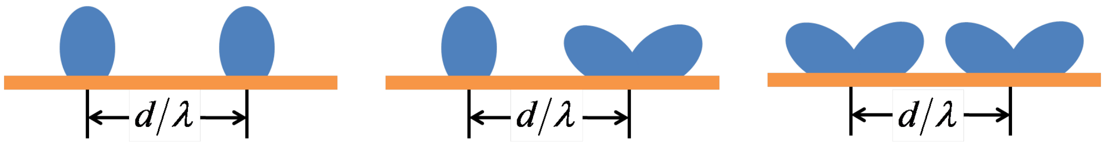

(a) Patch-patch pair.
(b) Patch-mono pair.
(c) Mono-mono pair.

Figure 5.12: Three different element pairs used in the analysis of cross-coupling versus interelement spacing (d/λ)

The optimal input match S_{11}, S_{22} needed to realize the maximum gain is equal to the coupling between ports S_{21} and defined in terms of the cross-coupling parameter τ.

$$S_{11} = \pm S_{21} = \sqrt{\frac{1}{2}\frac{|\tau|}{1+|\tau|}} \tag{5.27}$$

Using the simulated radiation field patterns for each antenna element from the previous section, we can generate the cross coupling parameters for the cases shown in Fig. 5.12. The cross-coupling parameter τ depends on the amount of overlap between the pair of element radiation patterns and the separation of their phase centers d/λ. As discussed in [9], the phase center location of an antenna is influenced by the scattering of adjacent elements and is not necessarily collocated with the physical center. However, we will make the assumption that the two are collocated for the purposes of this analysis. Not surprisingly, Fig. 5.13 shows that both pairs of identical elements (patch-patch and monopole-monopole) have maximum coupling as the interelement spacing decreases toward zero. In contrast, the monopole-patch pair maintains zero coupling when collocated. That is, the directional patch and omni-directional monopole radiation patterns are indeed orthogonal. Fig. 5.13 also plots the radiation efficiency parameter $|S_{31}|^2$ showing that the orthogonal elements have the highest efficiency when collocated. As the monopole-patch pair approaches half wavelength spacing, the coupling is maximized thereby minimizing the efficiency. This is an undesired coupling mode that will have some impact on the array performance. At this same interelement spacing, the monopole-monopole coupling is at a local minimum leading to highly efficient radiation. The optimal input reflection coefficient needed to maximize the gain is better than -15 dB at $d/\lambda = 0$ and $d/\lambda = 0.5$ for the monopole-patch and monopole-monopole pairs, respectively. In comparison, the optimal input reflection coefficient for the patch-patch pair degrades significantly with decreasing interelement spacing. These observations are important since the proposed

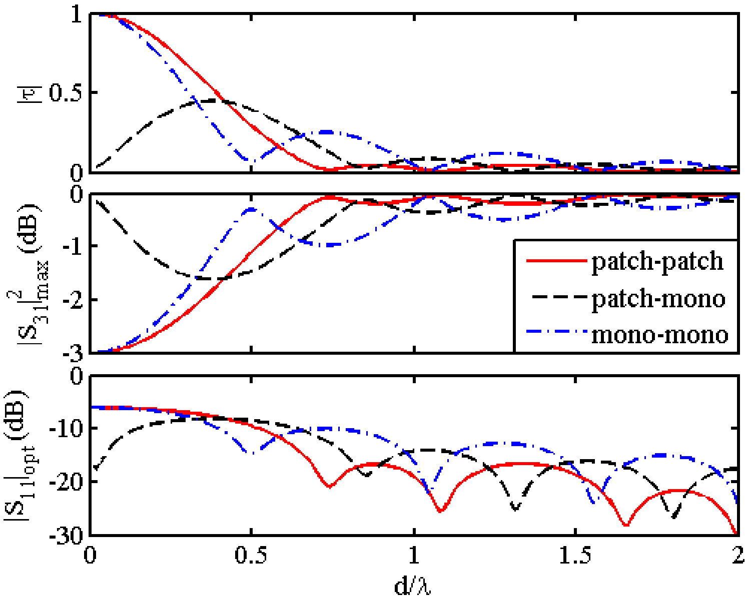

Figure 5.13: Plots of coupling, gain and input reflection coefficient parameters for pairs of elements as indicated in the legend.

hybrid phased array configuration consists of multiple collocated monopole on patch sub-arrays separated by half-wavelength and therefore consists of all three element pair types (i.e. patch-patch, patch-monopole and monopole-monopole).

This analysis does not capture the interdependency between the embedded element pattern and reflection coefficient. Simulated radiation pattern data for the isolated elements from the previous section were used here. In practice, these patterns will distort due to scattering from adjacent elements, which is also a function of element spacing. This does not invalidate the general conclusion that a monopole on patch multiple mode sub-array can be arranged to radiate efficiently in a hybrid phased array configuration.

5.5 Array Geometries

The convention used to identify each of the three array types is ($m \times n \times p$), where m is the number of unit cell locations along the x-axis, n is the number of unit cell locations along the y-axis and p is the number of feed points at each location. The simplest of these arrays ($2 \times 2 \times 2$) consists of 4 patch antennas with $\lambda/2$ interelement spacing as shown in Fig. 5.14b. Two feed points are used to excite each patch antenna since this enables arbitrarily polarized radiation patterns in any particular scan plane. Since we are interested in improving the scan range of the array, an obvious approach is increasing the sampling of the aperture by adding more elements as shown in Fig. 5.14a where the area occupied by the patches ($w_a \times w_a$) is constant. Our proposed hybrid phased array architecture ($2 \times 2 \times 3$) is shown in Fig. 5.14c and is composed of driven 4 monopole and 4 patch antenna elements for a total of 12 feed points. Note that the half-wavelength spacing between monopole on patch sub-arrays is used as indicated by the analysis in the previous section. In terms of number of feed points, the hybrid phased array is greater than the 8 feed point ($2 \times 2 \times 2$) array and less than the 18 feed point ($3 \times 3 \times 2$) array.

Coupling between the monopoles and collocated patches is already less then -20 dB due to the orthogonality of the current distributions induced on the patch by the monopole and the dominant patch modes. However, currents induced on adjacent patches due to monopoles which are not collocated are not radially symmetric. Therefore, a component of these currents is coupled into an adjacent patch port with an efficiency determined by the angle between the monopole to patch port radius and the polarization of the patch. As this angle decreases, the coupling increases. The design parameters for each of the 3 array types under consideration is given in Table 5.2.

5.6 Array Simulation Studies

Each of the arrays described in the preceding section was modeled and simulated in the commercial full-wave electromagnetic solver, Ansys HFSS. Properties of the

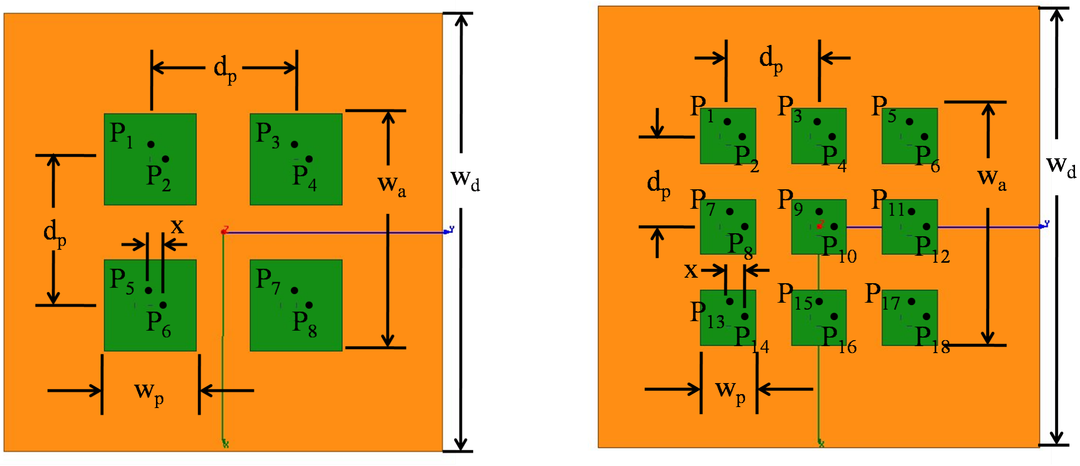

(a) Patch array ($2 \times 2 \times 2$) with $\lambda/2$ interelement spacing.

(b) Patch array ($3 \times 3 \times 2$) with $\lambda/4$ interelement spacing.

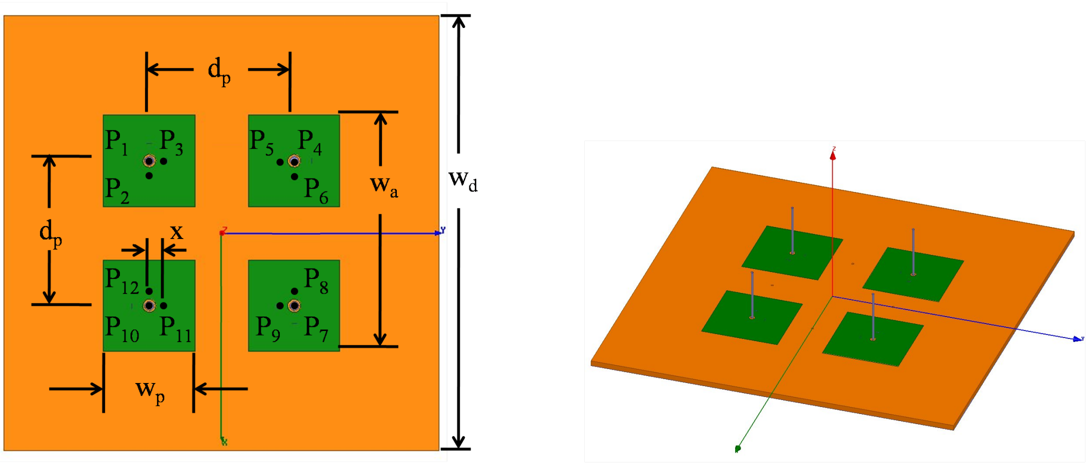

(c) Patch and monopole array ($2 \times 2 \times 3$) with $\lambda/2$ interelement spacing.

(d) Perspective view ($2 \times 2 \times 3$)

Figure 5.14: Three candidate arrays with relevant dimensional parameters labeled.

Table 5.2: Design parameters for the 3 array types under consideration.

Parameter	$(2\times2\times2)$	$(2\times2\times3)$	$(3\times3\times2)$
h_d	60 mil	60 mil	60 mil
w_d	267 mm	267 mm	267 mm
w_a	267 mm	267 mm	267 mm
ε_r	2.2	2.2	6.15
w_p	21 mm	21 mm	10 mm
d_p	33.3 mm	33.3 mm	20.7 mm
x	3.5 mm	3.5 mm	2.0 mm
h_m	14.0 mm	—	—
r_m	0.5 mm	—	—

synthesized array patterns and the overall beam steering performance derived from these simulations are discussed in this section.

5.6.1 Array Pattern Synthesis

In order to quantify the maximum scanned gain and scan angle for each of the arrays, we would like to synthesize a desired radiation pattern with constant beamwidth over all scan angles. An ideal 2D Gaussian beam pulse was chosen as the beam pattern to be synthesized. For the proposed monopole on patch sub-array, the co-polarized component of the steered pattern is always E_θ polarized. A Z-axis monopole will not be helpful in improving E_ϕ polarized beam characteristics. Therefore, we will restrict the comparison between arrays to the synthesis of a E_θ polarized Gaussian pulse pattern, which at ($\phi = 180°$, $\theta = 90°$) is defined by

$$\vec{E}_D(\phi = 180^\circ, \theta = 90^\circ) = \exp\left[\frac{(\phi-\pi)^2}{\sigma_\phi}\right]\exp\left[\frac{(\theta-\pi/2)^2}{\sigma_\theta}\right]\hat{\theta} \qquad (5.28)$$

where σ_ϕ and σ_θ are the width of the Gaussian pulse in the ϕ and θ dimensions, respectively.

This pattern can be rotated to any location on the sphere while maintaining the initial polarization properties using the method described in [83]. This approach is useful since a closed form expression for the desired pattern is not necessary. The method makes use of the Euler rotation theorem which states that an arbitrary rotation can be expressed in terms of Euler's angles α, β and γ. An arbitrary radiation pattern described by $E(\phi,\theta)$ can be rotated by the Euler angles by applying the Wigner D-matrix transformation to the spherical harmonic coefficients of the original pattern. The relationship between the spherical harmonic coefficients of the original radiation pattern ($\vec{a}_p$) and its counterpart in the rotated coordinate system ($\tilde{\vec{a}}_p$) as defined by

$$\vec{E}(\theta,\phi) = \sum_{p=1}^{P} \vec{a}_p Y_p(\theta,\phi) \tag{5.29a}$$

$$\tilde{\vec{E}}(\theta,\phi) = \sum_{p=1}^{P} \tilde{\vec{a}}_p Y_p(\theta,\phi) \tag{5.29b}$$

$$\tilde{\vec{a}}_p = \sum_{m'=-l}^{l} D_{lmm'}(\alpha,\beta,\gamma)\vec{a}_{lm'} \tag{5.29c}$$

where $D_{lmm'}$ are defined in terms of the Wigner D-matrix elements [83]. The Wigner D-matrix elements $d_{lmm'}$ are defined as

$$d_{lmm'} = \sqrt{(l+m')!(l-m')!(l+m)!(l-m)!} \sum_{k}(-1)^{(m'-m+k)} \frac{(\cos\frac{\beta}{2})^{(2l+m-m'-2k)}(\sin\frac{\beta}{2})^{(m'-m+2k)}}{k!(l+m-k)!(m'-m+k)!(l-m'-k)!} \tag{5.30}$$

where the subscript k is chosen such that the factorial arguments are non-negative or

$$k_{min} = \max(0, m-m'), \qquad k_{max} = \min(l+m, l-m') \tag{5.31}$$

Due to the discontinuous nature of a radiation pattern expressed in terms of spherical coordinates, the pattern must be converted to Cartesian coordinates. The transformation described above can be applied to each Cartesian component of the radiation pattern

$$\vec{\tilde{E}}(\phi,\theta) = \tilde{E}_{x'}\hat{x}' + \tilde{E}_{y'}\hat{y}' + \tilde{E}_{z'}\hat{z}' \tag{5.32}$$

where $\hat{x}'$, $\hat{y}'$ and $\hat{z}'$ are the basis vectors of the rotated coordinate system.

The final step is to express the rotated pattern in terms of the original Cartesian coordinate basis vectors $\hat{x}$, $\hat{y}$ and $\hat{z}$

$$\begin{bmatrix} E_x \\ E_y \\ E_z \end{bmatrix} = \mathbf{R_z}(\alpha)\mathbf{R_y}(\beta)\mathbf{R_z}(\gamma) \begin{bmatrix} \tilde{E}_{x'} \\ \tilde{E}_{y'} \\ \tilde{E}_{z'} \end{bmatrix} \tag{5.33}$$

where the rotation matrices are given by

$$\mathbf{R_z}(.) = \begin{bmatrix} \cos(.) & \sin(.) & 0 \\ -\sin(.) & \cos(.) & 0 \\ 0 & 0 & 1 \end{bmatrix}, \qquad \mathbf{R_y}(.) = \begin{bmatrix} \cos(.) & 0 & -\sin(.) \\ 0 & 1 & 0 \\ \sin(.) & 0 & \cos(.) \end{bmatrix} \tag{5.34}$$

Fig. 5.15 plots the polarimetric patterns for the desired Gaussian pulse at several different scan angles in θ. As expected, the pattern is entirely polarized in the E_θ direction at $\theta = 90^\circ$ and maintains this polarization at the beam peak as the beam is rotated in elevation angle. Also as expected, the E_ϕ polarization grows as the pattern approaches the pole along the Z-axis. The important point here is that beamwidth and polarization at the beam peak remain constant as the beam is scanned over the sphere thereby providing a good test pattern for the three arrays to synthesize.

The coefficients of each of the three arrays were separately optimized to synthesize the desired beam shown in Fig. 5.15c according to the method described in section 5.2.2.

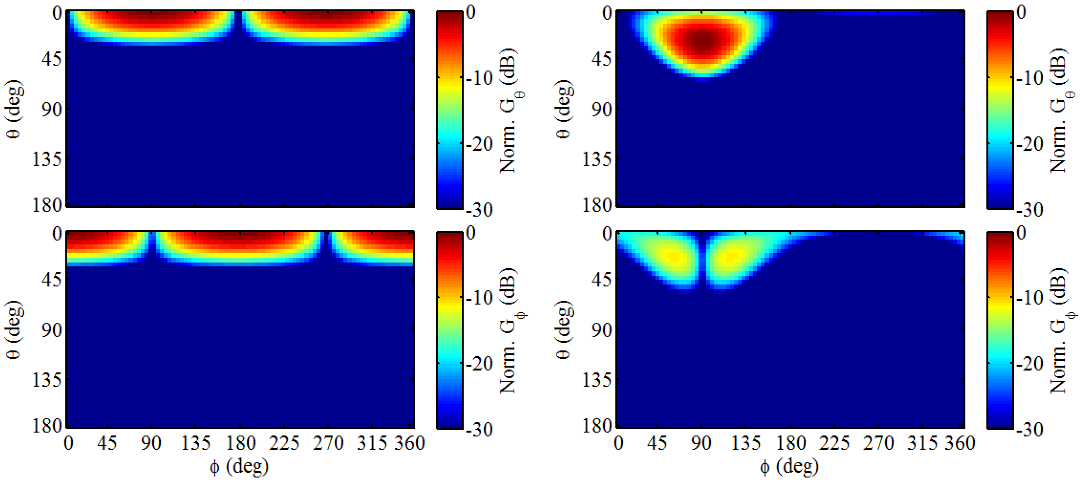

(a) $\phi = 90°, \theta = 0°$ (b) $\phi = 90°, \theta = 30°$

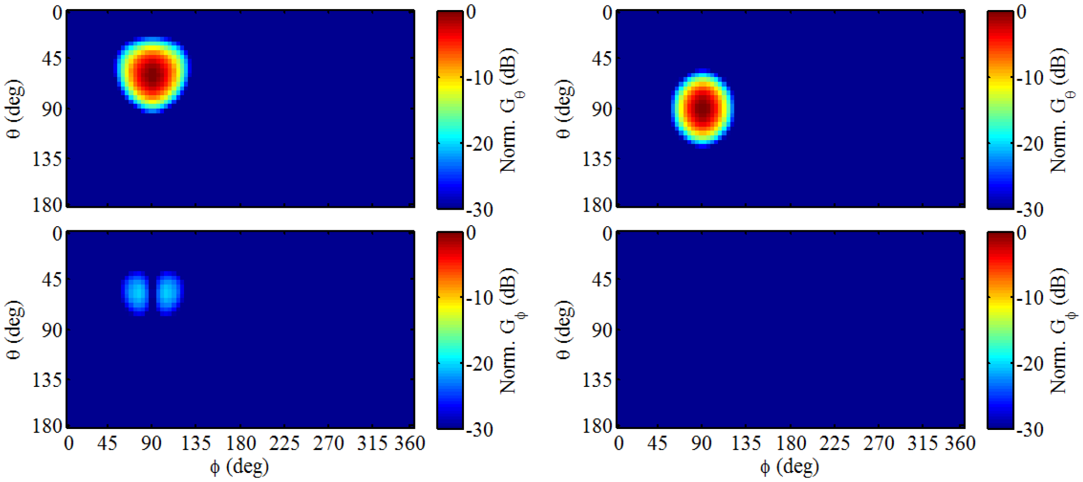

(c) $\phi = 90°, \theta = 60°$ (d) $\phi = 90°, \theta = 90°$

Figure 5.15: Polarimetric plots of the normalized desired pattern for different elevation scan angles.

In this case, the desired beam peak is located at $\phi = 90^\circ$ and $\theta = 60^\circ$. The conventional array ($2 \times 2 \times 2$) of patch antennas is capable of scanning the co-polarized component of the normalized radiation pattern G_θ to a maximum elevation angle of $\theta_{SCAN} = 28^\circ$ as shown in Fig. 5.16b. A grating lobe only 4.4 dB below the main lobe is also clearly visible located 180° away in azimuth with respect to the beam peak. This array also suffers from relatively high cross-polarization near the beam peak in comparison to the desired pattern. Fig. 5.16c demonstrates that scan performance improvement is possible using the proposed hybrid phased array ($2 \times 2 \times 3$) with both patch and monopole radiating modes. The maximum elevation scan angle has increased to $\theta_{SCAN} = 45^\circ$ while maintaining low sidelobe and cross-polarization levels. Perhaps not surprisingly so, the conventional patch antenna array ($3 \times 3 \times 2$) provides the best ability to synthesize the desired pattern, at least when looking at normalized data. However, this higher directivity and slightly wider scan range is due to oversampling the aperture with more closely spaced elements. In doing so, mutual coupling between patch antenna elements is much greater and will decrease the total efficiency and therefore scanned gain of the array.

5.6.2 Scan Performance

In this section, each of the three arrays will be compared in terms of four scan performance metrics. The first two parameters, peak gain G_T and the 3 dB elevation scan range θ_{3dB}, describe the ability of each array to accurately and efficiently synthesize an array pattern over a range of scan angles. The second set of parameters, sidelobe (SLL) and cross-polarization (E_ϕ/E_θ) levels, describe the ability of each array to spatially filter signals polarized parallel to the scan plane. Furthermore, all of these parameters are characterized in two scan planes defined by $\phi_{SCAN} = 0^\circ$ and $\phi_{SCAN} = 45^\circ$. The scan plane defined by $\phi_{SCAN} = 45^\circ$ is often called the D-plane as it is diagonal to the square lattice geometry of all three arrays. It should be noted that the $\phi_{SCAN} = 0^\circ$ and $\phi_{SCAN} = 90^\circ$

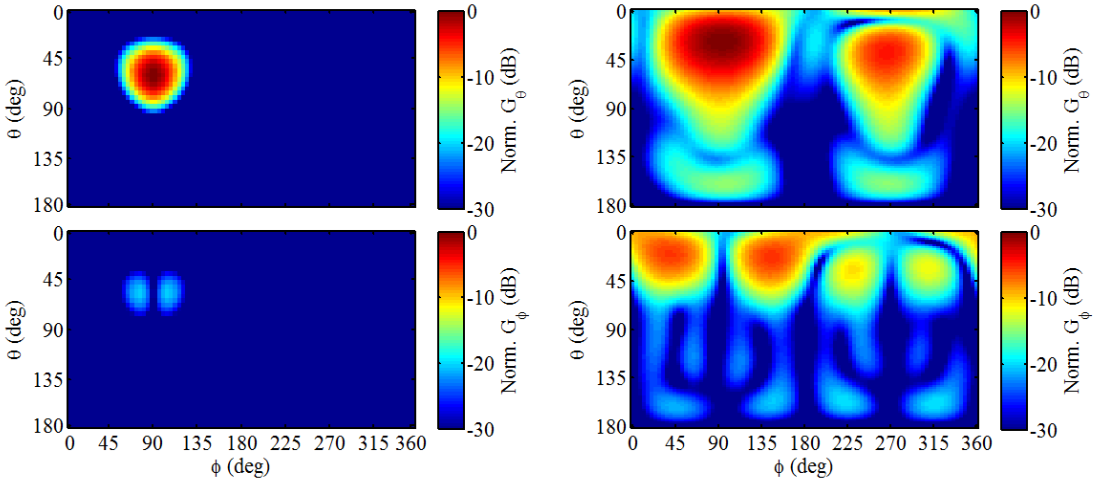

(a) Desired

(b) Conventional (2 × 2 × 2)

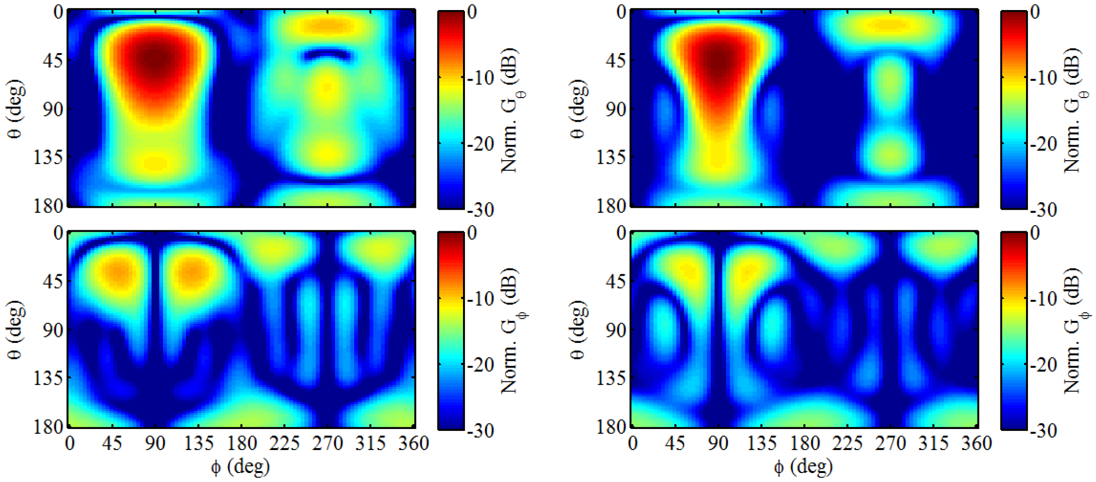

(c) Multiple mode (2 × 2 × 3)

(d) Conventional (3 × 3 × 2)

Figure 5.16: Polarimetric plots of the normalized desired pattern ($\phi = 90^\circ, \theta = 60^\circ$) and synthesized radiation patterns for the three candidate arrays.

scan plane performances are identical given the 90° rotational symmetry of the radiating elements and their feed points.

Both G_T and θ_{3dB} can be derived from the data plotted in Fig. 5.17. The simplest conventional array ($2 \times 2 \times 2$) has the least scan range in both scan planes although it maintains the highest scanned total efficiency of all three arrays. The lower total efficiency demonstrated by the hybrid phased array ($2 \times 2 \times 3$) is due to the coupling between the monopoles and adjacent patches and monopoles. It was discussed in section 5.3 that coupling between the monopole and the collocated patch was less than -20 dB due the radial currents induced on the patch which do not couple efficiently to the patch modes. The currents induced by the monopole on adjacent patch antennas are no longer radial with respect to the patch center and therefore couple more efficiently to the patch modes leading to reduced efficiency. Mutual coupling effects are even more detrimental for the conventional array ($3 \times 3 \times 2$). Although this array has the highest directivity over the widest scan range, the scanned gain of this array is the lowest of the three arrays. For all three arrays, the maximum scan range is improved in the $\phi_{SCAN} = 45^\circ$ diagonal to the array lattice.

Fig. 5.18 plots the sidelobe and cross-polarization levels for all three arrays under consideration. Although the simplest conventional patch array ($2 \times 2 \times 2$) shows the lowest initial SLL, it quickly rises with scan angle until reaching a maximum of -1.5 dB in the $\phi = 0^\circ$ plane and -6.7 dB in the $\phi = 45^\circ$ plane at the respective maximum scan angles. This is due to the fact that the sidelobe is actually a grating lobe for a 2 element array at half-wavelength spacing. In contrast, the oversampled conventional array ($3 \times 3 \times 2$) pushes this grating lobe out of the visible region and demonstrates the lowest SLL of all three arrays over its respective 3 dB scan range. Our proposed hybrid phased array ($2 \times 2 \times 3$) shows similarly low SLL since the omnidirectional monopole patterns are weighted in such a way to add constructively with the main lobe and destructively

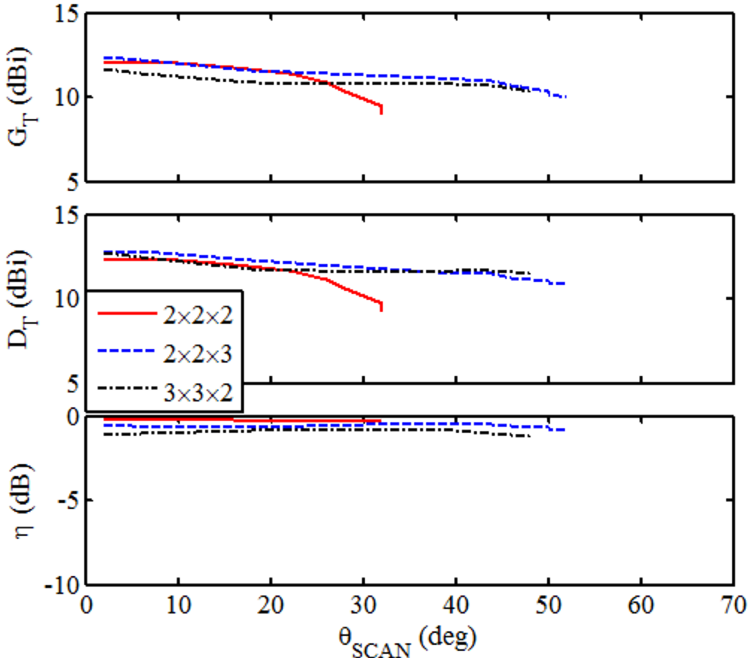

(a) $\phi_{SCAN} = 0°$ scan plane

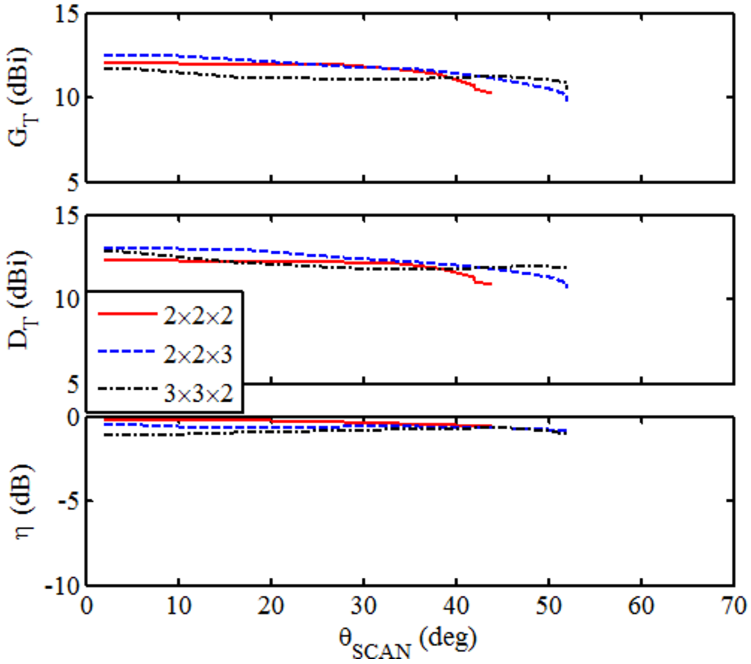

(b) $\phi_{SCAN} = 45°$ scan plane

Figure 5.17: Plots of the scanned peak gain (G_T), peak directivity (D_T) and total efficiency (η) for each array versus elevation scan angle (θ_{SCAN}).

Table 5.3: Summary of scan performance parameters for each of the three arrays.

(a) $\phi_{SCAN} = 0^\circ$ scan plane

Parameter	$(2 \times 2 \times 2)$	$(2 \times 2 \times 3)$	$(3 \times 3 \times 2)$	Unit
G_T	11.7	12.5	9.4	dBi
θ_{3dB}	32	50	37	deg
SLL_{max}	-1.5	-6.7	-10.5	dB
E_ϕ/E_θ	-19.4	-23.1	-23.1	dB

(b) $\phi_{SCAN} = 45^\circ$ scan plane

Parameter	$(2 \times 2 \times 2)$	$(2 \times 2 \times 3)$	$(3 \times 3 \times 2)$	Unit
G_T	11.7	12.5	9.4	dBi
θ_{3dB}	42	49	41	deg
SLL_{max}	-4.8	-9.6	-15.3	dB
E_ϕ/E_θ	-19.7	-24.1	-24.1	dB

with the grating lobe generated by the patches. All three arrays show reasonably low cross-polarization levels over their respective scan ranges although the hybrid $(2 \times 2 \times 3)$ and oversampled conventional $(3 \times 3 \times 2)$ arrays show superior performance.

A summary of the four scan performance parameters for all three arrays is presented in Table 5.3. Of the three arrays, the hybrid phased array $(2 \times 2 \times 3)$ shows the highest peak gain, widest 3 dB scan range, excellent polarization discrimination and reasonable sidelobe levels. This performance is not free and in fact comes at the cost of a 50% increase in number of feed points compared to the simplest conventional array $(2 \times 2 \times 2)$. However, the hybrid phased array requires 33% fewer feed points than the oversampled conventional array $(3 \times 3 \times 2)$. Additionally, the hybrid phased array is not planar and requires up to a quarter wave increase in height over the conventional patch arrays.

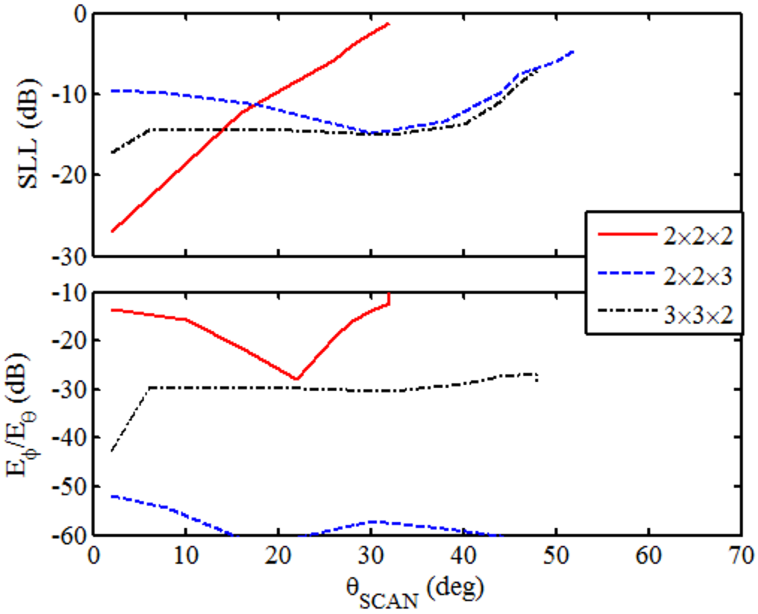

(a) $\phi_{SCAN} = 0°$ scan plane

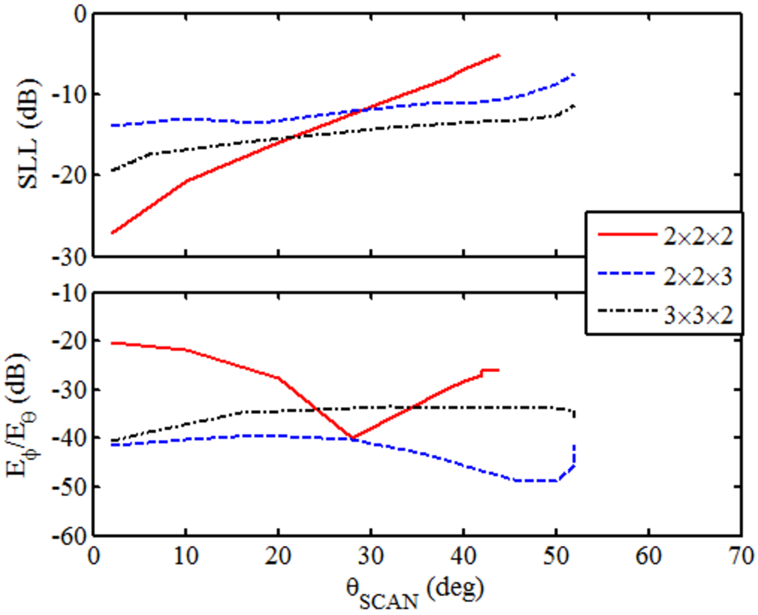

(b) $\phi_{SCAN} = 45°$ scan plane

Figure 5.18: Plots of the maximum side lobe level (SLL) and cross-polarization (E_ϕ/E_θ) for each array versus elevation scan angle (θ_{SCAN}).

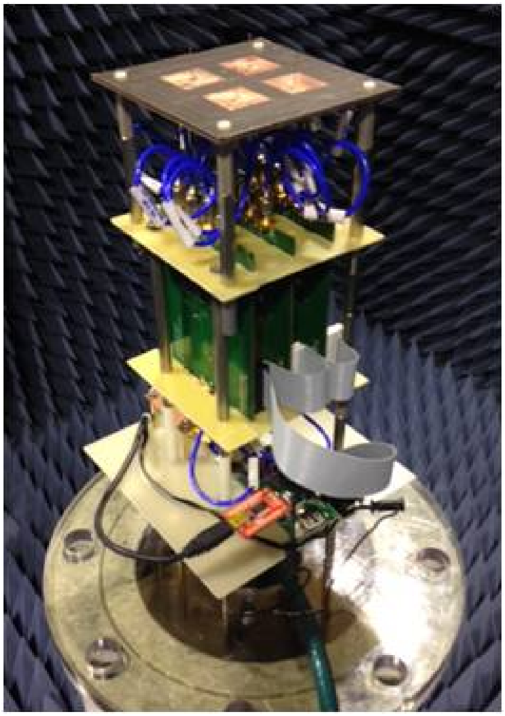

Figure 5.19: Fully fabricated multiple mode monopole on patch array $(2 \times 2 \times 3)$.

5.7 Fabrication and Measurement

A prototype of the hybrid phased array composed of monopole on patch antenna sub-arrays was fabricated as shown in Fig. 5.19. The system architecture is very similar to the one shown in Fig. 4.20 with the dipole array replaced by the monopole on patch array. In this prototype, only three active feeds boards were required to accommodate a total of 12 receive channels. We used the same method of GUI assisted serial control to set the states of the 24 programmable phase shifting and amplitude attenuation devices.

5.7.1 Feed Network

The monopole and patch antenna elements were connectorized on a lower 30 mil FR4 panel. This interface board shown in Fig. 5.20 contains 50 Ω grounded CPW transmission lines used to increase the spacing between the feed points of each sub-array

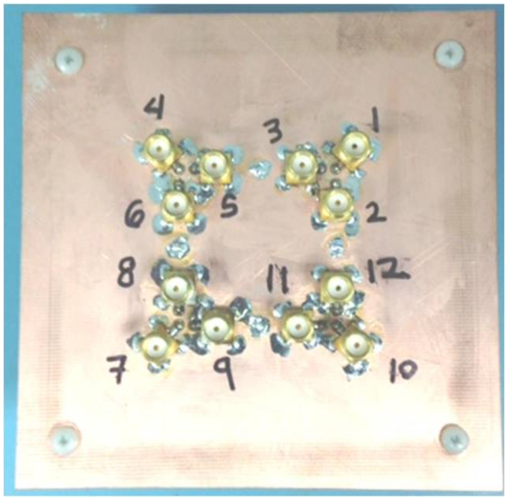

Figure 5.20: Connectorized passive interface board to the monopole on patch array ($2 \times 2 \times 3$).

in order to make room for the surface mount SMA connectors. The interface board was then connected to three of the active feed boards previously described in section 4.5.2 using length matched 6 inch coaxial cables. A four way Wilkinson power combiner combined the three active feed outputs. The fourth input of the Wilkinson combiner was terminated in a 50 Ω load.

5.7.2 Aperture

The hybrid phased array aperture shown in Fig. 5.19 was tested with the connectorized interface board to verify the scattering parameters. Fig. 5.22 plots the output reflection coefficients for one of the multiple mode sub-arrays (ports 1, 2 and 3). Given the 90° rotational symmetry of the array, the other sub-arrays can be expected to and were verified to have similar performance. There is slight detuning of the measured patch ports, S_{22} and S_{33}, with respect to the simulated data. This 35 MHz (8%) deviation in center frequency is likely due to manufacturing tolerances of the dielectric substrate material properties such as permittivity, loss tangent and physical dimension. There are a number of other likely sources of fabrication error including the unknown air

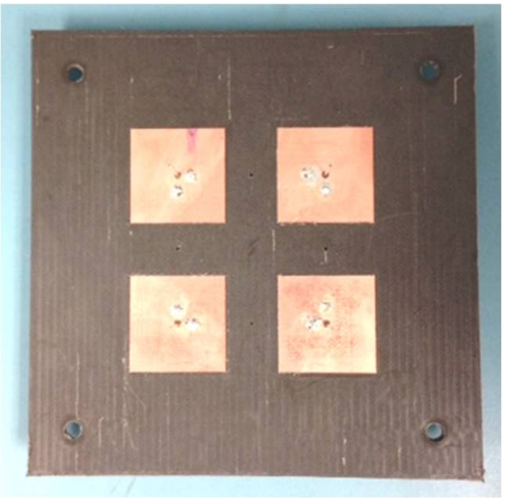

Figure 5.21: Monopole on patch hybrid phased array aperture ($2 \times 2 \times 3$).

gap between interface FR4 board and Rogers 5880 antenna substrate and milling error of the transmission line structures and patches. Although the monopoles are matched over the same bandwidth (4 to 5 GHz), there is some difference between the simulated and measured matching levels. The monopoles were cut by hand with a tolerance of approximately ±0.5 mm. Deviation in the actual monopole dimension can influence the matching level both through the properties of the monopole itself and its level of coupling to adjacent structures.

Coupling scattering parameters between unique pairs of antenna ports are plotted in Fig. 5.23. Only unique pairs of ports are considered given the 90° rotational symmetry of the array. Fig. 5.23a compares the simulated and measured coupling between unique pairs of ports that include the monopole port 1. Coupling between unique patch antenna port pairs including the patch port 3 are plotted in Fig. 5.23b. Both sets of scattering parameters demonstrate reasonable good agreement between the simulated and measured hybrid phased arrays. More importantly, the predictions from the element pair analysis in section 5.4 are visible in the data. For example, coupling between the monopole and collocated patch ports (S_{13}) is at a minimum at the patch resonance. In contrast, coupling

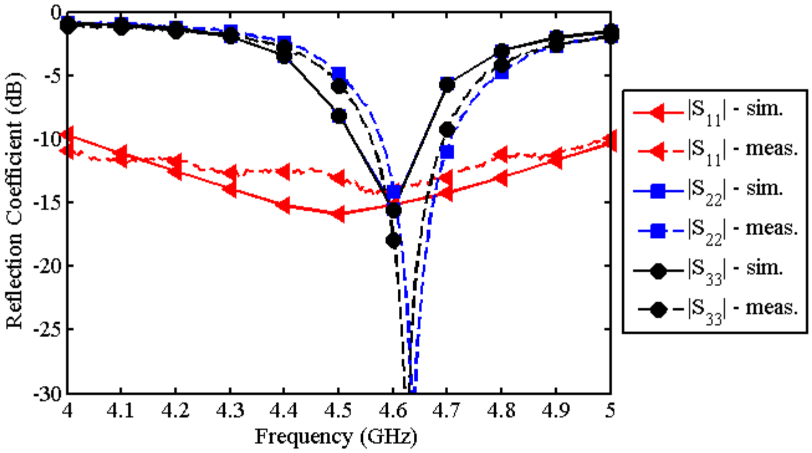

Figure 5.22: Element reflection coefficients for ports 1, 2 and 3.

between the monopole and the patch port located 0.5λ away (S_{15}) is maximized at the patch resonance. Also, co-polarized patch ports located 0.5λ away (S_{53} and $S_{11,3}$) exhibit maximum coupling at the patch resonance and have the largest coupling of the data shown in Fig. 5.23b. The interaction between monopoles (S_{14} and S_{17}) is an interesting exception to the element pair analysis. Both of these coupling coefficients are among the largest over the matching bandwidth of the monopoles. This illustrates the deficiency in the element pair analysis which does not consider the effects of mutual coupling on the radiation patterns. The effect of scattering from one monopole on the radiation pattern of the other is interdependent with the mutual impedance between them. In any case, the coupling coefficient between monopoles is less than -15 dB within the overlapping matching bandwidth of monopole and patch antennas.

5.7.3 Array Calibration

The array calibration procedure used is identical to the one presented in section 4.5.3. High level calibration tasks are reiterated here as a reminder and are as follows: (1) measure the 12 embedded element patterns, (2) compute the optimal element weights

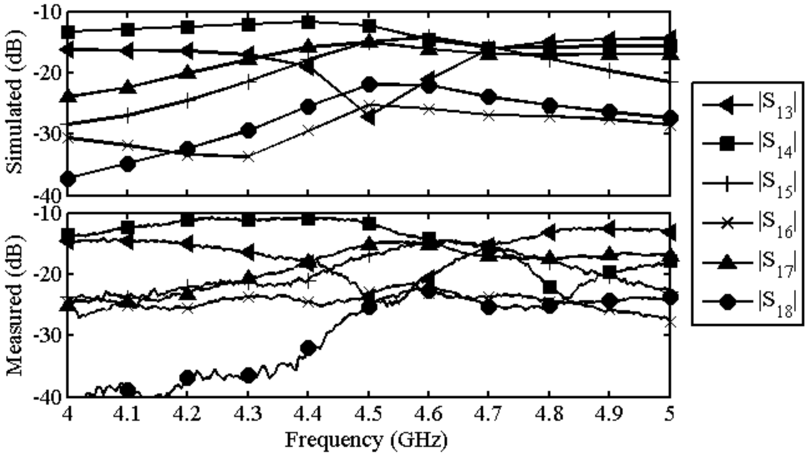

(a) Unique pairs of ports including monopole port 1.

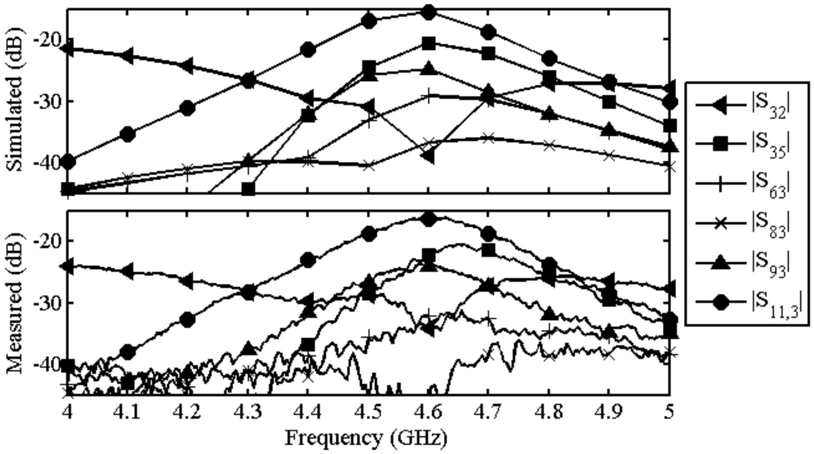

(b) Unique pairs of patch ports inlcuding port 3.

Figure 5.23: Plots of the unique measured and simulated coupling scattering parameters taking into account the 90° rotational symmetry of the array.

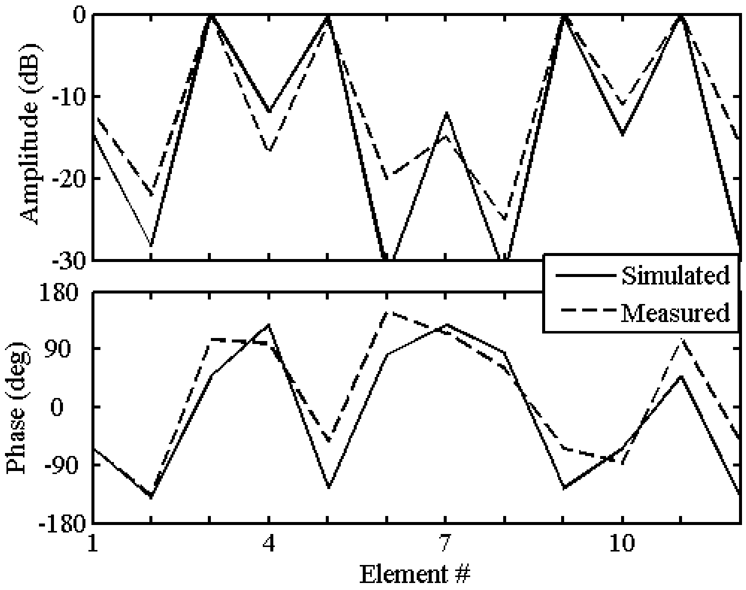

Figure 5.24: Amplitude and phase of the element weights for a broadside beam polarized in the ϕ = 0° plane.

needed to synthesize a desired beam, (3) apply the weights to the array and measure the resulting array radiation patterns and (4) compute the realized gain using the measured radiation patterns and the scattering parameters of the antennas and feed network. As an example, the element weights are plotted in Fig. 5.24 for the case of a desired broadside beam polarized in the ϕ = 0° plane. Element weights computed from either simulated or measured embedded element patterns show similar behavior. As expected, the 4 patch ports polarized in the ϕ = 0° plane (3, 5, 9 and 11) are the dominant contributors to the array radiation pattern. There is a 180° phase shift between the pairs of element weights (3,5) and (9,11) due to the physical 180° symmetry between these ports as seen in Fig. 5.20. The cross-polarized patch ports (2, 6, 8 and 12) contribute the least power. Due to the distortion of the monopole radiation patterns by scattering from adjacent monopoles, the patterns do not have a deep null in the broadside direction. Therefore, a small amount of power is also contributed from these ports (1, 4, 7 and 10).

Plots of the 3D array radiation patterns for four scan angles are shown in Fig.

5.25. The beam peak is shown scanning from broadside ($\theta_{SCAN} = 0^\circ$) to the widest scan angle of $\theta_{SCAN} = 50^\circ$ in two scan planes.

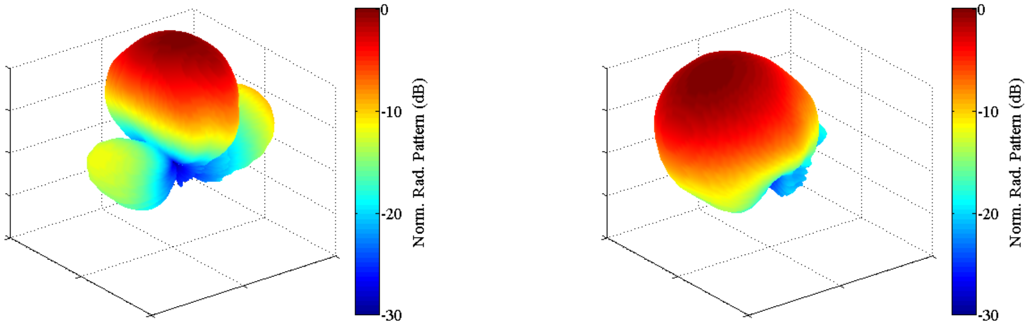

(a) ($\theta = 0^\circ$, $\phi = 0^\circ$)

(b) ($\theta = 40^\circ$, $\phi = 0^\circ$)

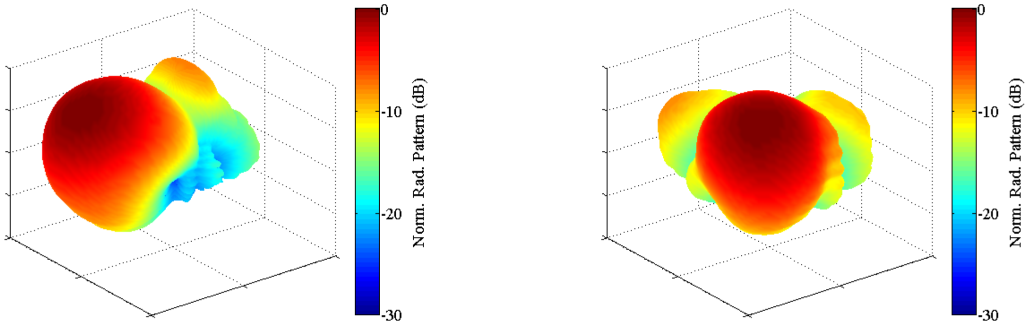

(c) ($\theta = 50^\circ$, $\phi = 0^\circ$)

(d) ($\theta = 50^\circ$, $\phi = 45^\circ$)

Figure 5.25: Plots of the measured 3D normalized radiation patterns for the hybrid phased array of monopole on patch antenna sub-arrays.

5.7.4 Scan Performance

After the completion of all calibration measurements, the data was processed in MATLAB to characterize the scan performance of the array over angle and frequency. Peak realized gain, peak directivity and total efficiency are plotted versus scan angle in Fig. 5.26. The array is clearly shown scanning to 50° in both scan planes with less than 3 dB of scan loss. The measured total efficiency is consistently less than simulated data most likely due to difference in the assumed and actual loss tangent of the substrate materials used. Peak realized gain, peak directivity and total efficiency of the array are plotted against frequency in Fig. 5.27. Within the overlapping matching bandwidth of the 12 antenna elements, there is reasonably good agreement between the measured and simulated data. In contrast to the simulated data, the measured data for both scan planes shows a reduction in the total efficiency and realized gain on either side of the peak. Interestingly, the measured directivity does not follow this trend and agrees with simulation quite well over the entire band. There may be higher order interactions in the feed network due to multiple reflections caused by the mismatch presented by the antenna outside its matching bandwidth. This would manifest itself as a frequency dependent variation consistent with the variation observed in the measured data.

5.8 Conclusions and Future Study

In this chapter, we discussed a synthesis method for 3D beam patterns using spherical harmonic coefficients. The relationship was derived between the spherical harmonic representation of the given set of element patterns and the desired array pattern. The monopole on patch multiple mode antenna element was introduced and characterized in terms of its null and beam steering capabilities. A pair wise analysis was used to predict the maximum gain and optimal impedance match of an array consisting of some combination of monopole and/or patch antenna pairs. Three different 2D scanning arrays consisting of these pairs were used to synthesize a desired beam pattern using the spherical harmonic synthesis method. The conventional patch antenna array ($2 \times 2 \times 2$), hybrid phased array ($2 \times 2 \times 3$) and conventional oversampled array ($3 \times 3 \times 2$) were compared on the basis of how well each was able to synthesize a desired beam with E_θ polarization. The desired Gaussian pulse beam was rotated along two scan planes in such

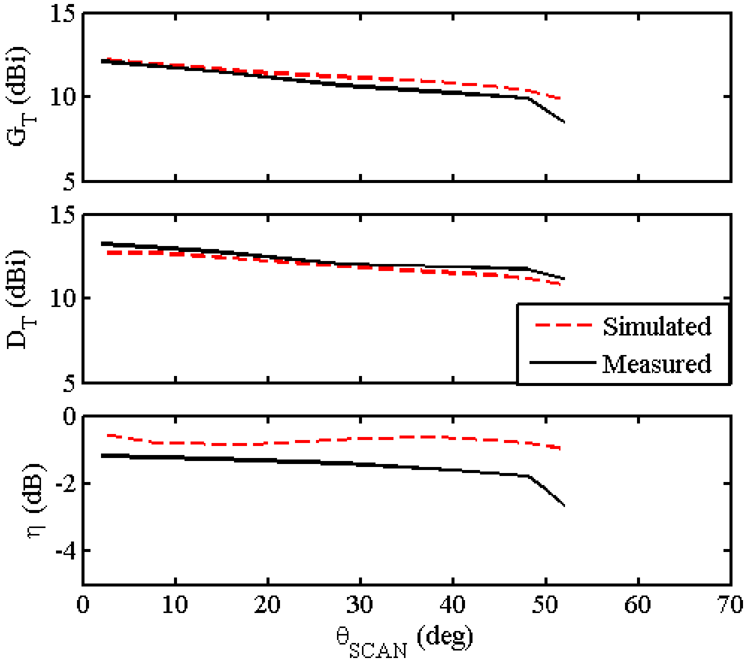

(a) $\phi_{SCAN} = 0°$ scan plane

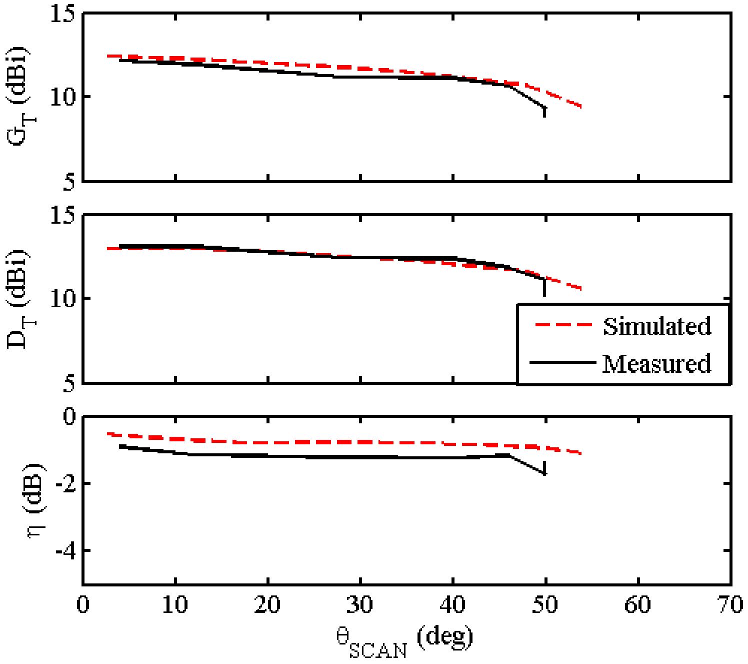

(b) $\phi_{SCAN} = 45°$ scan plane

Figure 5.26: Plots of the measured scanned peak gain (G_T), peak directivity (D_T) and total efficiency (η) versus scan angle for the hybrid phased array composed of monopole on patch antenna sub-arrays.

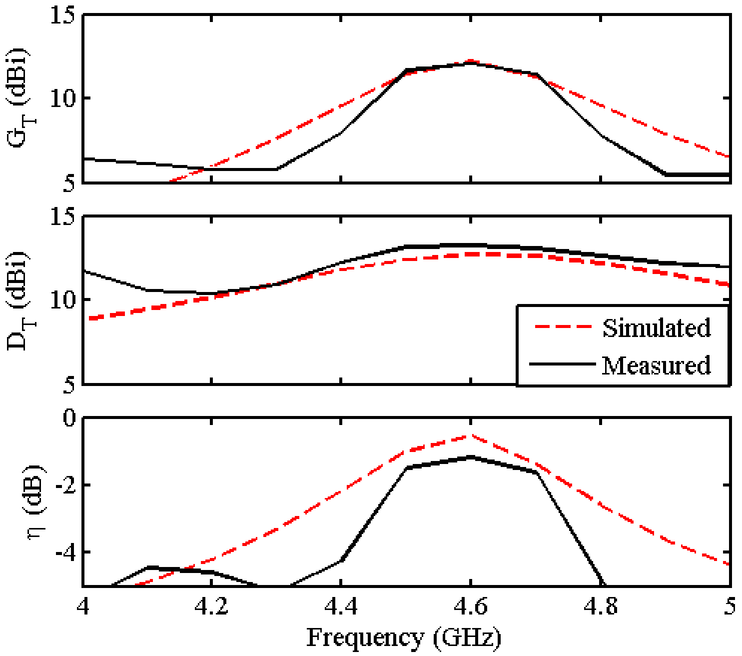

(a) $\phi_{SCAN} = 0°$ scan plane

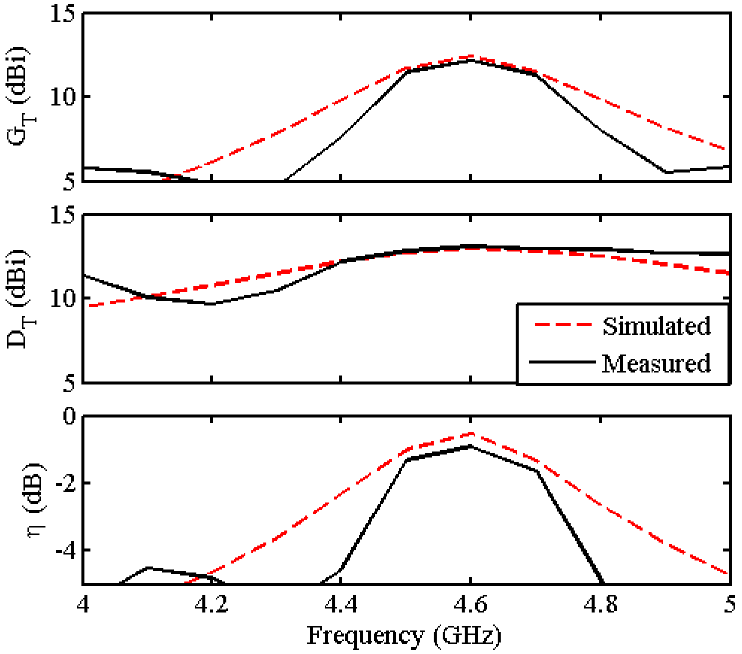

(b) $\phi_{SCAN} = 45°$ scan plane

Figure 5.27: Plots of the measured scanned peak gain (G_T), peak directivity (D_T) and total efficiency (η) versus frequency for the hybrid phased array composed of monopole on patch antenna sub-arrays.

a way as to preserve the beamwidth and polarization properties of the array. Four scan performance parameters were considered in which the hybrid phased array consisting of multiple mode sub-arrays demonstrated significant improvement over the conventional $(2 \times 2 \times 2)$ array. Finally, a prototype of the hybrid phased array was constructed and characterized. Measured data validated the improved scan range and efficiency predicted by the analysis and simulation of this novel array. Application of this multiple mode concept to more general 2D scanning arrays with wider bandwidth are topics of further research.

Acknowledgment

Chapter 5, in part, is currently being prepared for submission for publication of the material. Labadie, Nathan R.; Sharma, Satish K.; Rebeiz, Gabriel. The dissertation/thesis author was the primary investigator and author of this paper.

The work was carried out in part under the National Science Foundation (NSF)s CAREER grant ECCS-0845822.

Chapter 6

Conclusions and Future Study

We have presented several chapters detailing our original contribution to the field of antenna element design and array beam steering performance. We have made every effort to give proper context to our work and credit to our peers by citing directly and indirectly related research as available in the published literature. The concept of antenna apertures supporting multiple radiating modes is in itself not a novel concept. However, mention of the application of such apertures to the improvement of phased array beam steering in the literature is limited. To our knowledge, there are previously no examples of experimental protoypes. We were careful to distinguish the application of orthogonal modes formed at the aperture from those formed in a feed network (i.e. Butler matrix feed). Any improvement to phased array beam steering was presented with respect to a common baseline approach and in the context of other available methods. No claim was made that our approach is ”the best”, rather our philosophy is that the best approach must be selected based on the specific application at hand. In most examples of our work, we were able to fabricate and measure prototypes in addition to analysis and simulation in order to validate claimed benefits to our approach.

6.1 Summary of Work

We introduced a total of four novel antenna element designs in this dissertation. Three of these designs were capable of pattern reconfiguration using multiple radiating modes. In one case, conical beam peak and full hemispherical null steering were achieved while maintaining CP for a satellite receive application. The two remaining antenna designs were used as multiple mode sub-arrays implemented in a hybrid phased array. Scan performance improvement was shown both for a 1 dimensional scanning linear array and 2 dimensional scanning planar array with respect to reference conventional arrays. We provided extensive analysis to provide insight into the expected behavior for these novel antennas and arrays. However, the majority of the original work presented herein is in the design and implementation of these.

6.2 Future Work

It is an open question with respect to our work whether a multiple mode array can be designed to operate over a wide bandwidth. Key to answering this question is finding elements supporting higher order modes with significant bandwidth. The work presented in [35] indicates that the theory of characteristic modes can be used to design radiating element geometries and feed configurations that are optimized for pattern stability over wide bandwidths. We would like to use this approach to synthesize a set of optimized apertures from a given set of desired radiation mode patterns. Particular attention will also be given to the impact on increased implementation complexity required to realize benefits in performance using the multiple mode approach.

Appendix A

MATLAB Code

A.1 Fourier Synthesis

```
%%%%%%%%%%%%%%%%%%%%%%%%%%%%%%%%%%%%%%%%%%%%%%%%%%
% PURPOSE:
% This function uses a 1D radiation pattern cut to synthesize a
% desired beam pattern.
% ----------------------------------------------------------------
% INPUT PARAMETERS:
% 1. mode_pattern(m,t) = complex radiation pattern data for m
% elements in t directions (theta)
% 2. AF_desired(t)     = complex radiation pattern data to be
% synthesized in t directions
% 3. theta(t)          = array of elevation angles
% 4. M                 = the number of different element patterns
% used
% 5. N                 = the number of fourier coefficients used
% in the synthesis.
```

```
% ----------------------------------------------------------
% OUTPUT PARAMETERS:
% 1. Mm(m,2)           = two column matrix containg the magnitude
% (col 1) and phase (col 2) coefficients for M elements.
% 2. Am(m)             = array of complex coefficients for M
% elements.
% 3. AF_fourier(t)     = the synthesized complex radiation
% pattern.
%%%%%%%%%%%%%%%%%%%%%%%%%%%%%%%%%%%%%%%%%%%%%%%%

function [Mm, Am, AF_fourier] =...
    fourier_synth(mode_pattern, AF_desired, theta, d_off, M, N)

% CONSTANTS
rad2deg = 180/pi;
deg2rad = 1/rad2deg;
dtheta = theta(2)-theta(1);

% FOURIER ANALYSIS
for n = 1:N
    for m = 1:M
        % ELEMENT FOURIER COEFFICIENTS
        a(m,n) = 1/pi*sum(mode_pattern(m,:)...
            .*cos((n-1)*theta*deg2rad)...
            .*exp(1i*2*pi*d_off*cos(theta*deg2rad))...
            *dtheta*deg2rad);
        b(m,n) = 1/pi*sum(mode_pattern(m,:)...
            .*sin((n-1)*theta*deg2rad)...
            .*exp(1i*2*pi*d_off*cos(theta*deg2rad))...
           *dtheta*deg2rad);
```

```
    end
    % DESIRED PATTERN FOURIER COEFFICIENTS
    ap(n) = 1/pi*sum(AF_desired.*cos((n-1)*theta*deg2rad)...
        *dtheta*deg2rad);
    bp(n) = 1/pi*sum(AF_desired.*sin((n-1)*theta*deg2rad)...
        *dtheta*deg2rad);

end

ap(1) = ap(1)/2;
bp(1) = 0;
y = [ap bp];

a(:,1) = a(:,1)/2;
b(:,1) = 0;

% FOURIER SYNTHESIS: LEAST SQUARES FIT OF THE MODE COEFFICIENTS
Mab = [a b];
Am = conj(Mab'\y');
Mm = [abs(Am).^2/max(abs(Am).^2) round(angle(Am)*rad2deg)];

% BUILD MATRICES FROM COEFFICIENTS
n = 0:N-1;
[n theta_M] = meshgrid(n,theta);
[ap theta_M] = meshgrid(ap,theta);
[bp theta_M] = meshgrid(bp,theta);

% CONSTRUCT THE SYNTHESIZED PATTERN
AF_fourier = sum(ap.*cos(n.*theta_M*deg2rad)...
    + bp.*sin(n.*theta_M*deg2rad),2);
```

```
% OUTPUT COEFFICIENTS
[theta_M Am] = meshgrid(theta, Am);
```

A.2 1D Beamforming Example

```
%%%%%%%%%%%%%%%%%%%%%%%%%%%%%%%%%%
% PURPOSE:
% This code computes the 2D and 3D radiation patterns for hybrid
% phased arrays at a particular scan angle.
% ----------------------------------------------------------
% IMPORTANT PARAMETERS:
% 1. Ne = [] array of number of elements in the sub-array
% 2. Na = [] array number of sub-arrays in the hybrid array
% 3. M = total number of array element (M = Ne(i1)*Na(i1))
% 4. theta = 2D elevation angle array
% 5. T and P = 3D theta and phi matrices for 3D patterns only
% 4. see other "simulation parameters" and "array parameters"
% below
% 5. mm_mode_pattern(M,theta) = the 2D complex radiation pattern
% for each of M elements
% 6. mm_mode_pattern_3d(M,T,P) = the 3D complex radiation pattern
% for each of M elements
% 7. AF_desired(theta) = the desired radiation pattern, can be
% either a  pulse or sinc() function
% 8. Am_mm(i1,m) = the complex coefficients generated for all M
% elements and for each choice of Ne and Na
% 9. AF_mm(M,theta) = the complex synthesized radiation pattern
% over angle theta for each choice of Ne and Na
% 10. MSE_mm_curve(i1,theta) = the RMS error between the
% synthesized radiation pattern and the desired pattern
%%%%%%%%%%%%%%%%%%%%%%%%%%%%%%%%%%


clc;
```

```
clear all;
close all;

%%%%%%%%%%%%%%%%%%%%%%%%%%%%%%%%%%
%   SETUP FIGURE PARAMETERS
%%%%%%%%%%%%%%%%%%%%%%%%%%%%%%%%%%
fontsize        = 14;
linewidth       = 2;
markersize      = 8;
linecolor       = [[1,0,0];[0,0,1];[0,0,0];...
    [1,0.5,0];[0.5 0 1];[1,0,0];...
    [0,0,1];[0,0,0];[1,0.5,0];...
    [0.5 0 1];[1,0,0];[0,0,1];...
    [0,0,0];[1,0.5,0];[0.5 0 1];...
    [1,0,0];[0,0,1];[0,0,0];...
    [1,0.5,0];[0.5 0 1]];
markercolor     = linecolor;
markersize      = 10;
linestyle       = [' -' '--' '-.'...
    ' :' ' -' '--'...
    '-.' ' :' ' -'...
    '--' '-.' ' :'];
markershape     = ['s' 'o' '<'...
    '+' 'x' 's'...
    'o' '<' '+'...
    'x' 's' 'o'...
    '<' '+' 'x'];
markerspace     = 10;

fig_w           = 560;
fig_h           = 237;
```

```
%%%%%%%%%%%%%%%%%%%%%%%%%%%%%%%%%%%%%%%%%%%
% CONSTANTS
%%%%%%%%%%%%%%%%%%%%%%%%%%%%%%%%%%%%%%%%%%%
rad2deg = 180/pi;
deg2rad = 1/rad2deg;

%%%%%%%%%%%%%%%%%%%%%%%%%%%%%%%%%%%%%%%%%%%
% SIMULATION PARAMETERS
%%%%%%%%%%%%%%%%%%%%%%%%%%%%%%%%%%%%%%%%%%%
k                = 2*pi; % wave number
N                = 128; % number of fourier expansion modes
ts               = 45; % scan angle

beam_type        = 0; % 0 = sinc function, 1 = pulse function
beam_width_deg   = 1; % width of desired beam (for pulse only)
sll_depth        = -1000; % depth of sidelobes (for pulse only)

theta            = -89:1:89; % theta array for 2D patterns
p                = 0:2:360; % phi array for 3D patterns
t                = 0:0.5:86; % theta array for 3D patterns
[P T]            = meshgrid(p, t); % phi, theta matrices for 3D
                                               % arrays

%%%%%%%%%%%%%%%%%%%%%%%%%%%%%%%%%%%%%%%%%%%
% ARRAY PARAMETERS
%%%%%%%%%%%%%%%%%%%%%%%%%%%%%%%%%%%%%%%%%%%
Ne      = [1 2 4 8 16]; % number of sub-array elements
Na      = [16 8 4 2 1]; % number of sub-arrays
Mi      = Na.*Ne; % total number of elements
Nd      = 16; % number of conventional dipole elements
```

```
d_cv     = 0.5; % conventional array element spacing
d_d      = 0.5; % desired array pattern element spacing
d_eps    = 0.475; % equivalent multiple mode dipole spacing
h        = 0.1; % z-distance between multiple mode dipoles

%%%%%%%%%%%%%%%%%%%%%%%%%%%%%%%%%%%%%%%%%%%%%%%%%%%%%%%%%
% MAIN LOOP
%%%%%%%%%%%%%%%%%%%%%%%%%%%%%%%%%%%%%%%%%%%%%%%%%%%%%%%%%
for i1 = 1:length(Mi);
    display([num2str(Ne(i1)) 'X' num2str(Na(i1)) ' array\n'])

    M = Mi(i1); % number of multimodes
    d_mm = Ne(i1)*d_cv; % spacing between sub-arrays
    theta_scan = ts;
    dtheta = theta(2) - theta(1);
    theta_scan_diff = abs(theta - theta_scan);
    theta_scan_ind = find(theta_scan_diff ==...
                    min(theta_scan_diff));

    %%%%%%%%%%%%%%%%%%%%%%%%%%%%%%%%%%%%
    % COMPUTE MULTIPLE MODE PATTERNS
    %%%%%%%%%%%%%%%%%%%%%%%%%%%%%%%%%%%%
    % 2D PATTERNS
    % COMPUTE Y-DIRECTED LAMBDA/2 DIPOLE ELEMENT PATTERN
    psi_z = k*h/2*cos(theta*deg2rad);
    FD = (cos(2*pi*d_eps/2*cos(theta*deg2rad+pi/2))...
    -cos(2*pi*d_eps/2))./sin(theta*deg2rad+pi/2);
    nan_ind = find(isinf(FD));
    FD(nan_ind) = 0;
    mm_mode_pattern = zeros(M,length(theta));
```

```
% COMPUTE ALL MULTIPLE MODE DIPOLE ELEMENT PATTERNS
c = 1;
for q = 1:Na(i1)
    for m = 1:Ne(i1)
        mm_mode_pattern(c,:) = zeros(1,length(theta));
        if m > 1
            for r = 1:m
                mm_mode_pattern(c,:) = mm_mode_pattern(c,:)...
                    + (-1)^(r+1).*exp(1i*((m-(2*r-1))...
                    *(k*d_eps/2*sin(theta*deg2rad))))...
                    .*FD.*exp(1i*(m-1)*psi_z);
            end
        else
            mm_mode_pattern(c,:) = FD.*exp(1i*(m-1)*psi_z);
        end
        mm_mode_pattern(c,:) = exp(1i*(q - ((Na(i1)+1)/2))...
            *(k*d_mm*sin(theta*deg2rad)).*...
            mm_mode_pattern(c,:);
        mm_mode_pattern(c,:) = mm_mode_pattern(c,:)...
            /max(abs(mm_mode_pattern(c,:)));
        c = c + 1;
    end
end

%%%%%%%%%%%%%%%%%%%%%%%%%%%%%%%%%%%%%%%%%%%%%%%%%
% CREATE 3D PATTERNS
%%%%%%%%%%%%%%%%%%%%%%%%%%%%%%%%%%%%%%%%%%%%%%%%%
% COMPUTE Y-DIRECTED LAMBDA/2 DIPOLE ELEMENT PATTERN
psi_z_3d = k*h/2*cos(T*deg2rad);
FD_3d = (cos(2*pi*d_eps/2*cos(T*deg2rad+pi/2))...
```

```
        -cos(2*pi*d_eps/2))./sin(T*deg2rad+pi/2);
    nan_ind = find(isinf(FD_3d));
    FD_3d(nan_ind) = 0;
    mm_mode_pattern_3d = zeros(M,length(t),length(p));

    % COMPUTE ALL MULTIPLE MODE DIPOLE ELEMENT PATTERNS
    c = 1;
    for q = 1:Na(i1)
        for m = 1:Ne(i1)
            if M > 1
                for r = 1:m
                    mm_mode_pattern_3d(c,:,:) =...
                        mm_mode_pattern_3d(c,:,:)...
                        + reshape((-1)^(r+1).*...
                        exp(1i*((m-(2*r-1))...
                        .*(k*d_eps/2*sin(T*deg2rad).*...
                        cos(P*deg2rad)))).*FD_3d.*...
                        exp(1i*(m-1)*psi_z_3d),...
                        [1,length(t), length(p)]);%;
                end
            else
                mm_mode_pattern_3d(c,:,:) =...
             FD_3d.*exp(1i*(m-1)*psi_z_3d);
            end
            mm_mode_pattern_3d(c,:,:) =...
                reshape(exp(1i*(q - ((Na(i1)+1)/2)).*k*d_mm...
                *sin(T*deg2rad).*cos(P*deg2rad)),...
                [1,length(t), length(p)]).*,...
                mm_mode_pattern_3d(c,:,:);
            mm_mode_pattern_3d(c,:,:) =...
                reshape(mm_mode_pattern_3d(c,:,:),size(T));
```

```
        mm_mode_pattern_3d(c,:,:) =...
            mm_mode_pattern_3d(c,:,:)...
            /max(max(abs(mm_mode_pattern_3d(c,:,:))));
        c = c + 1;

    end
end

%%%%%%%%%%%%%%%%%%%%%%%%%%%%%%%
% GENERATE DESIRED PATTERN
%%%%%%%%%%%%%%%%%%%%%%%%%%%%%%%
if beam_type == 0
    % SINC FUNCTION
    psi_d = k*d_d*sin(theta*deg2rad)...
        - k*d_d*sin(theta_scan*deg2rad);
    AF_desired = 1/Nd*sin(Nd/2*psi_d)./sin(1/2*psi_d).*FD;
    AF_ind = find(isnan(AF_desired));
    if AF_ind > 1 & AF_ind < length(AF_desired)
        AF_desired(AF_ind) =...
            (AF_desired(AF_ind-1)+AF_desired(AF_ind+1))/2;
    elseif AF_ind == 1
        AF_desired(AF_ind) = AF_desired(AF_ind+1)
    elseif AF_ind == length(AF_desired)
        AF_desired(AF_ind) = AF_desired(AF_ind-1)
    end
    AF_desired = AF_desired/max(abs(AF_desired));
else
    % PULSE FUNCTION
    AF_desired = ones(size(theta))*10^(sll_depth/20);
    beam_width = round(beam_width_deg/dtheta);
    theta_diff = abs(theta_scan - theta); % main lobe
```

```
        theta_ind = find(theta_diff == min(theta_diff));
        AF_desired = circshift(AF_desired, [0, theta_ind]);

        n2 = theta_ind;
        n1 = round(n2 - beam_width/2);
        n3 = theta_ind;
        n4 = round(n3 + beam_width/2);

        if n1< 1
            n1 = n1 + length(theta);
            n2 = length(theta);
            n3 = 1;
        end
        if n4 > length(theta)
            n2 = length(theta);
            n3 = 1;
            n4 = n4 - length(theta);
        end

        AF_desired(n1:n2) = 1;
        AF_desired(n3:n4) = 1;
    end

    %%%%%%%%%%%%%%%%%%%%%%%%%%%
    %   FOURIER SYNTHESIS:
    %   COMPUTE REQUIRED COMPLEX COEFFICIENTS
    %%%%%%%%%%%%%%%%%%%%%%%%%%%
    % MULTIPLE MODE ARRAY
    [Mm_mm, Am_mm, AF_fourier] =...
        fourier_synth(mm_mode_pattern, AF_desired, theta,...
         0, M, N);
```

```
    AF_mm(i1,:) = sum(Am_mm.*mm_mode_pattern);

    % COMPUTE RMS ERROR
    MSE_mm_curve(i1,:) = ...
        (abs(AF_desired).^2 - abs(AF_mm(i1,:)).^2)./...
        abs(AF_desired);
    AF_mm_max = max(abs(AF_mm(i1,:)));
    max_ind = find(abs(AF_mm(i1,:)) == AF_mm_max);
    T_max(i1) = theta(max_ind);

    % COMPUTE THE 3D PATTERN AND DIRECTIVITY
    array_pattern = zeros(size(T));
    for c = 1:M
        array_pattern = reshape(Am_mm(c,1)...
            .*mm_mode_pattern_3d(c,:,:),size(T)) + array_pattern;
    end
    array_pattern = array_pattern./(max(max(abs(array_pattern))));
    max_ind = find(array_pattern == max(max(array_pattern)));
    T_max(i1) = T(max_ind(1));
    P_max(i1) = P(max_ind(1));
    D(i1) = pattern_directivity(abs(array_pattern), P, T);

    %%%%%%%%%%%%%%%%%%%%%%%%%%%%
    % PLOT NORMALIZED PATTERNS
    %%%%%%%%%%%%%%%%%%%%%%%%%%%%

    if length(Mi) >1
        figure(10)
        if i1 ≤ 1
            subplot(2,1,1)
            plot(theta, 20*log10(abs(AF_desired(i1,:)))',...
```

```
                'linestyle', linestyle((2*i1-1):(2*i1)),...
                'color', linecolor(i1,:),'linewidth',linewidth)
            hold on;
            ylabel('Norm. Rad. Pattern (dB)','fontsize',...
                fontsize,'fontname','times');
            set(gca,'fontsize',fontsize,'fontname','times',...
                'linewidth',linewidth, 'xticklabel','')
            axis([-90 90 -30 0])
        end
        subplot(2,1,1)
        plot(theta, 20*log10(abs(AF_mm(i1,:)))'...
            - 20*log10(max(abs(AF_mm(i1,:)))),...
            linestyle((2*i1+1):(2*i1+2)), 'color',...
            linecolor(i1+1,:),'linewidth',linewidth)
        hold on;
        ylabel('Norm. Rad. Pattern (dB)','fontsize',...
            fontsize,'fontname','times');
        set(gca,'fontsize',fontsize,'fontname','times',...
            'linewidth',linewidth, 'xticklabel','')
        axis([-90 90 -40 0])
        subplot(2,1,2)
        plot(repmat(theta,[length(Mi),1])',...
            10*log10(MSE_mm_curve(i1,:))',...
            linestyle((2*i1+1):(2*i1+2)), 'color',...
            linecolor(i1+1,:),'linewidth',linewidth)
        hold on;
        xlabel('Elevation (deg)','fontsize',...
            fontsize,'fontname','times');
        ylabel('Error (dB)','fontsize',fontsize,...
            'fontname','times');
        set(gca,'fontsize',fontsize,'fontname',...
```

```
            'times','linewidth',linewidth)
        axis([-90 90 -40 10])
    end
end


figure(10)
if length(Mi) > 1
    legend(['Desired (' num2str(Nd) ' feeds)'],...
        [num2str(Mi(1)) ' modes'],[num2str(Mi(2)) ' modes'],...
        [num2str(Mi(3)) ' modes'])
end
```

A.3 Spherical Harmonic Synthesis

```
function [AF_sph_x AF_sph_y AF_sph_z...
    AF_mm_x AF_mm_y AF_mm_z] =...
    spherical_synth(T, P, L, N_modes,...
    mm_mode_pattern, AF_desired)

%%%%%%%%%%%%%%%%%%%%%%%%%%%%%%%%%%%%%%%%%%%%%%%%%%
% SETUP COORDINATE SYSTEM
%%%%%%%%%%%%%%%%%%%%%%%%%%%%%%%%%%%%%%%%%%%%%%%%%%
deg2rad      = pi/180;
rad2deg      = 1/deg2rad;

T_pol        = T;
P_pol        = P;

theta        = T_pol(:,1);
phi          = P_pol(1,:);
dphi         = P(1,2) - P(1,1);
dtheta       = T(2,1) - T(1,1);

%%%%%%%%%%%%%%%%%%%%%%%%%%%%%%%%%%%%%%%%%%%%%%%%%%
% PRECOMPUTE SPHERICAL HARMONICS
%%%%%%%%%%%%%%%%%%%%%%%%%%%%%%%%%%%%%%%%%%%%%%%%%%
B = zeros(L^2+2*L+1, length(T_pol(:)));
for l = 0:L-1
    for m = -l:l
        if m<0
            Yml = shlib_Yml(l, abs(m),...
                T_pol(:), P_pol(:));
```

```
            Yml = (-1)^m*conj(Yml);
        else
            Yml = shlib_Yml(l, m,...
                T_pol(:), P_pol(:));
        end
        indx = l^2 + l + m+1;
        B(indx,:) = Yml;
    end
end


%%%%%%%%%%%%%%%%%%%%%%%%%%%%%%%%%%%%%%%%%%%%%%%%%%
% COMPUTE SPHERICAL HARMONIC ANALYSIS
%%%%%%%%%%%%%%%%%%%%%%%%%%%%%%%%%%%%%%%%%%%%%%%%%%
%% SPHERICAL HARMONIC COEFFICIENTS
%% integrate over the mm_mode_patterns to compute
%% the cofficients
%%%%%%%%%%%%%%%%%%%%%%%%%%%%%%%%%%%%%%%%%%%%%%%%%%
for d = 1:indx
    for n = 1:N_modes
        % compute multimode SPH coefficients
        a_mm_x(n,d) = sum(sum(reshape(...
            mm_mode_pattern(n,1:length(theta),:),...
            size(T_pol)).*conj(reshape((B(d,:)),...
            size(T_pol))).*sin(T_pol)*dphi...
            *dtheta*deg2rad^2));
        % compute multimode SPH coefficients
        a_mm_y(n,d) = sum(sum(reshape(...
            mm_mode_pattern(n,length(theta) +...
            1:2*length(theta),:),size(T_pol))...
            .*conj(reshape((B(d,:)),size(T_pol)))...
```

```
            .*sin(T_pol)*dphi*dtheta*deg2rad^2));
        % compute multimode SPH coefficients
        a_mm_z(n,d) = sum(sum(reshape(...
            mm_mode_pattern(n,2*length(theta) +...
            1:3*length(theta),:),size(T_pol))...
            .*conj(reshape((B(d,:)),size(T_pol)))...
            .*sin(T_pol)*dphi*dtheta*deg2rad^2));
    end
    % compute desired pattern SPH coefficients
    a_ds_x(d) = sum(sum(AF_desired(1:length(theta),:)...
        .*conj(reshape((B(d,:)),size(T_pol)))...
        .*sin(T_pol)*dphi*dtheta*deg2rad^2));
    % compute desired pattern SPH coefficients
    a_ds_y(d) = sum(sum(AF_desired(length(theta) +...
        1:2*length(theta),:).*conj(reshape((B(d,:)),...
        size(T_pol))).*sin(T_pol)*dphi*dtheta*deg2rad^2));
    % compute desired pattern SPH coefficients
    a_ds_z(d) = sum(sum(AF_desired(2*length(theta) +...
        1:3*length(theta),:).*conj(reshape((B(d,:)),...
        size(T_pol))).*sin(T_pol)*dphi*dtheta*deg2rad^2));
end

%%%%%%%%%%%%%%%%%%%%%%%%%%%%%%%%%%%%%%%%%%%%%%%%%%
% COMPUTE SPHERICAL HARMONIC SYNTHESIS
%%%%%%%%%%%%%%%%%%%%%%%%%%%%%%%%%%%%%%%%%%%%%%%%%%
%% Least Squares fit of the mode coefficents
Mab     = [a_mm_x a_mm_y a_mm_z];
y       = [a_ds_x a_ds_y a_ds_z];
Am_mm_x   = conj(Mab'\y');

AF_sph_x = zeros(size(T));
```

```
AF_sph_y = zeros(size(T));
AF_sph_z = zeros(size(T));
AF_mm_x = zeros(size(T));
AF_mm_y = zeros(size(T));
AF_mm_z = zeros(size(T));


for n = 1:N_modes

    element_pattern_x = reshape(mm_mode_pattern...
        (n,1:length(theta),:),size(T));
    element_pattern_y = reshape(mm_mode_pattern...
        (n,length(theta)+1:2*length(theta),:),size(T));
    element_pattern_z = reshape(mm_mode_pattern...
        (n,2*length(theta)+1:3*length(theta),:),size(T));

    [E_t E_p E_r] = xyz2tpr(T, P, element_pattern_x,...
        element_pattern_y, element_pattern_z);

    % reconstruct the multiple mode patterns from SPH
    AF_mm_x = AF_mm_x + (Am_mm_x(n))...
        *element_pattern_x;
    AF_mm_y = AF_mm_y + (Am_mm_x(n))...
        *element_pattern_y;
    AF_mm_z = AF_mm_z + (Am_mm_x(n))...
        *element_pattern_z;

end

% reconstruct the desired array pattern from SPH
for d = 1:indx
```

```
    AF_sph_x = AF_sph_x + a_ds_x(d)...
        *reshape(B(d,:),size(T));
    AF_sph_y = AF_sph_y + a_ds_y(d)...
        *reshape(B(d,:),size(T));
    AF_sph_z = AF_sph_z + a_ds_z(d)...
        *reshape(B(d,:),size(T));
end
```

A.4 2D Beamforming Example

```
%%%%%%%%%%%%%%%%%%%%%%%%%%%%%%%%%%%%%%%%%%%%%%%%%%%%%%%%%%%%%%%%%%
%   PURPOSE:
%   This code uses Spherical Harmonic basis functions to analyze
%   element radiation patterns and synthesize desired array
%   radiation patterns.
%   -------------------------------------------------------------
%   USER DEFINED PARAMETERS:
%     Nx           = number of elements in x-direction
%     Ny           = number of elements in y-direction
%     dx           = interelement spacing in x-direction
%                    in wavelengths
%     dy           = interelement spacing in y-direction
%                    in wavelengths
%     N_mm         = number of unique multiple modes
%     L            = number of spherical harmonic modes
%     el_type      = element pattern type
%     theta_scan   = theta scan angle [ts(1), ts(2), ..., ts(n)]
%     phi_scan     = phi scan angle  [ps(1), ps(2), ..., ps(n)]
%     beam_bw      = beam width properties [tbw(1), pbw(1), ...
%                                           tbw(2), pbw(2), ...
%                                           tbw(n), pbw(n)]
%
%   IMPORTANT VARIABLES
%     T = matrix of theta angles
%     P = matrix of phi angles
%     AF_desired     = matrix containing desired complex array
%     pattern, size = size(T).
%
```

```
%     mm_mode_pattern = matrices containing desired complex
%     element patterns, size = N_mmXsize(T)
%
%     [AF_sph_x AF_sph_y AF_sph_z] = matrices containing
%     Cartesian complex desired pattern reconstructed from
%     spherical harmonic coefficients,
%     size = [size(T), size(T), size(T)]
%
%     [AF_mm_x AF_mm_y AF_mm_z] = matrices containing
%     Cartesian complex desired pattern reconstructed
%     from mm_mode_pattern element patterns,
%     size = [size(T), size(T), size(T)]
%
%   DEPENDENT FUNCTIONS
%     % load desired array pattern
%     load_desired_planar_pattern(beam_bw, beam_pos, T, P)
%
%     % load element pattern
%     load_element_pattern_rev2(el_type, N_modes,...
%           T, P, Nx, Ny, dx, dy, N_mm);
%
%     % perform spherical decomposition and synthesis
%     spherical_synth(T, P, L, N_modes,...
%            mm_mode_pattern, AF_desired);
%
%     % convert Cartesian matrices to spherical
%     xyz2tpr(T, P, AF_mm_x, AF_mm_y, AF_mm_z);
%
%     % compute directivity of radiation pattern
%     pattern_directivity(20*log10(abs(AF_mm)),P,T)
%
```

```
%
%%%%%%%%%%%%%%%%%%%%%%%%%%%%%%%%%%%%%%%%%%%%%%%%%%%%%%%%%%%%%%

clc;
clear all;
close all;

%%%%%%%%%%%%%%%%%%%%%%%%%%%%%%%%%%%%%%%%%%%%%%%%%%%%%%%%%%%%%%
%   PLOT PARAMETERS
%%%%%%%%%%%%%%%%%%%%%%%%%%%%%%%%%%%%%%%%%%%%%%%%%%%%%%%%%%%%%%
fontsize    = 14;
linewidth   = 2;

%%%%%%%%%%%%%%%%%%%%%%%%%%%%%%%%%%%%%%%%%%%%%%%%%%%%%%%%%%%%%%
%   CONSTANTS
%%%%%%%%%%%%%%%%%%%%%%%%%%%%%%%%%%%%%%%%%%%%%%%%%%%%%%%%%%%%%%
rad2deg     = 180/pi;
deg2rad     = 1/rad2deg;
k           = 2*pi;

%%%%%%%%%%%%%%%%%%%%%%%%%%%%%%%%%%%%%%%%%%%%%%%%%%%%%%%%%%%%%%
%   USER DEFINED PARAMETERS
%%%%%%%%%%%%%%%%%%%%%%%%%%%%%%%%%%%%%%%%%%%%%%%%%%%%%%%%%%%%%%
Nx          = 2; % number of elements in x-direction
Ny          = 2; % number of elements in y-direction
dx          = 0.5; % interelement spacing in x-direction in
                   % wavelengths
dy          = 0.5; % interelement spacing in y-direction in
                   % wavelengths
N_mm        = 3; % number of unique multiple modes
L           = 30; % number of spherical harmonic modes
```

```
el_type     = 'hfmp'; % element pattern type
N_modes     = N_mm*Nx*Ny; % total number of modes

% define beam scan properties
theta_scan  = 60; % theta scan angle
phi_scan    = 180; % phi scan angle
beam_bw     = [10, 10]; % beam width properties
                        % [theta_bw, phi_bw]

% initialize spherical coordinate system
dtheta      = 4;
theta       = dtheta:dtheta:(90-dtheta);
dphi        = 4;
phi         = dphi:dphi:(360-dtheta);
Nt          = length(theta);
Np          = length(phi);
[P T]       = meshgrid(phi*deg2rad,theta*deg2rad);

for ts = 1:length(theta_scan)
    for ps = 1:length(phi_scan)

        %%%%%%%%%%%%%%%%%%%%%%%%%%%%%%%%%%%%%%%%%%%%%%
        % INITIALIZE RADIATION PATTERNS
        %%%%%%%%%%%%%%%%%%%%%%%%%%%%%%%%%%%%%%%%%%%%%%
        % beam steering parameters
        beam_pos    = [phi_scan(ps), theta_scan(ts)];

        % load desired array pattern
        AF_desired  = load_desired_planar_pattern...
            (beam_bw, beam_pos, T, P);
```

```
        % load element radiation patterns
        mm_mode_pattern = load_element_pattern_rev2...
            (el_type, N_modes, T, P, Nx, Ny, dx,...
            dy, N_mm);

        %%%%%%%%%%%%%%%%%%%%%%%%%%%%%%%%%%%%%%%%%%%%%%
        % SPHERICAL HARMONIC ANALYSIS AND SYNTHESIS
        %%%%%%%%%%%%%%%%%%%%%%%%%%%%%%%%%%%%%%%%%%%%%%
        [AF_sph_x AF_sph_y AF_sph_z...
            AF_mm_x AF_mm_y AF_mm_z] = ...
            spherical_synth(T, P, L, N_modes,...
            mm_mode_pattern, AF_desired);

        % convert cartesian into spherical coordinates
        %% reconstructed desired pattern from
        %% multiple mode elements
        [AF_mm_t AF_mm_p AF_mm_r] = xyz2tpr...
            (T, P, AF_mm_x, AF_mm_y, AF_mm_z);

        % find any NaN values and set them to zero
        AF_mm = sqrt(abs(AF_mm_p).^2 + abs(AF_mm_t).^2);
        nan_ind = find(isnan(AF_mm));
        AF_mm(nan_ind) = 0;

        %% reconstructed desired pattern from SPH
        [AF_sph_t AF_sph_p AF_sph_r] = xyz2tpr(T, P,...
            AF_sph_x, AF_sph_y, AF_sph_z);
        AF_sph = sqrt(abs(AF_sph_t).^2 + abs(AF_sph_p).^2);

        %% desired patterm
        [AF_desired_t AF_desired_p AF_desired_r] =...
```

```
            xyz2tpr(T, P, AF_desired(1:length(theta),:),...
            AF_desired(length(theta)+1:2*length(theta),:),...
            AF_desired(2*length(theta)+1:3*length(theta),:));
        AF_desired = sqrt(abs(AF_desired_p).^2 +...
            abs(AF_desired_t).^2);
        AF_desired = AF_desired/max(max(abs(AF_desired)));
        AF_sph = AF_sph/max(max(abs(AF_sph)));
        AF_mm = AF_mm/max(max(abs(AF_mm)));

        %%%%%%%%%%%%%%%%%%%%%%%%%%%%%%%%%%%%%%%%%%%%%%
        % COMPUTE ARRAY PATTERN PROPERTIES
        %%%%%%%%%%%%%%%%%%%%%%%%%%%%%%%%%%%%%%%%%%%%%%
        %% peak directivity
        D_peak(ps,ts) = pattern_directivity...
            (20*log10(abs(AF_mm)),P,T)
        peak_ind = find(20*log10(abs(AF_mm)) ==...
            max(max(20*log10(abs(AF_mm)))));
        ts_peak(ps,ts) = T(peak_ind(1));
        ps_peak(ps,ts) = P(peak_ind(1));

    end
end

%%%%%%%%%%%%%%%%%%%%%%%%%%%%%%%%%%%%%%%%%%%%%%
%   WRITE ARRAY PATTERN PROPERTIES TO FILE
%%%%%%%%%%%%%%%%%%%%%%%%%%%%%%%%%%%%%%%%%%%%%%
csvwrite([num2str(Nx) 'x' num2str(Ny) 'x'...
    num2str(N_mm) '_scan.csv'],...
    [D_peak; ts_peak; ps_peak]);

%%%%%%%%%%%%%%%%%%%%%%%%%%%%%%%%%%%%%%%%%%%%%%
```

```
%   3D DIRECTIVITY PLOTS
%%%%%%%%%%%%%%%%%%%%%%%%%%%%%%%%%%%%%%%%%%%%%%
figure
imagesc(theta_scan,phi_scan,D_peak',[10 20])
title([el_type ' (' num2str(Nx) '\times'...
    num2str(Ny) ')'],'fontsize',fontsize,...
    'fontname','times')
c = colorbar
set(get(c,'ylabel'), 'string','D (dB)',...
    'fontsize', fontsize, 'fontname',...
    'times','linewidth',linewidth)
set(c,'linewidth',linewidth)
xlabel('\phi (deg)','fontsize',fontsize,...
    'fontname','times')
ylabel('\theta (deg)','fontsize',fontsize,...
    'fontname','times')
set(gca, 'linewidth',linewidth,'fontsize',...
    fontsize,'fontname','times')



%%%%%%%%%%%%%%%%%%%%%%%%%%%%%%%%%%%%%%%%%%%%%%
%   3D PATTERN PLOTS
%%%%%%%%%%%%%%%%%%%%%%%%%%%%%%%%%%%%%%%%%%%%%%
%% desired array pattern
figure
imagesc(phi,theta,20*log10(abs(AF_desired))...
    ,[-30 0])
title('Desired','fontsize',fontsize,...
    'fontname','times')
c = colorbar
set(get(c,'ylabel'), 'string','D (dB)',...
```

```
    'fontsize', fontsize, 'fontname',...
    'times','linewidth',linewidth)
set(c,'linewidth',linewidth)
xlabel('Elevation Scan Angle (deg)',...
    'fontsize',fontsize,'fontname','times')
ylabel('Number of Modes','fontsize',...
    fontsize,'fontname','times')
set(gca, 'linewidth',linewidth,'fontsize',...
    fontsize,'fontname','times')

%% reconstructed array pattern from SPH
figure
imagesc(phi,theta,20*log10(abs(AF_sph)),...
    [-30 0])
title('Sph Harm','fontsize',fontsize,...
    'fontname','times')
c = colorbar
set(get(c,'ylabel'), 'string','D (dB)',...
    'fontsize', fontsize, 'fontname',...
    'times','linewidth',linewidth)
set(c,'linewidth',linewidth)
xlabel('Elevation Scan Angle (deg)',...
    'fontsize',fontsize,'fontname','times')
ylabel('Number of Modes','fontsize',...
    fontsize,'fontname','times')
set(gca, 'linewidth',linewidth,'fontsize',...
    fontsize,'fontname','times')

%% reconstructed array pattern from
%% multiple mode elements
figure
```

```
imagesc(phi,theta,20*log10(abs(AF_mm)),...[-30 0])
title('Multiple Mode','fontsize',fontsize,...
    'fontname','times')
c = colorbar
set(get(c,'ylabel'), 'string','D (dB)',...
    'fontsize', fontsize, 'fontname',...
    'times','linewidth',linewidth)
set(c,'linewidth',linewidth)
xlabel('Elevation Scan Angle (deg)',...
    'fontsize',fontsize,'fontname','times')
ylabel('Number of Modes','fontsize',fontsize,'fontname','times')
set(gca, 'linewidth',linewidth,'fontsize',...
    fontsize,'fontname','times')
```

Appendix B

Schematic Diagrams

B.1 4-Channel Active Feed Board

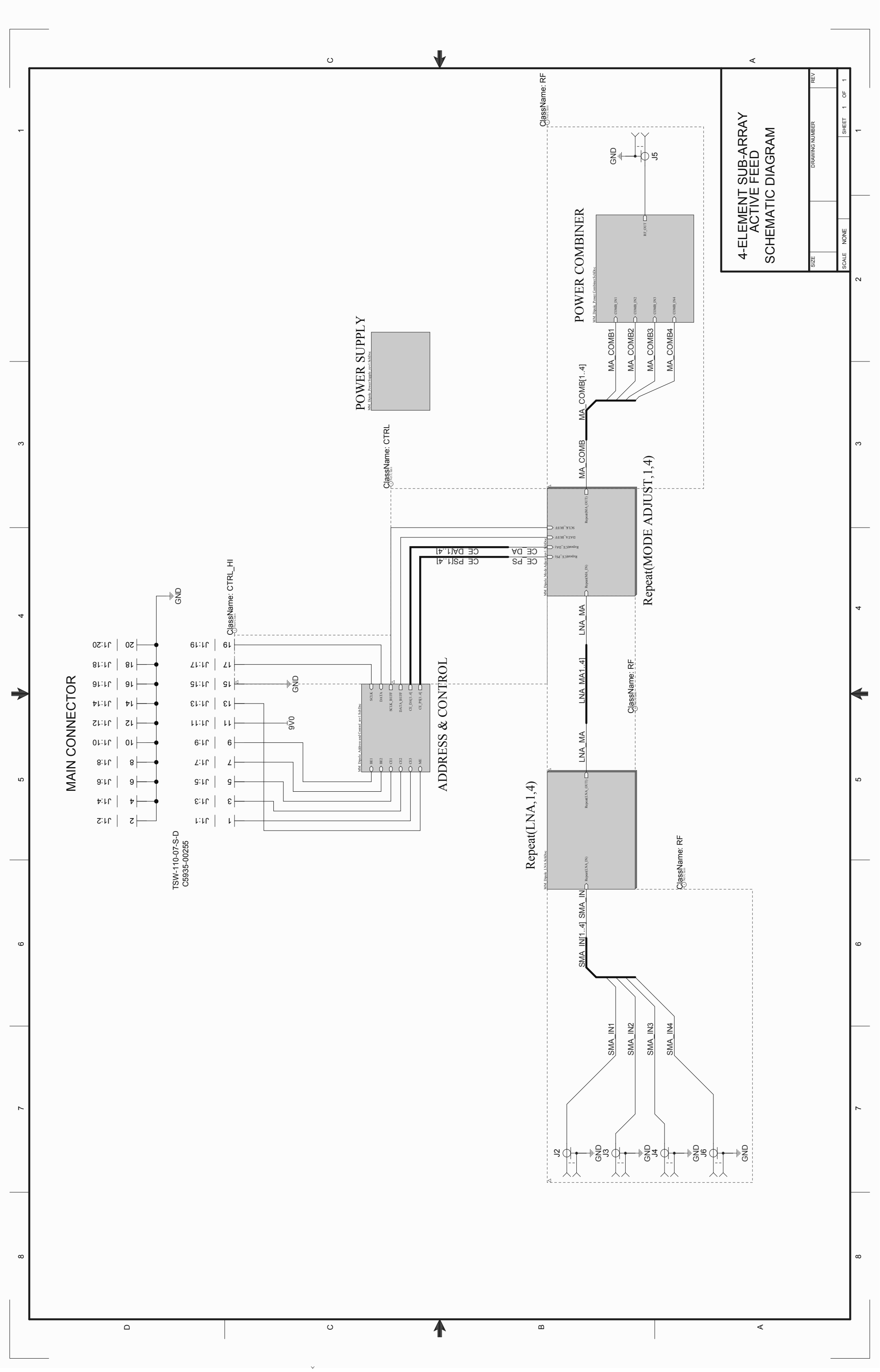
4-ELEMENT SUB-ARRAY
ACTIVE FEED
SCHEMATIC DIAGRAM
SIZE
SCALE NONE
DRAWING NUMBER
REV
SHEET 1 OF 1
MAIN CONNECTOR
TSW-110-07-S-D
C5935-00255
J1:1
J1:2
J1:3
J1:4
J1:5
J1:6
J1:7
J1:8
J1:9
J1:10
J1:11
J1:12
J1:13
J1:14
J1:15
J1:16
J1:17
J1:18
J1:19
J1:20
GND
9V0
ClassName: CTRL_HI
ADDRESS & CONTROL
CE_DA[1..4]
CE_PS[1..4]
CE_DA
CE_PS
ClassName: CTRL
POWER SUPPLY
Repeat(MODE ADJUST,1,4)
MA_COMB
MA_COMB[1..4]
MA_COMB1
MA_COMB2
MA_COMB3
MA_COMB4
POWER COMBINER
J5
ClassName: RF
LNA_MA
LNA_MA[1..4]
Repeat(LNA,1,4)
SMA_IN
SMA_IN[1..4]
SMA_IN1
SMA_IN2
SMA_IN3
SMA_IN4
J2
J3
J4
J6
A
B
C
D
1
2
3
4
5
6
7
8

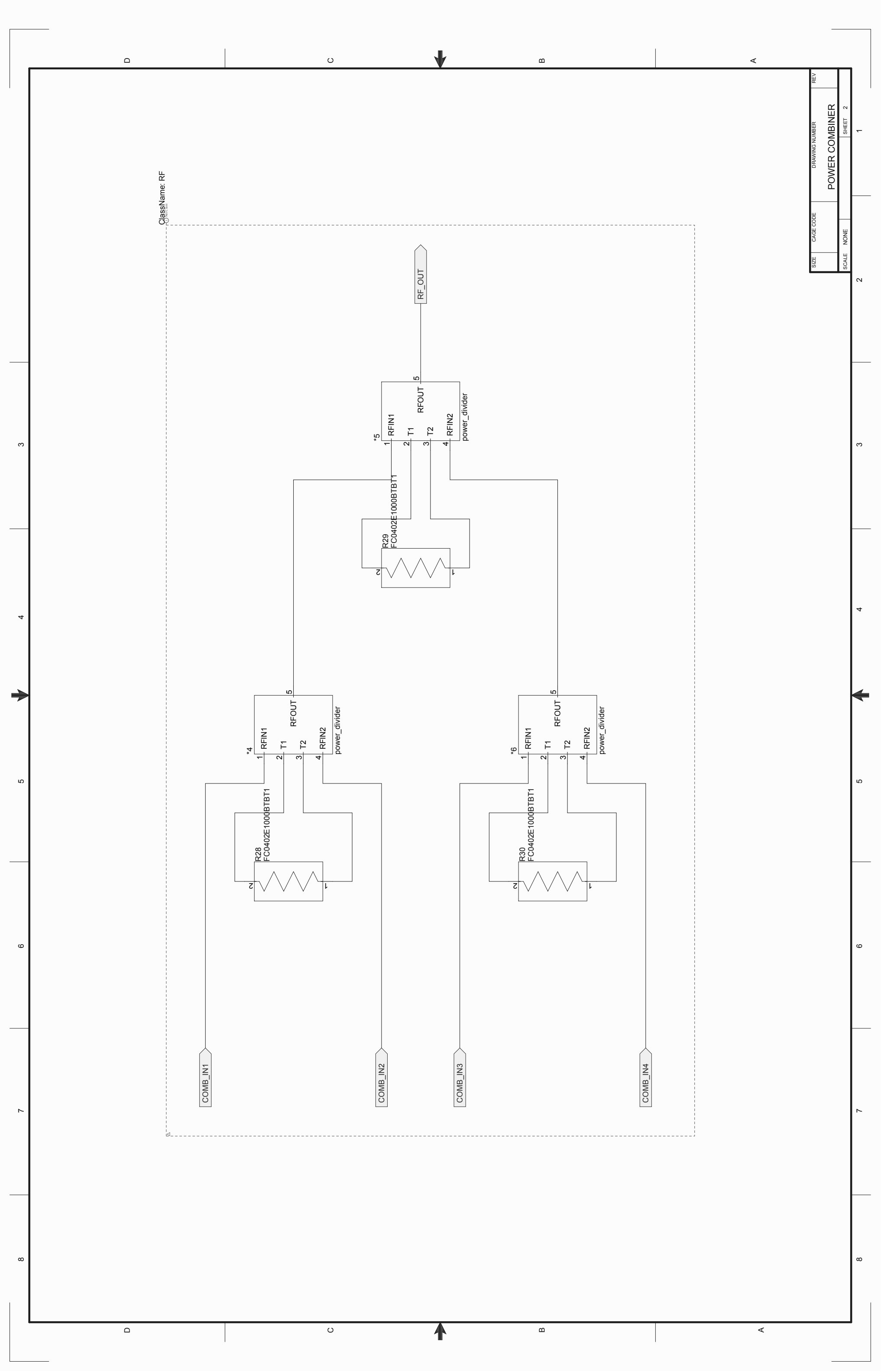
ClassName: RF
RF_OUT
RFOUT
RFIN1
T1
T2
RFIN2
power_divider
*5
*4
*6
R29
R28
R30
FC0402E1000BTBT1
COMB_IN1
COMB_IN2
COMB_IN3
COMB_IN4
SIZE
CAGE CODE
DRAWING NUMBER
POWER COMBINER
REV
SCALE
NONE
SHEET 2
1

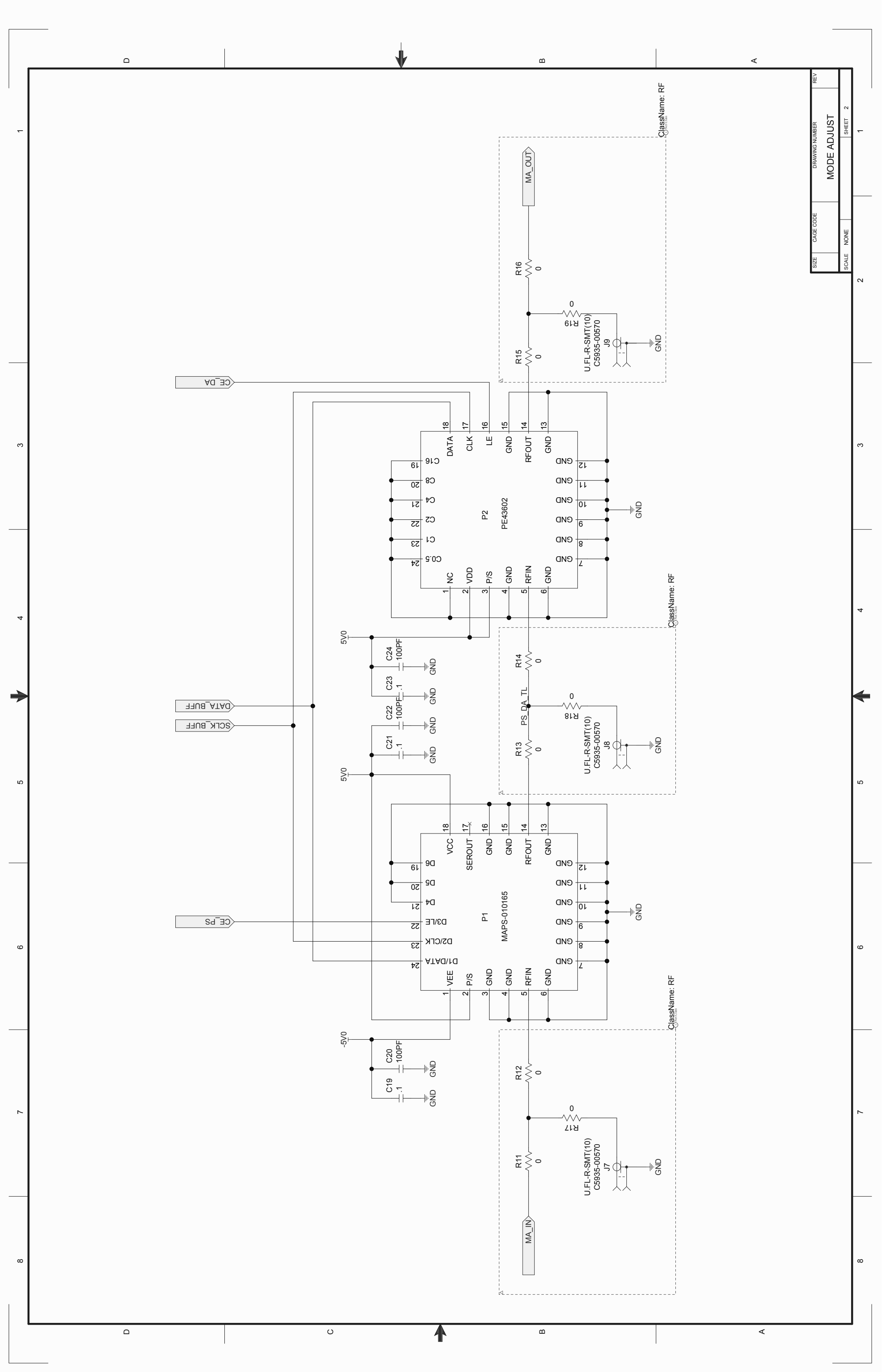
MODE ADJUST
DRAWING NUMBER
SIZE
CAGE CODE
SCALE NONE
SHEET 2
REV
P2
PE43602
DATA
CLK
LE
GND
RFOUT
C16
C8
C4
C2
C1
C0.5
NC
VDD
P/S
RFIN
P1
MAPS-010165
VCC
SEROUT
D6
D5
D4
D3/LE
D2/CLK
D1/DATA
VEE
CE_DA
CE_PS
DATA_BUFF
SCLK_BUFF
MA_OUT
MA_IN
PS_DA_TL
5V0
-5V0
C19 .1
C20 100PF
C21 .1
C22 100PF
C23 .1
C24 100PF
R11 0
R12 0
R13 0
R14 0
R15 0
R16 0
R17 0
R18 0
R19 0
J7
J8
J9
U.FL-R-SMT(10)
C5935-00570
GND
ClassName: RF

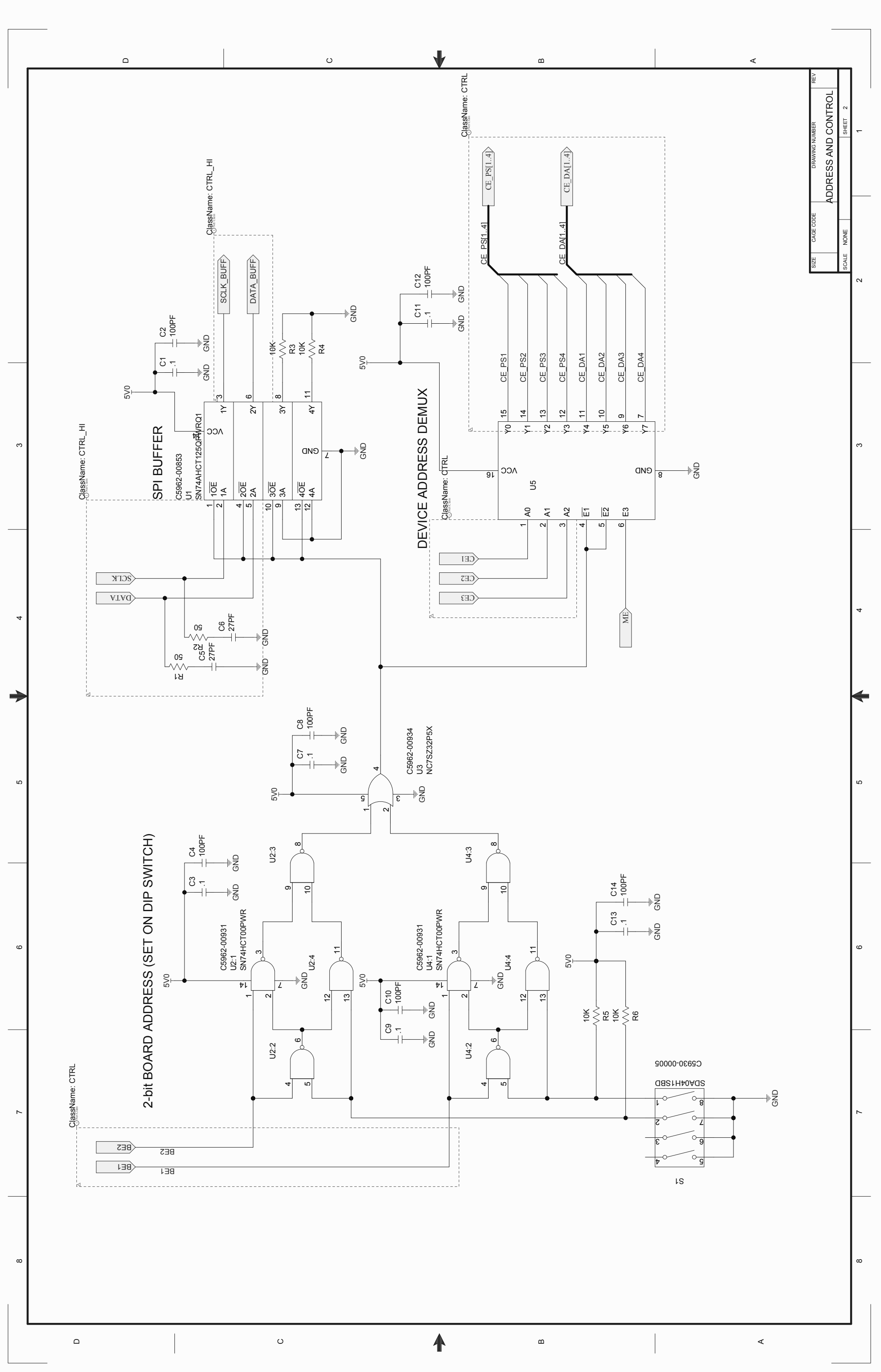
ADDRESS AND CONTROL
DRAWING NUMBER
CAGE CODE
SIZE
SCALE NONE
SHEET 2
REV
SPI BUFFER
C5962-00853
U1
SN74AHCT125QPWRQ1
ClassName: CTRL_HI
SCLK_BUFF
DATA_BUFF
SCLK
DATA
C1 .1
C2 100PF
R1 50
R2 50
C5 27PF
C6 27PF
R3 10K
R4 10K
5V0
GND
DEVICE ADDRESS DEMUX
U5
ClassName: CTRL
CE1
CE2
CE3
ME
CE_PS[1..4]
CE_DA[1..4]
CE_PS1
CE_PS2
CE_PS3
CE_PS4
CE_DA1
CE_DA2
CE_DA3
CE_DA4
C11 .1
C12 100PF
C5962-00934
U3
NC7SZ32P5X
C7 .1
C8 100PF
2-bit BOARD ADDRESS (SET ON DIP SWITCH)
C5962-00931
U2:1
SN74HCT00PWR
U2:2
U2:3
U2:4
U4:1
U4:2
U4:3
U4:4
C3 .1
C4 100PF
C9 .1
C10 100PF
C13 .1
C14 100PF
R5 10K
R6 10K
S1
SDA04H1SBD
C5930-00005
BE1
BE2
A
B
C
D
1
2
3
4
5
6
7
8

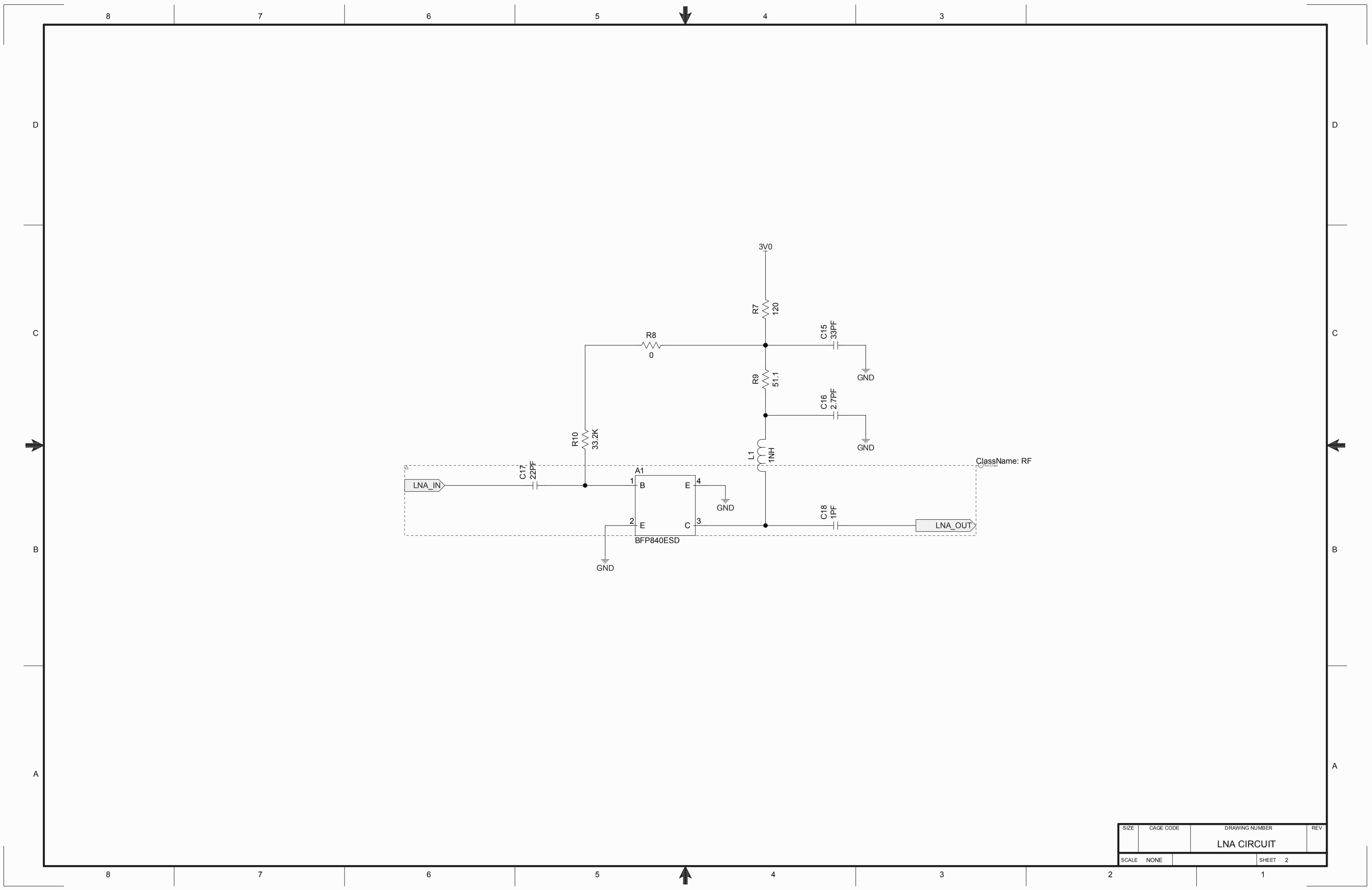
3V0
R7
120
R8
0
C15
33PF
GND
R9
51.1
C16
2.7PF
GND
R10
33.2K
L1
1NH
ClassName: RF
LNA_IN
C17
22PF
A1
1
B
E
4
GND
2
E
C
3
BFP840ESD
GND
C18
1PF
LNA_OUT
8
7
6
5
4
3
2
1
D
C
B
A
SIZE
CAGE CODE
DRAWING NUMBER
REV
LNA CIRCUIT
SCALE
NONE
SHEET
2

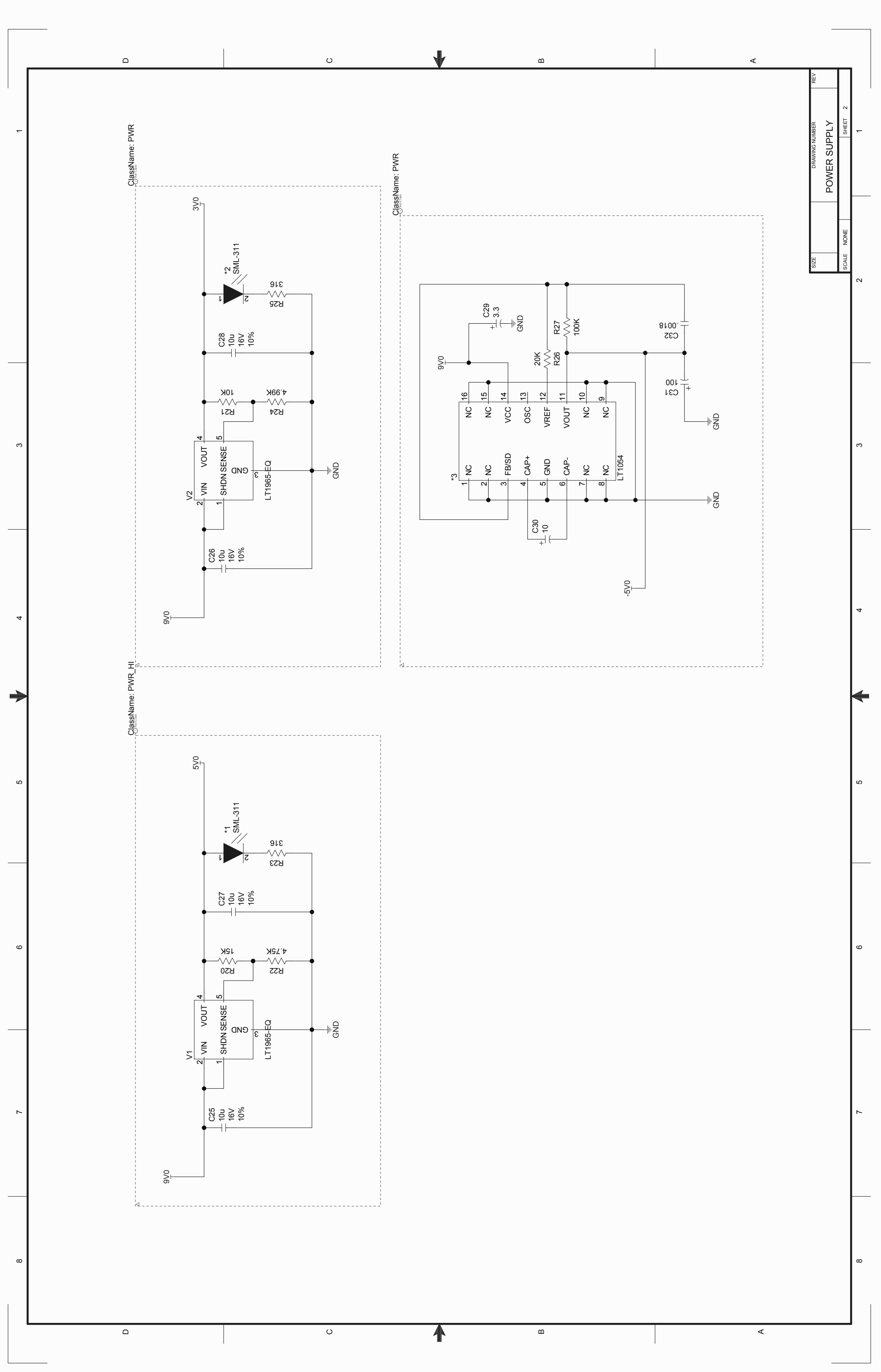
ClassName: PWR
3V0
*2
SML-311
R25
316
C28
10u
16V
10%
R21
10K
R24
4.99K
V2
VIN
SHDN
SENSE
VOUT
GND
LT1965-EQ
GND
C26
10u
16V
10%
9V0
ClassName: PWR_HI
5V0
*1
SML-311
R23
316
C27
10u
16V
10%
R20
15K
R22
4.75K
V1
VIN
SHDN
SENSE
VOUT
GND
LT1965-EQ
GND
C25
10u
16V
10%
9V0
ClassName: PWR
C29
3.3
GND
9V0
20K
R26
R27
100K
C32
.0018
C31
100
GND
*3
NC
NC
FB/SD
CAP+
GND
CAP-
NC
NC
LT1054
NC
NC
VCC
OSC
VREF
VOUT
NC
NC
C30
10
GND
-5V0
DRAWING NUMBER
POWER SUPPLY
SIZE
SCALE
NONE
SHEET
2
REV
A
B
C
D
1
2
3
4
5
6
7
8

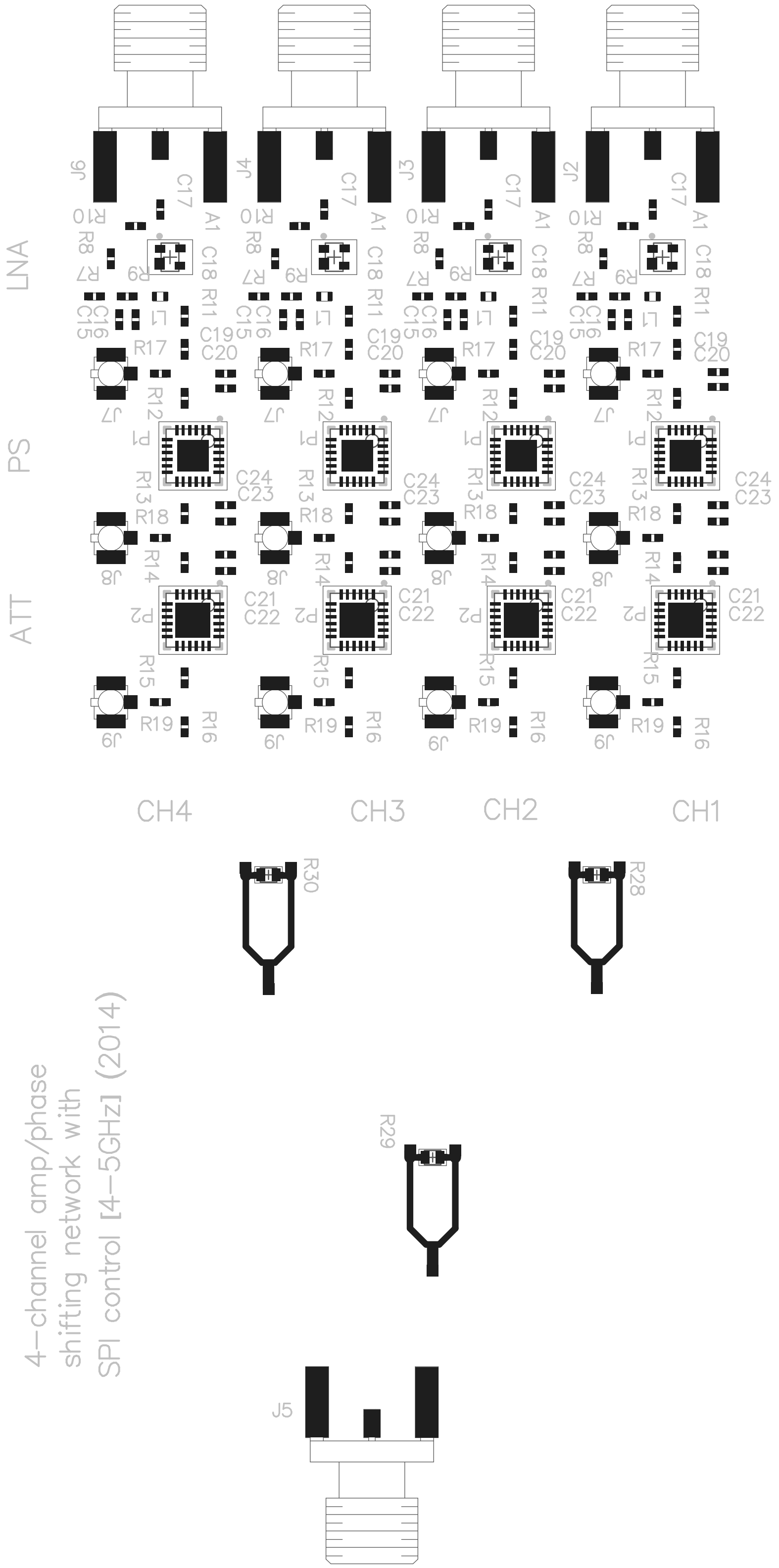
LNA
PS
ATT
J6
J4
J3
J2
C17
A1
R10
R8
R7
R9
C18
R11
C15
C16
L1
C19
C20
R17
J7
R12
P1
R13
C24
C23
R18
J8
R14
P2
C21
C22
R15
J9
R19
R16
CH4
CH3
CH2
CH1
R30
R28
R29
J5
4-channel amp/phase
shifting network with
SPI control [4-5GHz] (2014)

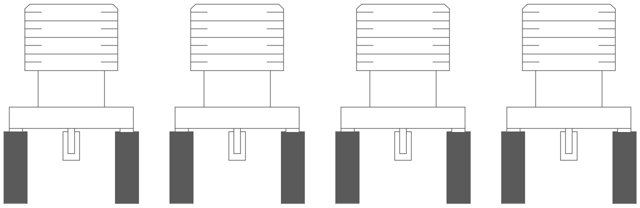

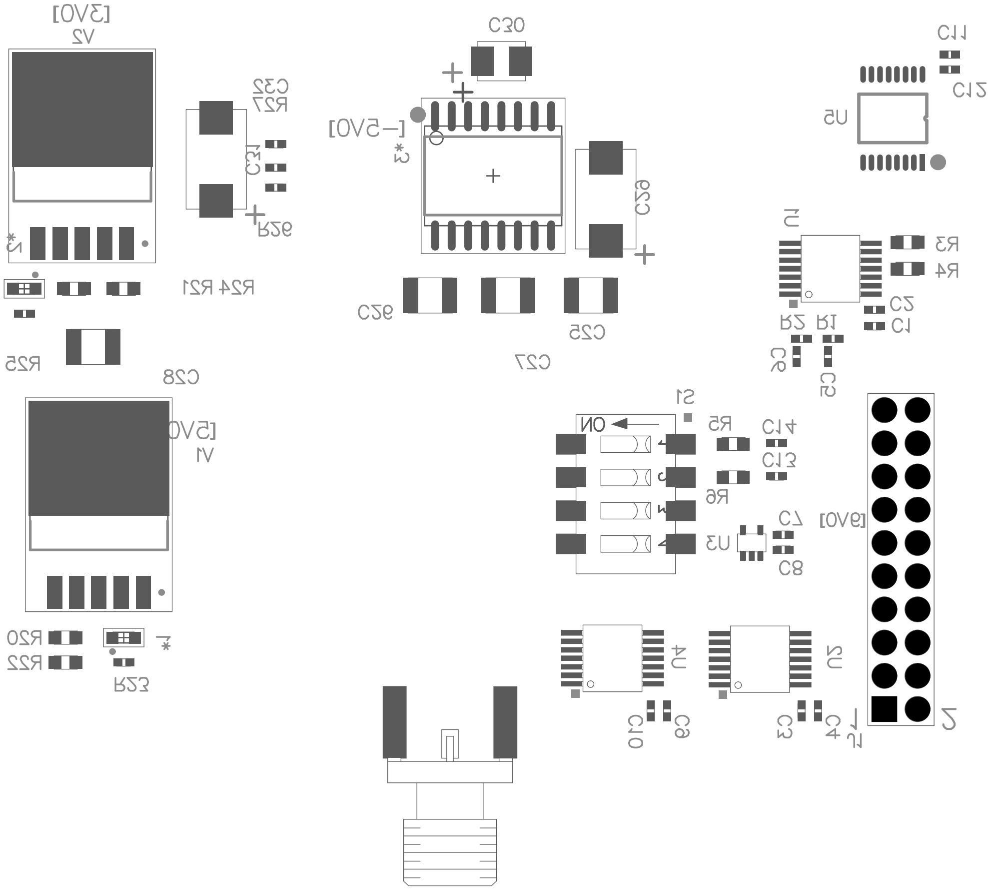
[3V0]
V2
C30
C32
R27
C31
R26
[-5V0]
*3
C29
C11
C12
U5
U1
R3
R4
C2
C1
R2
R1
C6
C5
R24 R21
R25
C28
C26
C25
C27
*1
S1
ON
R5
C14
C13
R6
C7
[6V0]
U3
C8
[5V0]
V1
R20
R22
R23
*2
U4
U2
C10
C9
C3
C4
J1
J2

Bibliography

[1] W. Massie and C. Underhill, *Wireless Telegraphy and Telephony Popularly Explained.* D. Van Nostrand, 1911.

[2] D. Sengupta and T. Sarkar, “Maxwell, hertz, the maxwellians, and the early history of electromagnetic waves,” *IEEE Antennas Propag. Mag.*, vol. 45, pp. 13–19, April 2003.

[3] H. Sobol, “Microwave communications - an historical perspective,” *IEEE Trans. Microw. Theory Techn.*, vol. 32, pp. 1170–1181, September 1984.

[4] R. F. Harrington, “Matrix methods for field problems,” *Proceedings of the IEEE*, vol. 55, pp. 136–149, Feb 1967.

[5] A. Taflove and S. Hagness, *Computational Electrodynamics: The Finite-difference Time-domain Method.* Artech House antennas and propagation library, Artech House, 2005.

[6] R. Coccioli, T. Itoh, G. Pelosi, and P. Silvester, “Finite-element methods in microwaves: a selected bibliography,” *IEEE Antennas Propag. Mag.*, vol. 38, pp. 34–48, Dec 1996.

[7] “Ferdinand braun - biographical.” http://www.nobelprize.org/nobel_prizes/physics/laureates/1909/braun-bio.html. Accessed: 2015-01-12.

[8] R. Hansen, *Phased Array Antennas.* Wiley Series in Microwave and Optical Engineering, Wiley, 1998.

[9] A. Ludwig, “Mutual coupling, gain and directivity of an array of two identical antennas,” *IEEE Trans. Antennas Propag.*, vol. 24, pp. 837–841, Nov. 1976.

[10] H.-S. Lui, H. T. Hui, and M.-S. Leong, “A note on the mutual-coupling problems in transmitting and receiving antenna arrays,” *IEEE Antennas Propag. Mag.*, vol. 51, pp. 171–176, Oct 2009.

[11] D. Pozar, “The active element pattern,” *IEEE Trans. Antennas Propag.*, vol. 42, pp. 1176–1178, Aug 1994.

[12] D. Kelley, “Relationships between active element patterns and mutual impedance matrices in phased array antennas,” in *IEEE Antennas and Propagation Society International Symposium*, vol. 1, pp. 524–527 vol.1, 2002.

[13] C. A. Balanis, *Antenna Theory*. John Wiley and sons, 2005.

[14] S. Stein, “On cross coupling in multiple-beam antennas,” *IRE Trans. Antennas Propag.*, vol. 10, pp. 548–557, Sept. 1962.

[15] A. Rudge, *The Handbook of Antenna Design*. No. v. 1 in IEE electromagnetic waves series, P. Peregrinus, 1982.

[16] L. J. Chu, “Physical limitations of omnidirectional antennas,” *J, Appl. Phys.*, vol. 19, pp. 1163–1175, Dec. 1948.

[17] R. F. Harrington, “Effect of antenna size on gain, bandwidth and efficiency,” *J. Res. Nat. Bur. Stand.-D*, vol. 64D, pp. 1–12, Jan.-Feb. 1960.

[18] R. F. Harrington and J. R. Mautz, “Computation of characteristic modes for conducting bodies,” *IEEE Trans. Antennas Propag.*, vol. 19, pp. 629–639, Sept. 1971.

[19] R. F. Harrington and J. R. Mautz, “Characteristic modes for dielectric and magnetic bodies,” *IEEE Trans. Antennas Propag.*, vol. 20, pp. 194–198, March 1972.

[20] M. C. Fabres, *Systematic Design of Antennas Using the Theory of Characteristic Modes*. PhD thesis, Universidad Polytecnica De Valencia, Feb. 2007.

[21] E. Antonino-Daviu, M. Cabedo-Fabres, M. Gallo, M. Ferrando-Bataller, and M. Bozzetti, “Design of a multimode mimo antenna using characteristic modes,” in *3rd European Conference on Antennas and Propagation (EuCAP)*, pp. 1840–1844, March 2009.

[22] T. Svantesson, “An antenna solution for mimo channels: the multimode antenna,” in *Conference Record of the Thirty-Fourth Asilomar Conference on Signals, Systems and Computers*, vol. 2, pp. 1617–1621 vol.2, Oct 2000.

[23] T. Svantesson, “Correlation and channel capacity of mimo systems employing multimode antennas,” *IEEE Trans. Veh. Technol.*, vol. 51, pp. 1304–1312, Nov 2002.

[24] C. Waldschmidt and W. Wiesbeck, “Compact wide-band multimode antennas for mimo and diversity,” *IEEE Tras. Antennas Propag.*, vol. 52, pp. 1963–1969, Aug 2004.

[25] A. Forenza and R. Heath, “Benefit of pattern diversity via two-element array of circular patch antennas in indoor clustered mimo channels,” *IEEE Trans. Commun.*, vol. 54, pp. 943–954, May 2006.

[26] A. Mukherjee and H. Kwon, "Compact multi-user wideband mimo system using multiple-mode microstrip antennas," in *IEEE 65th Vehicular Technology Conference*, pp. 584–588, April 2007.

[27] O. Klemp and H. Eul, "Factors affecting the diversity performance of multimode antennas in directive channel scenarios," in *IEEE Antennas and Propagation Society International Symposium*, pp. 1353–1356, June 2007.

[28] N. Herscovici, C. Christodoulou, E. Rajo-Iglesias, O. Quevedo-Teruel, and M. Sanchez-Fernandez, "Compact multimode patch antennas for mimo applications [wireless corner]," *IEEE Antennas Propag. Mag.*, vol. 50, pp. 197–205, April 2008.

[29] C. Jayasooriya, H. Kwon, S. Bae, and Y.-K. Hong, "Miniaturized multimode circular patch antennas for mimo communications," in *IEEE 70th Vehicular Technology Conference*, pp. 1–5, Sept 2009.

[30] A. Ocalan, A. Savasinabes, I. Gorge, O. Ertug, and E. Yazgan, "Compact space-multimode diversity stacked circular microstrip antenna array for 802.11n mimo-ofdm wlans," in *Antennas Propagation Conference (LAPC)*, pp. 525–528, Nov 2009.

[31] A. Besoli and F. De Flaviis, "Performance evaluation of a reconfigurable multimode pixeled antenna in indoor clustered mimo channels," in *URSI General Assembly and Scientific Symposium*, pp. 1–3, Aug 2011.

[32] J. Sarrazin, Y. Mahe, S. Avrillon, and S. Toutain, "A new multimode antenna for mimo systems using a mode frequency convergence concept," *IEEE Trans. Antennas Propag.*, vol. 59, pp. 4481–4489, Dec 2011.

[33] C. Redondo and L. de Haro, "On the analysis and design of reconfigurable multimode mimo microstrip antennas," *IEEE Trans. Antennas Propag.*, vol. 62, pp. 119–129, Jan 2014.

[34] S.-L. Yang and K.-M. Luk, "A wideband l-probe fed patch antenna for pattern reconfiguration," in *IEEE Antennas and Propagation Society International Symposium*, vol. 2B, pp. 581–584, July 2005.

[35] B. D. Raines, *Systematic Design of Multiple Antenna Systems Using Characteristic Modes*. PhD thesis, The Ohio State University, 2011.

[36] L. Shafai, "Scan gain enhancement in phased arrays by element pattern synthesis," in *IEE Seventh International Conference on Antennas and Propagation (ICAP)*, vol. 2, pp. 914–917, Apr 1991.

[37] P.-F. Z. H. W. Yuan, S.-X. Gong and X. Wang, "Wide scanning phased array antenna using printed dipole antennas with parasitic element," *Progress in Electromagnetics Reseach Letters*, vol. 2, pp. 187–193, 2008.

[38] Y.-Y. Bai, S. Xiao, M.-C. Tang, Z.-F. Ding, and B.-Z. Wang, "Wide-angle scanning phased array with pattern reconfigurable elements," *IEEE Trans. Antennas Propag.*, vol. 59, pp. 4071–4076, Nov 2011.

[39] J. Wu, C. Chang, T. Chin, S. Huang, and S. Chang, "Sidelobe level reduction in wide-angle scanning array system using pattern-reconfigurable antennas," in *IEEE International Microwave Symposium Digest (MTT-S)*, pp. 1–1, May 2010.

[40] S. Zhang, G. Huff, J. Feng, and J. T. Bernhard, "A pattern reconfigurable microstrip parasitic array," *IEEE Trans. Antennas Propag.*, vol. 52, pp. 2773–2776, Oct 2004.

[41] MATLAB, *version 8.3.0.532 (R2014a).* Natick, MA: The MathWorks Inc., 2014.

[42] HFSS, *version 14.* Canonsburg, PA: Ansys, 2014.

[43] LPKF Laser and Electronics AG, Osteriede 7, D-30827 Garbsen, *Manual: ProtoMat S42*, english, version 2.0 ed., 2006.

[44] Anritsu Corporation, 5-1-1 Onna, Atsugi-shi, Kanagawa, 243-8555 Japan, *Technical Datasheet and Configuration Guide: Lightning*, english, rev. c ed., 2007.

[45] G. S. Smith, "Loop antennas," in *Antenna Engineering Handbook* (J. Volakis, ed.), McGraw-Hill, 2007.

[46] B. Bai and Z. H. Feng, "A dual band meandering folded loop antenna," in *IEEE Antennas and Propagation Society International Symposium*, pp. 4304–4307, June 2004.

[47] K. Subramaniam, M. Esa, and S. Subahir, "Compact printed square meander loop antenna for a bluetooth headset," in *Asia-Pacific Conference on Applied Electromagnetics (APACE)*, pp. 5 pp.–, Dec 2005.

[48] C.-I. Lin and K.-L. Wong, "Internal meandered loop antenna for multiband mobile phone with the user's hand," in *IEEE Antennas and Propagation Society International Symposium*, pp. 3572–3575, June 2007.

[49] Y.-W. Chi and K.-L. Wong, "Compact multiband folded loop chip antenna for small-size mobile phone," *IEEE Trans. Antennas Propag.*, vol. 56, pp. 3797–3803, Dec. 2008.

[50] S. Tanaka, S. Hayashida, H. Morishita, and Y. Atsumi, "Wideband and compact folded loop antenna," *Electronics Letters*, vol. 41, pp. 945–946, Aug. 2005.

[51] N. R. Labadie and S. K. Sharma, "A novel volumetric folded ring resonator metamaterial structure," in *IEEE International Microwave Symposium Digest (MTT)*, pp. 1580–11583, May 2010.

[52] N. R. Labadie and S. K. Sharma, "A novel compact volumetric metamaterial structure with asymmetric transmission and polarization conversion," *Metamaterials*, vol. 4, pp. 44–57, May 2010.

[53] A. Voors, *4NEC2: NEC based antenna modeler and optimizer*. rev. 5.8.1.

[54] H. E. Green, "A simplified derivation of the capacitance of a two-wire transmission line," *IEEE Trans. Microw. Theory Techn.*, vol. 47, pp. 365–366, Mar. 1999.

[55] S. I. Babic and C. Akyel, "Calculating mutual inductance between circular coils with inclined axes in air," *IEEE Trans. Magn.*, vol. 44, July 2008.

[56] L. M. Milne-Thomson, "Elliptic integrals," in *Handbook of Mathematical Functions* (M. Abramowitz and I. A. Stegun, eds.), National Bureau of Standards, 1972.

[57] M. Trinkle and W.-C. Cheuk, "Null-steering gps dual-polarised antenna arrays," in *The 6th International Symposium on Satellite Navigation Technology Including Mobile Positioning and Location Services*, pp. 1580–11583, May 2003.

[58] M. Clenet, D. Roy, and D. Lee, "Arrays of 4 circularly polarised aperture-coupled-fed stacked patch antennas for gps interference mitigation," in *ANTEM/URSI 13th Int. Symp. on Ant. Tech. and App. Elect. and the Canadian Radio Science Meeting*, pp. 1580–11583, May 2009.

[59] P. Niemand, *Null Synthesis and Implementation of Cylindrical Microstrip Patch Arrays*. PhD thesis, University of Pretoria, August 2004.

[60] N. L. Scott, M. O. Leonard-Taylor, and R. G. Vaughan, "Diversity gain from a single-port adaptive antenna using switched parasitic elements illustrated with a wire and monopole prototype," *IEEE Trans. Antennas Propag.*, vol. 47, pp. 1066–1070, Jun 1999.

[61] T. Ohira and K. Gyoda, "Electronically steerable passive array radiator antennas for low-cost analog adaptive beamforming," in *IEEE International Conference on Phased Array Systems and Technology*, pp. 101–104, 2000.

[62] J. Cheng, Y. Kamiya, and T. Ohira, "Adaptive beamforming of espar antenna using sequential perturbation," in *IEEE Microwave Symposium Digest (MTT-S)*, vol. 1, pp. 133–136, May 2001.

[63] C. Sun, A. Hirata, T. Ohira, and N. Karmakar, "Fast beamforming of electronically steerable parasitic array radiator antennas: theory and experiment," *IEEE Trans. Antennas Propag.*, vol. 52, pp. 1819–1832, July 2004.

[64] M. N. Solomon, "Multimode rectangular microstrip antenna for gps applications," in *IEEE-APS Conference on Antennas and Propagation for Wireless Communications*, pp. 149–151, Nov 1998.

[65] B. R. Rao and E. N. Rosario, "Spatial null steering microstrip antenna array," 07 2003.

[66] N. R. Labadie, S. K. Sharma, and G. Rebeiz, "Multimode antenna element with hemispherical beam peak and null steering," in *IEEE Antennas and Propagation Society International Symposium (APSURSI)*, pp. 1–2, July 2012.

[67] T. Q. Tran and S. K. Sharma, "Radiation characteristics of a multimode concentric circular microstrip patch antenna by controlling amplitude and phase of modes," *IEEE Trans. Antennas Propag.*, vol. 60, pp. 1601–1605, March 2012.

[68] N. R. Labadie, S. K. Sharma, and G. Rebeiz, "A circularly polarized multimode patch antenna with full hemispherical null steering for gps applications," in *IEEE International Symposium on Antennas and Propagation (ISAP)*, pp. 1309–1312, Oct 2012.

[69] Y. Lin and L. Shafai, "Characteristics of concentrically shorted circular patch microstrip antennas," *Microwaves, Antennas and Propagation, IEE Proceedings H*, vol. 137, pp. 18–24, Feb 1990.

[70] J. Huang, "Circularly polarized conical patterns from circular microstrip antennas," *IEEE Trans. Antennas Propag.*, vol. 32, pp. 991–994, Sep 1984.

[71] N. Labadie, S. Sharma, and G. Rebeiz, "A circularly polarized multiple radiating mode microstrip antenna for satellite receive applications," *IEEE Trans. Antennas Propag.*, vol. 62, pp. 3490–3500, July 2014.

[72] D. M. Pozar, "The active element pattern," *IEEE Trans. Antennas Propag.*, vol. 42, pp. 1176–1178, Aug 1994.

[73] E. Magill and H. A. Wheeler, "Wide-angle impedance matching of a planar array antenna by a dielectric sheet," in *Antennas and Propagation Society International Symposium*, vol. 3, pp. 164–169, Aug 1965.

[74] S. K. Sharma, A. Sebak, and L. Shafai, "Scan range enhancement using waim sheets for infinite planar waveguide phased array antennas," in *Symposium on Antenna Technology and Applied Electromagnetics (ANTEM 2000)*, vol. 30, pp. 213–216, July 2000.

[75] N. H. Noordin, T. Arslan, B. Flynn, and A. T. Erdogan, "Low-cost antenna array with wide scan angle property," *Microwaves, Antennas Propagation, IET*, vol. 6, pp. 1717–1727, December 2012.

[76] T. Q. Tran and S. K. Sharma, "Radiation characteristics of a multimode concentric circular microstrip patch antenna by controlling amplitude and phase of modes," *IEEE Trans. Antennas Propag.*, vol. 60, pp. 1601–1605, March 2012.

[77] N. R. Labadie, S. K. Sharma, and G. Rebeiz, "Multimode antenna element with hemispherical beam peak and null steering," in *Antennas and Propagation Society International Symposium (APSURSI), 2012 IEEE*, pp. 1–2, July 2012.

[78] N. R. Labadie, S. K. Sharma, and G. Rebeiz, "1d beam steering using multiple radiating modes," in *IEEE Antennas and Propagation Society International Symposium (APSURSI)*, pp. 1365–1366, July 2014.

[79] N. R. Labadie, S. K. Sharma, and G. Rebeiz, "Investigation of hybrid phased arrays composed of multiple mode subarrays," in *IEEE Antennas and Propagation Society International Symposium (APSURSI)*, pp. 1367–1368, July 2014.

[80] L. Kuehnke, "Phased array calibration procedures based on measured element patterns," in *IEE Eleventh International Conference on Antennas and Propagation*, vol. 2, pp. 660–663, 2001.

[81] M. I. Skolnik, *Introduction to Radar Systems*. 3rd ed.

[82] N. R. Labadie, S. K. Sharma, and G. M. Rebeiz, "A novel approach to beamforming using arrays composed of multiple unique radiating modes," *IEEE Trans. Antennas Propag.*, 2015 (under review).

[83] G. Del Galdo, J. Lotze, M. Landmann, and M. Haardt, "Modelling and manipulation of polarimetric antenna beam patterns via spherical harmonics," *14th Eur. Signal Processing Conf.(EUSIPCO), Florence, Italy*, 2006.

[84] J. Rahola, F. Belloni, and A. Richter, "Modelling of radiation patterns using scalar spherical harmonics with vector coefficients," in *3rd European Conference on Antennas and Propagation (EuCAP)*, pp. 3361–3365, March 2009.

[85] M. Hoffman, "The utility of the array pattern matrix for linear array computations," *IRE Trans. Antennas Propag.*, vol. 9, pp. 97–100, Jan. 1961.

[86] C. Deng, Y. Li, Z. Zhang, and Z. Feng, "A hemispherical 3-d null steering antenna for circular polarization," *IEEE Antennas Wireless Propag. Lett.*, vol. PP, no. 99, pp. 1–1, 2014.

[87] Y. Li, Z. Zhang, C. Deng, and Z. Feng, "A simplified hemispherical 2-d angular space null steering approach for linearly polarization," *IEEE Antennas Wireless Propag. Lett.*, vol. PP, no. 99, pp. 1–1, 2014.